UNIVERSIDADE FEDERAL DE SANTA CATARINA
CURSO DE PÓS-GRADUAÇÃO EM ENGENHARIA MECÂNICA

FABRICAÇÃO DE GRADIENTES FUNCIONAIS ENTRE AÇO FERRAMENTA E COBRE POR FUSÃO SELETIVA A LASER USANDO UM FEIXE DE LASER PULSADO Nd:YAG DE ALTA POTÊNCIA PARA APLICAÇÕES EM MOLDES DE INJEÇÃO

-

FABRICATION OF FUNCTIONAL GRADIENTS BETWEEN TOOL STEEL AND COPPER PARTS BY SELECTIVE LASER FUSION USING A HIGH POWER Nd:YAG PULSED LASER BEAM TO INJECTION MOULDS APPLICATIONS

Tese submetida à

UNIVERSIDADE FEDERAL DE SANTA CATARINA

para a obtenção do grau de

DOUTOR EM ENGENHARIA MECÂNICA

VALTER ESTEVÃO BEAL

Florianópolis, Dezembro de 2005

UNIVERSIDADE FEDERAL DE SANTA CATARINA
PROGRAMA DE PÓS-GRADUAÇÃO EM
ENGENHARIA MECÂNICA

FABRICAÇÃO DE GRADIENTES FUNCIONAIS ENTRE AÇO FERRAMENTA E COBRE POR FUSÃO SELETIVA A LASER USANDO UM FEIXE DE LASER PULSADO Nd:YAG DE ALTA POTÊNCIA PARA APLICAÇÕES EM MOLDES DE INJEÇÃO

-

VALTER ESTEVÃO BEAL

Esta tese foi julgada adequada para a obtenção do título de

DOUTOR EM ENGENHARIA

ESPECIALIDADE ENGENHARIA MECÂNICA
sendo aprovada em sua forma final.

____
Carlos Henrique Ahrens, Dr. Eng. – Orientador

____
Poonjolai Erasenthiran, PhD. – Coorientador

____
Paulo Antônio Wendhausen, Dr. Eng – Coorientador

____
José Antônio Bellini da Cunha Neto, Dr – Coordenador do Curso

Banca Examinadora

____
Paulo Antônio Wendhausen, Dr. Eng – Presidente

____
Alexandre Lago, PhD.

____
Gean Salmoria, Dr. Ing.

____
Jonas Carvalho, PhD.

____
Neri Volpato, PhD.

Work hard, play harder.
Unknown author

Make the most of your regrets…To regret deeply is to live afresh.
Henry David Thoreau

I would prefer to be climbing.
Unknown author

Aos meus Pais, Flávio e Isolde.

Meus irmãos Silvia e Tiago.

Ao meu amor, Aline.

Agradecimentos

Agradeço ao Programa de Pós-Graduação em Engenharia Mecânica da Universidade Federal de Santa Catarina, a Universidade de Loughborough, ao Ministério da Educação – CAPES, ao Ministério da Ciência e Tecnologia - CNPq e ao Engineering and Physical Sciences Research Council (EPSRC). Sem os apoios físicos, logísticos e financeiros destas estas instituições este trabalho não poderia ter sido realizado.

Agradeço em especial ao pessoal da UFSC: Luis Alberto Gomes, Frederic Dabbas, Bruno Alcântara, Marcelo Fraga, Luis Eraldo Pereira e Gean Vitor Salmoria.

Agradeço a todos os meus amigos e parentes, sem exceções, colegas da UFSC, da academia, de escaladas e de festas (não citarei nome para não deixar ninguém de fora!). Vocês deram em algum momento o suporte ou a descontração necessários para que eu pudesse restabelecer minhas energias. Saibam que sempre poderão contar comigo.

Ao pessoal do TNO Industrial Technology: Frits Feenstra, Rik Knoppers e Jeoren van den Hout.

Ao pessoal da Universidade de Loughborough: Andy Sandaver, Andy Norwwod, Peter Wileman, Rod Springthorpe , Bob Temple, Hadi Zarringhalam, Richard Moore, Uzoma Ajoko, Naguib Saleh entre tantos outros.

Aos professores, Carlos Henrique Ahrens, Alexandre Lago, Paulo Antônio Wendhausen, Neil Hopkinson e Phil Dickens.

Em especial, quero deixar meu agradececimento ao Raaja (Poonjolai Erasenthiran) pelo grande apoio recebido para a realização da minha pesquisa.

Acknowledgments

I would like to thank to Post-Grad program on Mechanical Engineering from Universidade Federal de Santa Catarina, to Loughborough University, to the Ministry of Education - CAPES, to the Ministry of Science an Technology - CNPq and to the Engineering and Physical Sciences Research Council (EPSRC). Without the physical, logistics and financial supports provided by these institutions this work would not be possible.

Especial thanks to people from UFSC: Luis Alberto Gomes, Frederic Dabbas, Bruno Alcântara, Marcelo Fraga, Luis Eraldo Pereira and Gean Vitor Salmoria.

Thanks to all my friends and parents, without exceptions friends from UFSC and LBORO, gym, climbing and parties (I will not cite names to do not leave anyone outside!). You gave moment the support or the distraction that I needed to replace my energies. You can count on me.

Thank to the TNO Industriial Prototyping: Frits Feenstra, Rik Knoppers & Jeoren van den Hout.

Thank to the people at Louoghborough University: Andy Sandaver, Andy Norwwod, Peter Wileman, Rod Springthorpe, Bob Temple, Hadi Zarringhalam, Richard Moore, Uzoma Ajoku, Naguib Saleh among many others.

Thank to the professors/lectures, Carlos Henrique Ahrens, Alexandre Lago, Paulo Antônio Wendhausen, Neil Hopkinson and Phil Dickens.

In special, I have to thank Raaja (Poonjolai Erasenthiran) for his great support for the realization of my research.

Atenção

O autor gostaria de anunciar que muitas partes deste trabalho têm sido usadas na publicação de artigos e em conferências. É esperado que sejam encontradas figuras, tabelas, gráficos, parágrafos e até mesmo tópicos inteiros com formatação mínima ou igual a trabalhos já publicados ou submetidos. De qualquer forma, todo o conteúdo é original do autor ou adaptado e referenciado a outros autores. No final deste trabalho, existe uma lista de artigos publicados e submetidos (ainda em avaliação por comitês técnicos) gerados a partir desta pesquisa até a data presente da versão final deste documento escrito.

Warning

The author would like to state that many parts of this work have been used in the publication of papers in journals and conferences. Figures, tables, graphs, paragraphs and even whole sections with minimal formatting or equal to already published or submitted papers are present in this text. Nevertheless, all content is original from the author or adapted and referenced to others authors. At the end of this work, there is a list of published and submitted (under evaluation of the technical committees) papers generated from this research until the present date of the final version of the written document.

Esclarecimento

Devido as regras da universidade na qual este trabalho foi defendido, o documento escrito do trabalho não pode estar em língua estrangeira. Como grande parte desse trabalho foi desenvolvido na Inglaterra, sob supervisão de pessoas que não compreendem a língua portuguesa, ele foi escrito em sua totalidade na língua inglesa. Para suprir as regras da universidade, ao final da tese, um resumo estendido do trabalho, em português, é apresentado. O autor compreende que é necessário que a produção científica nacional cresça, no entanto, para que ela seja reconhecida pelos outros países, ela deve ser de fácil acesso, o que é garantido pela língua inglesa, meio comum de comunicação entre os pesquisadores, cientistas e engenheiros do mundo inteiro.

Index

List of Figures xiv
List of Tables xviii
Abbreviations xx
Basic Elements Symbols xxi
Symbols and Units xxi
Resumo xxiii
Abstract xxv

1. Introduction ________ **3**

1.1. Research objective 6

1.2. Structure and organization 6

2. Literature Review ________ **11**

2.1. Rapid manufacturing 11
2.1.1. Additive Layered Manufacturing 12
2.1.2. Principles 12

2.2. Functionally graded materials 15
2.2.1. FGM Fundamentals 15
2.2.2. FGM microstructure 17
2.2.3. FGM design 19
2.2.4. Manufacturing technologies 19
2.2.5. Applications and trends 21
2.2.5.(a). Aerospace 22
2.2.5.(b). Medical 23
2.2.5.(c). Sporting goods 24
2.2.5.(d). Dies and tools 25

2.3. Functionally graded materials by layered additive manufacturing technologies 25
2.3.1. Software 25
2.3.2. Local Composition Control 27
2.3.3. Examples of FGM produced by additive layered manufacturing 28
2.3.3.(a). Dies/Moulds 28
2.3.3.(b). Biomedical developments on FGM 29

2.4. Models for estimating material properties of FGM structures 29
2.4.1. Estimations by the rules of mixtures 30
2.4.2. Variational approach: Hashin-Shtrikman principles 31
2.4.3. Micromechanical approaches 32
2.4.3.(a). Kerner 33
2.4.3.(b). Wakashima and Tsukamoto 33
2.4.3.(c). Ravichandran 34
2.4.4. Estimated properties 34
2.4.4.(a). Thermal conductivity 35

2.4.4.(b). Expansion coefficient....36
2.4.4.(c). Elastic modulus....36
2.4.5. General comments about the properties estimation....38

2.5. Laser material processing....39
2.5.1. Laser principles....39
2.5.2. Processing powders with lasers....40
2.5.2.(a). Laser sintering....41
2.5.2.(b). Laser fusion....45
2.5.2.(c). Building parameters....48
2.5.3. Nd:YAG laser principles....51

3. Problem Statement ____ 57

3.1. Hypothesis....58

3.2. Objective....59

4. Materials and Methods ____ 63

4.1. Methods of manufacturing....63
4.1.1. Fixed frames....63
4.1.2. Platform and Hopper....64
4.1.2.(a). Feedhoper and gradient step design....66
4.1.3. JK701 laser and Laserdyne working principles and characteristics....69
4.1.4. Environment and substrates....74

4.2. Statistical analysis....76

4.3. Powders: characterization and preparation....77
4.3.1. Sieving....78
4.3.2. Blending and mixing....79
4.3.3. Particle size dispersion....79

4.4. Macro and microstructure analysis....81
4.4.1. Samples preparation....81
4.4.2. Optical microscope and stereoscope....82
4.4.3. Scanning electron microscope and X-ray dispersive analysis....82
4.4.4. Image analysis....82

5. Optimization of building strategy parameters ____ 87

5.1. Investigation of laser scan strategies and vector spacing for H13 power....87
5.1.1. Methodology....87
5.1.2. Results....89
5.1.3. Discussion on laser strategies....93

5.2. Evaluation of the spatter lost during the laser fusion....94
5.2.1. Methodology....94
5.2.2. Results....95
5.2.3. Discussion on spattering....95

5.3. Comparison of the heat distribution over the fused layer using different strategies 96
5.3.1. Methodology 96
5.3.2. Results 96
5.3.3. Discussion on heat concentration 98

5.4. Investigation of the effect of strategies on the fusion of H13-Cu% mixtures 99
5.4.1. Methodology 99
5.4.2. Results 100
5.4.3. Discussion on the Cu effect on strategies performance 102

5.5. Evaluation of the microstructure of a z-graded FGM specimen 103
5.5.1. Methodology 104
5.5.2. Results 105
5.5.3. Discussion on the z-gradient 108

5.6. Discussion on building parameters 109

6. Optimization of laser process parameters ____________ 113

6.1. Laser processing parameters for H13-12.5%Cu composition 113
6.1.1. Manufacturing method and specimens dimensions 113
6.1.2. Box-Behnken experiment 114
6.1.2.(a). Methodology 114
6.1.2.(b). Box-Behnken results and discussion 115
6.1.3. Factorial experiment 118
6.1.3.(a). Methodology 118
6.1.3.(b). Factorial experiment results 119
6.1.4. Overall Results and Discussion 121
6.1.5. Discussion 122

6.2. Laser processing parameters for H13-25, 37,5 and 50%Cu compositions 123
6.2.1. Methodology 123
6.2.2. Results for H13-25%Cu 125
6.2.3. Results for H13-37,5%Cu 126
6.2.4. Results for H13-50%Cu 128
6.2.5. Discussion on laser processing parameters 130

7. Material characterization of H13-Cu ____________ 135

7.1. Density analysis 135
7.1.1. Methodology 135
7.1.2. Density results 136

7.2. Thermal conductivity coefficient 138
7.2.1. Methodology 138
7.2.2. Thermal conductivity results 140
7.2.3. Conductivity comments 142

7.3. Linear thermal expansion coefficient 142
7.3.1. Methodology 144

7.3.2. Linear expansion coefficient results 144
7.3.3. Linear expansion comments 145

7.4. Microhardness 146
7.4.1. Methodology 146
7.4.2. Results 147

7.5. Depth and load sensing indentation 148
7.5.1. DSI test methodology 148
7.5.2. DSI Results 150
7.5.3. DSI general comments 154

7.6. Tensile test 155
7.6.1. Design of the specimens tensile 155
7.6.2. Theoretical model of a FGM tensile test specimen according to ROM 156
7.6.3. Fabrication of the specimens 157
7.6.4. Tensile test experiment preparation 160
7.6.5. Results of the tensile test 161
7.6.6. Discussion on tensile test 167

7.7. General comments on the obtained properties 168

8. Applications of FGM H13-Cu parts 173

8.1. Evaluation of potential use of FGM H13-Cu mould for injection moulding 173
8.1.1. Methodology 174
8.1.1.(a). Numerical model methodology 174
8.1.1.(b). Injection moulding experiment methodology 176
8.1.2. Results 180
8.1.2.(a). Numerical Analysis Results 180
8.1.2.(b). Injection Moulding Experiment Results 182
8.1.3. Discussion 184

8.2. Obtaining complex geometries 185
8.2.1. Geometry design and manufacturing 185
8.2.2. Results and comments about the complex shape 186

8.3. Summary about applications and complex shapes 187

9. Conclusions 191

9.1. Contributions to the research world 193

9.2. Recommendations for future work 194
9.2.1. Processing H13 and Cu gradient 194
9.2.2. Selective laser fusion system improvements 195
9.2.2.(a). Hardware 195
9.2.2.(b). Software 196
9.2.3. Developments for injection moulds 197

10. References 199

11. Resumo Estendido 208

11.1. Introdução (Capítulo 1) 208

11.2. Definição do problema (Capítulo 3) 211
11.2.1. Hipóteses 211
11.2.2. Objetivos 213

11.3. Materiais e métodos (Capítulo 4) 213

11.4. Otimização dos parâmetros das estratégias de construção (Capítulo 5) 215
11.4.1. Investigação sobre estratégias de deslocamento vetorial do laser e espaçamento dos vetores na fusão de pó de H13 215
11.4.2. Avaliação da perda de material fundido por detritos expelidos durante a fusão a laser 216
11.4.3. Comparação da distribuição do calor sobre camadas fundidas utilizando diferentes estratégias 216
11.4.4. Investigação do efeito das estratégias na fusão de misturas de cobre e H13 216
11.4.5. Avaliação da microestrutura de uma amostra com gradiente FGM na direção Z 217

11.5. Experimentos sobre parâmetros do laser (Capítulo 6) 217
11.5.1. Parâmetros do laser para o processamento de mistura de H13-12,5%Cu 218
11.5.2. Parâmetros do laser para o processamento de mistura de H13-25, 37,5 e 50%Cu 218

11.6. Caracterização experimental de propriedades de FGM de H13-Cu (Capítulo 7) 219
11.6.1. Análise da densidade 219
11.6.2. Coeficiente de condutividade térmica 219
11.6.3. Coeficiente de expansão linear 220
11.6.4. Microdureza 220
11.6.5. Nanodureza 220
11.6.6. Ensaio de tração 221

11.7. Aplicações de componentes feitos de H13-Cu FGM (Capítulo 8) 222
11.7.1. Avaliação do uso potencial para moldagem por injeção 222
11.7.2. Obtenção de geometrias complexas 222

11.8. Conclusões (Capítulo 9) 222
11.8.1. Contribuições para o mundo científico 224

12. Publications List 226

List of Figures

Figure 2-1. Applications and time-trend for the additive manufacturing technologies (Wohlers, 2004). 11
Figure 2-2: Basic sequence of the layer additive manufacturing technologies. 13
Figure 2-3. Graded structures: (a) continuous and (b) discrete (adapted from Miyamoto, 1999). 15
Figure 2-4. Example of a bone section showing graded structures. 16
Figure 2-5. (a) a homogeneous composite, (b) a surface coating and (c) a FGM gradient (Su, 2002). 17
Figure 2-6. Differences in dimensional gradients (Miyamoto *et al*, 1999). 18
Figure 2-7. Two-phase material schematic microstructure changes with the volume fraction (Miyamoto *et al*, 1999). 19
Figure 2-8. FGM processing methods classification according to Suresh and Mortensen (1998). 20
Figure 2-9. Classification of the FGM processing methods according to (Miyamoto *et al*, 1999). 20
Figure 2-10. Example of application of FGM for high performance thermal barrier (Hopkinson *et al*, 2005). 22
Figure 2-11. Example of FGM jaw implant adapted from Watari *et al* (1997). 23
Figure 2-12. Examples of ice and rock climbing gears and applicability of FGM. 25
Figure 2-13. Voxel representation of FGM components. 26
Figure 2-14. Different graded transitions of aluminium alloys obtained by LENS^{TM} process (Chavez, 2000). 27
Figure 2-15. Multimaterial SDM mould (Pinilla and Prinz, 2003). 28
Figure 2-16. A two-phase layered material with a field E_o applied parallel and perpendicular to the laminate (Adapted from Torquato, 2001). 31
Figure 2-17. Modulus of elasticity and thermal conductivity for H13 and Cu estimated by Reuss and Voight equations. 31
Figure 2-18. Estimated thermal conductivity coefficients. 35
Figure 2-19. Estimated thermal expansion coefficients (at 20^{o}C). 36
Figure 2-20. Estimated shear modulus. 37
Figure 2-21. Estimated elastic modulus. 38
Figure 2-22. Spontaneous and stimulated emission phenomena. 39
Figure 2-23. Basic example of a laser cavity (adapted from Steen, 1991). 40
Figure 2-24. A typical laser sintering system and its components (EOS, 2003). 42
Figure 2-25. Steps for different materials used by the indirect laser sintering (process DTM/3D Systems). 43
Figure 2-26. Heat treatments for indirect laser sintering (Dalgarno & Stewart, 2001). 43
Figure 2-27: Powers for LPS: (a) coated, (b) mixture, (c) partially coated and (d) pre-alloyed powder (Klocke *et al*, 1995) 44
Figure 2-28. Simplified sketch of the LENS^{TM} process. 46
Figure 2-29: Influence of the energy density on fusion depth (Lu *et al*, 2001). 46
Figure 2-30: Influence of the energy density on the density of the part (Lu *et al*, 2001). 47
Figure 2-31: Laser scan speed and power effects on the bead diameter (Lu *et al*, 2001). 47

Figure 2-32: Map of porosity regions using various laser power and scan speed (Lu *et al*, 2001). 48
Figure 2-33. An example of laser scanning strategy. 49
Figure 2-34. Difference between parallel and orthogonal (cross-hatched) layers. 50
Figure 2-35. Direct influence of the vector spacing (SP) in the overlap of the processed material. 50
Figure 2-36. Effect of the layer thickness (LT) into the layer bonding and gaps. 51
Figure 2-37. Schematic Nd:YAG energy level system (adapted from Tarrant, 2002). 52
Figure 2-38. General construction of a Nd:YAG laser (adapted from Steen, 1991). 52
Figure 4-1. Stacking fixed frames method for layering powder. 63
Figure 4-2: Sequence of the laser fusion using fixed frames where layer contraction is not compensated. 64
Figure 4-3. Schematic drawing of the levelling and hopper system. 65
Figure 4-4. Platform and hopper system assembled in the machine. 65
Figure 4-5. CAD model of the first hopper build for the experiments (platform 45x45mm) 67
Figure 4-6. CAD model of the second hopper used (platform 45x45mm). 67
Figure 4-7. CAD model of the hopper used to build tensile test specimens (platform 45x75mm). 68
Figure 4-8. Details of the hoppers and apertures. 68
Figure 4-9. Example of an x-graded layer (hopper shown in Figure 4-5). 69
Figure 4-10. Laserdyne and JK701H laser system configuration. 70
Figure 4-11. Modulation shape of a simple pulse. 71
Figure 4-12. Example of pulse shape segmented in many sectors (modulation above, output below). 73
Figure 4-13. A simple example of using pulse sectors to format the peak energy of a pulse shape. 73
Figure 4-14. Argon flow and protective lenses in the laser aperture. 75
Figure 4-15. Differences of the laser fusion with and without substrate. 76
Figure 4-16. SEM images of the H13 base powder. 77
Figure 4-17. SEM images of the base Cu powder. 78
Figure 4-18. SEM images of the small size Cu powder. 78
Figure 4-19. Dispersion size in volume of the powder particles for the H13 and large Cu from Table 4-3. 80
Figure 4-20. Bimodal dispersion sizes in volume of the blends from Table 4-4. 80
Figure 4-21. A polished top cross-section of a specimen and its black and white contrast. 83
Figure 5-1. The laser scanning strategies studied. 87
Figure 5-2. Cross hatched vectors sketch and outer wall for *sequential* strategy (only four layers shown). 88
Figure 5-3. A typical result: (a) outer border, (b) substrate & (c) specimen. 90
Figure 5-4. Top view of the specimens obtained using different strategies (0,5mm spacing). ... 90
Figure 5-5. A perceptible pore pattern in the *alternated* (a) strategy in contrast with *refill* (b). ... 91
Figure 5-6. The cross section of specimens build with 0,5mm spacing (a) *filling*, (b) *sequential*, (c) *alternated* and (d) *refill* (area lost is indicated in black). 91
Figure 5-7. Crack across the scan direction (b), top surface of the specimen (a) and re-heat marks (c). 92
Figure 5-8. SEM micrograph of the H13 microstructure. 93

Figure 5-9. Spattering occurring during the selective laser fusion process. 94
Figure 5-10. Mass lost by spatter measurement sequence. 95
Figure 5-11. An example of the spattering effect after the laser fusion. 95
Figure 5-12. (a) 3D temperature map, (b) layer obtained and (c) detail of the layer surface for the *filling* strategy. 97
Figure 5-13. (a) 3D temperature map, (b) layer obtained and (c) detail of the layer surface for the *sequential* strategy. 97
Figure 5-14. (a) 3D temperature map, (b) layer obtained and (c) detail of the layer surface for the alternate strategy. 98
Figure 5-15. (a) 3D temperature map, (b) layer obtained and (c) detail of the layer surface for the *refill* strategy. 98
Figure 5-16. Typical cross sections of specimens built with H13-Cu blends. (a) *filling*, (b) *sequential*, (c) *alternated* and (d) *refill* strategy. 100
Figure 5-17. Effect of the Cu percentage and strategies over the porosity. 101
Figure 5-18. Effect of the strategies and Cu percentage over the area reduction. 102
Figure 5-19. Powder contraction and void which causes the area reduction and porosity 103
Figure 5-20. Z-graded structures built and the build orientation. 104
Figure 5-21. The cross section of the two graded specimens: A) starting with H13, B) starting with H13+50Cu%. 105
Figure 5-22. Polished cross section of z-graded specimens: (a) only polished, (b) and (c) etched. 106
Figure 5-23. Microstructure of the pure H13. 106
Figure 5-24. Microstructure of the *H13+25%Cu* composition 107
Figure 5-25. Microstructure of the H13-50%Cu composition. 107
Figure 5-26. Cracks and pores formed in the cross section of a specimen made of H13+25%Cu. 108
Figure 6-1. Main effect plots for cracks and porosity. 116
Figure 6-2. An estimated cracks and pores response against pulse energy and pulse width at fixed pulse repetition rate (5mm/s) and repetition rate (20Hz). 117
Figure 6-3. Percentages of cracks and pores contour in function of pulse energies and pulse width. 117
Figure 6-4. Different cross-sections obtained with combinations of pulse energy and width. ...118
Figure 6-5. An estimated crack and pores response against pulse energy and pulse width at fixed pulse repetition rate (5mm/s) and repetition rate (20Hz). 120
Figure 6-6. Estimated response surface contours for minimum peak power and area defects for the H13-12,5%Cu composition. 121
Figure 6-7. Cross sections of specimens obtained using (a) original and (b) optimized parameters (factorial analysis experiment). 122
Figure 6-8. Response surface of the area defects against pulse energy and pulse width at fixed pulse repetition rate (5mm/s) and repetition rate (20Hz) for H13-25%Cu. 125
Figure 6-9. Estimated response surface contours for minimum peak power and area defects for the H13-25%Cu mixture. 126
Figure 6-10. Response surface of the area defects against pulse energy and pulse width at fixed pulse repetition rate (5mm/s) and repetition rate (20Hz) for H13-37,5%Cu. 127
Figure 6-11. Estimated response surface contours for minimum peak power and area defects for the H13-37,5%Cu mixture. 128
Figure 6-12. Response surface of the area defects against pulse energy and pulse width at fixed pulse repetition rate (5mm/s) and repetition rate (20Hz) for H13-50%Cu. 129

Figure 6-13. Estimated response surface contours for minimum peak power and area defects for the H13-50%Cu mixture. 129
Figure 7-1. Indication of the dimensions of the specimens for density measurement. 135
Figure 7-2. H13 and H13+50%Cu specimens after the laser fusion. 136
Figure 7-3. Specimens finished after grinding. 136
Figure 7-4. Average density against materials composition: models and laser fused parts. 137
Figure 7-5. Schematic drawing of the thermal conductivity test apparatus. 139
Figure 7-6. Graphical trend of the thermal conductivity measured for H13-Cu specimen. 141
Figure 7-7. Graphical comparison between the estimated values and measured values of the thermal conductivity coefficient. 142
Figure 7-8. Variation of the linear expansion coefficient of the Cu and H13 (based on Matweb 2005-1 and 2005-2). 143
Figure 7-9. Dimensional changes of the samples with the temperature. 144
Figure 7-10. Variation of the expansion coefficients with the temperature (H13* and Cu** ref. curves). 145
Figure 7-11. Gradient region of the specimen tested. 146
Figure 7-12. Microhardness variation along the graded specimen. 148
Figure 7-13. Schematic view of the DSI measurements taken in the specimen. 149
Figure 7-14. Specimen mounted in the DSI machine. 150
Figure 7-15. Representative average curves of Load x Displacement for each FGM region. 151
Figure 7-16. FGM hardness by microhardness and DSI measurements and ROM. 152
Figure 7-17. Indentation marks on H13 (a) and H13+25%Cu. 152
Figure 7-18. Indentation marks on H13+50%Cu regions. 153
Figure 7-19. Reduced elastic modulus (average and standard deviation) and prediction models. 153
Figure 7-20. Indication of the dimensions of the specimen for tensile test. 155
Figure 7-21. Axial gradient distribution of a specimen. 157
Figure 7-22. Photograph of the manufacturing of a layer for two specimens. 158
Figure 7-23. Specimens completed after the selective laser fusion. 158
Figure 7-24. Specimens with top surface grounded and drilled holes in the substrate for the wire spark erosion process. 159
Figure 7-25. Tensile test specimens after final wire spark erosion. 159
Figure 7-26. Comparison between specimens obtained with 250 and 500µm of layer thickness (LT) and the position of each material composition in the graded region. 160
Figure 7-27. Specimen assembled in the machine claws with the extensometer attached. 161
Figure 7-28. Stress x strain curves for the 250µm (thin) layer thickness specimens. 162
Figure 7-29. Polynomial regression applied to all points from the 250µm specimens. 163
Figure 7-30. Linear regression until 0.2% of deformation for the 250µm specimens. 164
Figure 7-31. Stress x strain curves for the 500µm (thick) layer thickness specimens. 165
Figure 7-32. Position where the specimens broke. 166
Figure 7-33. Closer images to a failed section of a 250µm layer thickness specimen. 166
Figure 7-34. SEM micrograph from a broke section of a specimen with 250µm of layer thickness. 167
Figure 7-35. Graphical comparison between the elastic modulus of materials and FGMs. 168
Figure 8-1. Volume control for the heat. 174

Figure 8-2. 2D model for the heat transfer of an injected part in contact with a metallic insert in a SL mould (initial temperature indicated for each area of the model). 175
Figure 8-3. FGM insert and the disposition of the gradients. 176
Figure 8-4. Position of the thermocouples in the cavity. 177
Figure 8-5. Injection mould (above) and in detail the interchangeable inserts (below). 178
Figure 8-6. Regions from where the PP samples were taken from the specimens. 180
Figure 8-7. Estimated temperature of the thermocouple (T_{tc}, mould surface) along the time simulating different material properties for the insert. 181
Figure 8-8. Temperature of the insert surface (T_{is}) along the time simulating different material properties for the insert. 181
Figure 8-9. Temperature of the mould during the injection moulding series at the first slot with different inserts. 182
Figure 8-10. Temperature of the mould during the injection moulding series at the second slot with different inserts. 182
Figure 8-11. Calorimetric plot of the samples taken from parts of the 2nd cycles at the same position (1st slot). 183
Figure 8-12. Calorimetric plot of the samples taken from parts of the 16th cycles at the same position (2nd slot). 183
Figure 8-13. CAD model of the designed complex geometry. 186
Figure 8-14. Graded complex geometry obtained. 187

List of Tables

Table 2-1. The whole RP family tree (adapted from Koukka, 2001). 14
Table 2-2. Function classification for FGM applications (Calder, 2001). 21
Table 2-3. Base properties for the calculus of the estimations. 35
Table 2-4. Process variables which affect laser sintering and densification (Agarwala *et al*, 1995). 45
Table 4-1. Main dimensions of the hoppers. 68
Table 4-2. Output specifications of the JK701 (GSI Lumonics, 2000). 70
Table 4-3. Powder characteristics. 77
Table 4-4. Blends prepared from different powder size mixtures. 79
Table 4-5. Percentile sizes of feedstock and blend powders and particle size ratio. 81
Table 5-1. Porosity, area reduction and total area reduction for strategies and spacings. 92
Table 5-2. The ANOVA table for porosity results (95% of confidence). 101
Table 5-3. The ANOVA table for area reduction. 102
Table 6-1. Design of the Box-Behnken experiment summary. 114
Table 6-2. Analysis of variance for the cracks and pores results of Box-Behnken design. 115
Table 6-3. Summary of the multi-level factorial experiment. 119
Table 6-4. ANOVA of the multilevel factorial experiment. 119
Table 6-5. Comparison between the parameters used before and after the RSM with H13-12,5%Cu. 122
Table 6-6. Factorial analysis design summary for the powder mixtures. 124
Table 6-7. ANOVA table for H13-25%Cu mixture. 125
Table 6-8. ANOVA table for H13-37,5%Cu mixture. 126

Table 6-9. ANOVA table for H13-50%Cu mixture. 128
Table 6-10. Summary of the parameters optimization. 130
Table 7-1. Volume, mass and density of the specimen of each mixture. 137
Table 7-2. Percentage of voids (pores and cracks) for each material composition compared to the estimation by the rules of mixtures. 138
Table 7-3. Calculated and corrected conductivity values for the H13-Cu specimens. 140
Table 7-4. Mass and dimensions of each sample. 144
Table 7-5: Microhardness test specifications. 147
Table 7-6. The measured microhardness results. 147
Table 7-7. Summary of standard, estimated and measured results values. 154
Table 7-8. Dimensions of the tensile piece test. 156
Table 7-9. Polynomial regression analysis for fine layer specimens. 162
Table 7-10. Analysis of variance for fine layer specimens. 163
Table 7-11. Linear regression analysis for the fine specimens until 0,2% of deformation. 163
Table 7-12. Analysis of the variance of the model for fine specimens until 0,2% of deformation. 164
Table 7-13. Summary of the properties obtained and comparison with other results and references. 167
Table 8-1. Material properties used in the numerical model. 176
Table 8-2. Injection moulding order and position of the inserts. 178
Table 8-3. Injection moulding parameters. 179
Table 8-4. DSC summary of the PP samples analysed. 184
Table 9-1. Summary of the optimized laser processing parameters. 191
Table 9-2. Summary of the measured properties for each mixture. 192

Abbreviations

12,5%Cu: same as H13-12,5%Cu;
1D: one-dimensional;
25%Cu: same as H13-25%Cu;
2D: bi-dimensional;
37,5%Cu: same as H13-37,5%Cu;
50%Cu: same as H13-50%Cu;
3D: three-dimensional;
3DP: 3D Printing;
AISI: American Iron and Steel Institute;
ANSI: American National Standard Institute;
ASTM: American Society for Testing and Materials;
BS: British Standards;
CAD: Computer Aided Design;
CAE: Computer Aided Engineering;
CAM: Computer Aided Manufacturing;
CNC: Computer Numerical Control;
CVD: Chemical Vapour Deposition;
DMLS: Direct Metal Laser Sintering;
DOE: Design of Experiments;
EDX: Energy Dispersion X-ray;
EN: European Norm;
FEA: Finite Element Analysis;
FEM: Finite Element Method;
FGM or FGMs: Functionally Graded Material or Materials;
FDM: Fused Deposition Modelling;
H10: Tool steel AISI H10;
H13: Tool steel AISI H13;
H13-12,5%Cu: material composed by 87,5%H13 plus 12,5%Cu (by weight);
H13-25%Cu: material composed by 75%H13 plus 25%Cu (by weight);
H13-37,5%Cu: material composed by 62,5%H13 plus 37,5%Cu (by weight);
H13-50%Cu: material composed by 5o%H13 plus 50%Cu (by weight);
IGES: International Graphics Exchange Standard;
ISO: International Organization for Standardization;
LASER: Light Amplification by Stimulated Emission of Radiation;
LENS^{TM}: Laser Engineering Net Shaping;
LMT: Layered Manufacturing Technologies;
LOM: Laminated Object Manufacturing;

LPS: Liquid Phase Sintering;
MASER: Microwave Amplification by Stimulated Emission of Radiation;
MJM: Multi Jet Modelling;
Nd:YAG: Neodymium – Yttrium Aluminium Garnet;
RP: Rapid Prototyping;
RM: Rapid Manufacturing;
ROM: Rules of Mixtures;
RSM: Response Surface Method;
RT: Rapid Tooling;
SEM: Scanning Electron Microscope;
SFF: Solid Free-Form;
SLA: Stereolithography, Stereolithography Apparatus;
SLF: Selective Laser Fusion;
SLS: Selective Laser Sintering;
STL: Structured Triangle Language;
STEP: Standard for the Exchange of Product;
TEM: Transverse Electromagnetic Mode;
TiC: Titanium carbide;
WC: Tungsten carbide;

Basic Elements Symbols

Al: Aluminium, basic element or alloy;
Ar: Argon, gas mixture with low percentage of oxygen;
Be: Beryllium, basic element or alloy;
C: Carbon, basic element;
Cu: Copper, basic element or alloy;
Fe: Iron, basic element or alloy;
Ni: Nickel, basic element or alloy;
P: Phosphorus, basic element;
Sn: Tin, basic element;
Ti: Titanium, basic element or alloy;
V: Vanadium, basic element;

Symbols and Units

Δsp: overlap between fused scanned lines [mm];
Δp: pulse overlap [%];
Ø: particle size diameter [μm];
ε: deformation [%];

σ: tension [Pa];

ρ: density [g/mm^3];

B: bulk modulus [MPa];

d: beam spot diameter [mm];

E: pulse energy [J] or Elastic modulus [MPa];

E_ρ: Energy density [J/mm^2];

f: repetition rate, frequency [Hz];

G: shear modulus [MPa];

h: electrical current height [%];

k: thermal conductivity coefficient [W/m.K];

L: vector length or length [mm];

LT: layer thickness [μm];

P: power average [W];

P_{peak}: pear power [kW];

SP: spacing between laser beam strategy vectors [mm];

Tsp: Total percentile overlap [%];

v: scanning speed, federate [mm/s];

V: volume fraction [%];

V_{ol}: volume of a body [cm^3];

w: pulse width [ms];

W: weight fraction [%] or weight [g];

Resumo

O desenvolvimento de novos produtos envolve novos materiais, processos e metodologias de projetos. Com relação a novos materiais, a otimização de forma e função num único componente pode ser obtida por *Functionally Graded Materials* (FGM) ou materiais com gradientes funcionais. Assim como em materiais compósitos, o emprego de FGMs explora obter com o uso de dois ou mais materiais, funções diferenciadas que produzam um componente final otimizado. Por exemplo: materiais rígidos mas leves ou duros e condutores de calor. No entanto, genericamente, FGMs possuem como diferença uma gradual transição entre cada um dos elementos que formam o componente, em oposição a transição bem definida entre os compósitos. Apesar das potenciais vantagens e aplicações, uma das principais limitações dos FGMs é a baixa complexidade obtenível pelos processos de fabricação existentes. Nos últimos 10 anos, pesquisas têm procurado obter FGMs a partir de tecnologias de fabricação por adição de camadas, também conhecidas por prototipagem rápida. Devido ao potencial de produzir virtualmente objetos de forma livre em qualquer tipo de material, acredita-se que estas tecnologias possam ser usadas para obter componentes FGM com geometrias complexas. Inserido neste contexto, a fabricação de moldes para injeção poderia ser beneficiada pela adoção da fabricação de geometrias complexas e inserção de FGMs. Um molde poderia ter regiões enriquecidas com carboneto de tungstênio para aumentar resistência ao desgaste. Alternativamente, regiões ricas em material de maior condutividade térmica proporcionariam extração diferencial de calor para homogeneizar a solidificação da peça injetada. Assim, moldes de alta performance poderiam ser obtidos, produzindo em ciclos menores peças com maior qualidade. Neste trabalho, a fabricação de FGM entre aço ferramenta H13 e cobre para obtenção de moldes através do processo de fusão seletiva a laser foi estudada. Para a obtenção de corpos-de-prova, um laser pulsado de Nd:YAG foi utilizado para fundir pós de H13 e cobre, camada por camada. Parâmetros de construção e de processamento do laser foram pesquisados por meios estatísticos a fim de obter composições de materiais entre H13 e cobre com o menor quantidade de defeitos. As propriedades das composições, densidade, microdureza, módulo de elasticidade, coeficiente de expansão térmica linear e condutividade térmica e do gradiente foram testadas. A adição de cobre ao H13 ocasionou a alteração das propriedades do material. No entanto, os defeitos resultantes da solidificação de H13 mais cobre indicaram que o processo precisa ser melhorado. Assim, propriedades mecânicas e térmicas mais condizentes para as aplicações desejadas poderão ser obtidas. Um inserto FGM também foi utilizado na moldagem de polipropileno para verificar o efeito da adição do Cu ao material base H13. Os resultados indicaram que a adição de cobre alterou a transferência de calor no molde. Uma geometria de maior complexidade também foi produzida, provando que é possível obter componentes para outras aplicações e moldes complexos.

Palavras-chave: fusão seletiva a laser, materiais com gradientes funcionais, fabricação rápida, fabricação por adição de camadas

Abstract

The development of new products involves new materials, processes and design methodologies. Concerning new materials, the optimization of form and function into a single component is explored by the use of Functionally Graded Materials (FGMs). Similar to composites, in FGMs two or more materials are used to optimise the properties of each functional element that could produce an optimized final component. As examples: materials that are tough but light or hard but thermally conductive. Nevertheless, generically speaking, in FGMs materials are subjected to a gradual transition between each one of the elements that form the component, in opposition to the well defined transition in composites. Despite the potential advantages and applications, one of the main limitations of FGMs is the low complexity obtained by actual manufacturing processes. In the last 10 years, researchers had been attempted to manufacture FGMs from layer additive manufacturing technologies, also known as Rapid Prototyping (RP). As these technologies had the potential to virtually build free-form objects in any kind of material, it is believable that they might be used to obtain FGMs components with complex shapes such as graded moulds with conformal cooling channels. In this context, highly efficient injection moulds integrated with "smart" cooling channels can be produced by implementing additive layer manufacturing and FGMs. A mould could have richer regions of tungsten carbide to increase wear resistance. Alternatively, richer regions on material with higher thermal conductivity might extract heat differentially to homogenously solidify the injected part. Consequently, high performance moulds could be obtained, producing in shorter cycles higher quality parts. In this work, the manufacturing of FGM between H13 tool steel and copper (Cu) to obtain moulds by selective laser fusion was the subject of study. This work was carried out to optimise process parameters using high power pulsed Nd:YAG laser. H13 and Cu powders were used. Building and laser processing parameters were optimized using statistical analysis to process various material compositions of H13 and Cu in order to minimise defects such as pores and cracks. The Cu addition to the H13 changed the properties of the material. The material compositions properties, density, microhardness, elastic modulus, linear thermal expansion coefficient and thermal conductivity and of the gradient were tested. Nevertheless, the defects from the solidification of H13 plus Cu indicated that the process must be improved. This improvement, would allow to obtain mechanical and thermal properties more appropriate to the desired applications. X-graded FGM inserts also were fabricated and used in the injection moulding of polypropylene to verify the effect of Cu addition to the H13 base material. The results indicated that the addition of Cu affected the heat transfer in the mould. A complex geometry also had been produced, proving that it is possible to obtain parts for other applications and complex moulds.

Keywords: selective laser fusion, functionally graded materials, rapid manufacturing, layered additive manufacturing

Chapter 1

Introduction

"...
E a cada hora que passa
Envelhecemos dez semanas
Vamos lá, tudo bem - eu só quero me divertir
Esquecer, dessa noite ter um lugar legal pra ir
Já entregamos o alvo e a artilharia
Comparamos nossas vidas
E mesmo assim, não tenho pena de ninguém."

Legião Urbana – O Teatro dos Vampiros

1. Introduction

The development of new products depends on three main pillars: materials, design and manufacturing. Each one of these factors interacts with the other two and the way this is made follows a complex interrelationship. Nevertheless, it is not easy to determine which factor has more influence over the development of new products/technologies (Ashby, 1999). If design pushes the boundaries of form/shape/functions of products, new materials and methods for manufacturing these materials have to cope with the new limits imposed by design. If new materials are available, designers can extend their limits further. Manufacturing technologies must be improved/created to produce faster and cheaper quality products. Therefore, new product developments must contain new materials, improved and innovative design and new manufacturing methods.

In the materials field, functionally graded materials (FGM) has been a subject of research for the last 25 years (Miyamoto *et al*, 1999). Most of the nature materials such as minerals and tissues have a gradual change from one functional region to another. This example of nature inspires integrated form and function design all in the same component/unit. FGM is not completely new between the manufacturing processes but only after the 80's it started to receive more attention and to be classified as a specific research subject. The basic idea of FGM is to add extra functions to a component by varying the quantity of an "ingredient" at specific regions into the volume of this component in order to achieve the extra functionality intended. The extra functionality is established by the material properties variation obtained in the component. An ingredient could be a basic element such as carbon being used to increase the hardness of a steel part only at the surface. This variation could be from richer carbon concentration in the surface gradually reducing to the inner core of the part and restricted to few millimetres. In animal bone for instance, the main ingredient is the pores where the size of the pores determines the stiffness in the boundaries and the weight reduction by the spongy core among other functions of the bone tissue. By using this variation from one material to another, highly optimized components can be obtained. Reduced number of joints and fasteners, weight reduction, structural enhancement, differential heat extraction, thermal barriers, embedded sensors and biocompatible implants are some of the potential advantages of FGM (Suresh and Mortensen, 1998; Miyamoto *et al*, 1999; Calder, 2001). Using the FGMs method also could gradually join dislike materials with different properties in the same component. The principle is similar to composites materials. The difference is that composites have distinctive phases and do not vary its composition in the volume of the component. In addition, designers and engineers are not yet prepared to design with FGM integration as no system can successfully build fully dense and functional parts. Most of the present alternatives are attained to surface deposition of thin layers of a material to the base material of the component. This is very restricted on form and function.

Despite the idea copied from nature being very simple, most of the potential FGM applications still are restricted to technological limitation and high cost. Difficulties to control and deposit the gradient composition and to produce complex shapes with Computer Aided Design (CAD), Computer Aided Manufacturing (CAM) and Finite Element Analysis (FEA) integration are causes of this relative slow development.

In the mid 80's, new manufacturing technologies know as SFF (Solid Free-Form Fabrication) emerged (Jacobs, 1996). The main difference of these technologies opposing to the traditional ones was that they were based on the layer additive principle. Also known as Rapid Prototyping (RP), these technologies can produce parts in low volume production in virtually any form and material. The variety of available materials is limited, however, RP processes can build parts in metal, ceramics and polymers (Jacobs, 1992).

RP technologies are highly automated and they are also called as three-dimensional printers as the machines almost "print" solid parts from data generated from computer software. Designers and engineers can build and verify designed parts directly from the computer without misunderstandings, inaccuracies and delays. The basic principle of RP technologies is to build, layer-by-layer, material corresponding to the data of the designed part. Raw materials can be liquid resins, wires, pastes, powders and sheets. The way to shape these materials and bond layers can be diverse from ultraviolet lasers, lamps, power lasers, spray of glue, extrusion of fused material and others.

These additive-layered manufacturing technologies (LMT) have been also used to produce tools for injection moulding. Depending on the technology and material used to build, complexity of the mould impression (injected part) and the injected material, these moulds can be competitive to traditional cast/milled moulds. It is possible to build moulds for dozen to ten thousand parts according to the technology, material and application. One of the advantages is to produce in short time a complex mould impression. The second advantage is the possibility of including conformal channels for heat control in the cavity. Conformal channels are designed in the CAD system and built within the mould by the RP machines. A good design could effectively extract heat from the cavity (Ahrens *et al*, 2001; Dalgarno and Stewart, 2001).

Although RP moulds with conformal channels can be used to produce injected parts, it is necessary to improve and optimize the heat extraction from the moulds cavity. As an example, thin and long features might not be affected efficiently by the conformal channel heat extraction. This can lead to longer injection moulding cycles to allow the material on specific features to achieve a solid state when part can be ejected safely from the mould. Additionally, the differential solidification of the part might cause diverse side effects. It is not rare to input design modifications in the part geometry to avoid/correct defects. Some of the defects are sink marks, weld lines and warping (Menges and Mohren, 1993; Pötsch and Michaeli, 1995). The limitations for the use of conformal channels are not only related directly to the mould impression geometry but other factors might limit the design freedom of the channels. The design of ejector system (slides, ejector pins), runners and split planes and the manufacturing method to obtain these features increase the difficulties to control the heat extraction from the cavity.

Another alternative the extract concentrated heat energy from the cavity/part is the use of Cu-Be inserts on moulds manufactured by conventional manufacturing methods (Top Grade Molds, 2003). These inserts are used to replace the mould base material in the hot regions because they have a higher capacity to transport heat energy. Nevertheless, they are expensive and non-ecological as the beryllium as elemental form is a cancerigenous substance (Center for Epidemiologic Research, 2005). Also, the manufacturing of a cavity with inserts might cause an abrupt change in the properties the mould surface what might cause marks in the injected part.

The use of RP technologies to produce FGM parts has been investigated by many researchers (Shishkovsky, 2001). Since RP technologies can produce free form parts and can handle different materials it is possible to use them to produce FGM components. Most of the researchers investigating the fabrication of FGM by LMT technologies process the materials with the heat source delivered by a laser beam. As lasers can be easily automated and can deliver high energy densities with precision and speed they virtually can process any material (Steen, 1991). Other aspect of FGM and RP is the often use of materials in the form of powder to be fused or pre-sintered under a laser spot.

FGM and RP could improve moulds performance in many aspects. Specific surfaces could be hardened to reduce wear. Regions or features in the mould impression could be enriched with more thermal conductive materials such as copper. It would be possible to extract heat more effectively to reduce part's defects and hence to increase productivity.

A common material used to build injection moulds is the AISI H13 tool steel. This material stands with high temperature applications with low wear and high toughness (Smith, 1993; Norton, 1996). However, its thermal conductivity is low (24W/mK, Matweb, 2005-1). Based on this disadvantage and to increase the heat extraction from the cavity, channels with a controlled temperature fluid (e.g. water with additives) are often used (Menges and Mohren, 1993). The fluid requires a chiller to keep the fluid temperature constant and heat extraction from the molten injected material under control. Also, it is pumped into the channels at determined speed to obtain the desired results. Usually, the heat extraction is not a problem for simple geometries but in the case of more complex shapes, the poor heat extraction could cause defects in the part as discussed previously. In such cases, especially when conformal cooling cannot be used, copper could be added to the mould on specific regions. Nevertheless, it is necessary to develop a process that can build such materials with gradients between H13 and copper.

1.1. Research objective

In the previous section, it was briefly exposed that there are issues on the development of new materials and manufacturing methods especially regarding FGM. The objective of this work was to investigate the fabrication of functionally graded tool steel copper parts by selective laser fusion. Using a Nd:YAG laser, the fabrication of dense graded parts was pursued. The aim was to evaluate the use of such gradient to improve the heat transfer in injection moulds. Building and laser parameters were explored in order to optimize the laser fusion process. Additionally, the materials properties were characterized by tests such as tensile test, depth and sensing indentation, thermal conductivity and hardness. Simple injection moulding experiments were performed with polypropylene. Moreover, a complex shape was produced to demonstrate that it is possible to obtain complex parts and moulds, however further commercial application depends on the building system improvements, which is included in the scope of this work.

1.2. Structure and organization

This written work, including this introductory chapter, was organized in nine chapters.

In Chapter 2, a review over the state of the art is presented. There, rapid prototyping and tooling are explained together with an introduction about FGM. A section of Chapter 2 presents techniques to estimate material properties of the combination in FGMs. Additionally, a brief introduction about lasers is presented.

The problem statement of the work is presented in Chapter 3. It resumes the main aspects of FGM and additive layered technologies that stimulated this work. Also, the hypothesis and targeted objectives of the research are shown.

The materials and methods for fabrication and analysis are presented and explained in Chapter 4. As many experiments had similar procedures, this chapter avoids too much repetition in the other chapters (5, 6, 7 and 8). In depth information about the laser system used in the work is presented in Chapter 4.

As no data was available about processing together the materials used in this work (H13 and Cu powders) with high power pulsed Nd:YAG laser, this was one of the investigations, in Chapter 5, analysing what were the influences of some building parameters. The laser parameters were kept constant to avoid too much noise in the experiments. It explores the use of different scan laser spacings, strategies and the influence of copper addition to the H13 on crack and pore formation. The objective was to achieve the maximum density in the laser fused specimens.

The results obtained from the experiments presented in Chapter 5 indicated that laser parameters had to be optimized for the H13 and Cu compositions. Consequently, in Chapter 6, the laser processing parameters were explored. Different laser parameters (pulse energy, pulse width, repetition rate and feedrate) and their influence on the reduction of defects in different fused H13-Cu compositions were probed.

In the sequence, Chapter 7 describes the analysis of different properties of the materials compositions and the gradient obtained. Density, thermal expansion coefficient, thermal conductivity, elastic modulus and hardness were investigated.

Chapter 8 presents applications of FGM parts. The objective explored in this work was to investigate differential conductivity mould impressions by FGM and additive layered technologies. The use of such gradients between copper and tool steel is presented in this chapter. The temperature of a mould with graded inserts was recorded and the influence of the gradient in the injected part was analysed by differential scanning calorimetry. It also shows the fabrication of a part with higher complexity than the specimens obtained in the other experiments. It demonstrates that, in future, it would be possible to obtain moulds with higher degree of shape complexity.

Finally, the overall conclusion about the work performed in Chapters 5, 6, 7 and 8 is presented in Chapter 9. Suggestions for future research work are also stated.

Chapter 2

Literature Review

"...
Here we go again
Asking where I've been
You can't see these tears are real
I'm crying

We can't go on together
With suspicious minds
And be can't build our dreams
On suspicious minds"

Elvis Presley – Suspicious Minds (ori. Mark James)

2. Literature Review

2.1. Rapid manufacturing

Rapid Manufacturing (RM) is a term generated from the Rapid Prototyping (RP) niche were machines with highly automated capabilities can build models/prototypes directly from CAD data in manner of hours. The RP industry started to make the difference since the late 80's when 3D Systems presented the stereolithography machine (Jacobs, 1992). At the beginning, acrylate resin models were built and used to evaluate product design. Latter, different technologies and materials were developed diversifying the applications of the products generated from these machines. Nowadays, objects from polymeric, metallic, ceramics and composites materials can be obtained with precision and properties that can replace traditional manufacturing techniques in many cases. Industries such as aerospace, racing sports, medical implants, luxury cars and military present many cases where this objects defined so far as "models" or "prototypes" were used as final product or replacement parts. From these specific niches where low production and highly customized products are often required is where the rapid manufacturing term adapts better (Jacobs, 1996).

The Wohlers Reports (Wholers, 2004) presented a time-trend with the areas of the additive manufacturing technologies and their correlation with the number of parts produced (Figure 2-1). It is believed that rapid manufacturing has a tendency for growing in the market as niches for highly customized products will be supported by these technologies. Also, concept modelling (non-highly technical models) will increase as concurrent market and new technologies have been bringing prices down. The use of technical prototypes would increase but not the market segment, as the use of cheap models would test products on early phases in the development reducing latter changes. Also, the improvement of the CAx integrated systems (computer aided design, engineering, manufacturing, etc.) have been improving design evaluation, reducing errors on broad sense.

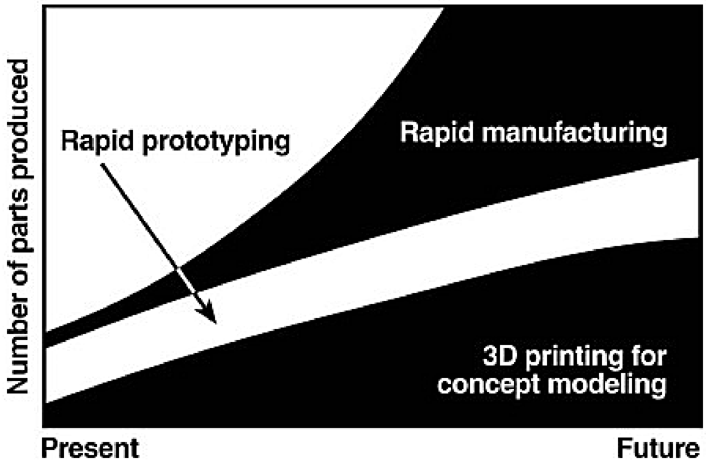

Figure 2-1. Applications and time-trend for the additive manufacturing technologies (Wohlers, 2004).

At National Aeronautics and Space Administration (USA), NASA, two directions have been explored for the use of RM. The first one is the use of RP machines to build parts for space shuttles and other apparatuses (Hopson and Paulsen, 2003; 3D Systems, 2002-1; 3D Systems 2002-2). The second field is the development of technologies that could build free-form parts in microgravity for replacement or repairing damaged parts in long space missions (Taminger *et al*, 2002).

2.1.1. Additive Layered Manufacturing

The term rapid manufacturing only makes sense when it is associated with the rapid prototyping technologies, otherwise any fast manufacturing process could be called rapid as well. RP technologies can be better denominated as layered additive manufacturing. This denomination avoids confusion with other technologies that are rapid but do not embrace the same manufacturing principle of building a three dimensional (3D) object from CAD data adding material layer by layer.

2.1.2. Principles

The start of all additive layered manufacturing process of the is based on the assumption of the compatibility of the CAD software used to model the 3D geometry of a product and the rapid prototyping system. CAD data intercommunication has been always a problem. Each CAD software has its own way to represent and build 2D and 3D models internally. As it becomes necessary to exchange data between different CAD and other softwares (CAM, Computer Aided Manufacturing; CAE, Computer Aided Engineering) exchangeable formats were created. To mention some of them: IGES (International Graphics Exchange Standard) and STEP (STandard for the Exchange of Product). Even though these formats are standards many problems were common and valuable time was expended to fix geometries before being able to use it. This compatibility issue was very important for the success of RP as it was necessary that any 3D model, modelled in any CAD software, would be able to be correctly interpreted by the RP machine and built without mismatches. Based on this, it was developed the STL file (**st**ereo**l**ithography file). The STL file is a translation of the CAD model to a triangular shell mesh which delimits the inside and outside of an object. Being so simple to write and read it has limitations. The quality of curves is always approximated by numerous flat triangles and the smaller the triangles to obtain better accuracy the greater the size of the file. The STL object can be generated from solid or surface CAD models if they correctly represent a 3D closed volume. Nowadays, the STL file format is so popular that all RP machine are able to work with it. Also, it has been used in other applications for generating finite element analysis elements mesh, reverse engineering and quality control.

After obtaining the STL file, it is imported on specific CAM software for the RP technology which is intended to use to build the part. The CAM has to be able to identify STL file errors and if possible, to fix eventual errors that might be present in the geometry. The operator do decides what would be the best orientation of the part to build, to increase the precision, reduce time and cost and to edit support data depending on the technology. In this CAM, the STL file is sliced and each slice receives the toolpath and building strategy for the layer. Then it is translated in machine language and it is sent to the machine that will build the object, layer by layer. This basic sequence can be visualized in Figure 2-2.

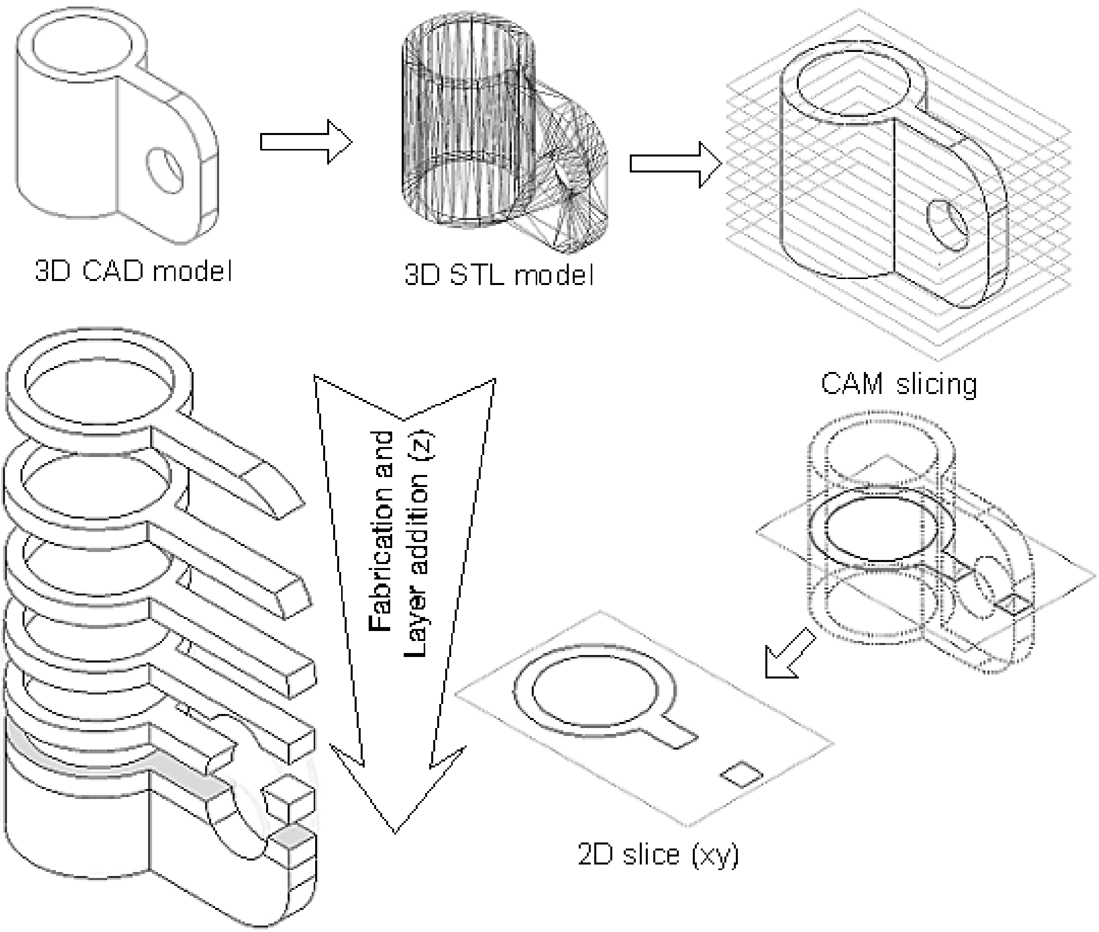

Figure 2-2: Basic sequence of the layer additive manufacturing technologies.

The tool that aids the layer building can be a laser beam, a mini-extrusion device, inkjet technology and many others. A popular way used to group the RP processes is by the material used to build the object. The "Whole RP Family Tree" adapted from Koukka (2001) is presented in Table 2-1. Even so this tree has being last updated in 2001, this stills covers most of the commercial and under development RP technologies.

Table 2-1. The whole RP family tree (adapted from Koukka, 2001).

Feedstock	*Nature of the material*	*Principle (number of cited technologies)*
Liquids	Photocurable Liquids	Curing by laser light through masks (4)
		Curing with a visible light laser (1)
		Curing with a UV-laser (single beam) (12)
		Curing with Two Laser Beams Simultaneously (3)
		Curing by visible light with a DVD-device (1)
		Hybrid combining inkjet technique and curing with an UV-lamp (1)
	Electric conducting liquid	Electroplating (1)
	Water	Freezing of water (1)
Powders	Melting of powder	Sintering with a heat transferring laser (6)
		Melting with a heat transferring laser (8)
		Using conventional sintering and HIP (1)
	Binding powder by adhesives	Methods based on MIT's 3D Printing (5)
		Extrusion of ceramics with melted binder (1)
		Other methods (2)
Solid materials	Extrusion of melted material	Extrusion of plastics (3)
		Methods based on welding (4)
		Spraying of metal (2)
		Extrusion and milling of multiple materials (1)
		Inkjet techniques (5)
Sheets	Bond-first lamination	Cutting material with a laser (6)
		Cutting material with a knife (1)
		Cutting material with a milling machine (1)
	Cut-first lamination	Cutting material with a laser (1)
		Cutting material with water (1)
		Cutting material with a knife (2)
		Cutting material with a heated electrode (1)
		Cutting material with a milling machine (1)
Gas & atoms manipulation	Miscellaneous	Gas (5)
		Individual atoms or molecules (2)

Usually, parts built go through post-processing stage. Depending on the technology/building principle, this could be the removal of powder, detaching supports, cleaning, post-cure, furnace treatment, surface finishing (sanding, painting, polishing), infiltration and/or others operations.

To list some of the technologies available at present are Stereolithography (SLA), Fused Deposition Modelling (FDM), Selective Laser Sintering (SLS), Direct Metal Laser Sintering (DMLS), Laminated Object Manufacturing (LOM), 3D Printing (3DP), Object 3D Printing, Laser Engineering Net Shaping (LENS^{TM}) and Multi Jet Modelling (MJM).

2.2. Functionally graded materials

2.2.1. FGM Fundamentals

Form and function are the premises for designing products. To achieve the required design specifications materials are selected according to support form/function and other variables such as manufacturing process, logistics, assemblage of parts, maintenance, reliability, costs, etc. The form of a specific component can have different functions. A one-piece kitchen knife must have an edge to cut/slice food and a maniple to hold the knife and move it with one hand. The knife material has an edge function where the cutting edge must be hard and the form/structural functions where it must be strong and tough (Suresh and Mortensen, 1998). This is a simple example but explain how in many components the required material performance can change with the location in the component. If the material performance must change this implies that the material properties have to change. Functionally graded materials are those where the properties of the material varies because composition and microstructure change gradually over the volume. Materials properties can change in different ways. It can be by chemical composition, physical state and geometrical configuration (Miyamoto *et al*, 1999).

The direct interface between two distinctive materials can cause stress. The stress might be internal to the structure or might appear between the interfaces of the materials when applied external loads. The FGM theory implies that the stress can be minimized when gradual transitions between these two materials exist. These transitions can be found in two ways: continuous or discrete (step-wise). Figure 2-3 shows examples of these graded structures. In the continuous structure (a), the properties change continuously over the volume. In the discrete structure, the gradient is formed by distinctive regions (b).

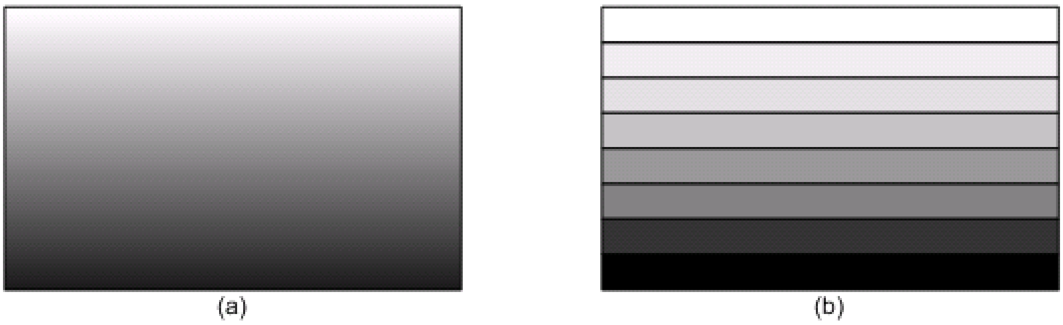

Figure 2-3. Graded structures: (a) continuous and (b) discrete (adapted from Miyamoto, 1999).

According to Miyamoto *et al* (1999), the idea of structural gradients started back in 1972 for advancements in composites and polymeric structures. The real investigations about the graded structures started in the 80's. In 1996 the term functionally gradient materials was introduced and later in 1994 it was changed for functionally graded materials to be more accurate descriptively and grammatically. The boost for FGM studies was a 5 year Japanese governmental program in 1987 for the development of thermal stress tailored graded structures. This program was target to develop high temperature FGMs for use in supersonic planes. The results of this program had stimulated the research in the field not only in Japan with a second project focussed on energy conversion but also around the world (Suresh and Mortensen, 1998; Miyamoto *et al*, 1999). The unusual combination of distinctive properties not common for the different classes of materials such as heat, wear and oxidation resistance of ceramics with high toughness, high strength, machinability and bonding capabilities of metals to name some of the familiar FGM research cited. At present, engineered biomedical tissues has become one of the major FGM applications.

FGM is not a human idea. Many examples of graded structures are found from nature. From molluscs' shells, trees trunks to bones and teeth gradient variations in their structures are present. The characteristics of the biological structures/tissues makes difficult to distinguish structures and materials according to Miyamoto *et al* (1999). The way living organisms adapt them self to external loads could be classified in three ways from a macroscopic point of view. Usually, the variations in the structure of the biological tissues happen by changing the microstructure. This could be made by moderating the thickness or shape of the elements that compose the material (bamboo, mollusc shell). Changing the size and shape of the body is another alternative such as trees trunk and stem of a plant. The other way is combining the microstructural and shape changes. This can be verified in mammal bones as shown in Figure 2-4. Bones are complex structures with shape and microstructure adapted to the loads directions. Also, other biological functions are given to them such as blood production. The bone tissue has generally three distinctive tissues: spongy bone, compact bone and narrow cavity. The basic difference between the spongy and compact bone is the size and distribution of the pores. The spongy bone gives flexibility, stress relaxation and weight reduction for the joints. The compact bone offers stiffness with reduced section (Miyamoto *et al,* 1999).

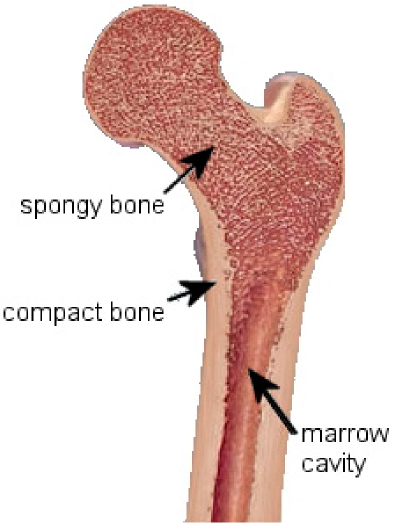

Figure 2-4. Example of a bone section showing graded structures.

Many literature sources cited FGM as new generation of composite materials (Su, 2002; Shishkovsky, 2001). Depending on the microstructural level of the elements that compose the gradient this can not be affirmed. In the definition of composite materials, the phases that constitute the material are separated and distinguishable (Figure 2-5). Also, gradients are not a common goal in the components. Nevertheless, it is possible to say that, in some sub-microstructural level a gradient will be formed between the phases of some composite materials. As Suresh and Mortensen (1998) say: *The functionally graded materials approach is currently far from being the norm.* According to Torquato (2001), the characteristic of the materials with multiple phases is a composite material. By this point of view, a FGM could be a material which is formed by composite transitions from each "ingredient" that forms a component.

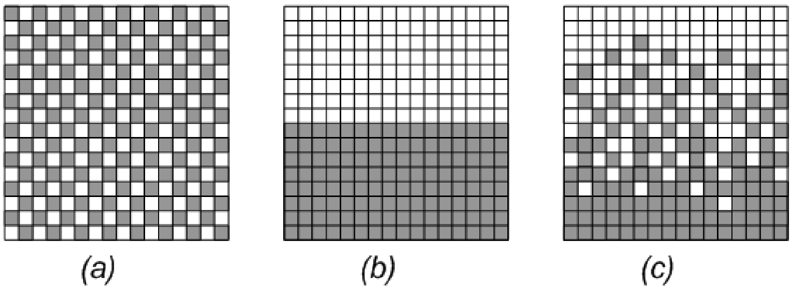

Figure 2-5. (a) a homogeneous composite, (b) a surface coating and (c) a FGM gradient (Su, 2002)

Even the manufacturing of samurai swords centuries ago with gradient transitions from the hard surface rich in carbon to the soft poorer carbon core can be considered as FGM. Nevertheless, many authors suggest the main issue for functionally graded materials is how to produce, mass production, cost effective, complex shapes (Shishkovsky, 2001; Kieback *et al*, 2003; Calder, 2001).

2.2.2. FGM microstructure

A material which exhibits microstructure variation associated with variation on properties and /or functions in at least one dimension can be considered as FGM. Figure 2-6 shows how parts can be composed with 1, 2 and 3 dimensional gradients. There is also the possibility of a fourth dimension that is time when considering materials designed to change over the time (drug deliver device, further explanation in following section 2.3.3.(b)). In most cases in literature the gradients obtained have 1D or are restricted to the component geometry (gradients from the surface to the inner core direction). The ability to produce free 3D complex shapes with complex gradients is the aim of many researches on RM field (described in section 2.3).

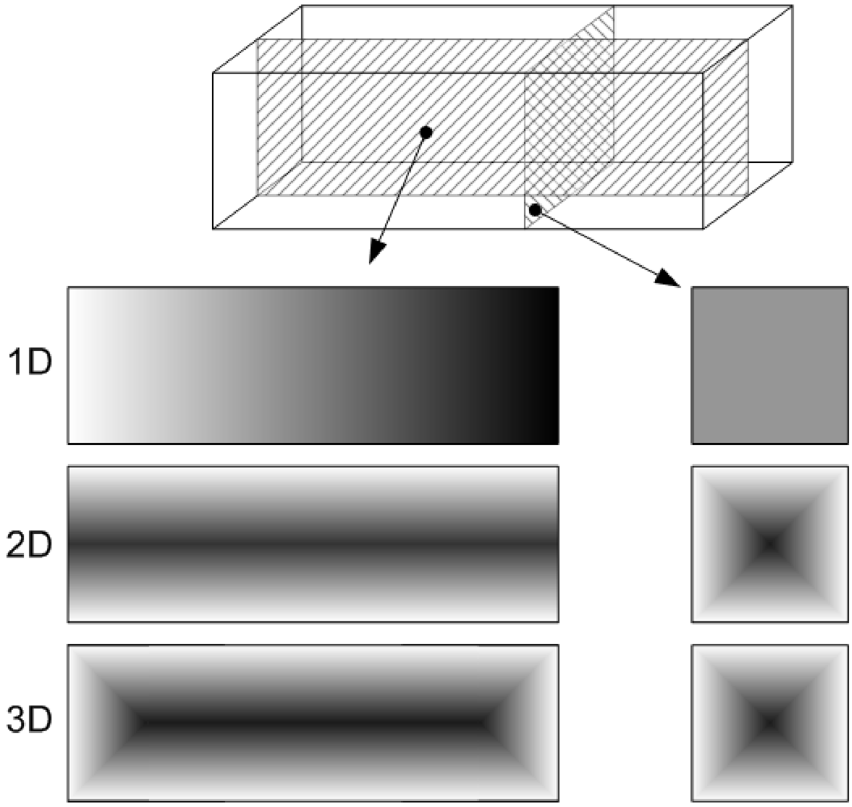

Figure 2-6. Differences in dimensional gradients (Miyamoto *et al*, 1999).

Different ingredients can build a gradient structure. The primary variable that might be used is the chemical composition but even the size of the grains in a homogeneous material can perform distinguished functions. If the size of the grain is reduced nearby the surface of the component to increase the material resistance it can be considered a FGM according to Miyamoto *et al* (1999). So, FGM are more popular and many do not realise that they are present in their products. On engineering design point of view, FGM graded material will be any material that in the same component acquires different function by variation of an ingredient (chemical, phase, physical and/or biological).

Because of its nature, FGM microstructure is not easy to analyse. Phases, interfaces and defects are wide range and depend on the type of combination between the different materials. However, analysing the microstructure of a material is the easiest way to describe if it is or not a functionally graded material (Suresh and Mortensen, 1998; Miyamoto *et al*, 1999). In Figure 2-7, a two-phase material changing the volume fraction of each ingredient is represented. Note that in this case there is no interaction between the phases. Nevertheless, this is a specific case and in many other cases different phases, pores and defects become part of the gradient during the manufacturing process.

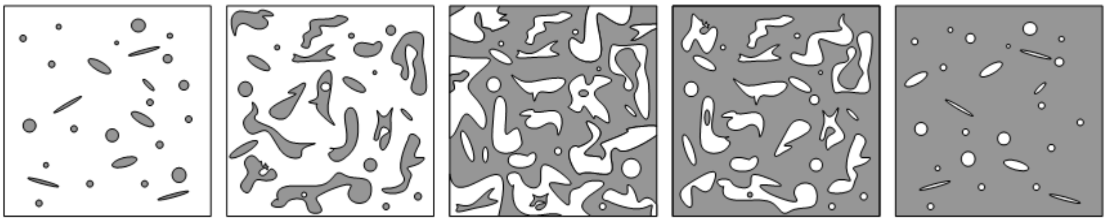

Figure 2-7. Two-phase material schematic microstructure changes with the volume fraction (Miyamoto *et al*, 1999).

The way a gradient varies into the volume of the component has been the focus in many researches. Mathematical models have been proposed to describe how an ingredient varies along a direction. Usually, they are described by power law equations. This subject can be seen in details in Suresh and Mortensen (1998), Miyamoto *et al* (1999) and Torquato (2001).

2.2.3. FGM design

The development of FGM role technology involves not only the materials but also the manufacturing processes. Virtually, any material can be joined to other material. The idea of giving the free will to the designer to choose whatever material combination that suite better the application is a utopia. Authors such as Suresh and Mortensen (1998) prefer to say that only a range of materials and processes will be available to designers and engineers. Design methodologies for FGM are research subjects restrained by the fact that the materials and processes have to be developed in order to provide information to designers and engineers. Another important aspect is the estimation of properties when combining different materials. This is further discussed in section 2.4.

2.2.4. Manufacturing technologies

The challenging on the development of new materials has two fronts. One is to develop a complete new material that did not existed before. Secondly, it is the combination of materials that can produce different properties. Various research work are being carried out in the field of FGMs and composites in order to improve technical performance of a component. It is well known that the major concern for composites is the manufacturing that can be expensive and technically difficult. Most of the composites had to be manufactured in different steps and with increased non-automated work.

Unfortunately, this is the major concern for FGM components production too. Complex shapes have been difficult to obtain on the part and on the gradient itself. In addition, the combination of materials or elements is critical. Poor bonding and defects might become another obstacle to produce FGMs. Nevertheless, since the 80`s manufacturing techniques for FGM have been developed, most of them for low volume production or laboratorial scale. From the literature, diverse classifications of the manufacturing process of FGM can be found. Figure 2-8 and Figure 2-9 show two distinctive classifications. Although the classification presented by

Suresh and Mortensen (1998) being more technically divided (Figure 2-8), Miyamoto *et al* (1999) presented an easier classification by the way the material is processed (Figure 2-9). Kieback *et al* (2003) showed some classification based on the German program for FGM development close to Miyamoto *et al* (1999) classification.

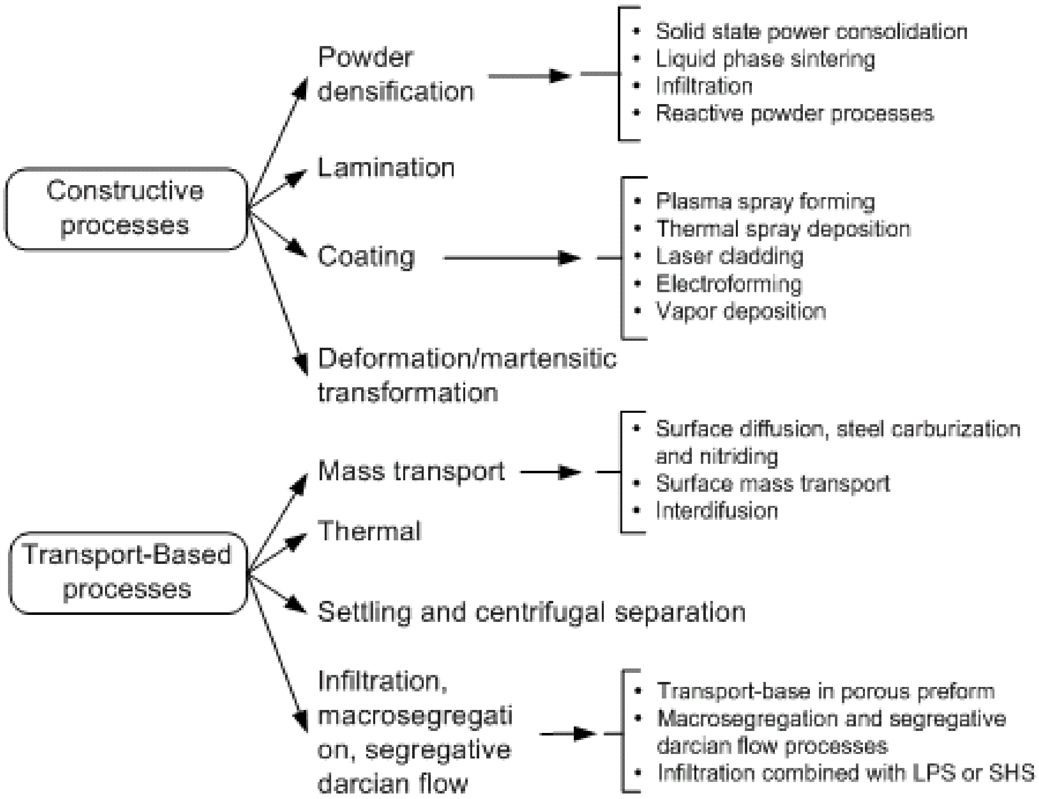
Constructive processes
Powder densification
Solid state power consolidation
Liquid phase sintering
Infiltration
Reactive powder processes
Lamination
Coating
Plasma spray forming
Thermal spray deposition
Laser cladding
Electroforming
Vapor deposition
Deformation/martensitic transformation
Transport-Based processes
Mass transport
Surface diffusion, steel carburization and nitriding
Surface mass transport
Interdifusion
Thermal
Settling and centrifugal separation
Infiltration, macrosegregation, segregative darcian flow
Transport-base in porous preform
Macrosegregation and segregative darcian flow processes
Infiltration combined with LPS or SHS

Figure 2-8. FGM processing methods classification according to Suresh and Mortensen (1998).

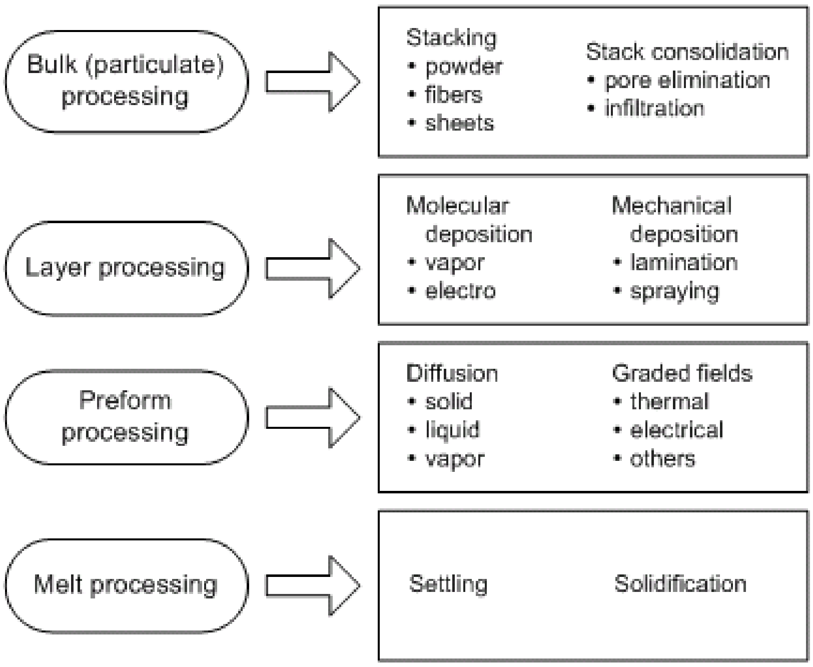
Bulk (particulate) processing
Stacking
• powder
• fibers
• sheets
Stack consolidation
• pore elimination
• infiltration
Layer processing
Molecular deposition
• vapor
• electro
Mechanical deposition
• lamination
• spraying
Preform processing
Diffusion
• solid
• liquid
• vapor
Graded fields
• thermal
• electrical
• others
Melt processing
Settling
Solidification

Figure 2-9. Classification of the FGM processing methods according to (Miyamoto *et al*, 1999).

Miyamoto *et al* (1999) classified additive layer manufacturing technologies under the bulk processing technologies, which is by staking powder layers. On the other hand, Mortensen and Suresh (1998) classified the process under constructive processes of coating and also as powder densification methods.

2.2.5. Applications and trends

The idea behind FGM is that if a material can not deliver all functions that the component is designed for it should have an extra material that would overcome these limitations. The connexion between these materials is made by a gradual changing of composition between them. This generic approach shows that any kind of component/application will be suited by FGM. The truth, as commented previously, is that FGM has been used for quite a long time, specially manufactured by diffusion processes but they are restricted to the form and surface inner core direction. The key for further development is the ability to design and to manufacture complex FGM gradients with non-easy combining materials. So far, the manufacturing capabilities for this have shown that these are very expensive processes and only specific high performance niches will be suitable for FGM.

According to Calder (2001), the function applications for FGM can be classified as presented in Table 2-2. This only indicates the type of desired effect that could be achieved combining different materials.

Table 2-2. Function classification for FGM applications (Calder, 2001).

Function	Type of desired effect	Examples of applications
Structural	Stiffness Toughness Hardness / Wear resistance	Lightweight shuttle tanks Lightweight performance engines
Thermodynamic	Thermal conductivity / Diffusivity Thermoelectric Emissivity / Absorptivity	Differential conductivity in moulds Heat resistant turbine blades
Electrical	Conduction / Insulation Dielectric Piezoelectric Semiconduction Active battery Thermocouple	Embed sensoring Light deformable batteries Energy generation
Chemical	Corrosion Composition	Protected structures
Biological	Bio-compability biochemical	Prosthesis Bio-sensors Drug delivering devices
Optical	Diffraction / Refraction	Graded lenses

Applications have been described in literature from razor blades on electric barber machines, baseball shoes tips, cutting tools, watches to fibre optics (JAXA and JST, 2002). On the following sections, a general view of FGM applications is given divided by some areas of interest.

2.2.5.(a). Aerospace

The aerospace sector is one of the sectors that shows more interest on the development of the FGM. NASA and JAXA had shown crescent interest on the development of these technologies. As the cost for launching space shuttles depends on the weight they lift to the space, creating parts with less connection elements is a solution. Also, the optimum design, balancing weight and performance can reduce costs for launching. Performance and safety are always great concern on aerospace field. The heat shield protection of space shuttles could be optimised to reduce weight and increase reliability by using FGM plates. Bhatt (2000) showed the use of silicon nitride ceramics for turbine nozzle guide vanes. Silicon nitride supports high temperature but has high processing cost and low impact resistance. Grading using SFF technologies, powder metallurgy and gel casting was studied as alternative to produce viable parts. Aboudi *et al* (2000) presented the use of FGM for tailoring the response of structural components by the high order theory. This intended to analyse the performance of the gradient by the microstructure modelling on FEM analysis. Later work presented by Arnold (2001) applied the theoretical model for simulating the response of FGM for cooling thermal shield plates for space shuttles. Combining a thermal barrier material (e.g. ceramic) with a conductive material with higher toughness, higher efficiency could be achieved. Figure 2-10 shows an example of how the gradient would provide a smooth transition between these two materials helping to maintain the integrity of the shuttle.

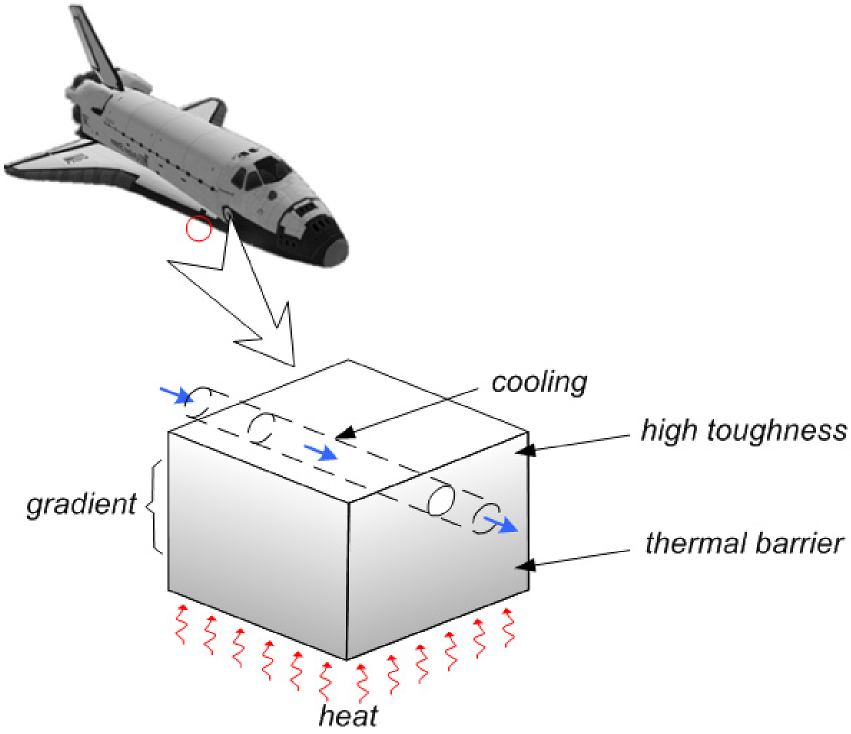

Figure 2-10. Example of application of FGM for high performance thermal barrier (Hopkinson *et al*, 2005).

One of the targets for new space missions is the use of reusable equipment to reduce costs. Laux *et al* (1998) explore the manufacturing of FGM by atmospheric plasma spraying and gradients between Inconel 625 and proper heat shield materials (ZrO_2 or TiO_2). The target of this initial research was to produce more reliable and reusable shuttle shield fuselage.

2.2.5.(b). Medical

Among the applications for FGM, medical implants appear as a strong field of research. The aim of using FGM to produce implants is to use the mechanical properties of the alloys, ceramics and composites grading with bio-compatible materials. So a bone implant can be formed by a strong and tough material in the core with graded bone tissue compatible material to the surface and low friction material in the joints.

Watari *et al* (1997) presented a method for the fabrication of dental implants of titanium and ceramic hydroxyapatite. The base of the implant was made of hydroxyapatite to be inserted in the jaw. The implant was titanium graded until the top to receive the teeth prosthesis. The experiment showed successful bone tissue growing around the insert. The implant was produced by grading the titanium and hydroxyapatite powders inside and rubber silicon mould that was submitted to cold isostatic pressure and then sintered in a furnace.

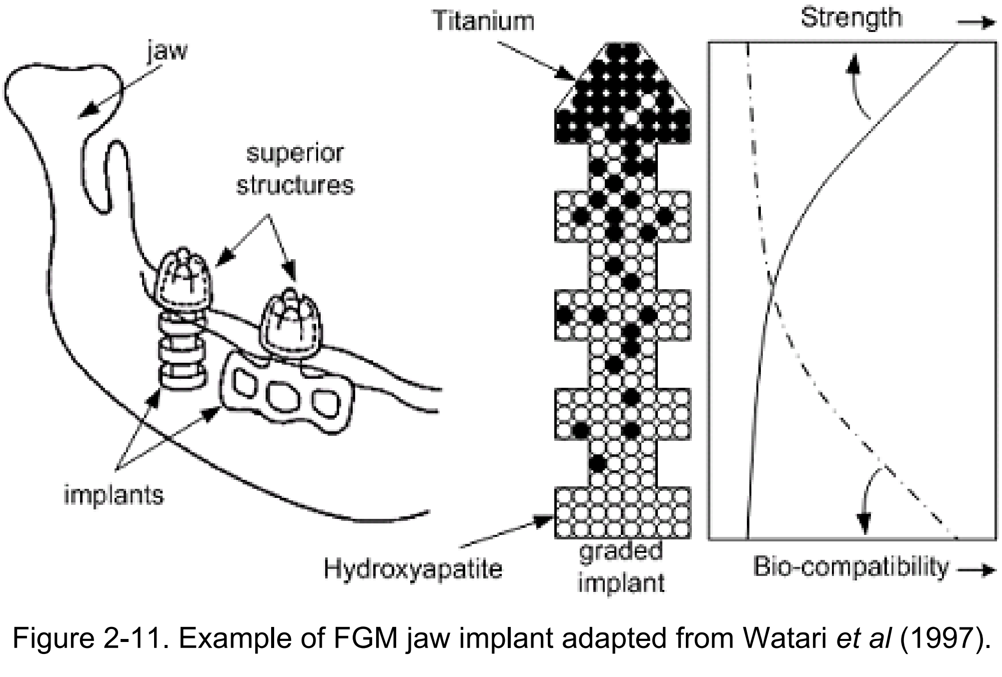

Figure 2-11. Example of FGM jaw implant adapted from Watari *et al* (1997).

Chu *et al* (1999) also have studied FGMs with titanium and hydroxyapatite and the results showed that better mechanical properties for the implant was obtained as no interfacial problem was detected. Roop Kumar and Maruno (2002) also added glass to the hydroxyapatite powder and coated titanium implants for better bio-compatibility. Glass and glass-matrix/zirconia graded layers were used to coat alumina substrates in Vitale Brovarone *et al* (2001). The grading was necessary due to the different expansion coefficient mismatch between the substrate and the coatings. The coatings provided good biocompatibility as the alumina provided good mechanical properties. Castillo *et al* (2003) presented the fabrication of FGM biocompatible by combustion synthesis. Results have been found better when producing gradients in low gravity to form more homogeneous and continuous smooth gradient. Also, pores and grains formed in low gravity where rounded differently from those formed under terrestrial experiments with lamellar and longitudinal structures. The structural format of the bone implant can be affected this differences in the formed structure. It was shown that materials produced in low gravity can increase the rate of tissue growing around the implant. Khor *et al* (2003) produced FGM structures of hydroxyapatite coated with Ti-6Al-4V by plasma spray. Different percentages of Ti-6Al-4V were added to the hydroxyapatite to form the graded layers. The results indicated good cohesion without strong distinction between the layers. The Ti-6Al-4V provides the good mechanical strength as the hydroxyapatite the bone biocompatibility. Pompea *et al* (2003) describe many cases of implants based on functionally graded materials. Joint knees implants could be manufactured by ultra-high molecular weight polyethylene fibre reinforced with high-density polyethylene in gradients for producing low friction joints but strengthened close to the bone. Also, hydroxyapatite could be produced by different ways and porosity could be controlled to make bone tissue regeneration more efficient.

2.2.5.(c). Sporting goods

Many sports can benefit from the use of FGM. Baseball shoes had received special WC tips for reducing the wear. Between the WC tip and the structure of the shoes a graded structrure was used to reduce the impact in the tips (JAXA and JST, 2002). This is only one small example of how FGM could be used to produce high performance sporting goods. With the same idea of wear reduction, ice climbing tools such as crampons and ice axes could be graded with tungsten carbide in the sharp edges that picks the ice. Rock climbing technical friends also could have the same advantage to reduce the wear on cam surfaces. Examples of these applications are illustrated in Figure 2-12. Football shoes base could be made of FGM. With FGM the support midsole could be made with stiffer material and more flexible material could be used for the front base allowing free movements for the player.

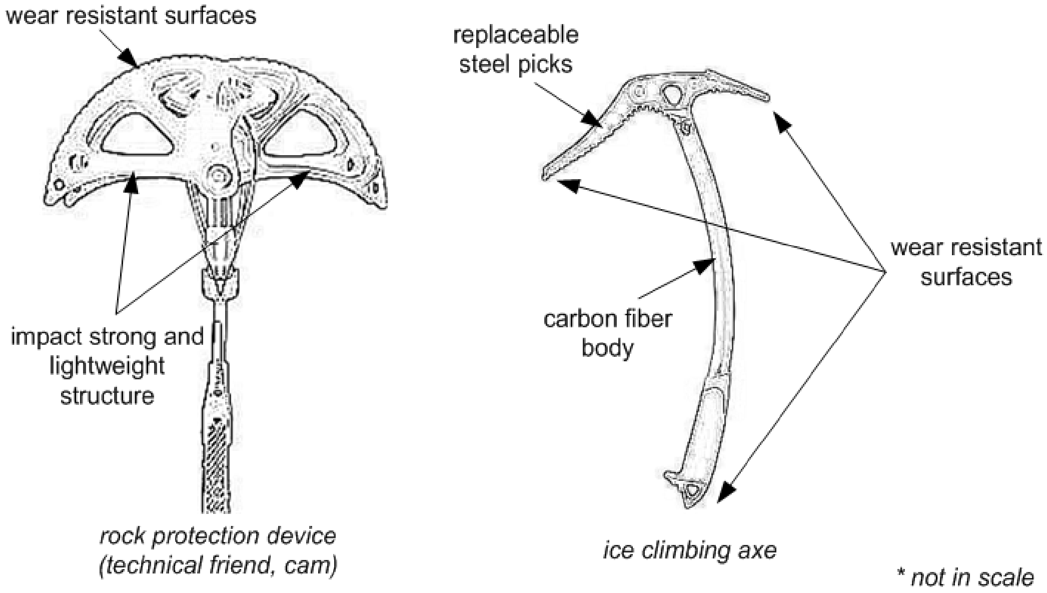

rock protection device (technical friend, cam)

ice climbing axe

Figure 2-12. Examples of ice and rock climbing gears and applicability of FGM.

2.2.5.(d). Dies and tools

The development of new dies and tools with functionally graded materials is crucial for the industry. Governments have been concerned with this development and sponsor research on this field. The U.S. Department of Energy is sponsoring the research in this area (U.S. Department of Energy, 2004 & 2005). The claim is that improved tools and dies can reduce the number of scraps and waste in parts manufacturing reduced production cycles times and increasing tooling life. This could be achieved by producing tools with superior wear resistance, improved thermal management, dimensional stability and resistance to die degradation.

Tools/Inserts for cutting manufacturing operations have been developed by FGM use as well. As an example, Mitsubishi Miracle coated indexable inserts are produced on tungsten carbide base and coated with graded layers by Chemical Vapour Deposition (CVD) (JAXA and JST, 2002). Sandvik has also developed cemented carbides with “Dual Properties” grades. In this case, the binder worked in a way that the properties of the material change from the surface to the core of the part (Sandvik, 2004).

2.3. Functionally graded materials by layered additive manufacturing technologies

The use of layered additive manufacturing technologies, or Solid Free-Form Fabrication technologies (SFF), has been cogitated as a way to produce FGM complex shapes (Miyamoto *et al*, 1999; Shishkovsky, 2001; Calder, 2001; Kieback, *et al*, 2003). This section presents an overview of the researches that have been made.

2.3.1. Software

SFF processes are characterized by their high degree of automation. From CAD data parts must be made without much effort on programming the manufacturing steps. To be able to produce FGM parts by these technologies it is necessary to receive and process data which carries the information about the gradients. One reason for the great success of SFF was the use of a common and easy way to transfer the data from CAD systems to the CAM systems of the different SFF technologies. As discussed previously in section 2.1.2, the STL format was accepted as a standard for this industry. In the same way, a new format will be necessary to carry the gradient information and many researchers have started to work in this direction. Algorithms have been developed to transform STL objects into discrete heterogeneous structures as presented in Sum *et al* (2004). Currently, many researchers had implemented the representation of heterogeneous objects in electronic data. Rvachev *et al* (2000) showed the possibility of using R-function method to represent FGM solids. This R-functions were used to make the gradient from the boundaries to the interior of the solid. Other approach was presented by Jackon (2000). His alternative to design the gradients in the parts by creating tetrahedrical mesh where the gradients could be assigned to the mesh elements. In the same way, Voxel-based representation uses a 3D spatial grid to define finite material properties to each cell of the grid (Russ & Dehoff, 2000). Knoppers (2204), had shown a STL/Voxel hybrid modeller for designing functionally graded parts. The software could create gradients based on user inputs and how it should blend geometrically inside the volume body of the component. The advantage of this software was that it could export slices directly of the model so that any 3D printing machine, with some previous processing, can use to build a 3D part (Knoppers, 2004). Nevertheless, voxel representation requires great computer power processing. In Figure 2-13, the representation of a component into a voxel space is shown.

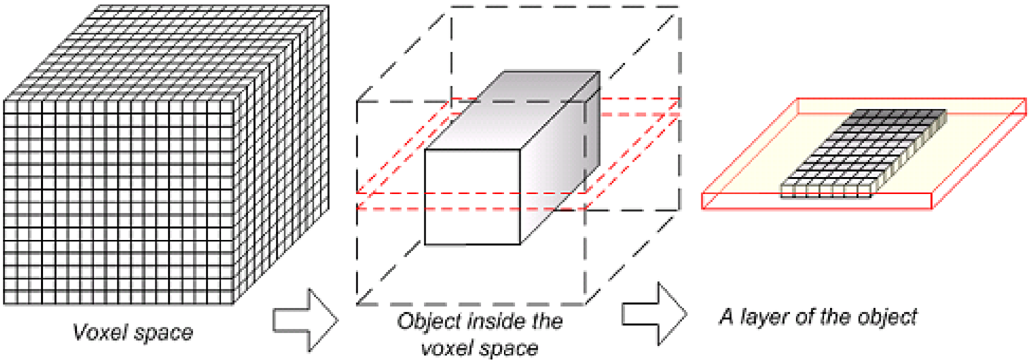

Figure 2-13. Voxel representation of FGM components.

Kumar and Wood (1999) had shown the possibility of using r_m-object model to design FGM solids. It also represents the heterogeneity of the solid by associating the material distribution with functions. Patil *et al* (2002) reported considerations on implementing FGM data in the STEP format, from ISO 10303, which is used in industry to describe the model and manufacturing process of the object. They concluded that the r_m-object model could be used for implementing FGM capabilities in the STEP format. Bhashyam *et al* (2000) presented a CAD system for generating FGM parts. In this system, the r_m-object was also used for designing heterogeneous CAD solid models. Some advances on designing FGM parts have been made on commercial CAD packages. Liu *et al* (2003) and Siu *et al* (2002) have developed applications for popular CAD software where it was possible to design solid parts and to apply material compositions. Liu *et al* (2003) developed the application for the commercial CAD package Solidworks and the approach was to produce the gradient based on the distance from the features of the model. Siu *et al* (2002)implemented on the Unigraphics software the concept of grading source for designing the gradient in the CAD model.

2.3.2. Local Composition Control

Despite the possibilities of manufacturing FGMs by layered technologies all future success depends on the development of the Local Composition Control (LCC). To give the freedom of materials and design, layers must be multi-materials. This means that the layer deposition system must have the ability to deposit more than one material, in different proportions and in specific regions with accuracy. Laser cladding technologies have the advantage of not placing the layer as the powder is coaxially sprayed in the laser focus. Ensz *et al* (2002) produced FGM thin walls of H13 and M300 steels controlling the powder composition of the spray. On a case study for the development of heat shield attachment clips for space shuttles, Domack and Baughman (2005) obtained gradients between a Ti alloy and a Ni alloy. The material were processed by laser cladding but cracks were present in the final specimens produced. By this same technology, Chavez (2000) also presented gradients of titanium alloys. In Figure 2-14, transitions between gamma titanium aluminide (Ti-48Al-2Nb-2Cr), orthorhombic titanium aluminide (Ti-22Al-23Nb) are shown.

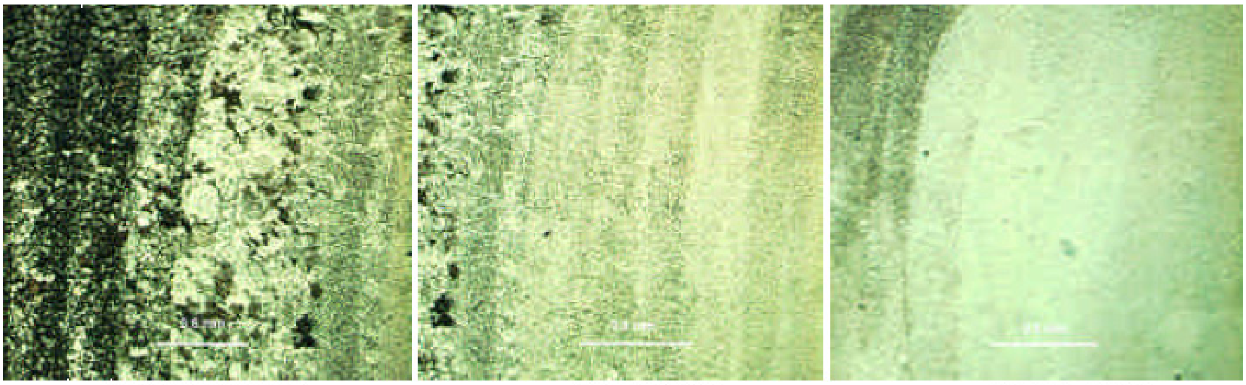

Ti-48Al-2Nb-2Cr gradient region Ti-22Al-23Nb

Figure 2-14. Different graded transitions of aluminium alloys obtained by LENS^{TM} process (Chavez, 2000).

For pre-placed powder beds, Kumar *et al* (2004) had researched the use of fine hoppers to deposit powders. The hoppers used were attached to a numeric controlled table and the powder deposition was tested by gravity, gas pressure assisted and vibration. This system could be used to deposit different materials using many hoppers as necessary depending on the graded transition needed. The apparatus could be similar to an ink-jet printer but instead of ink it would deposit powders over the bed. Yang *et al* (2004) had studied the same principle of hoppers but with capillary diameters. The powder deposition was excited by acoustic vibration. A more complex process for local composition control is by Shape Deposition Method (SDM) where FGM parts can be produced by combination of milling, resin casting and embedded inserts (Hatanaka and Cutkosky, 2003). Also by this technique is possible to produce metallic parts using Nd:YAG laser to make graded regions using powder fusion (Fessler *et al*, 1997).

2.3.3. Examples of FGM produced by additive layered manufacturing

2.3.3.(a). Dies/Moulds

In Loughborough University, FGM projects were initiated in year 2001 to investigate and build graded parts. Generally, they were focused on using chromium based tool steel (H10 and H13) and grading with tungsten carbide and copper. The addition of tungsten carbide to the tool steel matrix increased the hardness and should reduce the surface wear of tools (Su, 2002). The copper can be used to extract heat more efficiently from tool or die and is the subject of this work. Partial and preliminaries results have been presented in Beal *et al* (2004).

By the SDM, developed at the Stanford University (Stanford, CA, USA) it was possible to produce a graded tool of stainless steel, Invar and Cu (Figure 2-15). Nevertheless, the process is quite complex and involves complex planning as parts are manufactured by different traditional manufacturing process (Fessler *et al*, 1997). This process/method still is restricted to laboratory manufacturing scale.

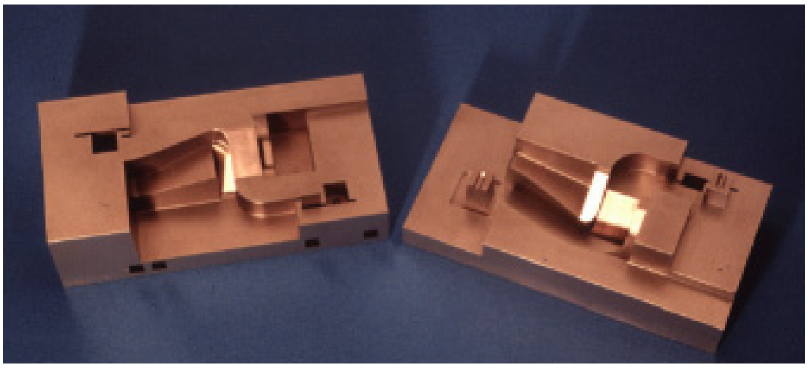

Figure 2-15. Multimaterial SDM mould (Pinilla and Prinz, 2003).

Jiang and Molian (2002) used a CO_2 by a variation of the cladding process to produce gradients from a Ni-alloy and TiC. The objective was to use a TiC layer to obtain wear resistant injection moulding. Cracks were found in the solidified layer of TiC and hardness was higher than the reference values of hardness. In another work, Jiang *et al* (2004), a FGM insert was made with H13, Ni/Cr alloy and TiC. The mould insert was manufactured by a variation of the laser cladding process. The results showed high density obtained and apparently good thermal fatigue resistance.

2.3.3.(b). Biomedical developments on FGM

Although many examples of FGM for biomedical applications were reported previously, the free form capabilities for the production are still in early stages. SFF technologies have been used since the mid 90's producing models for planning surgeries and models for the implants manufacturing (Jamieson, 1995; Swann, 1996; Sanguera *et al*, 2001; Gopakumar, 2004). Some recent researches have demonstrated the capability of SFF technologies for producing 3D human tissues. Wang *et al*, 2004-1 produced scaffolds for human tissue using FDM process. In Mironov *et al* (2003), a 3D printing tissue machine was presented. The machine could be able to build blood vessels. Future research reveals the fabrication with more than one material. Yan *et al* (2003) also used FDM technology to produce parts of biocompatible polymer. The future for FGM for biomedical might stand on the development of SFF technologies capable of working with more than one material to produce FGM implants.

Functionally graded materials technique was also used to produce controlled drug release devices. The technique used to build this high tech capsules is the 3DP process. Wu *et al* (1996) presented a study where different devices were built using this rapid prototyping technique and the rate dispersion control of the drug in the live specimen organism could be controlled by composition, geometric and gradient features. Such device would be very useful for controlling treatments in patients. The dissolution of the polymeric walls of the gradient device would act as a fourth dimension for the gradient which changes over the time.

2.4. Models for estimating material properties of FGM structures

The role idea of FGM is the same as composites: to combine the properties of different material to obtain a material with properties that suites better the design requirements. Nevertheless, on FGM this material combination is made spatially and joined by a gradient region. However, it is necessary to have an idea of the material properties of a graded region. In this section, a few suitable methods to predict the material properties from the combination between H13 and Cu are presented.

The equations of the next sections are based on the volume fraction (V) of each phase constituent. However, the powder mixtures were made by the weight percentages. The relation between the volume and the weight fraction can be obtained based on the density of each phase of the material composition. This is considered an approximation as the density can not be guaranteed as the same from the elementary phases to the final bi-phase material. Nevertheless, when the densities of the phases are not too different it can be considered a good approximation (Callister, 2001). The density ρ is defined by equation 2.01 where W is the weight of a body with volume V_{ol}.

$$\rho = \frac{W}{V_{ol}}; \qquad [\mathrm{g/cm^3}] \qquad \text{Eq. 2.01}$$

The volume of a material formed by two phases of A and B materials can be calculated by the summation of the volume of each phase (equation 2.02). This assumes that phases α[1] and β[2] still with the same density after "bonding" both A and B original materials.

$$V_T = V_A + V_B;\ [\text{cm}^3] \qquad \text{Eq. 2.02}$$

The summation of the weight fraction of phase of the material has to be equal to 1. So, the weight fraction (W_β) of the B material that forms the β phase is defined in equation 2.03 (α is the phase of the A material).

$$W_\beta = 1 - W_\alpha;\ \ [\text{g}] \qquad \text{Eq. 2.03}$$

So, the volume fraction of α phase (V_α) can be defined by equation 2.04. Analogous equation can be made for the volume fraction of the β phase.

$$V_\alpha = \frac{V_A}{V_T} = \frac{\frac{W_\alpha}{\rho_A}}{\frac{W_\alpha}{\rho_A} + \frac{W_\beta}{\rho_B}} = \frac{\frac{W_\alpha}{\rho_A}}{\frac{W_\alpha}{\rho_A} + \frac{1-W_\alpha}{\rho_B}}; \qquad [\%] \qquad \text{Eq. 2.04}$$

2.4.1. Estimations by the rules of mixtures

The Rules Of Mixtures (ROM) are basic equations which can estimate a material property based on the volume fraction of each phase of a two phase material. The simplest one is the arithmetic averaged of the properties, Voight equation (Miyamoto *et al*, 1999), described by equation 2.05. P_e is the equivalent property of the composite, V_α and V_β are the volume fractions of α and β phases/materials and P_α and P_β are the properties of each corresponding phase/material. This is also known as the linear estimative.

$$P_e = V_\alpha P_\alpha + V_\beta P_\beta \qquad \text{Eq. 2.05}$$

The other alternative is the use of Reuss formula, or harmonic average, described in equation 2.06.

$$P_e = \left(\frac{V_\alpha}{P_\alpha} + \frac{V_\beta}{P_\beta} \right)^{-1} = \frac{P_\alpha P_\beta}{V_\alpha P_\beta + V_\beta P_\alpha} \qquad \text{Eq. 2.06}$$

Both formulas are simple to use and can give an idea of what the final properties achievable by the combination of two phases. Nevertheless, the Voight formula super estimates the results and Reuss under estimates. In Figure 2-16 a field E_o is applied to a composite laminated material. The arithmetic average represents the field applied parallel to the laminate direction and the harmonic average the field applied perpendicular to the composite slabs. This is a very specific case where a few FGM or composites fit and ROM will be fully suitable.

---

[1] α: phase material from “A” material.

[2] β: phase material from “B” material.

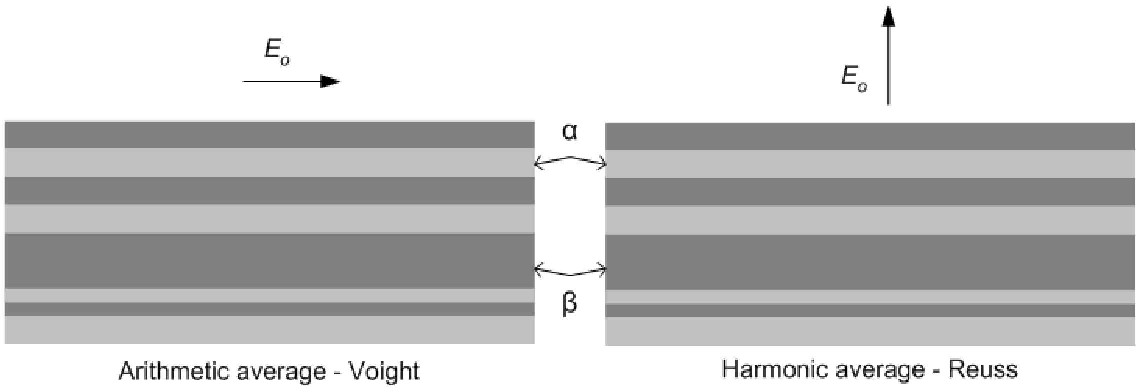

Figure 2-16. A two-phase layered material with a field E_o applied parallel and perpendicular to the laminate (Adapted from Torquato, 2001).

Figure 2-17 presents a FGM specimen formed by H13 tool steel and Cu. In this component, the distribution is a stepwise type due to its manufacturing process. The graphs show the estimative of modulus of elasticity and thermal conductivity properties calculated using Voight and Reuss equations.

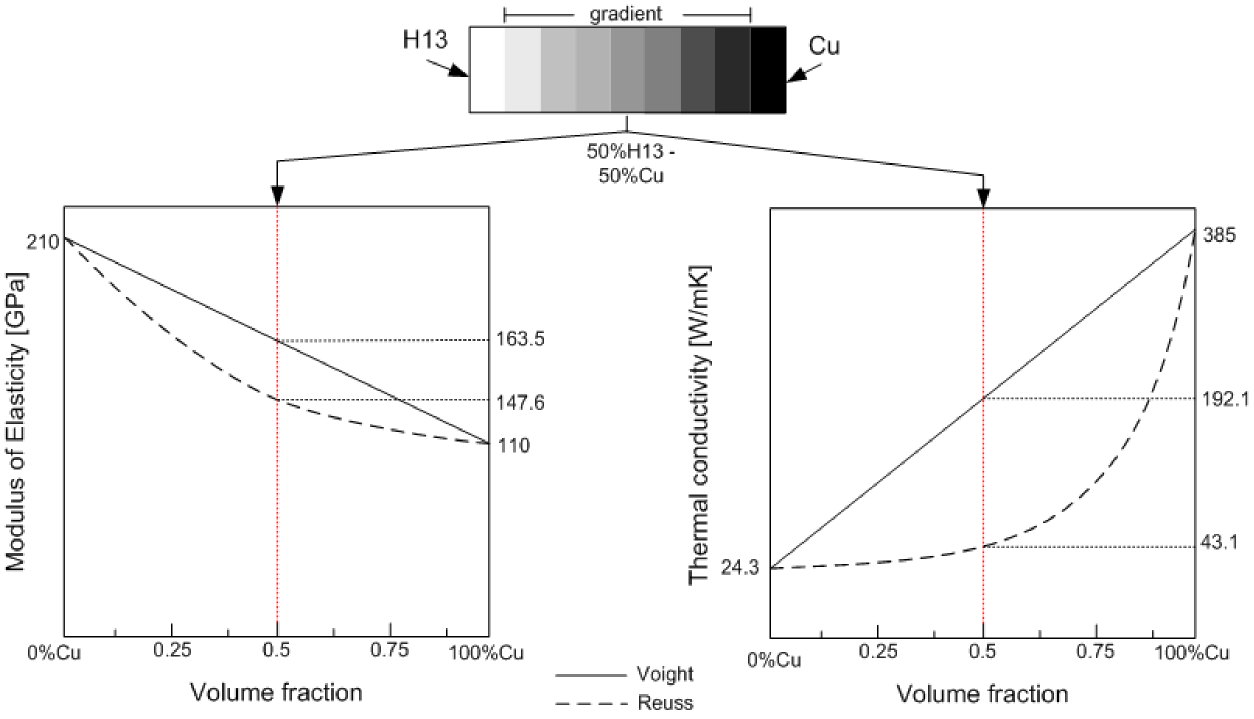

Figure 2-17. Modulus of elasticity and thermal conductivity for H13[3] and Cu[4] estimated by Reuss and Voight equations.

2.4.2. Variational approach: Hashin-Shtrikman principles

In different bibliography sources, the Hashin-Shtrikman, HS, principle is cited for determining properties of heterogeneous materials (Miyamoto *et al*, 1999; Torquato, 2001). This approach considers two isotropic phases and calculates upper and lower bounds for different properties. It is based on liner elasticity theory and variational methods to formulate equations for different properties. From equation 2.07 to 2.12 the bulk modulus (K), shear modulus (G) and thermal conductivity (k) are presented in upper and lower limits (Miyamoto *et al*, 1999).

---

[3] Material properties source: Matweb (2005-1)

[4] Material properties source: Matweb (2005-2)

$$K_{lower} = K_\alpha + \frac{V_\beta}{\frac{1}{K_\beta - K_\alpha} + \frac{3V_\alpha}{3K_\alpha + 4G_\alpha}} \quad ; \quad [\text{Pa}] \qquad \text{Eq. 2.07}$$

$$K_{upper} = K_\beta + \frac{V_\alpha}{\frac{1}{K_\alpha - K_\beta} + \frac{1V_\beta}{3K_\beta + 4G_\beta}} \quad ; \quad [\text{Pa}] \qquad \text{Eq. 2.08}$$

$$G_{lower} = G_\alpha + \frac{V_\beta}{\frac{1}{G_\beta - G_\alpha} + \frac{6V_\alpha(K_\alpha + 2\mathrm{G}_\alpha)}{5G_\alpha(3K_\alpha + 4\mathrm{G}_\alpha)}} \quad ; \quad [\text{Pa}] \qquad \text{Eq. 2.09}$$

$$G_{upper} = G_\beta + \frac{V_\alpha}{\frac{1}{G_\alpha - G_\beta} + \frac{6V_\beta(K_\beta + 2\mathrm{G}_\beta)}{5G_\beta(3K_\beta + 4\mathrm{G}_\beta)}} \quad ; \quad [\text{Pa}] \qquad \text{Eq. 2.10}$$

$$k_{upper} = k_\alpha + \frac{V_\beta}{\frac{1}{k_\beta - k_\alpha} + \frac{V_\alpha}{3k_\alpha}} \quad ; \quad [\text{W/m.k}] \qquad \text{Eq. 2.11}$$

$$k_{lower} = k_\beta + \frac{V_\alpha}{\frac{1}{k_\alpha - k_\beta} + \frac{V_\beta}{3k_\beta}} \quad ; \quad [\text{W/m.k}] \qquad \text{Eq. 2.12}$$

The HS principle is based only in the material isotropic properties and volume fractions of the constituent but information about the special distribution of the phases can be adapted to the principle and might increase the accuracy of upper and lower bounds (Torquato, 2001).

2.4.3. Micromechanical approaches

The estimation of material properties in the micromechanical approaches are based on the geometric dispersion of the phases into the microstructure. The following section presents a few available equations from the literature that could be used to estimate the value of some properties in a two-phase material based on standard methods. Other standard methods that are not described here are the numerical solutions and higher order methods where Suresh and Mortensen (1998) cover both cases. The other standard methods, Kerner, Wakashima and Tsukamoto and Ravichandran are presented in the next sections.

2.4.3.(a). Kerner

One of the first methods and simplest of micromechanical models assume the spherical reinforcement particle in an isotropic medium. The phases should have perfect bonding and bulk modulus (K_{kerner}), shear modulus (E_{kerner}), conductivity coefficient (k_{kerner}) and linear expansion coefficient (α_{kerner}) are calculated by equations 2.13 to 2.16 (Miyamoto *et al*, 1999).

$$K_{\ker ner} = \frac{V_\alpha K_\alpha + V_\beta K_\beta \left[\dfrac{3K_\alpha + 4G_\alpha}{3K_\beta + 4G_\alpha}\right]}{V_\alpha + V_\beta \left[\dfrac{3K_\alpha + 4G_\alpha}{3K_\beta + 4G_\alpha}\right]}; \qquad \text{[Pa]} \qquad \text{Eq. 2.13}$$

$$G_{\ker ner} = G_\alpha \left[\frac{\dfrac{V_\beta G_\beta}{(7-5\gamma_\alpha)G_\alpha + (8-10\gamma_\alpha)G_\beta} + \dfrac{V_\alpha}{15(1-\gamma_\alpha)}}{\dfrac{V_\beta G_\alpha}{(7-5\gamma_\alpha)G_\alpha + (8-10\gamma_\alpha)G_\beta} + \dfrac{V_\alpha}{15(1-\gamma_\alpha)}}\right]; \qquad \text{[Pa]} \qquad \text{Eq. 2.14}$$

$$k_{\ker ner} = \frac{V_\alpha k_\alpha + V_\beta k_\beta \left[\dfrac{3k_\alpha}{k_\beta + 2k_\alpha}\right]}{V_\alpha + V_\beta \left[\dfrac{3k_\alpha}{k_\beta + 2k_\alpha}\right]}; \qquad \text{[W/m.k]} \qquad \text{Eq. 2.15}$$

$$\alpha_{\ker ner} = V_\alpha \alpha_\alpha + V_\beta \alpha_\beta + 4(\frac{G_\alpha}{K_{kener}}) \left[V_\beta(\alpha_\alpha - \alpha_\beta) \left[\frac{K_{\ker ner} - K_\beta}{4G_\alpha + 3K_\beta}\right]\right]; \qquad \text{[mm/mm.k]} \qquad \text{Eq. 2.16}$$

2.4.3.(b). Wakashima and Tsukamoto

In the Wakashima and Tsukamoto (WT) approach, the model developed by Kerner is improved for ellipsoids and many of these ellipsoids have interaction. This would mean a saturated phase formed by ellipsoid bounded in a matrix phase. Equations 2.17 to 2.21 calculate the bulk (K_{WT}) and shear modulus (G_{WT}), the conductivity coefficient (k_{WT}), specific heat (C_{WT}) and expansion coefficient (α_{WT}) (Miyamoto *et al*, 1999).

$$K_{WT} = V_\alpha K_\alpha + V_\beta K_\beta + V_\alpha V_\beta \left[\frac{(K_\alpha - K_\beta)\left[\dfrac{1}{K_\alpha} - \dfrac{1}{K_\beta}\right]}{\dfrac{V_\alpha}{K_\alpha} + \dfrac{V_\beta}{K_\beta} + \dfrac{4G_\alpha}{3K_\alpha K_\beta}}\right]; \qquad \text{[Pa]} \qquad \text{Eq. 2.17}$$

$$G_{WT} = V_\alpha G_\alpha + V_\beta G_\beta + V_\alpha V_\beta \left[\frac{(G_\alpha - G_\beta)\left[\frac{1}{G_\alpha} - \frac{1}{G_\beta}\right]}{\frac{V_\alpha}{G_\alpha} + \frac{V_\beta}{G_\beta} + \frac{9K_\alpha + 8G_\alpha}{3G_\alpha(K_\alpha + 2G_\alpha)}} \right]; \qquad \text{[Pa]} \qquad \text{Eq. 2.18}$$

$$k_{WT} = V_\alpha k_\alpha + V_\beta k_\beta + V_\alpha V_\beta \cdot \frac{(k_\alpha - k_\beta)}{\frac{3}{(V_\beta / V_\alpha) - 1} + V_\alpha}; \qquad \text{[W/m.K]} \qquad \text{Eq. 2.19}$$

$$C_{WT} = V_\alpha C_\alpha + V_\beta C_\beta \quad ; \qquad \text{[J/g.k]} \qquad \text{Eq. 2.20}$$

$$\alpha_{WT} = V_\alpha \alpha_\alpha + V_\beta \alpha_\beta + V_\alpha V_\beta \cdot \frac{(\alpha_\alpha - \alpha_\beta)(K_\alpha - K_\beta)}{V_\alpha \alpha_\alpha + V_\beta \alpha_\beta + \frac{3K_\alpha K_\beta}{4G_\alpha}}; \qquad \text{[mm/mm.k]} \qquad \text{Eq. 2.21}$$

It is clear that equation 2.20 for the specific heat is same arithmetic average from the rules of mixtures.

2.4.3.(c). Ravichandran

The previous models were suited for spherical inclusions dispersed in a matrix. Ravichadran developed an upper and lower bound of the elastic modulus for an arrangement of cubic inclusions distributed in a matrix. Again, the assumption of isotropic materials was made and equations 2.22 and 2.23 present the upper and lower limits defined for the elastic modulus. The c_{ravi} is a coefficient which defines the matrix of the two phase material (equation 2.24). In this model, the Poisson coefficient was considered equivalent for both phases.

$$E_{lower\_ravi} = \frac{(c_{ravi} E_\beta E_\alpha + E_\alpha^2)(1 + c_{ravi})^2 - E_\alpha^2 + E_\beta E_\alpha}{(c_{ravi} E_\beta + E_\alpha)(1 + c_{ravi})^2}; \qquad \text{[Pa]} \qquad \text{Eq. 2.22}$$

$$E_{upper\_ravi} = \frac{(E_\beta E_\alpha + E_\alpha (1 + c_{ravi})^2 - E_\alpha^2)(1 + c_{ravi})}{c_{ravi}(E_\beta - E_\alpha) + E_\alpha (1 + c_{ravi})^3}; \qquad \text{[Pa]} \qquad \text{Eq. 2.23}$$

$$c_{ravi} = \left(\frac{1}{V_\beta} \right)^{1/3} - 1; \qquad \text{Eq. 2.24}$$

2.4.4. Estimated properties

Based on the previous methods, some properties of the H13 and Cu mixtures can be estimated. In the next sections, the equations are plotted in graphs and comments about them are made.

The estimated properties were based on the values for standard H13 and Cu obtained from references (Matweb, 2005-1 for H13 and Matweb, 2005-2 for Cu). These values are listed in Table 2-3.

Table 2-3. Base properties for the calculus of the estimations.

Property	H13	Cu	Units
Density	7,8	8,96	g/cm3
Specific heat	0,46	0,385	J/g.K
Thermal conductivity	24,3	385	W/m.K
Expansion coefficient	11×10^{-6}	$16{,}4 \times 10^{-6}$	1/K
Elastic modulus	210	110	GPa
Bulk modulus	140	140	GPa
Shear Modulus	81	46	GPa
Hardness	5,384	0,9807	GPa
Poisson's coefficient	0,3	0,343	-

Some properties were not chosen to be plotted as they only where calculated by the ROM equations or because it was the same for both materials (Bulk modulus). These properties are density, bulk modulus, hardness, specific heat and Poisson's coefficient are calculated at the final table of this section for each H13-Cu composition.

The calculus and graphs are all in function of the weight fraction defined by equation 7.04. So, for the weight fraction 0 it means 100% H13 and 0,5% means H13-50%Cu.

2.4.4.(a). Thermal conductivity

The thermal conductivity properties estimated by the presented equations are shown in Figure 2-18. In this graph, only the proportions between H13 and H13-50%Cu are plotted as they are the compositions of study in this work. The Reuss ROM (k_{reuss}) shows the lowest values for the conductivity. HS upper limit (k_{upper}) and Kerner (k_{kerner}) present the same curve. The odd curve is the one from Wakashima and Tsukamoto (k_{WT}) where the curve does not converge to the pure H13 value of conductivity. The lower bound of HS (k_{lower}) is slightly higher than the ROM Reuss estimative.

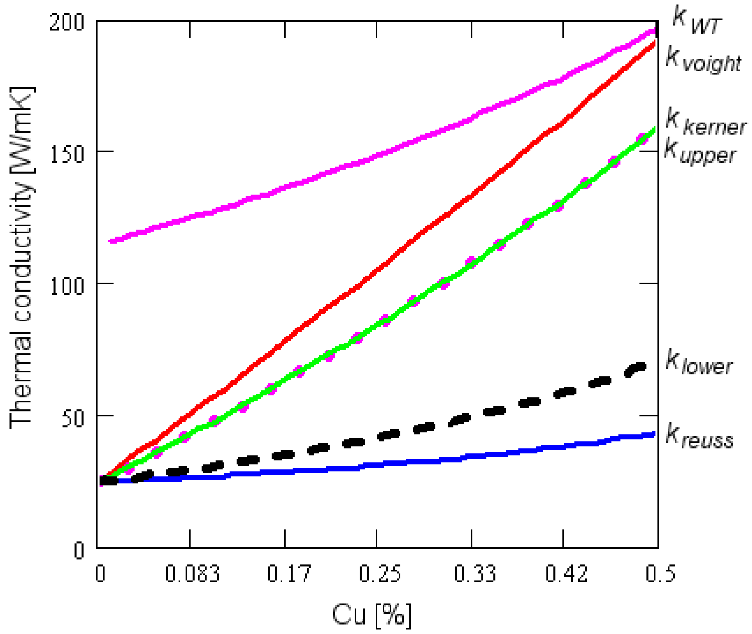

Figure 2-18. Estimated thermal conductivity coefficients.

2.4.4.(b). Expansion coefficient

The difference between the expansion coefficients of Cu and H13 is around 30% at room temperature (H13: 11,0*10^{-6} °C^{-1}; Cu: 16,4*10^{-6} °C^{-1}) and it increases at higher temperatures. Figure 2-19 shows the estimation for the expansion coefficients (α) of the materials used in this work. The α_{WT}, α_{kerner}, and α_{voight} presented the same behaviour and the expansion coefficient calculated by Reuss equation of ROM presented a more conservative estimation.

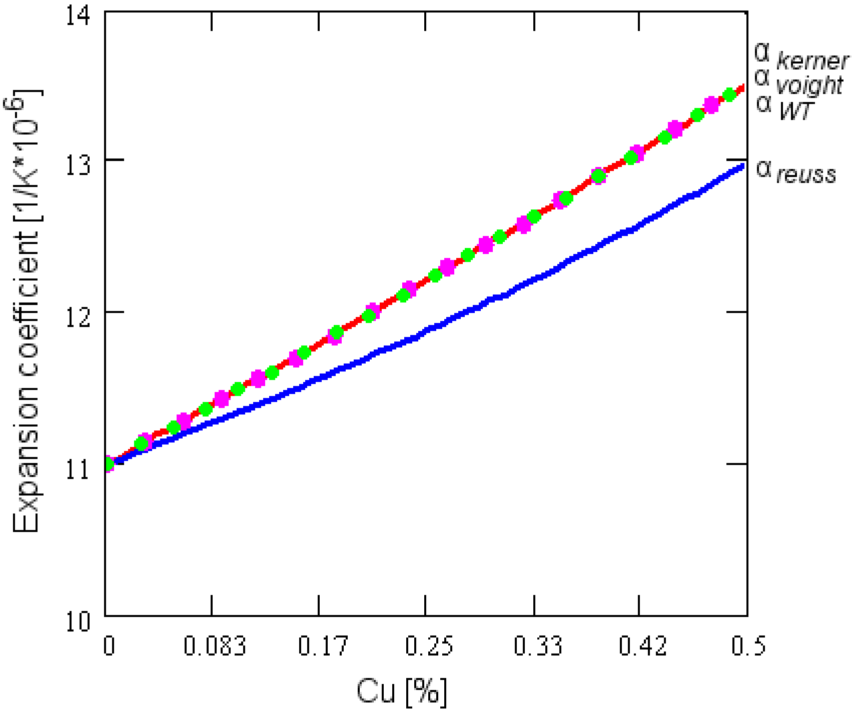

Figure 2-19. Estimated thermal expansion coefficients (at 20°C).

2.4.4.(c). Elastic modulus

In the previous sections, many of the estimations for the elastic properties of the materials were based on the shear (G) or bulk (K) modulus. The estimated shear modulus is plotted in Figure 2-20. The Voight and Reuss ROM presented to be upper and lower limits of the estimations for the compositions. The others shear modulus curves remained inside between these limits stabilized by the ROM equations.

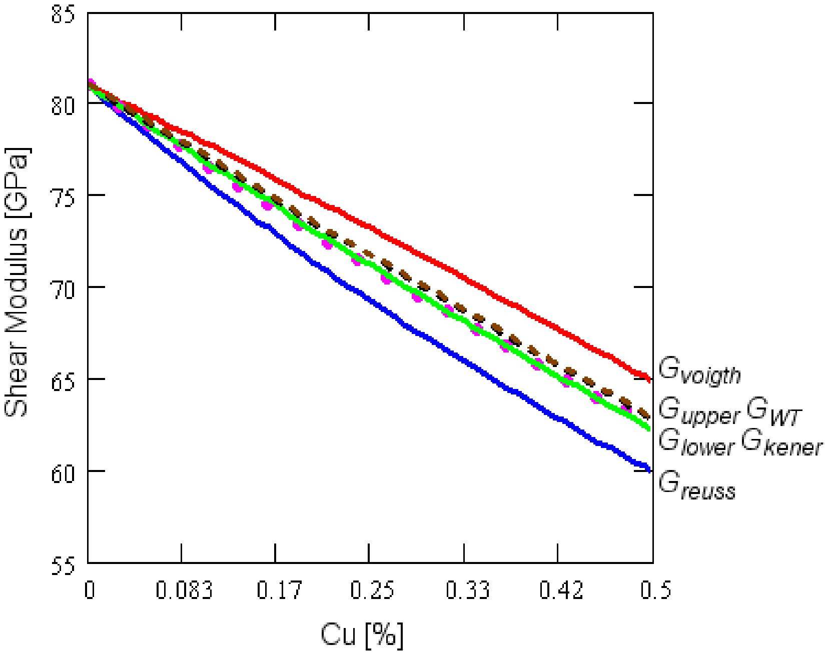

Figure 2-20. Estimated shear modulus.

Both Cu and H13 present the same value for the compression modulus (K: 140GPa) so all estimations calculated a linear constant that presumably did not correspond to the true response of the material.

The most direct elastic property is the elastic modulus (E) which a direct reference to the material property. From the above presented estimations, the elastic modulus only could be directly calculated by the ROM equations and by Ravichandran model. However, the elastic modulus can be related to the shear and bulk modulus by the Poisson coefficient. It is assumed that for an isotropic media, all other elastic properties can be derived from the bulk and shear modulus using the relations from equations 2.25 to 2.28 where σ is the stress, ε is the deformation, E the elastic modulus and γ the Poisson coefficient. The indices x, y and z are for the planes that stress and deformations are actuating. V_f and V_o are the final and initial volume of the solid isotropic body.

$$K = \frac{\sigma}{\Delta V / V} = \frac{\sigma}{\varepsilon_{xx} + \varepsilon_{yy} + \varepsilon_{zz}} = \frac{E}{3(1-\gamma)}; \qquad \text{[Pa]} \qquad \text{Eq. 2.25}$$

$$\frac{\Delta V}{V_0} = \frac{V_f - V_0}{V_0} \approx \varepsilon_{xx} + \varepsilon_{yy} + \varepsilon_{zz}; \qquad \text{Eq. 2.26}$$

$$G = \frac{\sigma_{xy}}{\varepsilon_{xy} + \varepsilon_{yx}} = \frac{\sigma_{xy}}{2\varepsilon_{xy}} = \frac{\sigma_{xy}}{\gamma_{xy}} = \frac{E}{2(1+\gamma)}; \qquad \text{[Pa]} \qquad \text{Eq. 2.27}$$

$$\gamma_{xy} = \varepsilon_{xy} + \varepsilon_{yx} = 2\varepsilon_{xy} \qquad \text{Eq. 2.28}$$

Replacing shear and bulk modulus from the previous models presented in the above equations (2.25 and 2.28), it was possible to estimate the variation of the elastic modulus according to the powder fused composition. The elastics properties are plotted in Figure 2-21. The major difference from the shear modulus in Figure 2-20 is the upper and lower bounds from the Ravichandran model. The upper limit (E_{upper_ravi}) of this model remains between the ROM equations (E_{reuss} and E_{voight}). The lower limit of Ravichandran (E_{lower_ravi}) delimited the lower values obtained from all estimations. As some curves were superposed the E_{upper} curve represents all curves from HS (upper and lower bounds), WT and Kerner models calculated using the bulk modulus in equation 2.25. Additionally, the same models calculated using the shear modulus in equation 2.27 were superposed in curve E_{lower}. The estimations by E_{lower} and E_{lower_ravi} presented lower values than the material only formed by Cu (E_{Cu}=110GPa; Matweb, 2005-2) even in the case of 100% H13.

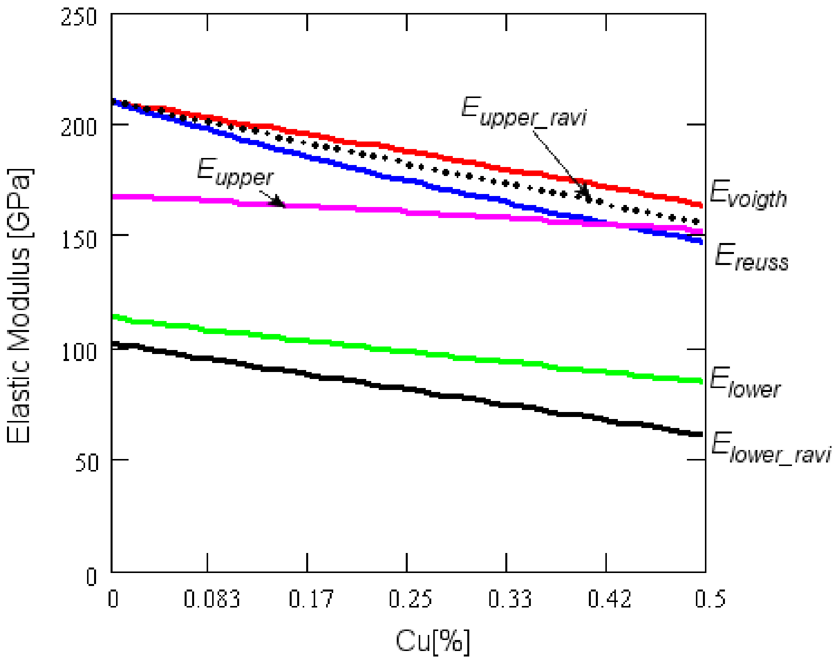

Figure 2-21. Estimated elastic modulus.

2.4.5. General comments about the properties estimation

The major objective using these estimations was to obtain an idea of the properties that could be achievable by mixing the H13 and Cu powders and fusing it with a laser beam. From the models presented it was showed that there are a few alternatives from literature that cover the microstructures obtained in the experiments performed in this work (further covered in Chapter 5). The selective laser fusion process itself can not produce isotropic materials although these are rarely found in any manufacturing process. Other important fact is that the models do not include defects from the microstructure. As it is discussed latter in Chapter 5, cracks and pores might be present in the microstruture hence certainly affected the materials properties. Also, the models do not cover the microstructure changes with the Cu addition. So, possibly it would be necessary to create specific models for each range where the microstructure remains almost the same. The estimation models presented here demonstrate that experimental data is necessary to backup engineering decisions. As it could be seen, the variation of the properties by the estimations is large. It would be difficult to define a gradient composition based only in the models.

2.5. Laser material processing

This section was written to introduce laser basic concept, how laser is used nowadays for processing materials and some information about the Nd:YAG lasers and characteristics and working capabilities of the laser used in this work.

2.5.1. Laser principles

LASER is an acronym for “Light Amplification by Stimulated Emission of Radiation”. Its development comes from the early 60’s when Theodore Harold Maiman developed the first laser device using a ruby crystal rod pumped by a flashlamp to produce a red laser beam. Before it, the MASER (Microwave Amplification by Stimulated Emission of Radiation) was developed in mid 50’s by Charles Townes and Arthur Schawlow. The principle of the stimulated emission was theorized by Albert Einstein in 1917. Lasers didn’t had many applications when first created. It was an invention searching for a use. Nowadays it is impossible to think on the technical developments achieved by human kind without the contribution of lasers.

The laser works based on the stimulated emission phenomenon of an active medium inside a cavity called resonator. The atoms or molecules of the active medium can absorb and emit energy. Considering a medium formed by atoms, when energy is added to an atom a electron might change its energy level. At the time this energy is released, the emission of a photon occurs. This might happen by spontaneous or stimulated emission. Figure 2-22 exemplifies the different between these two emissions. In the spontaneous emission, an electron changes its energy level after absorbing the energy in form of a photon. Latter, it releases this energy photon returning to its original and more stable energy level. This is a very common phenomenon in the nature. The stimulated emission happens when an already excited electron is stimulated by other photon to release its energy. When this happens, another photon with identical characteristics of the trigger photon is released.

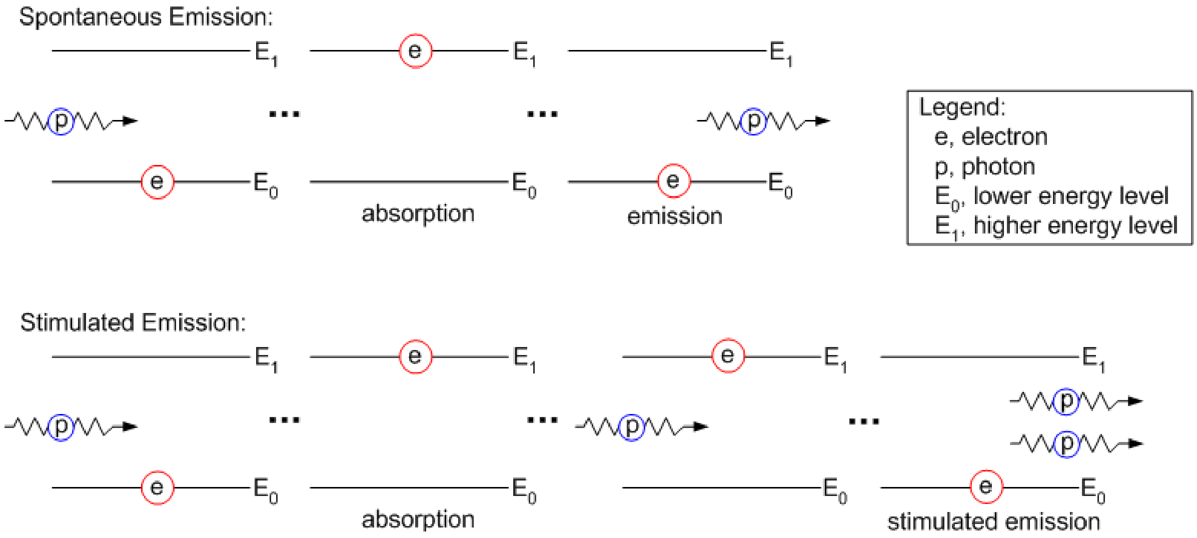

Figure 2-22. Spontaneous and stimulated emission phenomena.

There are many properties that describe the laser beam according to the laser medium, if it is pulsed or continuous, wavelength, transverse electromagnetic mode (TEM), power, energy density and others that depends on the optical and electronic systems used to manipulate the output laser. Without extending this revision, some of these properties will be discussed in the practical use of lasers in the next sections. The characteristics of the laser beam will determine which application is more suitable for it. The most usual classification of the laser is by the type of active medium. In the active medium of a laser, the atoms or molecules are excited, pumped, by an external source such as electrical discharge, flash light, chemical reaction, diode or another laser. After pumping a particle, this will try to release this energy as a photon. This photon travelling inside the active medium will hit other excited particle and this particle also will release a photon. Now two photons will be travelling at the same wavelength, phase and direction. The resonant phenomenon described by Einstein continues through the cavity and more photons are generated. It reaches a condition called population inversion when the number of stimulated species is higher than normal state species and the medium amplifies the photonic emission process. The population inversion can only be found on specific materials that allow this to happen. Figure 2-23 shows a basic example of a laser cavity. To resonate and to direct the laser light, two mirrors are used in each extreme of the cavity. They are important to increase the stimulation of the medium stabilizing the inversion of the population. One mirror might partially reflect the laser light, leaving some energy to escape to form the laser beam. Different designs can be used to permit the laser light to come out of the cavity.

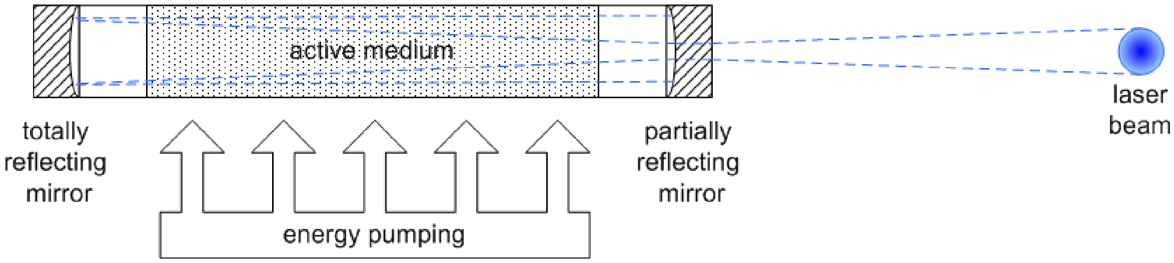

Figure 2-23. Basic example of a laser cavity (adapted from Steen, 1991).

2.5.2. Processing powders with lasers

Electromagnetic radiation can be described as waves or particles depending on the wavelength. When this radiation interacts with a surface some of this radiation is reflected, some is absorbed and some is transmitted by the surface matter. The amount of energy reflected, absorbed or transmitted will, basically, depend on the intensity, wavelength and medium (matter). If the frequency of the radiation does not corresponds to the natural resonance frequencies of the particles the electric field will excite particles to vibrate. This forced vibration makes the electrons susceptible to absorb the energy and it will be transmitted to the molecule/structure by heat diffusion. The absorption of the energy can make the material to melt and to evaporate. This is how laser light works to manipulate matter. By this principle, it is possible to use laser for many applications such as marking, cutting, drilling, surface modification, welding and surgical aid among other applications.

For any system of material, laser and optics, all parameters are related to that system. The factor that can be used to compare different systems is the energy density, E_ρ. The energy density is defined by equation 2.29 where P is the average power of the laser beam, v is the scanning speed (feedrate) and d is the laser beam spot diameter over the material. If the utilized laser is a pulsed, it can be described also by E, the pulse energy and f the pulse repetition rate. As energy density is also dependable of scanning speed and beam diameter it should be used in place of laser energy power for material processing (Lu *et al*, 2001).

$$E_\rho = \frac{P}{v*d} = \frac{E*f}{v*d} \quad ; \qquad [\mathrm{J/mm^2}] \qquad \text{Eq. 2.29}$$

Other important parameters are the absorptance and reflection of the material. The success in processing the material depends on the coupling efficiency of the energy density into the material. The incident radiation over a material is divided in transmission, absorption and reflection. The transmission is the phenomena where the material transmit the energy through its medium. Usually it is more associated to the gases, liquids and translucent solids. For opaque materials the transmission is restrained to few microns in the surface. So, for the opaque materials absorption and reflectance are more important properties. The reflectance is the part of energy radiation that is not absorbed by the material. So, summarizing, the absorptance is the material property which makes possible to process it. The absorptance of the material is dependent of the wavelength, incident angle and surface condition (Incropera & de Witt, 1992). In general, metallic materials are absorbed better small wavelengths and ceramics and polymers are better processed by longer wavelength. As an example, Fe and Cu have an absorptance coefficient of 0,64 and 0,59 respectively to a wavelength of 1,06μm (e.g. Nd:YAG lasers). For a wavelength of 10,6μm Fe has an coefficient of 0,45 and Cu 0,26 of absorptance (Lu *et al*, 2001). As commented, the absorptance does not only depend on the material composition but also its condition. Surface roughness and temperature affect directly the amount of energy reflected and absorbed.

In the next following sections, the use of laser for sintering and fusing powder is commented.

2.5.2.(a). Laser sintering

The most popular laser sintering process is the formerly known as DTM process developed by the Texas University in Austin (nowadays it is part of 3D Systems, Valencia, CA, USA). The process uses a CO_2 laser to melt polymer powders and generate three-dimensional parts. Other similar processes have been developed and are commercialized by a German based company, EOS. Figure 2-24 shows a schematic drawing of a laser sintering system from EOS. The powder bed is scanned by the laser beam which melts the powder forming a solid layer. A piston lowers the powder and a new powder layer is spread over the powder bed by a hopper. In the case of a 3D Systems machine, the hopper is replaced by a rolling cylinder. After recoating the new powder layer, the laser scans a new layer bonding the powder to the previous one. The process continues until the completeness of the part. As the part is embedded into the powder bed it does not requires supports. The most common material used for direct laser sintering in this process is the polyamide which delivers strong prototypes for engineering tests. But, polycarbonate, polystyrene and elastomeric can also be found (Jacobs, 1992). Special concern is the temperature control in the building chamber to keep particles heated enough that the laser energy necessary to fuse the particles is relatively low. This helps to maintain layers/parts stability during the process avoiding distortions. By the indirect sintering, metallic parts and sand cores for casting can be produced.

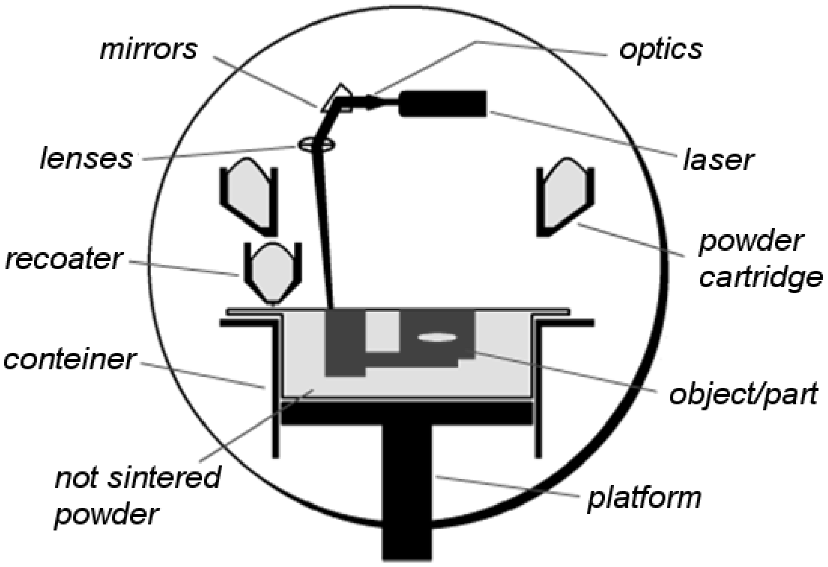

Figure 2-24. A typical laser sintering system and its components (EOS, 2003).

The actual 3D Systems process is called indirect metal laser sintering because the laser does not sinter metallic particles in the powder bed. The metallic powder is pre-mixed with a polymer which can coat or partially coat the metallic particles. The laser action when scanning the powder spread over the bed melts the polymer making the metallic parts to connect to each other and this forms the geometry of the 3D part. The process is carried as the same way for the polymer parts, spreading and scanning layer after layer. After completing the part geometry in the rapid prototyping machine, the part has to go through heat treatments. The first treatment is to burn the polymer which holds the part structure and to for pre-necks between the particles (initial stage of conventional sintering). After, a second heat treatment is applied to infiltrate by the capillarity network left by the polymer extracted from the part a lower melting point alloy such as copper alloy or brass. This increases parts density and mechanical/thermal properties. Figure 2-25 shows this steps for two commercial available materials and Figure 2-26 shows their heat treatments cycles.

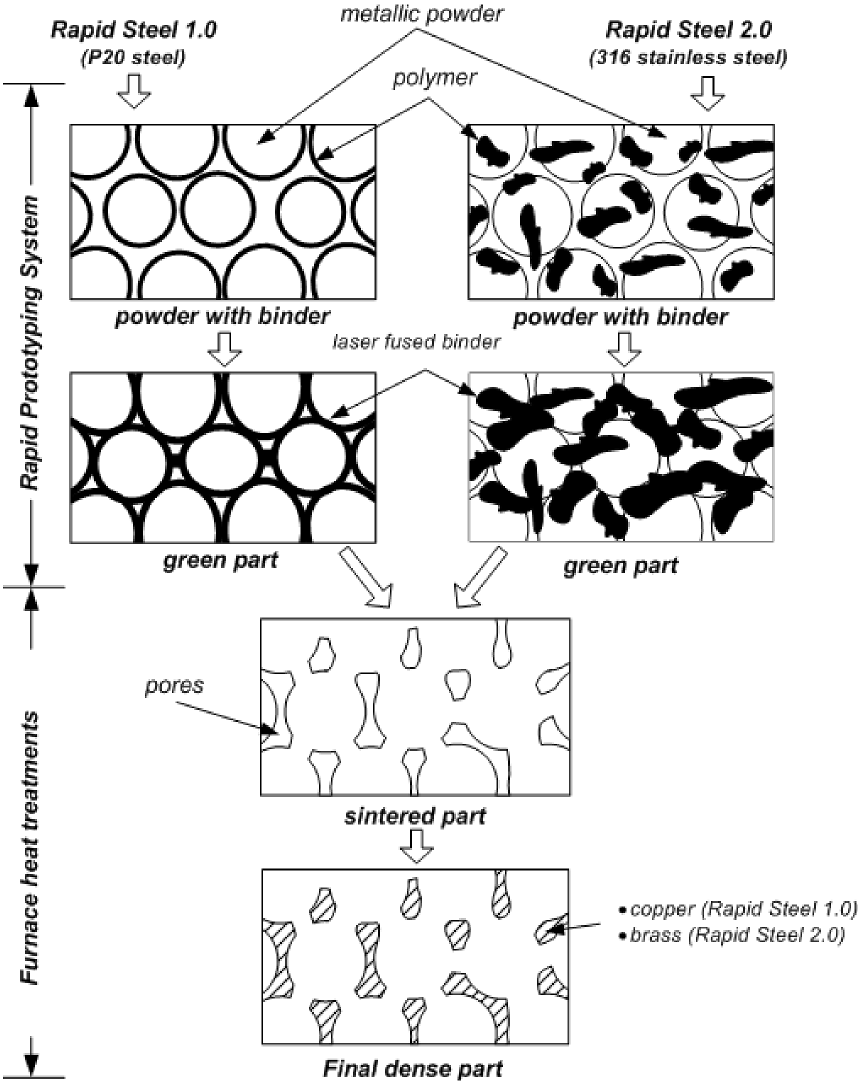
Rapid Steel 1.0
(P20 steel)
metallic powder
polymer
Rapid Steel 2.0
(316 stainless steel)
Rapid Prototyping System
powder with binder
powder with binder
laser fused binder
green part
green part
pores
sintered part
Furnace heat treatments
•copper (Rapid Steel 1.0)
•brass (Rapid Steel 2.0)
Final dense part

Figure 2-25. Steps for different materials used by the indirect laser sintering (process DTM/3D Systems).

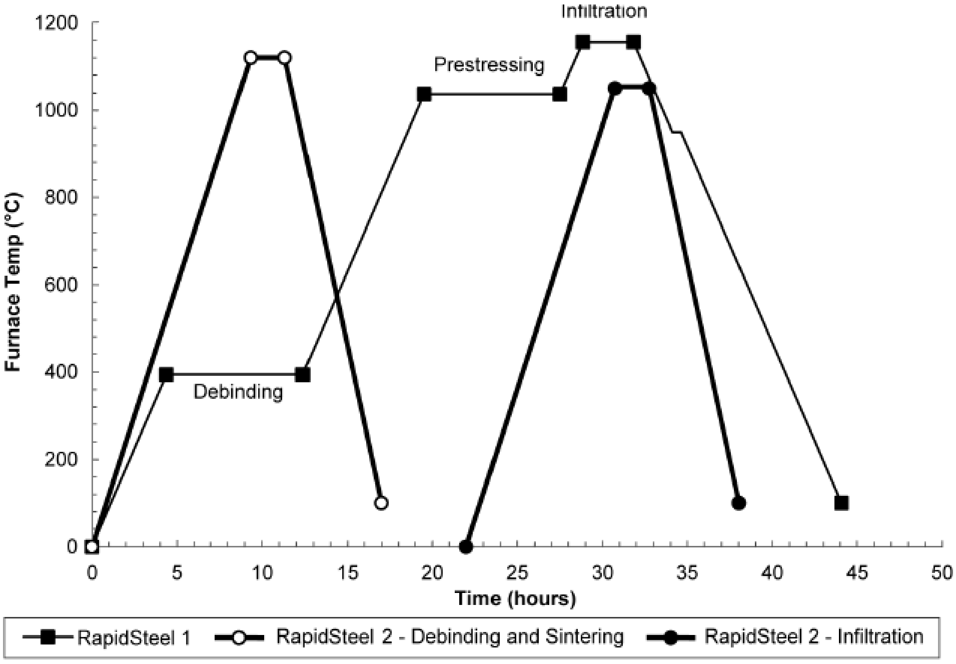

Figure 2-26. Heat treatments for indirect laser sintering (Dalgarno & Stewart, 2001).

The usual sintering process (powder die compaction and furnaces) has the objective to increase contact between the particles and reduction of the surface energy. From lose powder to almost full density part, large shrinkage is observed. This characteristic makes difficult to obtain full dense parts from directly from the laser action into the machine. That is the reason for the DTM/3D Systems process for producing metallic parts infiltrating a lower melting point metal into the "non-densificated" pore network instead of trying to increase density of the part in the machine. Also, the power required by the laser beam is higher implying in different optics, laser unit, higher temperatures in the building chamber, higher accuracy temperature control and/or even laser type (e.g.: from CO_2 is better for polymers and ceramics compared to Nd:YAG which is suitable for metals).

Normally sintering takes time to make a part dense. Densification of the part is carried out to achieve better mechanical properties by reduction of pores for many applications. For the sintering of metallic parts most of the applications try to achieve 5% or less of pores (Thümmler & Oberacker, 1993). The two main sintering states are Solid-state and Liquid Phase sintering. Liquid phase sintering (LPS) is a way to increase the sintering ratio. LPS happens when a liquid phase is formed during the sintering. The liquid phase helps to transport mass to particles contacts making pore reduction faster (Emerenko *et al*, 1970, German, 1985 & 1994). Usually powders for LPS are alloyed and a component of the blend has a lower melting point. The blend can be found in the coated, mixture, partially coated and pre-alloyed powders (Figure 2-27).

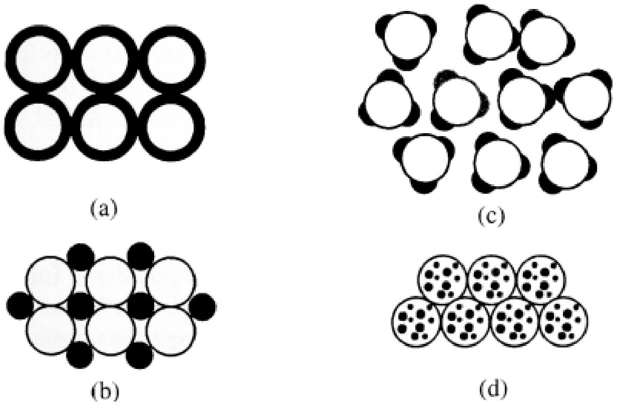

Figure 2-27: Powers for LPS: (a) coated, (b) mixture, (c) partially coated and (d) pre-alloyed powder (Klocke *et al*, 1995)

The commercial RP/RM process that build metal parts directly form the machine uses LPS as the physical process to bond the powder particles (Li *et al*, 2000; EOS, 2003). The Directmetal material is based on Cu (75,7%), Ni (15,3%), Sn (6,6%) and P (1,6%). Phosphorus promotes the LPS at lower temperatures and avoids the oxidation from oxygen. The other available material, Directsteel, is based on Fe (58,4%), Cu (8,8%), Ni (29,3%) and P (1,4%). In both cases, Sn, Cu, and P help the process to improve the LPS (Sustarsic *et al*, 2004). The commercial denomination of this process is DMLS, Direct Metal Laser Sintering. Although it has fewer steps than the indirect process parts present higher porosity and lower mechanical properties compared to those obtained by other process (Sustarsic *et al*, 2004; Storch *et al*, 2003).

Many issues concern using laser energy to activate LPS in powder beds. Agarwala *et al* (1995) stated the main parameters that are shown on Table 2-4. This table is divided in system parameters and material properties. It is possible to say that each one of these variables interact with the other ones producing different results as it was commented previously in Section 2.5.2.

Table 2-4. Process variables which affect laser sintering and densification (Agarwala *et al*, 1995).

System parameters	Material properties
Controlled: • Laser scanners • Laser power • Mechanical layering of powder • Atmosphere control • Air flow • Heaters (bed temperature) *Machine-specific:* • Laser type • Scan radius *Geometry-specific:* • Scan vector length	• Viscosity • Surface tension • Particle size distribution • Particle shape • Absorptivity/reflectivity • Specific heat • Emissivity • Melting temperature

Laser sintering, direct and indirect, has been successfully used to build injection moulding tools. These tools can be used to replace traditional cutting methods for tooling manufacturing for highly geometric complex parts. Nevertheless, in some cases, small features on the mould impression are not susceptible for high production especially due to fatigue. One of the advantages of laser sintering is the possibility for free design of the cooling/heating channels for temperature control in the mould (Wohlers, 2004). Although heat extraction can be some how optimized however it is still a complex and FGM could help to improve the optimization process.

2.5.2.(b). Laser fusion

The fusion of the powder bed by the laser is the most common resource to achieve higher densities. Fusing the powder and solidifying it to the previous layer is the base of many processes that can be divided in two main approaches: laser cladding and selective laser fusion. The selective laser fusion works almost in the way the selective laser sintering with spread layers over a powder bed. The difference is that in place of sintering, powder particles are fused completely (Lü *et al*, 2001). In laser cladding, powder is not pre-placed but a flow of inert gas with the powder particles is streamed in the direction of the laser spot (Figure 2-28).

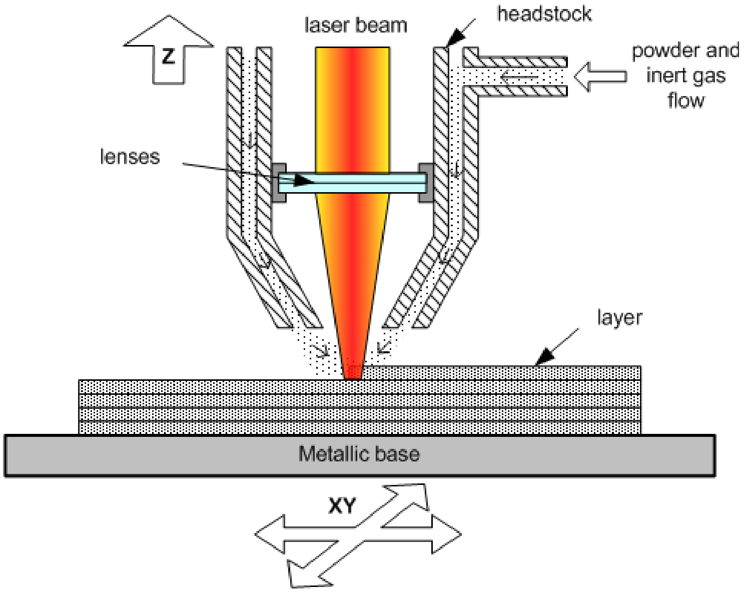

Figure 2-28. Simplified sketch of the LENS^{TM} process.

The fusion and solidification of the powder can cause high thermal gradients in the layer. Due to the contraction of the material, from powder to solidified beads, both approaches use substrates to attach the first layer of the object. The volume change from the fused to solidified material might retain residual stresses in the part after building (Pogson *et al*, 2003).

Lu *et al* (2001) presented various theory and fundamentals explained by other researchers on laser processing parameters for selective laser fusion/melting. In Figure 2-29, the sintering depth shown in function of the energy density. It is interesting to note that depth increases reducing the scan speed or increasing the beam power. Low variation was observed varying the spot diameter. Nevertheless, increasing the spot diameter the energy sintering depth decreased. Notice that in this case, sintering depth means the fusion depth.

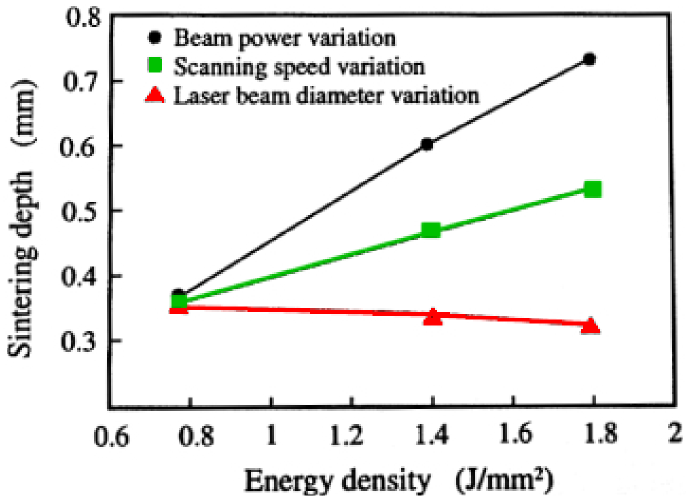

Figure 2-29: Influence of the energy density on fusion depth (Lu *et al*, 2001).

The final density of parts was also presented in function of the energy density. As expected, higher energy densities lead to denser parts. The influence over the density of the parts obtained was higher by the reduction of the scanning speed than increasing the average laser power or reducing the laser beam diameter (Figure 2-30). The higher the energy used, the denser the parts produced, however, if the energy is too high (depending on the materials adsorption), high energy could vaporise the material.

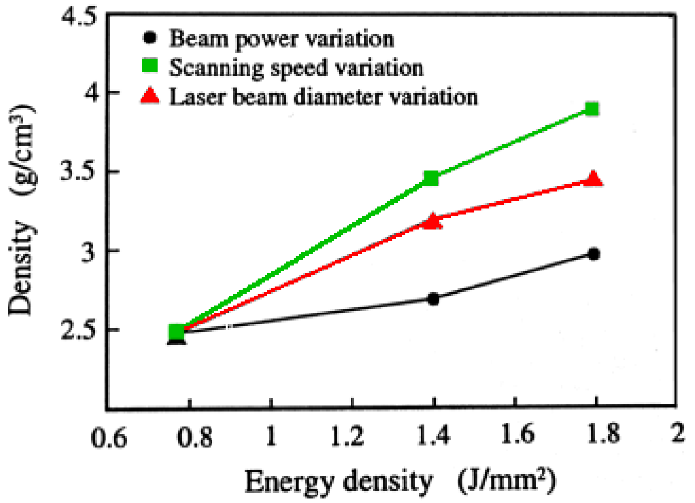

Figure 2-30: Influence of the energy density on the density of the part (Lu *et al*, 2001).

The fused material tends to form shaped cylinders. The diameter of the cylinder (laser fused bead) varies with the laser parameters. In Figure 2-31 a relation between the average power and the scan speed (rate) is shown. Combining higher average laser power and faster scanning speed, laser fused beads diameters were kept constant. Keeping the speed constant and increasing the laser power increased the laser beads as the energy density was increased.

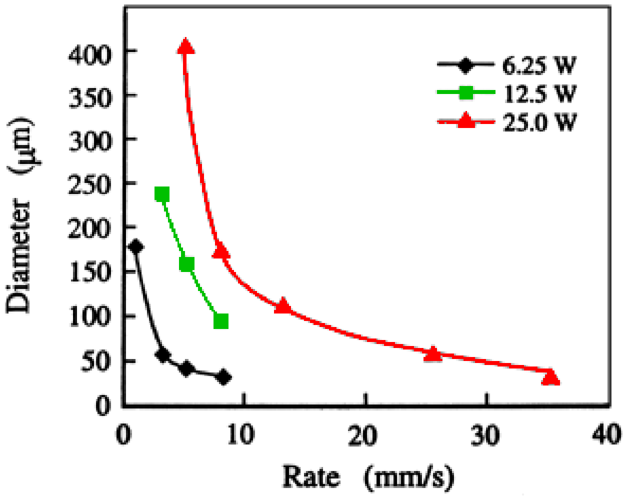

Figure 2-31: Laser scan speed and power effects on the bead diameter (Lu *et al*, 2001).

The graph in Figure 2-32 shows a map of the regions of porosity/density for laser processing of high-speed steel (M2) powder. Each region is delimited by a combination of laser power and the scan rate. As energy density increases by low scan rate and higher power, higher densities were obtained.

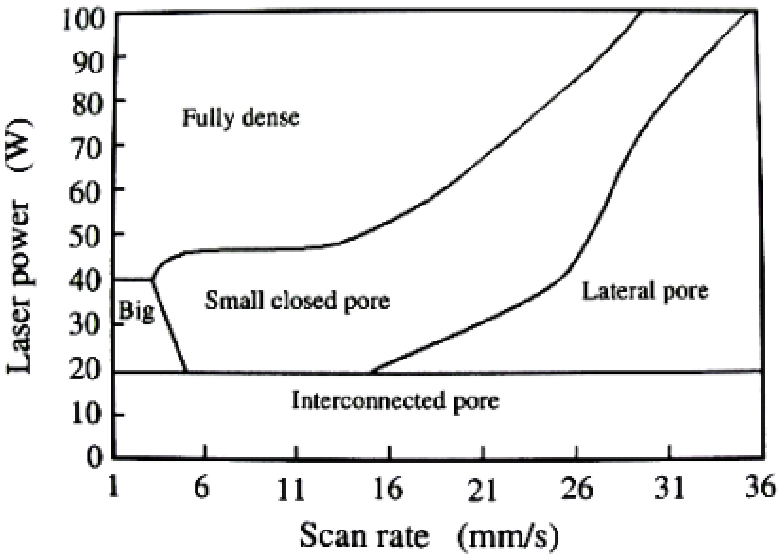

Figure 2-32: Map of porosity regions using various laser power and scan speed (Lu *et al*, 2001).

The figures previously shown are results of many different works, using different lasers types and materials. Nevertheless, they are a good reference for the fusion behaviour using different process parameters.

The LENS^{TM} process and others commercial technologies that shares the same principle of laser cladding have been used to build or to fix injection moulding tools. Despite the great versatility of the process on handling different materials, the surface finish is poor compared to other rapid prototyping technologies. Usually, these processes are used to build a bulk volume geometry of the mould/part and milling operations are necessary to obtain the final dimensions of the mould or part (Ensz *et al*, 2002).

2.5.2.(c). Building parameters

From references it is found that great concern involves not only the laser parameters (power, focus position, wavelength, scan speed, etc.) but also the building parameters. Here, some of these parameters that were important in this work are described. To cite some of the most important parameters are: laser scan strategy, vector spacing and layer thickness. The parameters that directly affect the bonding (fusion of sintering) between the powder are determined by the lasers parameters (average power, peak power, pulse width, pulse energy, scan speed). The laser parameters for the Nd:YAG laser used in this work are discussed in section 4.1.3, where the materials and methodology used are discussed.

The laser scanning strategy is the way that the laser is programmed to move its beam focus over the powder bed (Figure 2-33). It is used to fuse or sinter areas of the powder bed by “drawing” slices of the object being fabricated.

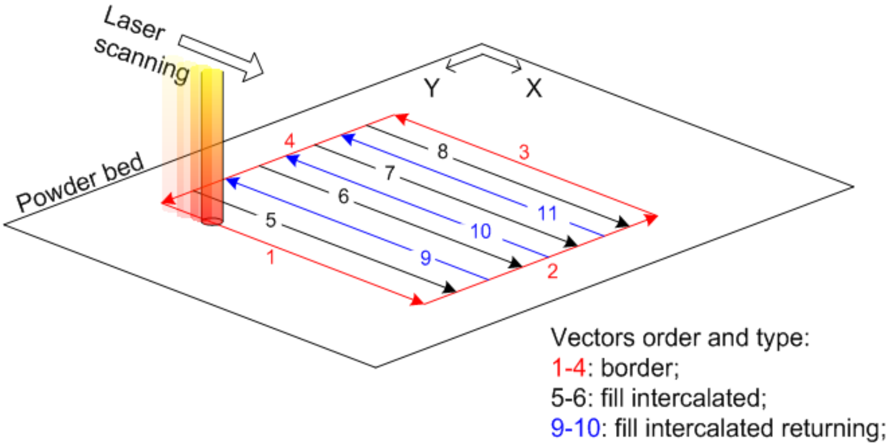

Figure 2-33. An example of laser scanning strategy.

The scanning strategy has great influence over the parts result. Matsumoto *et al* (2002) used finite element analysis (FEA) to minimize the layer distortions. In this work, it was suggested to subdivide the filling vectors in small regions to diminish curl on the layer. The other main concern is the heat concentration and hence the effect of distortion. Dai and Shaw (2002) analyzed the layer distortion simulating two different laser scan strategies. The results pointed that scanning strategies with parallel vectors should be avoided because the thermal gradients increase the layer distortion. A profile strategy, contouring the outside border to inside the centre of the layer should produce better results. Also, most of the distortion occurred in the layer was occasioned by transient thermal gradient and small affect had residual thermal stresses. Nevertheless, Dai and Shaw (2002) simulation model considered a layer sintered/fused over a powder bed without the use of substrates or pre-sintered layers. Su (2002) explored the use of different scanning strategies for fusing H10 tool steel and tungsten carbide. The research concluded the "refill" strategy would better suit the material densification although some large porosity was found in parts at high percentages of tungsten carbide mixed with H10 as base material. More about the *refill* laser scanning strategy is explained in Chapter 5, where it was subject of research in this work.

One characteristic of the layer addition manufacturing is anisotropy. To reduce the difference of the thermal/mechanical properties in the different directions laser scanning patterns can be adjusted. Figure 2-34 shows parallel and cross-hatched vector layers. The part build with the vectors cross-hatched will have higher isotropy.

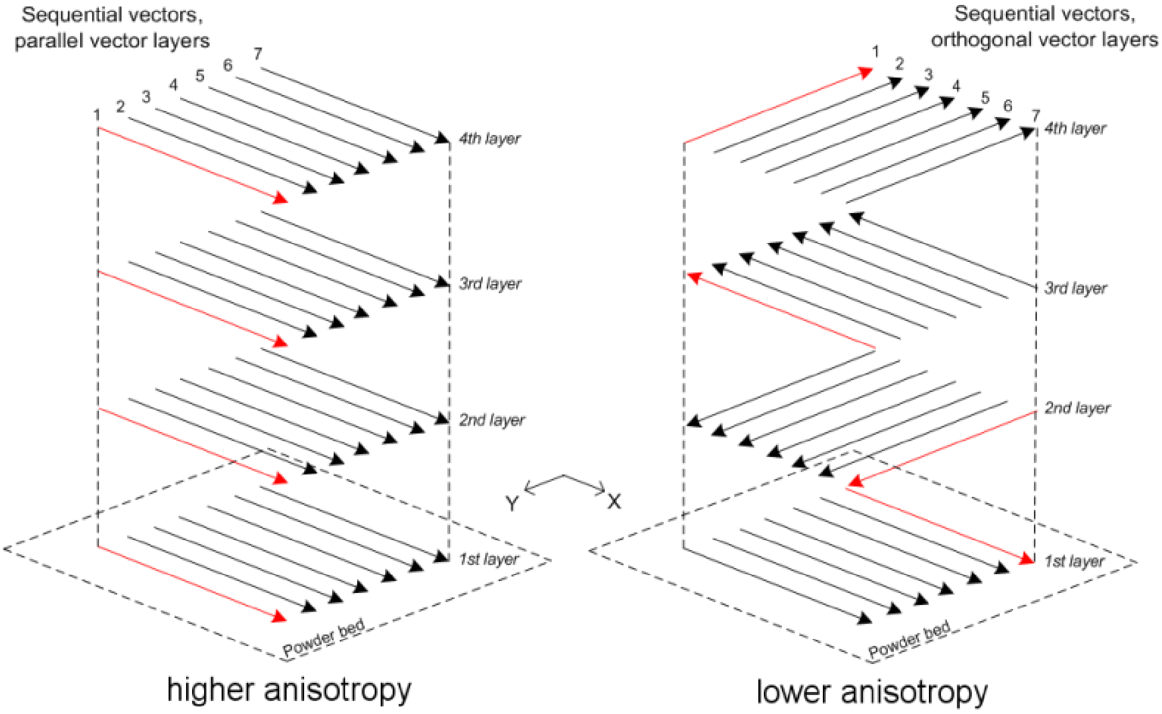
Sequential vectors, parallel vector layers
1
2
3
4
5
6
7
4th layer
3rd layer
2nd layer
1st layer
Powder bed
higher anisotropy
Y
X
Sequential vectors, orthogonal vector layers
4th layer
3rd layer
2nd layer
1st layer
Powder bed
lower anisotropy

Figure 2-34. Difference between parallel and orthogonal (cross-hatched) layers.

Other building parameter is the vector spacing. The vector spacing is the distance between the centres of two vectors. Independently from the strategy used to draw the layer, the spacing between the vectors of the strategy changes the density of energy delivered to the layer. In Figure 2-35 the influence of the vector spacing (smaller distance: SP1, larger distance: SP2) can be observed by the lateral overlap of the laser beads (pulsed laser in this case).

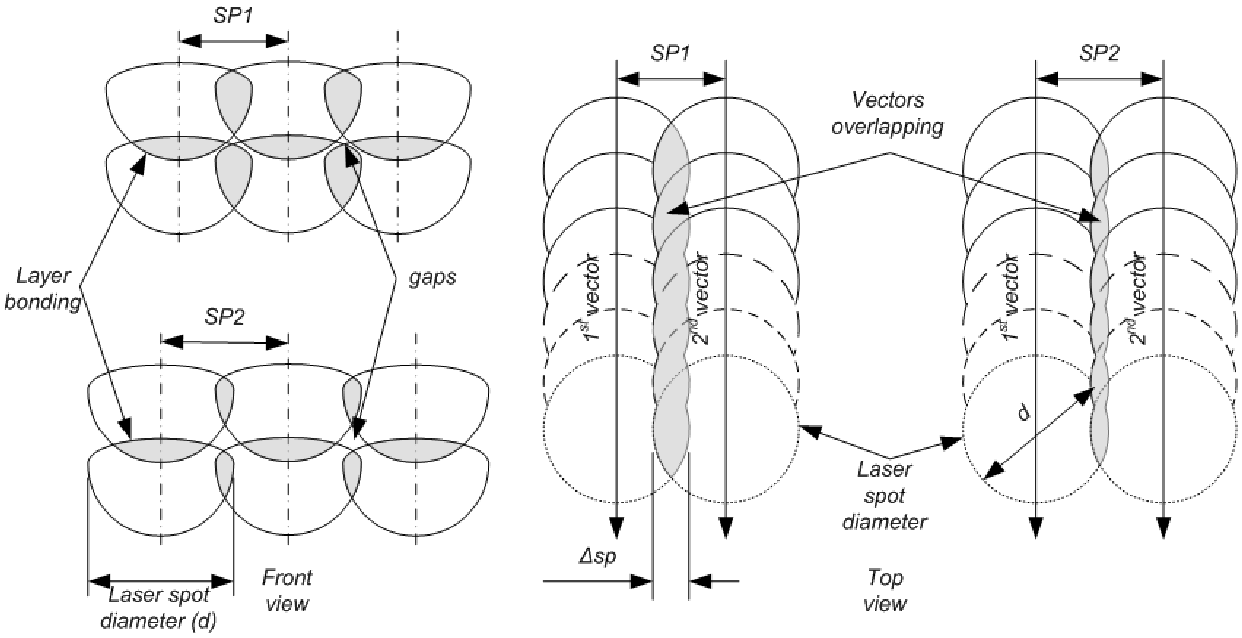
SP1
Layer bonding
gaps
SP2
Laser spot diameter (d)
Front view
SP1
SP2
Vectors overlapping
1st vector
2nd vector
1st vector
2nd vector
d
Laser spot diameter
Δsp
Top view

Figure 2-35. Direct influence of the vector spacing (SP) in the overlap of the processed material.

The percentage overlap for each spacing can be calculated by equations 2.30 and 2.31. The first calculated the Δsp which is the overlapped length of one side of the scanning vector. The second equation calculates the total percentage overlapped (T_{sp}) for both sides of a scan vector overlapped.

$$SP = d/2 + (d/2 - \Delta sp) \Rightarrow \Delta sp = d - SP\,; \qquad \text{[mm]} \qquad \text{Eq. 2.30}$$

$$T_{sp} = \left(\frac{2 * \Delta sp}{d}\right) * 100\%\,; \qquad \text{[\%]} \qquad \text{Eq. 2.31}$$

One of the major building parameter for layered manufacturing technologies is the layer thickness. The more perceptible effect of the layer thickness is the reduction of the stair step effect in the surfaces that are not parallel or perpendicular to the building direction. Internally, especially in the case of laser fusion/sintering, the layer reduction affects the layer bonding. Nevertheless, the thermal gradient by reducing the layer thickness might cause curl and other types of layer distortion. Also, it depends on the particle size, particle sizes distribution, surface roughness of the particles and powder levelling and deposition system.

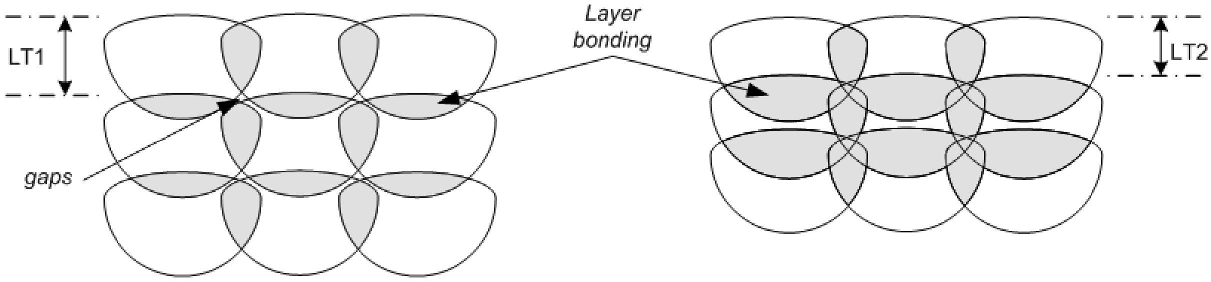

Figure 2-36. Effect of the layer thickness (LT) into the layer bonding and gaps.

2.5.3. Nd:YAG laser principles

A Nd:YAG is a 4 levels solid state laser that uses a crystal of Yttrium-Aluminium-Garnet ($Y_3Al_5O_{12}$) doped with the rare earth Neodymium (Nd). For lasing applications, the YAG crystal is doped with Nd^{3+} from 0,2 to 1,4% at atomic level (VLOC, 2005). The trivalent ions from the neodymium increase the energy state and its relaxation emits photons at 1,064μm of wavelength. To increase the energy levels of the neodymium flash lamps, tungsten arc lamps or diode laser can be used. Figure 2-37 shows the energy level system of the Nd:YAG laser.

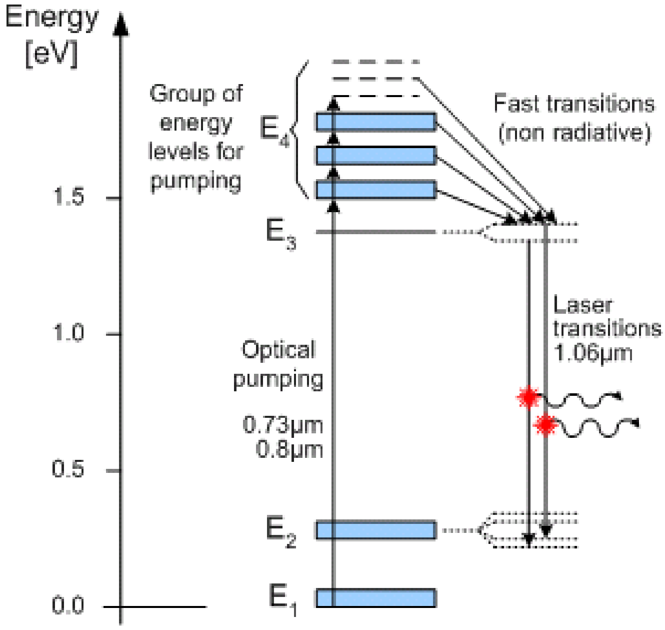
Energy
[eV]
1.5
1.0
0.5
0.0
Group of
energy
levels for
pumping
E4
E3
E2
E1
Fast transitions
(non radiative)
Laser
transitions
1.06µm
Optical
pumping
0.73µm
0.8µm

Figure 2-37. Schematic Nd:YAG energy level system (adapted from Tarrant, 2002).

The usual construction of a Nd:YAG laser system is presented in Figure 2-38. The rod crystal is bombarded with an optical source as a flash lamp inside an elliptical cavity. The energy efficiency of the laser (output power in the laser head/power consumed in the wall plug) is low as the lamp emits light in broad spectrum range that do not excite the neodymium. The wavelengths that pump the energy levels of the Nd are 0,73 and 0,8µm. All other wavelength emitted by the lamp is transformed in heat. This heat is prejudicial to the laser rod that can distort and degenerate the beam quality. So, cooling is important and can be provided by deionised, filtered and chilled water running into the cavity.

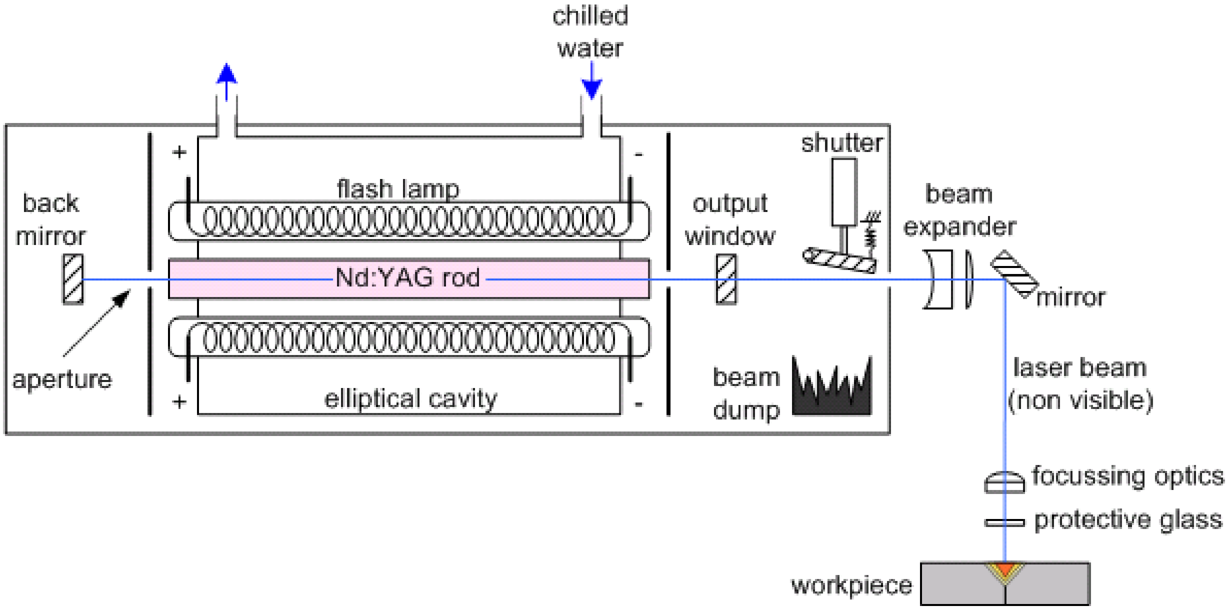
chilled
water
+
-
flash lamp
back
mirror
Nd:YAG rod
aperture
+
-
elliptical cavity
output
window
shutter
beam
dump
beam
expander
mirror
laser beam
(non visible)
focussing optics
protective glass
workpiece

Figure 2-38. General construction of a Nd:YAG laser (adapted from Steen, 1991).

Nd:YAG lasers can be operated in continuous or pulsed mode. Continuous mode power is from 0,1 to 100W (Tarrant, 2002). In pulsed mode, the output peak power can achieve hundreds of kilowatts for nanoseconds depending of the system. High frequencies (kHz range) Nd:YAG laser can be obtained using Q-switching elements into the cavity. Usually, due to the heat and distortion, the usual average output power per rod of Nd:YAG is 400W but higher power outputs have been obtained. Average powers above this value are obtained combining the output of individual rods (Steen, 1991).

Chapter 3

Problem Statement

"Eu quis cantar
Minha canção iluminada de sol
Soltei os panos sobre os mastros no ar
Soltei os tigres e leões nos quintais
Mas as pessoas da sala de jantar
São ocupadas em nascer e morrer

Mandei fazer
De puro aço luminoso punhal
Para matar o meu amor e matei
Às 5 horas na Avenida Central
Mas as pessoas da sala de jantar
São ocupadas em nascer e morrer

Mandei plantar
Folhas de sonho no jardim do solar
As folhas sabem procurar pelo sol
E as raízes, procurar, procurar
Mas as pessoas da sala de jantar
Essas pessoas da sala de jantar
São as pessoas da sala de jantar
Essas pessoas da sala de jantar
São ocupadas em nascer e morrer "

Caetano Veloso – Panis et Circenses

3. Problem Statement

In the previous chapter, a general view of the state-of-art of FGM and additive layered manufacturing was discussed. It was seen that FGMs are limited in the range of studied materials and production methods that can produce complex geometries and gradients. Nevertheless, FGM has great potential to improve the performance of many components from medical to aerospace industries. Although various materials combinations and processes have been developed they only attend to laboratorial scale with few industrial large scale cases.

Some researches have presented FGM specimens produced by layered additive manufacturing technologies. The main concerns on the development of FGM by additive manufacturing technologies are local composition control, software and material processing.

The technologies that are capable of handling different materials, those that use lasers as a heat source have been explored more intensively. Researches with laser cladding (e.g. LENS^{TM}) showed that it is possible to produce FGM from metallic alloys. The composition of the materials can be controlled by adjusting the powder composition being blown into the laser spot. It is, so far, the best achievable local composition control system. Nevertheless, this technology has some disadvantages as low accuracy and lower shape complexity (when compared to other technologies).

On the other hand, pre-placed powder beds technologies such as selective laser fusion and sintering, have higher degree of accuracy and shape complexity for single materials. Some researchers have been investigating the automated control of different powders deposition in the powder bed but it is in early stages of development. So far, no effective deposition system has been created and tested. The functionally graded parts fabricated by these processes, fusion or sintering, are limited and most of the research performed at the time, had the gradient on the z-axis direction. So only the gradient on the layer deposition direction has been investigated. Also, the majority of the studies involved gradients between a metallic alloy and materials for wear resistance or insulation. None investigated the fabrication of a gradient to produce more thermal conductive regions on a mould impression. Moreover, the investigations have not been explored on the properties of the materials obtained but were restricted to the hardness and microstructure analysis of the gradients.

3.1. Hypothesis

Moulds and dies usually are the most expensive item in the manufacturing process if not in all cost of an entire project. The performance of these tools depends on many factors based on the material, design and manufacturing of the part to be processed by this product or the tool itself. As a result, on many cases, it is imperative for these components to achieve high performance. This performance can be measured by a degree of complexity of the mould impression, the production rate and the lifetime expectancy.

The H13 tool steel is considered high temperature resistant steel with dimensional stability, low wear and high toughness. Its mechanical properties make it suitable for building injection moulds and dies (Norton, 1996, Smith 1993). Nevertheless, the thermal performance of the H13 could be considered poor as it has low capability for conducting heat energy. The thermal conductivity coefficient of the H13 is 24.3W/mK (MatWeb, 2005-1). Alternatives to improve the thermal conductivity of the injection mould are the use of heat/cooling channels and copper-beryllium (Cu-Be) inserts. Heat/cooling channels are geometry dependable, restricted by the manufacturing process and have small effect on complex thin wallet and small features. Copper-beryllium inserts are expensive, non-ecological and present an abrupt properties change in the mould surface from the insert to the base mould material. On the other hand, they present a high thermal conductivity coefficient (100-130W/mK; Matweb, 2005-3). The objective of this research work was to investigate the fabrication of functionally graded materials to be used for building high thermal performance tools for injection moulding in order to reduce ecological impact, to increase the free form building and to improve the thermal design of tools. This research was focussed on the development of functional graded parts of tool steel (AISI H13 or BS EN ISO 4957:2000 XV40CrMoV5-1) and copper. The use of copper added to the H13 could increase the thermal conductivity of the new alloy formed. A controlled distribution of copper in the H13 base material would optimize the heat extraction from plastic parts during the cooling period of the injection moulding cycle. This kind of optimization could reduce differential shrinkage and defects such as warpage, sink marks and cold welding.

To build free form geometries considering the local composition control of the copper added to the H13, selective laser fusion process was chosen to be used for the manufacturing of the functionally graded parts. As previously seen in Chapter 2, the selective laser fusion process offers the possibility for manufacturing full dense parts based on the layered manufacturing techniques. It could be used to achieve the requirements for the production of new materials formed by the mixture of Cu and H13. In this process, the use of a Nd:YAG laser could be preferable as it is recommended to process metals due to its short light wavelength (Steen, 1991).

3.2. Objective

As mentioned in Chapter 1, the objective of this research was to produce functionally graded materials from H13 and Cu powders using a high power pulsed Nd:YAG laser, fusing layer by layer powders spread over a platform to build a 3D geometry based on the principles of the layered manufacturing, focused on the injection moulding application.

The research targets to achieve the main objective were:

- To investigate the laser fusion process of H13 and mixtures of H13/Cu powders;
- To optimise laser processing parameters for high density (near full) produced parts;
- To characterise the new materials formed and the FGM structures;
- To evaluate the performance of mould graded inserts produced by this process.

Chapter 4

Materials & Methods

> *"Cause it's a bittersweet symphony, this life*
> *Try to make ends meet*
> *You're a slave to money then you die*
> *I'll take you down the only road I've ever been down*
> *You know the one that takes you to the places*
> *where all the veins meet yeah"*
>
> The Verve – Bittersweet Symphony

4. Materials and Methods

The objective of this chapter is to present the techniques, methods and materials that were used in the experiments. Many procedures and described in the following sections were repeatedly used in the experiments that are described in Chapters 5, 6, 7 and 8. To avoid repetition of descriptions, this chapter presents techniques, materials and analysis commonly used during this research work.

4.1. Methods of manufacturing

4.1.1. Fixed frames

In order to build specimens, two methods for layering the powder were used. The first applied method was the same used by Su (2002). In this method, fixed frames were used for determining the layer thickness and a blade was used to spread the powder over the frame pocket. The frames were hold together by a bolster and layers were added over a substrate. The sequence of building a specimen is shown in Figure 4-1. After each layer fused, the laser head was elevated the same length of the layer thickness of the used frame in order to adjust the position of the laser beam focus.

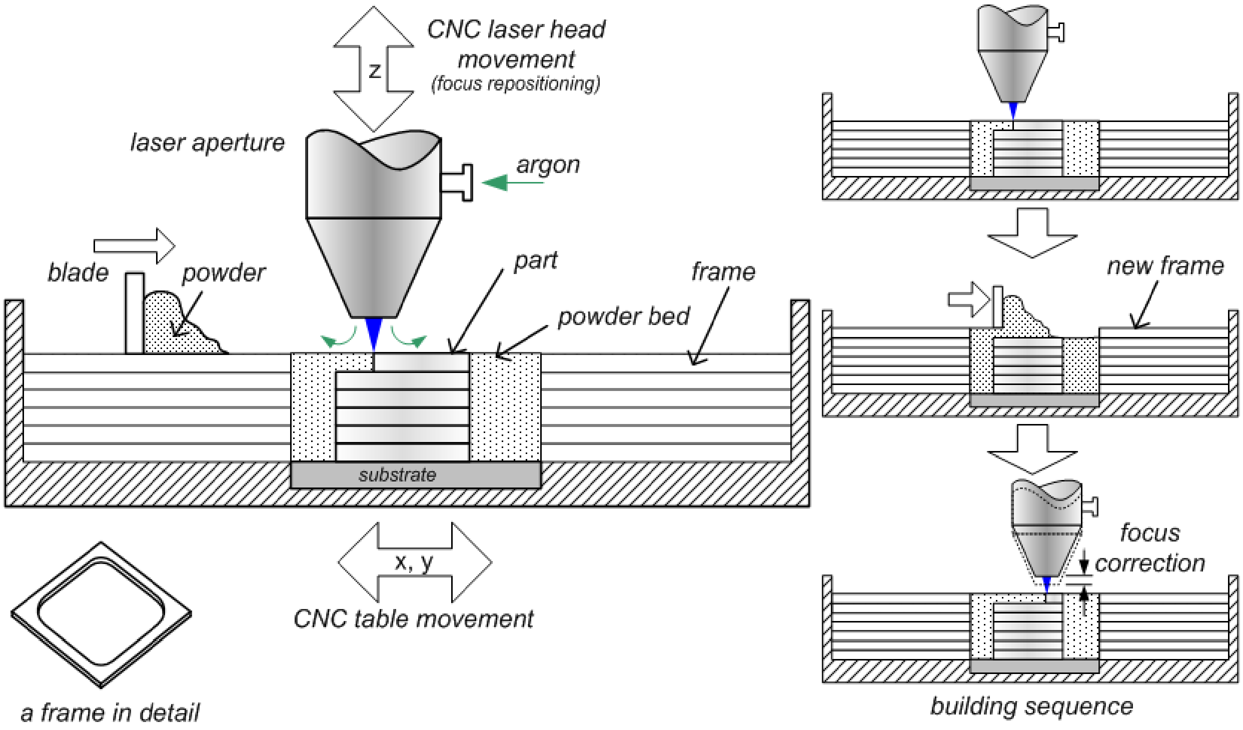
CNC laser head movement (focus repositioning)
z
laser aperture
argon
blade
powder
part
frame
powder bed
substrate
x, y
CNC table movement
a frame in detail
new frame
focus correction
building sequence

Figure 4-1. Stacking fixed frames method for layering powder.

This building method was flexible and useful for preliminary tests. Nevertheless, the minimum layer thickness was limited by the thickness of the metal sheets used to make the frames. It was also necessary to avoid frame distortions (bended frames) and to keep clean the frames from powder to maintain layer thickness constant. Another disadvantage of this method is the fact that the contraction of the layer is not compensated by the fixed frame thickness. Consequently, at the latest layers built might be thicker than the first ones. Additionally, this could help to produce voids of non fused powder. In Figure 4-2 a schematic view of the laser fusion using fixed frames can be seen. It shows why voids might occur due to non compensation of the layer contraction.

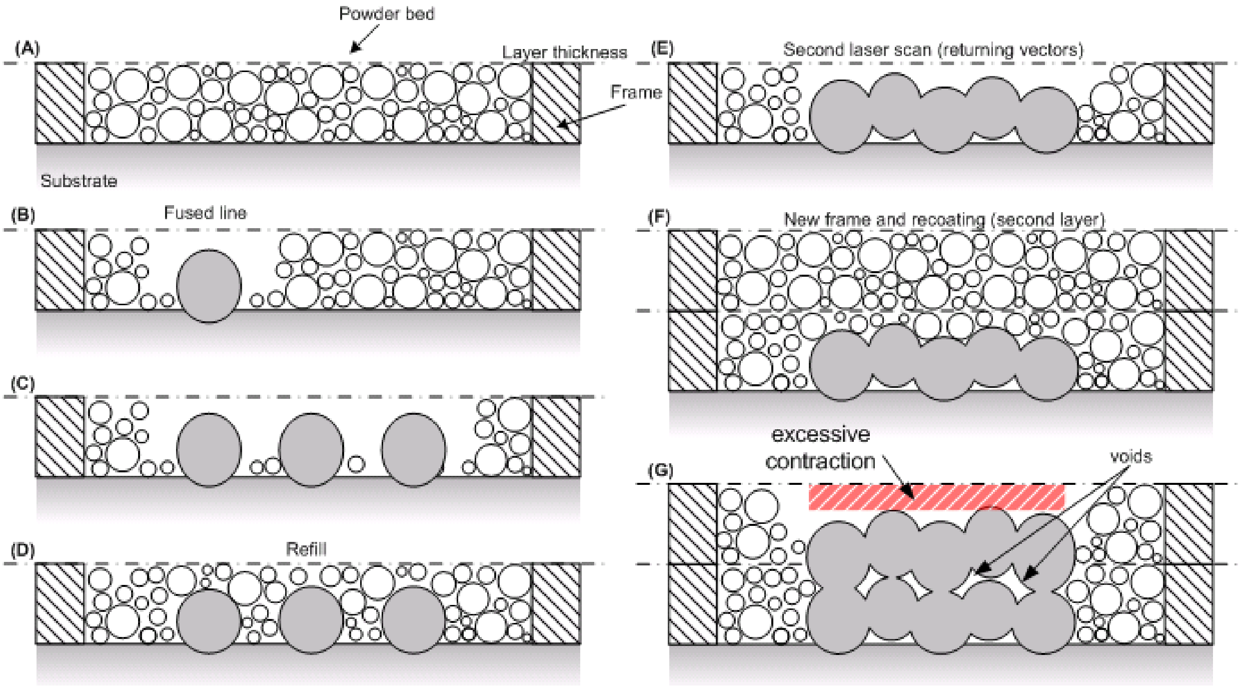

Figure 4-2: Sequence of the laser fusion using fixed frames where layer contraction is not compensated.

4.1.2. Platform and Hopper

In order to layer powder and control the layer thickness and to compensate the layer contraction, a better layering method was required. Moreover, larger parts needed to be produced for further investigations such as for the tensile test and thermal conductivity specimens, it would be appropriate to establish a better powder layering method which could deposit graded powders.

For the layer thickness control, a platform was assembled over a lab jack with a dial indicator for levelling the platform at the desirable height (layer thickness). Substrates also were used to start building parts. In this system, a hopper slides over a base were the platform descends. The user stipulated the height and adjusted the lab jack using the dial indicator as reference. Once adjusted the layers thickness, the hopper was slid over the platform adding a new layer of powder. The laser then scans a profile to fuse the new layer. The process of height adjustment and hopper sliding was done manually and between each built layer the user needed to open the machine chamber door, adjust the height, slide the powder, close the door and activate the laser fusion process again. A schematic drawing of the system is shown in Figure 4-3. Two platform sizes were built, one for using substrates of 45x45mm and other for substrates of 45x75mm. The system as it was assembled in the machine can be seen in Figure 4-4 with the 45x75mm platform. The system, except for the hopper, was made of aluminium. The lab jack was a commercially available and made from aluminium and steel. The connection bar between the lab jack and the platform was made of mild steel.

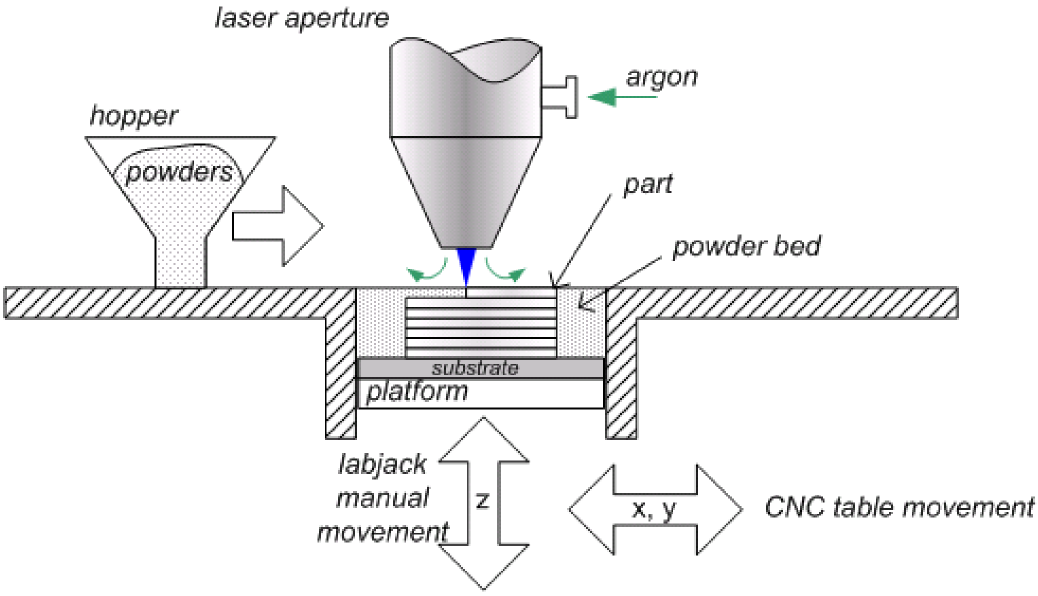
laser aperture
argon
hopper
powders
part
powder bed
substrate
platform
labjack
manual
movement
z
x, y
CNC table movement

Figure 4-3. Schematic drawing of the levelling and hopper system.

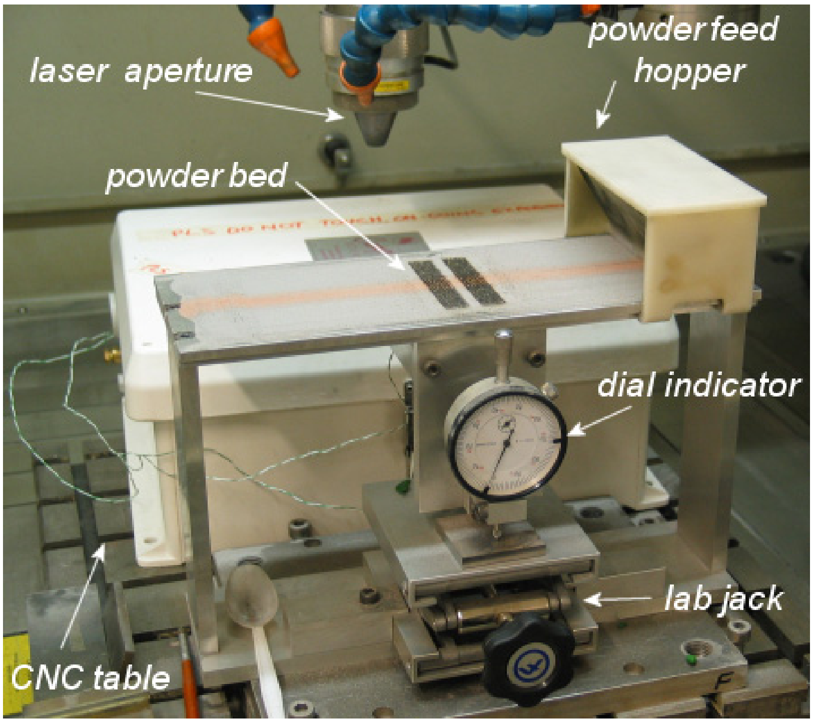
laser aperture
powder feed
hopper
powder bed
dial indicator
lab jack
CNC table

Figure 4-4. Platform and hopper system assembled in the machine.

4.1.2.(a). Feedhoper and gradient step design

As the objective of this work was to develop FGM it was necessary to have a system with capabilities to build parts with gradients. As seen previously in the bibliography revision, there was no method available yet for spreading the powder over a powder bed. Currently, the most successful method in development is as used in laser cladding where the powders are blown coaxially with the laser beam (Ensz *et al*, 2002). The amount of powder required in this method is high, as the powders must be fed continuously and hopefully fused in the laser melted pool. The non-fused powder were scrapped and could not be re-used as contaminated with spatters and also oxidised to some extent. The other method is using layers of different compositions, building a gradient in the z direction (direction of layer addition) (Jepson *et al*, 2003; Suresh and Mortensen, 1998; Miyamoto *et al*, 1999). This technique has two problems: feeding the deposition system with the different powder compositions when necessary and the size of the parts that can be obtained. Building FGM tensile specimens would take long time as the taller the part the longer it takes to build and also high amount of wastage of non-fused (or non-sintered) powder. To overcome these problems, a system based on multi-compartment hopper was designed.

The kind of gradient produced in this work was the discrete gradient (section 2.2.1). Each step of powder compositions made from H13 and Cu were made with 12,5% of Cu addition until 50%. Therefore, five powder compositions, including only H13 powder, were used. More about the powders characteristics and preparation is discussed in section 4.3. The step of the gradient was determined by the fact that usually a Cu-Be alloy for mould applications, which contains 50% of each element, has little more than one fourth of pure Cu thermal conductivity. It would be expected that to increase the thermal conduction of H13 a large amount of Cu should be used.

The use of intermediary steps were not practical at that point of the research work. Powder material handling would be difficult as the steps dimension of each material composition of the gradient needed to be reduced. It would become more challenging to analyse the results with the required accuracy.

The basic concept of the hoppers used in this work, was a sequence of small hoppers, assembled side by side that when slid over the platform formed an x direction gradient. In this work, the gradient formed in the layer along one direction of the layer plane (xy) was called x-gradient. It was a unidirectional gradient with stepwise distribution. With the deposition system used in this building method, less powder was wasted and processing time was shorter. In total, 3 different designs were made to test in the platforms, two for the 45x45mm and one for the 45x75mm. Due to the complexity and one-of-kind part, all hoppers were made by stereolithography. The basic difference between each one of them was the aperture of the individual compartment hoppers. In Figure 4-5, Figure 4-6 and Figure 4-7, the CAD models of the feed hoppers are presented. The sequence was an evolution from the first design used in the initial experiments to the latest design. For each investigation in the following chapters, it is cited which feed hopper was used. The fist was made using the DSM SOMOS 7120 resin, from DSM, and the other two with Huntsman RenShape 7580 resin.

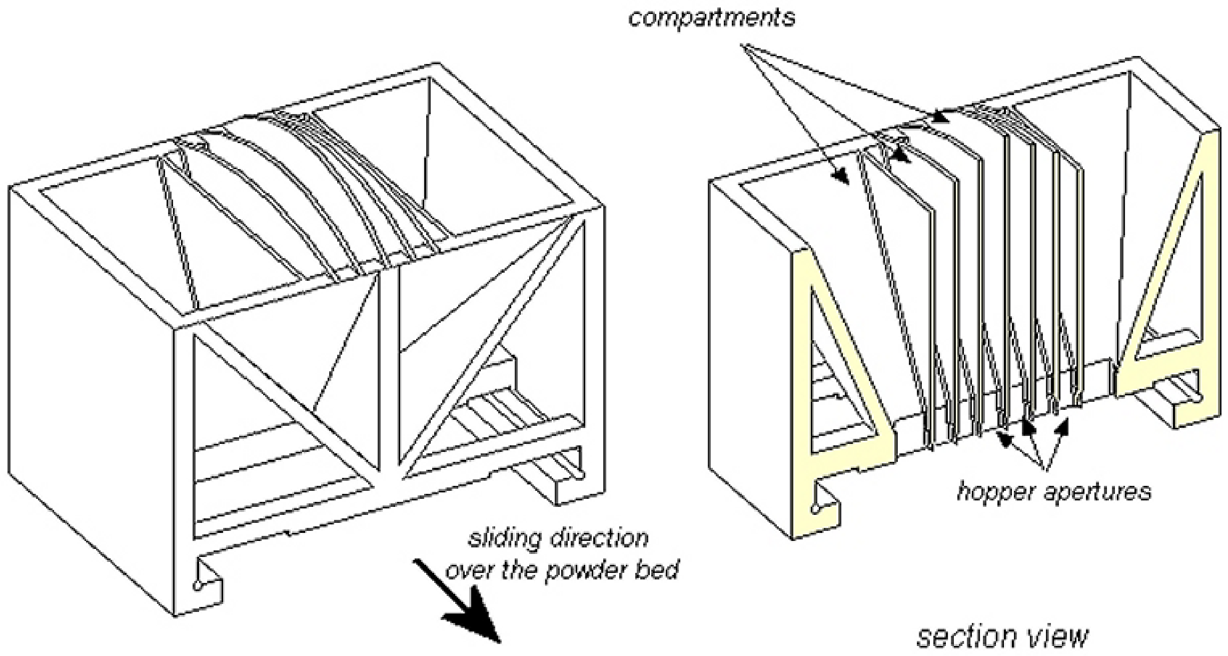
compartments
sliding direction
over the powder bed
hopper apertures
section view

Figure 4-5. CAD model of the first hopper build for the experiments (platform 45x45mm)

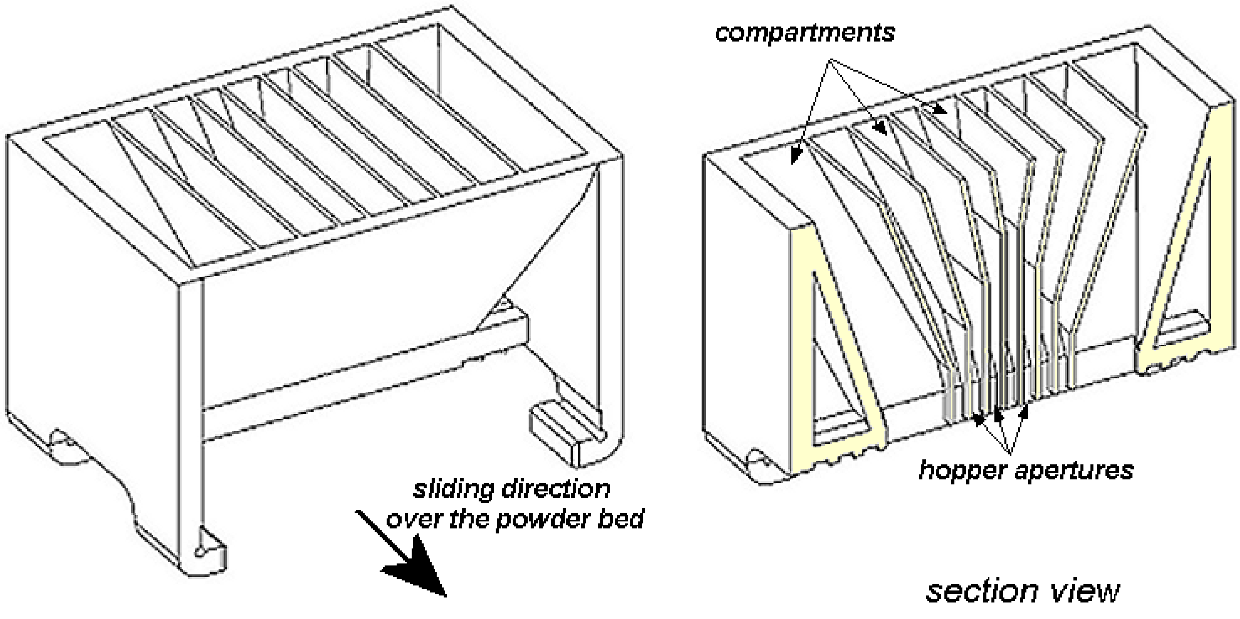
compartments
sliding direction
over the powder bed
hopper apertures
section view

Figure 4-6. CAD model of the second hopper used (platform 45x45mm).

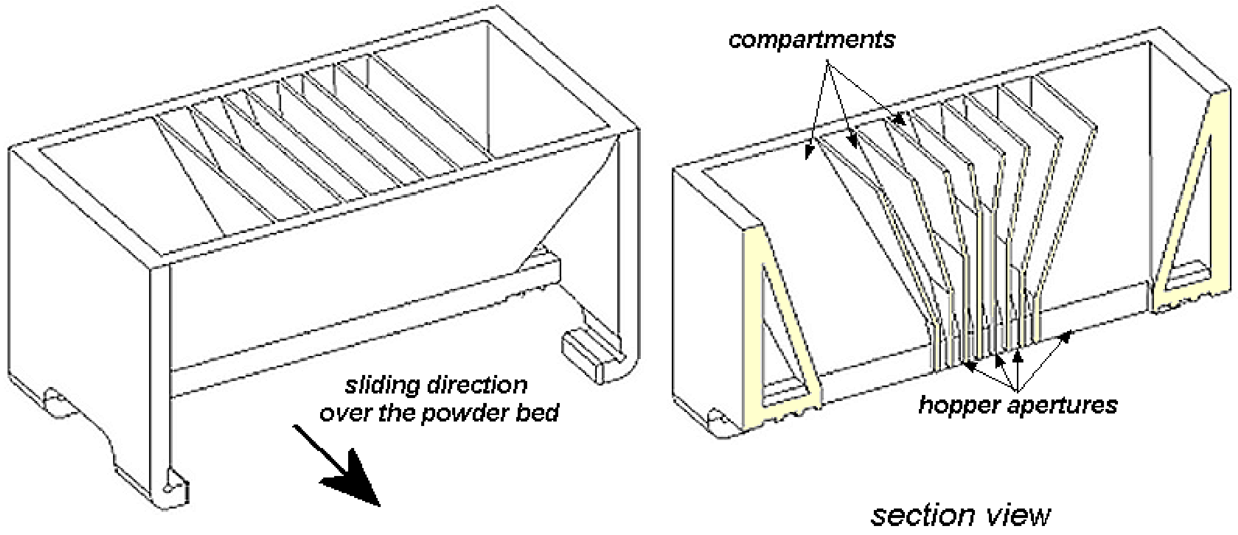
compartments
sliding direction
over the powder bed
hopper apertures
section view

Figure 4-7. CAD model of the hopper used to build tensile test specimens (platform 45x75mm).

The most critical dimensions of the hoppers are presented in Figure 4-8. The area aperture of each compartment was defined by ExB. In Table 4-1 these dimensions are summarized for each one of the hoppers.

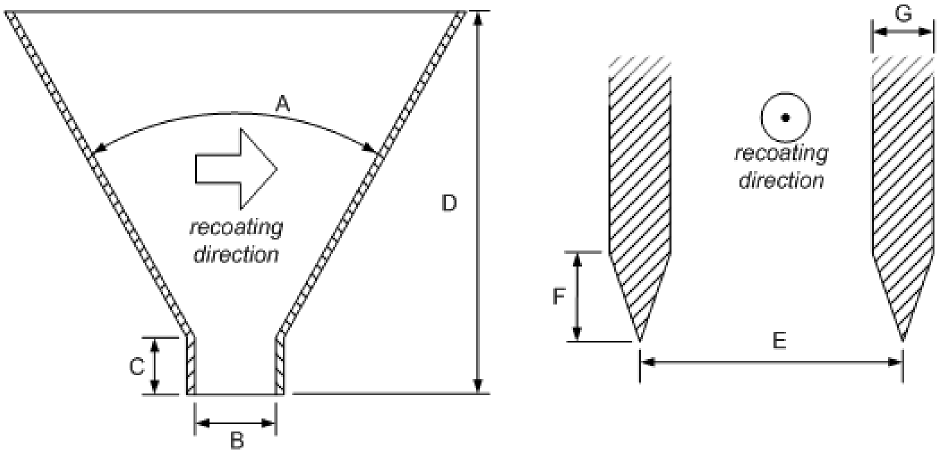
A
recoating direction
D
C
B
G
recoating direction
F
E

Figure 4-8. Details of the hoppers and apertures.

Table 4-1. Main dimensions of the hoppers.

Hopper	A	B	C	D	E	F	G
1st 45x45mm	60°	3,0mm	7,7mm	49,0mm	7,0mm	4,0mm	1,0mm
2nd 45x45mm	60°	3,0mm	7,2mm	49,0mm	3,5mm	1,0mm	1,0mm
3rd 45x75mm	60°	3,0mm	7,2mm	49,0mm	3,5mm	1,0mm	1,0mm

As the focus of this work was not on the design of the hopper, many improvements can be performed in future work. So, it is necessary to present some of the characteristics of the hoppers performance during the experiments that are described in the next chapter.

It was found that the larger the aperture and the powder particle size the flow of the powder was better. Bimodal distributions of the particle size do not help the flow. Some conclusion were that when using small particle sizes or good particle ratio for increasing the apparent density (7:1 proportions according to German, 1994) it was necessary to use larger apertures in the hoppers and with maximum aperture area possible. Nevertheless, this would have mean that the powder tracks with different powder blends would have generated larger gradients with larger steps between each material composition to be formed in the part. Concluding, FGM design and functionality would be restrained. This would defeat the purpose of graded structure as larger gradients would possibly perform as discrete graded structure.

The aim for the use of RM and FGMs integrated technologies is to obtain free form parts with local composition control. Using an x-graded powder feed hoppers the local composition was limited to the x building direction. It is important to say that researcheres have been trying to develop hopper-powder delivery system, especially for fully functional local composition control as described in Kumar *et al* (2004) and Yang and Evans (2004). An example of an x-graded layer produced in this work can be seen in Figure 4-9.

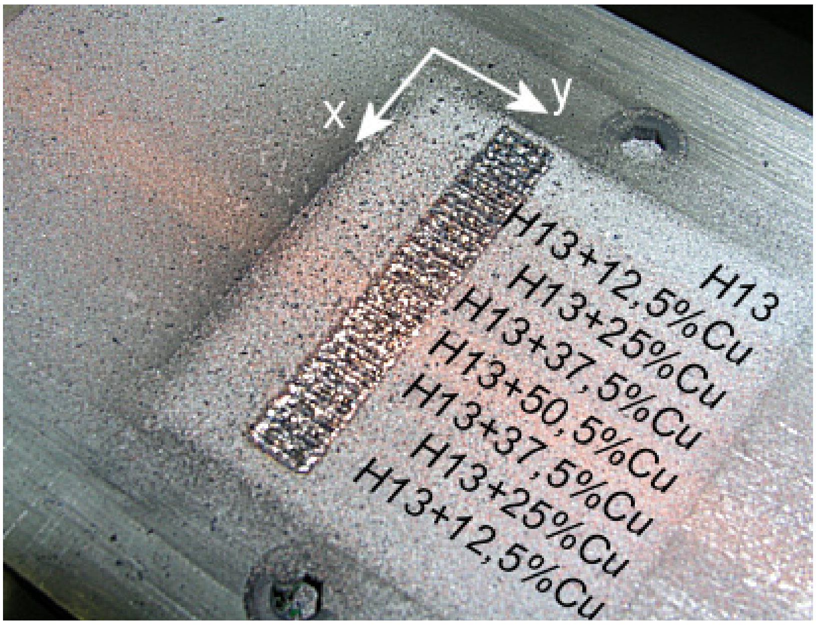

Figure 4-9. Example of an x-graded layer (hopper shown in Figure 4-5).

4.1.3. JK701 laser and Laserdyne working principles and characteristics

This section explains the characteristics and capabilities of the laser system used to perform this research work. The system was configured by two systems, one with the laser head, laser power source and cooling units (GSI Lumonics JK701H) and the other was the numerically controlled axes (Laserdyne 350). Both systems were controlled together by a unique computer which joined the laser controls with the programmable movement of the axes. Figure 4-10 shows a schematic drawing of this system.

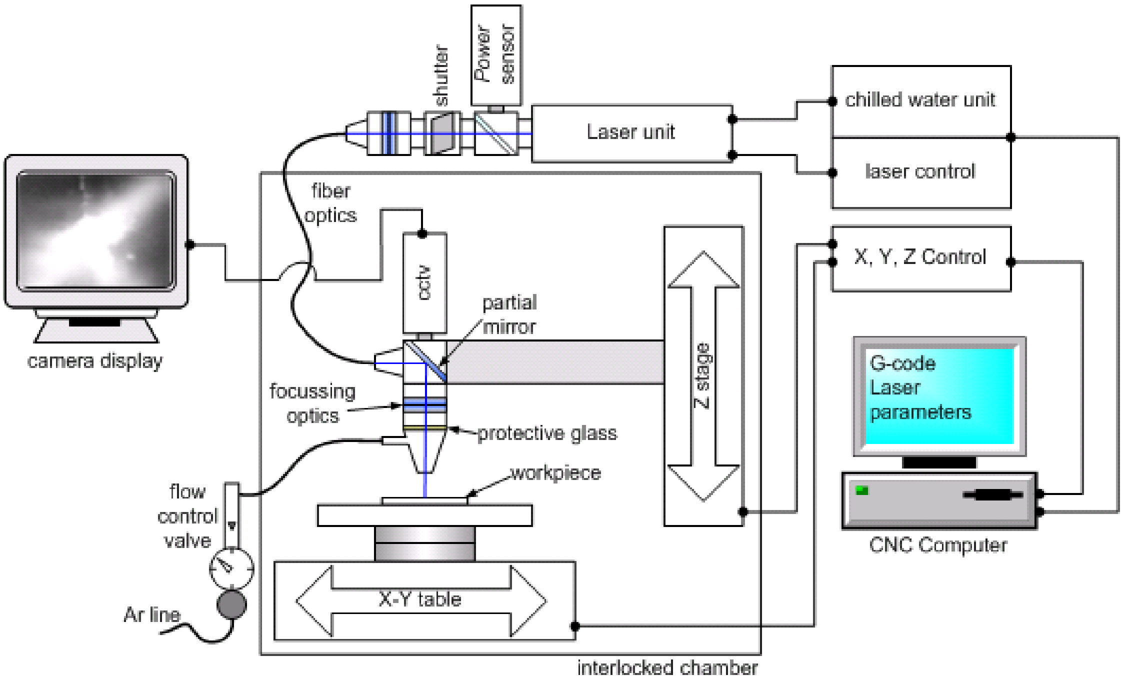
Power sensor
shutter
Laser unit
chilled water unit
laser control
fiber optics
X, Y, Z Control
cctv
partial mirror
G-code
Laser
parameters
camera display
focussing optics
protective glass
Z stage
workpiece
CNC Computer
flow control valve
X-Y table
Ar line
interlocked chamber

Figure 4-10. Laserdyne and JK701H laser system configuration.

The laser head unit configuration was almost the same presented previously in Figure 2-38. The laser medium was pumped by two krypton flash lamps disposed side by side of the laser rod. Table 4-2 presents the output specifications range of the laser system.

Table 4-2. Output specifications of the JK701 (GSI Lumonics, 2000).

Parameter	**Range**
Mean Power	0-550W
Pulse Energy	0,1-55J
Pulse Width	0,5-20ms
Repetition Rate	0,2-500Hz
Wavelength	1064nm

The characteristics of this system permitted the modulation of the electric current applied to the flash lamps to control the output of the laser. The power of the pulse was proportional to the current applied to lamps. Figure 4-11 shows theoretically how the input power in the lamp affects the instantaneous power (peak power) in the laser pulse.

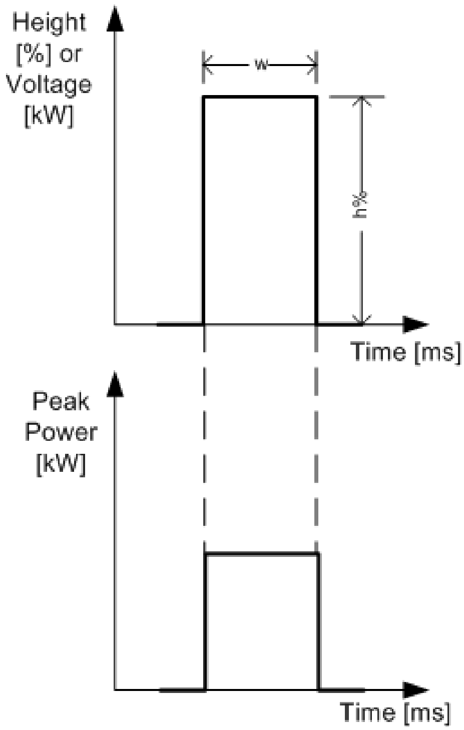

Figure 4-11. Modulation shape of a simple pulse.

To control the laser unit output the user had to set the pulse duration (pulse width), repetition rate and the electric current applied to the lamps. As the lamps have limited life, the current control was made by percentage height. The user setup could adjust the height as it is proportional to the pulse energy. There were an inferior limit where the Nd:YAG rod did not emitted radiation and a superior limit were too high current could cause the distortion in the rod, optics damage or burnout the lamp filament. As the lamps lost their brightness capabilities with the time use, to obtain the same output power the user needed to correct the energy current height. The laser head unit had a power sensor which measured the pulse energy obtained for each current height.

The pulse energy (E) could be calculated proportionally to the pulse width (w, in seconds) and the voltage applied to the lamps (V, in volts). In equation 4.01, this is expressed and a variable B is also included. This variable is necessary as the energy absorbed by the laser rod and used to lasing can not be considered equal to the energy applied to the lamps. Only 30% of the applied current became light when applied to the lamp filament (GSI Lumonics, 2000). From these 30% of energy, only a small part of the light spectrum is capable of exciting the laser rod. The rest of the energy is converted into heat.

$E = B * V * w$ [J, joules] Eq. 4.01

The average power output is equal to the laser energy delivered in one second, so it depends on the repetition rate of the pulses. Equation 4.02, where frequency (f) is in hertz, shows this direct relation. So, an energy pulse of 10J at 10Hz of repetition rate could produce an output average power of 100W.

$P = E * f$ [W, watts] Eq. 4.02

The pulse energy also could be described as a quadratic relation between the current height (h) and the pulse width. Equation 4.03 shows how this can be described. A system constant (c) is used to compensate the energy lost from the energy applied to the lamps to the laser beam output. Su (2002) demonstrated that this system constant was not a real constant and it varied with the other laser parameters. For practical endings, this means that it was not possible to do a direct relation between the pulse width and the pulse energy. Only after adjusting all the parameters for the laser it was possible to read the output pulse energy and average power.

$$P = E * f = c * (h^2 * w) * f \qquad \text{[W]} \qquad \text{Eq. 4.03}$$

So, for changing the laser parameters, it was necessary to adjust the pulse width, the repetition rate and the current height. Based in the output pulse energy that the laser system measured the average and peak power were calculated. The peak power was calculated using Equation 4.04, where, P_{peak} is the peak power.

$$P_{peak} = \frac{E}{w}; \qquad \text{[kW]} \qquad \text{Eq. 4.04}$$

As this laser was a pulsed laser it was necessary to establish a relation between the repetition rate, scan speed and spot diameter. This relation was called pulse overlap, Δ_p, is a percentage value of the overlapping pulses. The higher the percentage the higher the energy delivered to the same region. For welding applications, an overlap of 70% is recommended for making hermetic welds (Dawes, 1992), however, Su (2002) identified and used an overlap percentage of 53.7% for fusing H10 tool steel. Equation 4.05 defines the pulse overlap where L is the length of the scanned vector, v is the scanning speed and d is the laser beam diameter over the material.

$$\Delta p = \left(1 - \frac{L * v}{(L * f - v) * d}\right) * 100\%; \qquad \text{[\%]} \qquad \text{Eq. 4.05}$$

Additionally, the laser system permitted the pulse shaping. Pulse shaping is the segmentation of the pulse width until 10 sectors. For each sector, different time (width) and current height could be adjusted. Figure 4-12 shows an example of pulse shaping where the pulse is segmented in four different sectors with specific width and height. The output pulse power obtained from this modulation is presented accordingly.

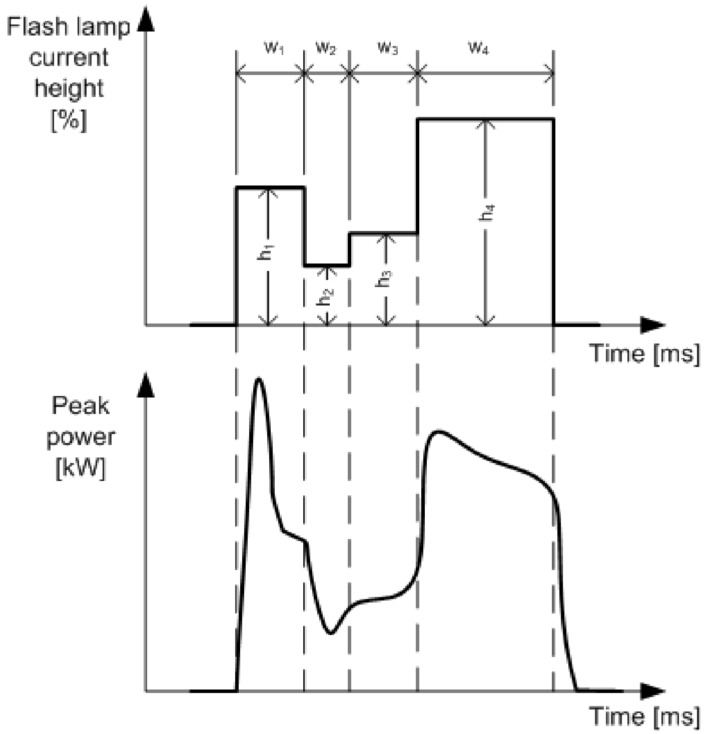
Flash lamp current height [%]
w1
w2
w3
w4
h1
h2
h3
h4
Time [ms]
Peak power [kW]
Time [ms]

Figure 4-12. Example of pulse shape segmented in many sectors (modulation above, output below).

This resource of shaping the pulse can be very useful in many industrial applications. In Figure 4-13, the example shows how the use of a short initial pre-pulse could cut the initial peak power of the pulse. This peak was formed by the characteristic from lamp filament that emitted more brightness at the beginning of the current passage. The pulse shaping is used in many processes such as welding to increase the absorbance of reflective materials with a pre-pulse or to stress relieve with a post-pulse for annealing high carbon steels (GSI Lumonics, 2000).

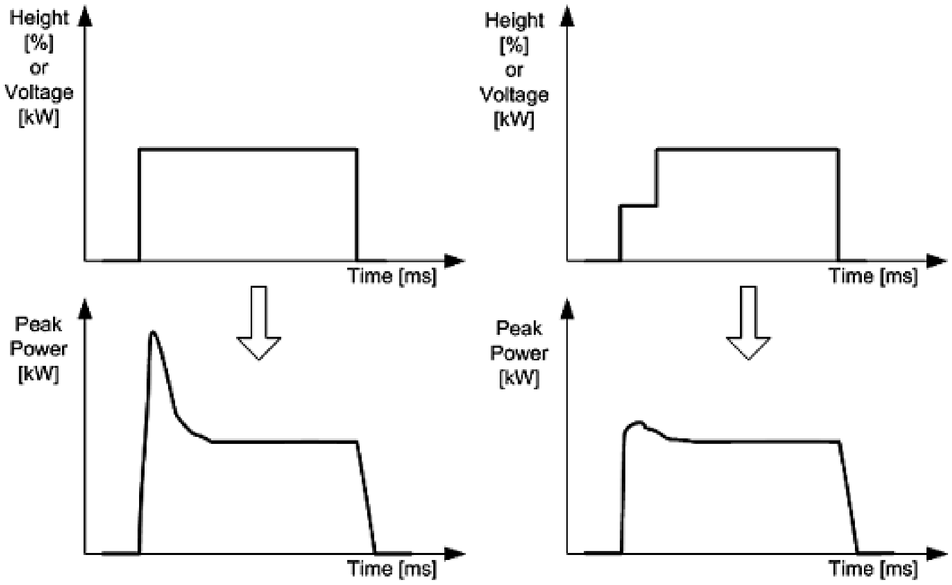
Height [%] or Voltage [kW]
Time [ms]
Peak Power [kW]
Time [ms]
Height [%] or Voltage [kW]
Time [ms]
Peak Power [kW]
Time [ms]

Figure 4-13. A simple example of using pulse sectors to format the peak energy of a pulse shape.

The output pulse energy was measured inside the laser head. From the laser head until the workpiece, the laser beam had to pass by an optical fibre (see Figure 4-10), focussing lenses and a lens protection glass. In all this way loses in the beam power occurred. The optical fibre blocked from 10 to 12% of the power. In the optical elements a lost of 0.5% per element was usual (GSI Lumonics, 1987). The protective glass could block 10% of the laser power or more depending on the debris accumulated on it due to the spatter and fumes that could occur during the materials processing. So, it is reasonable to admit that power losses could be around 23% from the power measured by the system. Nevertheless, for practical reasons, all the power values used in this work were the values displayed by the system.

An argon line was used in the system for two purposes: lens protection and welding assistance. The argon was injected in front of the protection glass and directed to the workpiece by a nozzle. This prevented debris and fumes from sticking into the glass. Moreover, the argon is an inert gas and helped to protect the workpiece from oxidation and to reduce plasma formation. Plasma can be prejudicial to the process as it can reduce the amount of energy delivered to the workpiece (Steen, 1991; Dawes, 1992).

The Laserdyne was a CNC (computer numerical control) machine that could execute programs in G-Code language as any other CNC machine despite that the tools were the laser pulses that have to be programmed as described previously. It could control an X and Y table where the workpiece would be assembled and a Z axis that could adjust the focus position. A camera also was installed and the focal position of the laser could be easily checked and adjusted prior to the program execution (Figure 4-10).

4.1.4. Environment and substrates

In the methods of manufacturing explained previously in section 4.1, an argon mixture was used to protect the material from oxidation. Unfortunately, using the Laserdyne chamber and the manual methods for layering and spreading the powder it was not possible to keep the process without oxygen and moisture completely. The mixture of argon used to protect the part during the laser fusion was the BOC Pureshield (98%Ar, 2%O_2). This was provided by the laser aperture (Figure 4-14) and also helped to protect the lens. The argon flow helped to protect the glass from debris of the spatter, fumes and to cool down the temperature of the glass. A flow and pressure valve helped to maintain the flow at 15l/min during the experiments. This flow rate was found appropriate without blowing the layered powder.

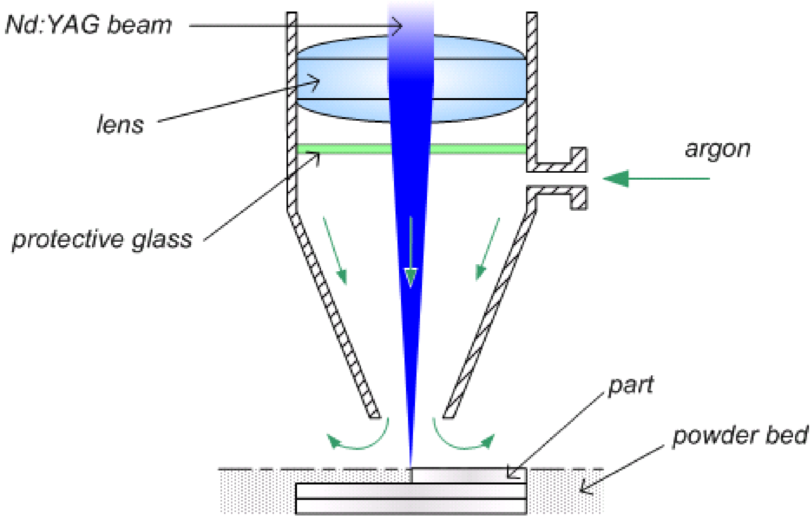

Figure 4-14. Argon flow and protective lenses in the laser aperture.

Even though references show that the laser fusion/cladding (Brooks *et al*, 1999; Lü *et al*, 2001), laser sintering (Bourell *et al*, 1992; Dalgarno & Stewart, 2001) and laser welding (Steen, 1991; Dawes, 1992) must be performed at controlled temperature environment, in this work it was not possible to heat the powder, substrate or the environment. So, all experiments were performed at room temperature, between 19 to 23°C.

In order to build the specimens, it was necessary to use substrates to fuse the first layer of powder and to attach to the substrates. Without the substrates, during the solidification, the fused line curl and the process became not feasible. Also, with the substrates, the layer thickness control was more accurate as the part stayed anchored to the substrate. The substrates were made of mild steel, having the same dimensions of the platforms (45x45 or 45x75mm) and could be 3 or 4 mm thick, specified in each experiment description. Figure 4-15 shows the differences for fusing the powder with and without substrate. This figure presents the cross-section of scanned lines: schematic and images. The images were obtained by embedding a low viscosity acrylate-base resin over the powder bed after the laser fusion of single scan lines. The parameters used to fuse the lines were pulse energy (E) of 10J, pulse width (w) of 5ms, repetition rate (f) of 10Hz and scanning speed (v) of 3,333mm/s. The layer thickness in the scan line made with fixed frames was 500μm and the powder fused was H13.

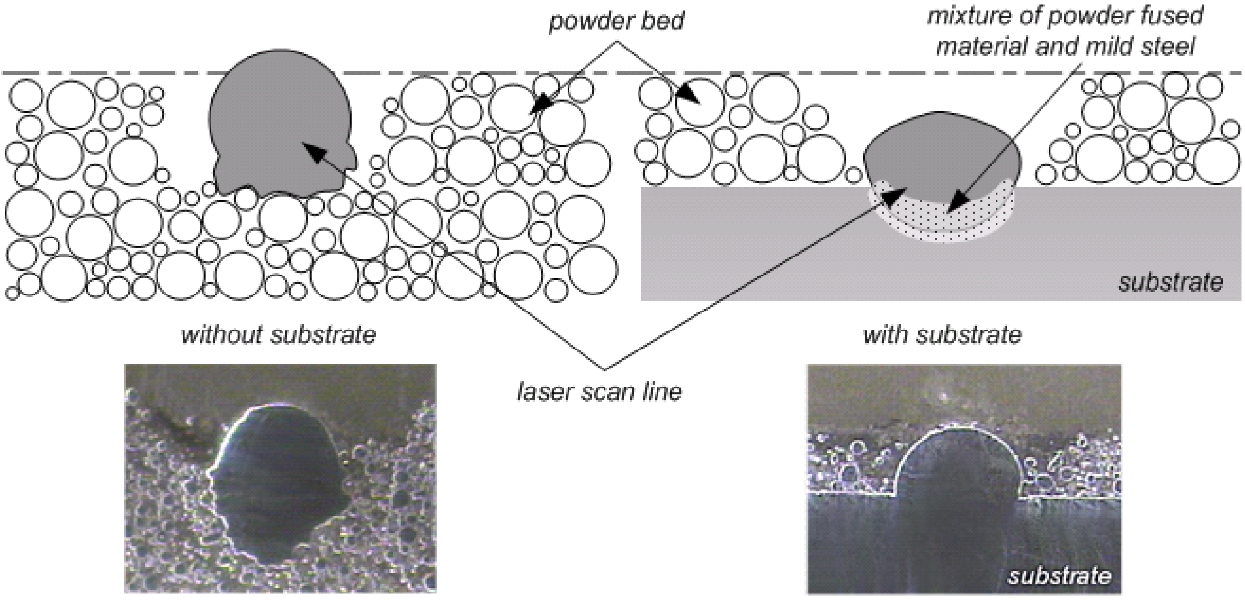

Figure 4-15. Differences of the laser fusion with and without substrate.

4.2. Statistical analysis

This work intended to be supported on statistical science. As ever as possible, at least 5 samples were taken even for analysis of any experiment, unless specified. As the research was based on the development of an experimental process, not fully automatic, with expensive materials and machinery, in some cases it was not possible to build or test some properties extensively.

Design of Experiments (DOE) was used to plan many of the experiments in this work. DOE was very useful to manipulate and to understand how the system in study reacted by changing its variables. Two experiments based on design of experiments deserved more attention. For the laser parameters optimization, response surface method (RSM) was used extensively. As seen in section 4.1.3 about the laser processing parameters, many possible parameters can affect the manufacturing of parts by selective laser fusion.

Factorial experiments were used in two ways. First, as screening experiments to determine an operating process window from the wide range of parameters available. Second, it was used as a base for the RSM experiments in multi-level factorial. The factorial experiment was a clever way to explore the dependency of the variables and how they affected the outputs. Blocks were frequently used to determine if batches of specimen's buildings/runs were affecting the results. The range of the variables in the experiments was large and reduced number of runs was crucial for time and economics aspects of this research. For that reason, the RSM design chosen to the experiments was the Box-Behnken. This design was considered appropriate for the limited number of samples that could be produced compared to other central composite designs (Montgomery, 2001).

To help in the design and analysis of the experiments, a commercial statistical package was used. The Statgraphics Plus version 5.0 has a graphical interface which helps the user to design and analyse the experiment. Its flexibility and methodology helped to broaden tests that were necessary to analyse the quality of the data obtained in the experiments.

4.3. Powders: characterization and preparation

In this section, the characterization of the used powders is presented. All feedstock powder was provided by Osprey Powder and basically it was divided in three source powders that are listed in Table 4-3. From these powders it was obtained the blends and particles sizes that were used in the experiments.

Table 4-3. Powder characteristics.

Base material	**H13**	**Cu (large)**	**Cu (fine)**
Commercial name	H13 Tool Steel Powder	Oxygen-Free Electronic Copper Powder	Oxygen-Free Electronic Copper Powder
Grade	-212µm	-212µm	80% -22µm
Composition (*)	Fe 90.8% Cr 4,75 – 5,25% C 0,32 – 0,42% Mo 1,25 – 1,75% Mn 0,4% (max) Si 0,85 – 1,15% V 0,9 – 1,1%	Cu 99,9% O 0,15% (max) Pb 0,001% (max) S 0,002% (max)	Cu 99,9% O 0,15% (max) Pb 0,001% (max) S 0,002% (max)

(*) weight percentages

All the powders were produced by gas atomization. The H13 and the fine Cu powders were spherical. However, the large Cu powder was less spherical, more shape irregular and susceptible to agglomerate. SEM (Scanning Electron Microscope) images of these base powders are shown in Figure 4-16, Figure 4-17 and Figure 4-18, corresponding to the H13, large Cu and fine Cu powder.

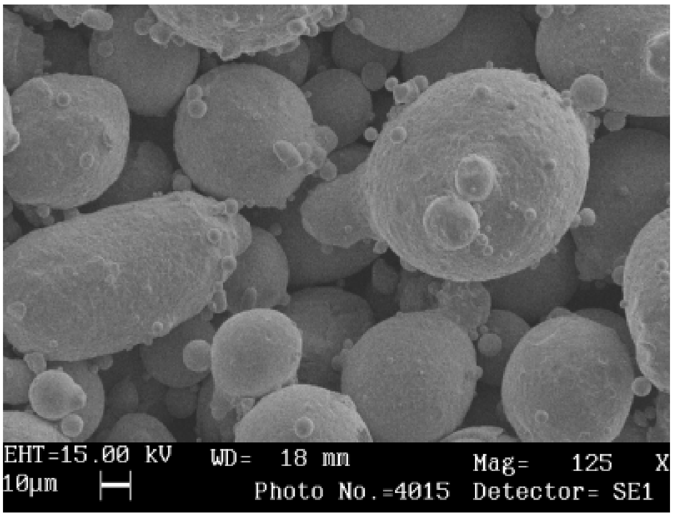

Figure 4-16. SEM images of the H13 base powder.

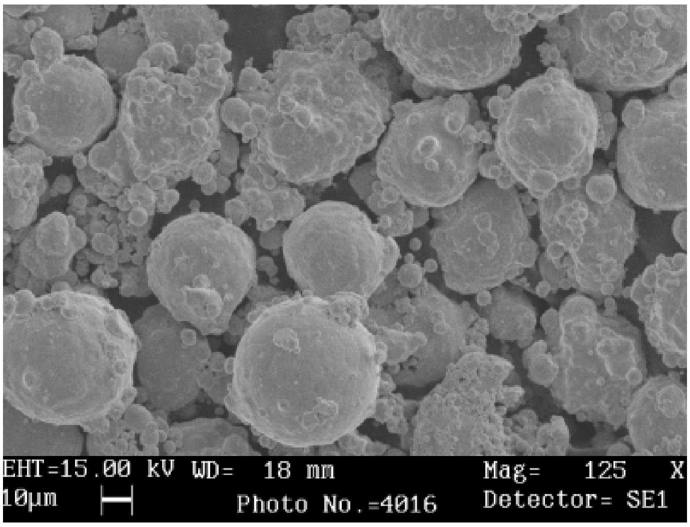
EHT=15.00 kV WD= 18 mm Mag= 125 X
10µm Photo No.=4016 Detector= SE1

Figure 4-17. SEM images of the base Cu powder.

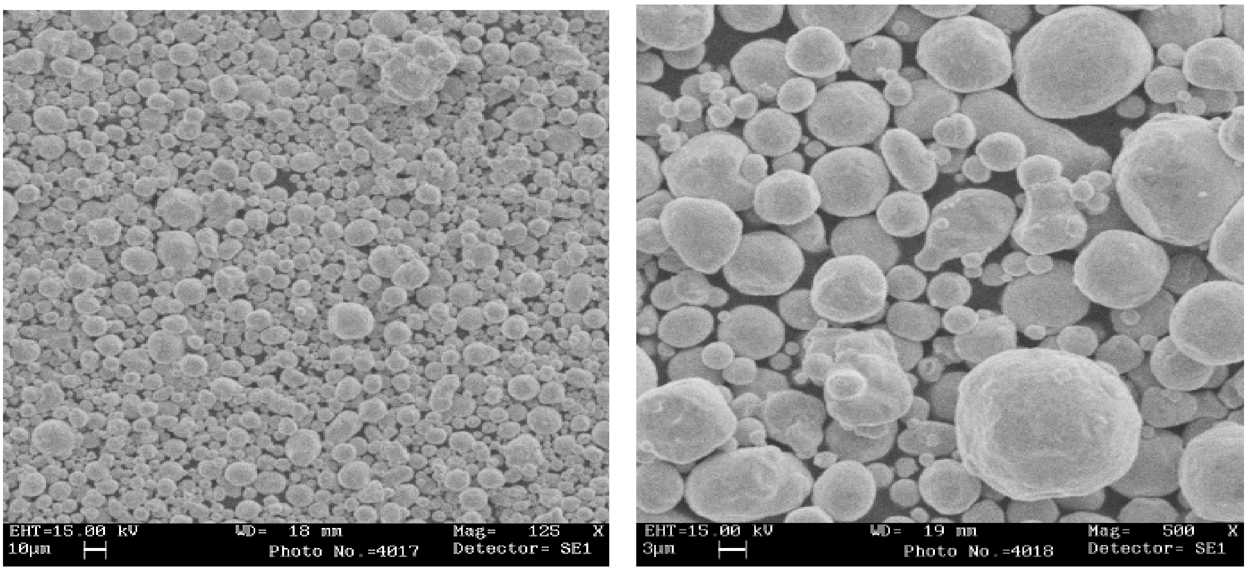
EHT=15.00 kV WD= 18 mm Mag= 125 X
10µm Photo No.=4017 Detector= SE1
EHT=15.00 kV WD= 19 mm Mag= 500 X
3µm Photo No.=4018 Detector= SE1

Figure 4-18. SEM images of the small size Cu powder.

4.3.1. Sieving

To achieve higher powder bed densities it was necessary to tailor the size of the powder to the distribution suggested by German (1994) that is 7:1 particle size ratio. From the feedstock powders previously presented, they were sieved on a ro-tap sieve shaker using ASTM standard sieves of 175, 150, 105, 50 and 36µm of aperture. The feedstock powders that were sieved for the experiments were the H13 and the large Cu to sizes of 105<∅<150µm and ∅<38µm. The small Cu powder was not sieved as the grade was 80% of the powder below 22µm.

The powders were left sieving until the sieves did not release more powder over a white surface after manual tapping. Before each test to check if the powder was sieved enough the powder remained at least 30 minutes in the shaker. The sieved powders were kept inside cans with silica gel bags to control the moisture and stored.

4.3.2. Blending and mixing

In total, five blends were prepared for the experiments. The blends were made of H13 and different proportions of Cu. The mixtures were made of the small particle sizes with large sizes of the blends. Table 4-4 shows the H13-Cu blends made from the size mixtures. As the objective of making FGM of H13 and Cu was to increase the thermal conductivity of the mould base material, the Cu was added until 50% of weight. As commented previously, for a good powder flow in the feed hopper the gradient steps must be relatively large. From these limitations, the steps between each composition were 12.5% of Cu as shown in Table 4-4.

Table 4-4. Blends prepared from different powder size mixtures.

			Blends				
			H13	H13-12,5Cu	H13-25Cu	H13-37,5Cu	H13-50Cu
		Cu percentage	-	12,5%	25%	37,5%	50%
Mixtures	H13	105<∅<150μm	73%	63,75%	54,75%	45,625%	36,5%
		∅<38	27%	23,625%	20,25%	16,875%	13,5%
	Cu	105<∅<150μm	-	9,125%	18,25%	27,375%	36,5%
		80% 22μm	-	3,375%	6,75%	10,125%	13,5%
(*) weight percentages							

The blends were all prepared using digital balance (accuracy ±0,01g) and placed in ceramic ball mills (Pascal Scientific Ltd., UK) with four different ball sizes for better mixing. Around 150 to 250g were blended each cycle. The powders were mixed for 6 hours at 90rpm and stored in airtight bottles with silica gel bags to avoid oxidation.

4.3.3. Particle size dispersion

The particle sizes of the feedstock powder (except the fine Cu powder) and the bimodal blends were analysed. The analyses were made using a Malvern Mastersizer X (Malvern Instruments, UK) assembled with the small sample dispersion unit. The powders were dispersed in deionised water and tests were carried with standard wet procedures. For the feedstock powders, the software settings were for polydisperse and for the bimodal powder blends it was adjusted for multimodal. Averages of 5 samples for each powder were taken. The graphs in Figure 4-19 and Figure 4-20 show the volume percentiles of the feedstock powder sizes (Figure 4-19) and the volume sizes of the mixed blends of H13 and Cu (Figure 4-20).

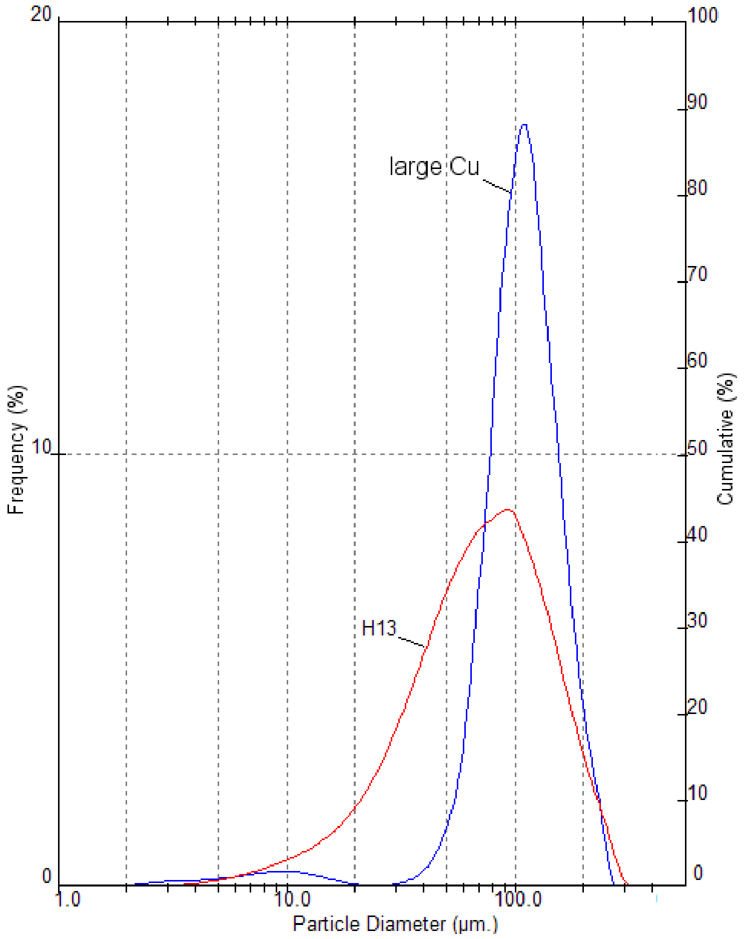

Figure 4-19. Dispersion size in volume of the powder particles for the H13 and large Cu from Table 4-3.

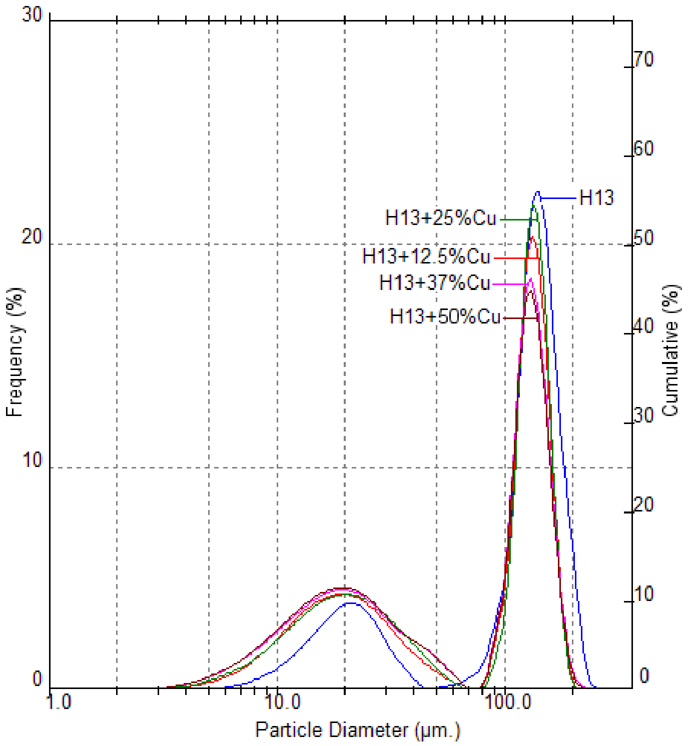

Figure 4-20. Bimodal dispersion sizes in volume of the blends from Table 4-4.

In Figure 4-20 the bimodal distribution of each mixed blend is perceptible. Table 4-5 presents the percentiles volume sizes with corresponding size. Also, the two modes of each mixed blend are presented and the particle size ratio is calculated. The ratio is approximately 7:1 for all blends.

Table 4-5. Percentile sizes of feedstock and blend powders and particle size ratio.

	Feedstock		Blends				
Percentiles	H13	Large Cu	H13	H13-12,5%Cu	H13-25%Cu	H13-37,5%Cu	H13-50%Cu
10%	24,45	65,26	17,89	11,91	11,52	11,37	13,74
20%	37,19	79,45	27,01	17,81	17,66	16,86	25,31
50%	72,58	107,79	129,00	114,61	114,41	103,89	123,92
80%	125,63	145,02	159,40	145,74	144,56	139,62	151,58
90%	160,91	169,61	176,75	161,38	159,05	154,90	167,44
Large size			138,65	132,93	134,52	130,10	132,93
Small size			21,27	19,16	20,47	19,41	17,91
Particle size ratio			6,4:1	6,9:1	6,6:1	6,7:1	7,4:1

(*) all sizes in μm

4.4. Macro and microstructure analysis

Optical and scanning electron microscope (SEM) were used to analyse the macro and microstructure. The optical microscopes, stereoscopes and SEM used in this work were available at Loughborough University, Mechanical and Manufacturing Engineering Department. Some results about the elemental composition of the material were obtained using an energy dispersion x-ray analysis (EDX) at the Institute of Polymer Technology & Materials Engineering (IPTME) at the same university. In the following sections the procedures to prepare and analyse the samples are described.

4.4.1. Samples preparation

To observe the structure, all the samples had been prepared in similar way, except when stated with a different method. The sequence of preparation was:

1. Cutting samples with abrasive wheel with cooling fluid, usually with the wheel for hard materials; After, samples were washed with liquid detergent to remove oil and coolant from the cutting wheel machine;
2. Sample mounting;
    a. Mounting in clear hot resin, or
    b. Mounting in carbon-rich hot resin (electric conductive), or
    c. Mounted in cold epoxy resin (large samples), or
    d. Mounted in cold epoxy resin with carbon powder (large samples).
3. Grinding using water with, in sequence:
    a. Grinding machines with pads with silicon carbide sand paper of 150 and 200mesh;

   b. Hand grinder with 240, 400, 600, 800 and 1200mesh silicon carbide sand paper;
4. Polishing with clothed pads in polishing machine using 6µm alumina fluid dispersed particles and 1µm diamond fluid dispersed particles;
5. Etching with 2 or 5% of nitric acid solution in alcohol by 15-30 seconds;
6. Drying on hot air blower.

Between the procedures of hand grinding, polishing with alumina and diamond, all samples were washed in abundant water. In some experiments, the manual polishing was avoided and an automatic polishing machine (capacity for 6 samples at each time) was used. Usually, each 6 parts were put 10 minutes in the automatic machine for each pad (6 and 1µm).

4.4.2. Optical microscope and stereoscope

To analyse the macro and microstructure a digital camera attached to an optical microscope was used. The images were captured directly to a computer and analysed. Similarly, the image of a scale was captured for reference on the analysis of the results. In the cases where the comparison between the samples was digitally made, it was always attempted to keep the lighting conditions constant.

4.4.3. Scanning electron microscope and X-ray dispersive analysis

The scanning electron microscope used in most part of this work was a LEO 140 Carl Zeiss SMT AG Company). For the analysis of the elemental composition in the microstructure of samples, a LEO S360 equipped with wavelength x-ray dispersive analysis unit.

4.4.4. Image analysis

Experiments where the optimum parameters for each composition of Cu and H13 (Chapters 5 and 6) were determined, image processing was used to compare pores and cracks obtained for each set of parameters combination. Images of each cross-section of the specimens were taken and analysed using ImageTool Version 3 software (UTHSCSA, 2004). Preparation for the analysis involved changing the coloured pictures to black and white and adjusting the threshold from the image histogram. The cracks and pores were clearly seen in contrast over the cross-section surface. The software counted the black and white pixels, returning the percentage value of cracks and pores. The more white pixels, the more cracks and pores in the cross section. To avoid errors, the edges of the cross section of the specimens were not considered when measuring the cracks. Figure 4-21 shows an example of the picture obtained from a cross section and its contrast in black and white.

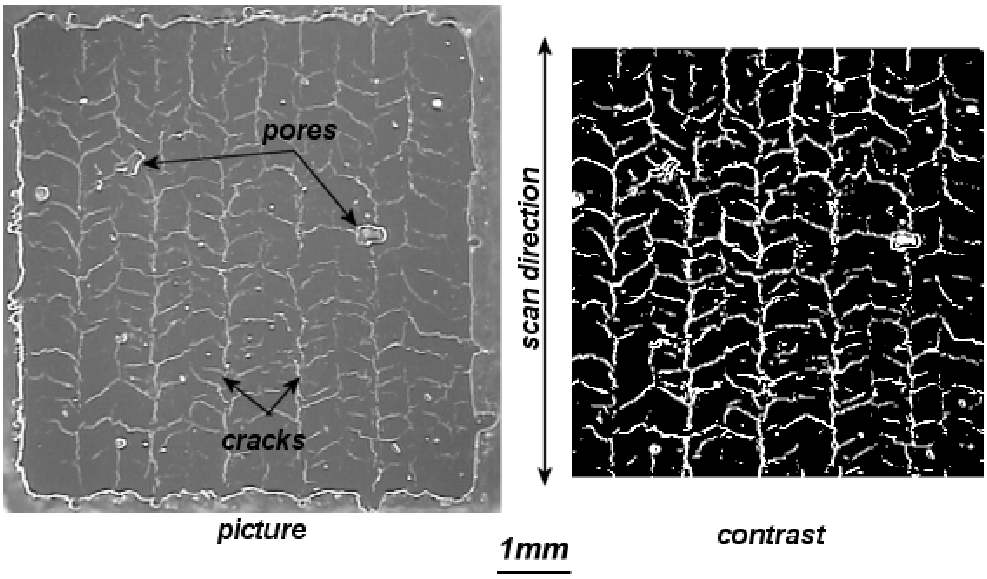
pores
cracks
scan direction
picture
1mm
contrast

Figure 4-21. A polished top cross-section of a specimen and its black and white contrast.

Chapter 5

Optimization of building strategy parameters

"So, so you think you can tell
Heaven from Hell,
Blue skies from pain.
Can you tell a green field
From a cold steel rail?
A smile from a veil?
Do you think you can tell?

And did they get you to trade
Your heroes for ghosts?
Hot ashes for trees?
Hot air for a cool breeze?
Cold comfort for change?
And did you exchange
A walk on part in the war
For a lead role in a cage?

How I wish, how I wish you were here.
We're just two lost souls
Swimming in a fish bowl,
Year after year,
Running over the same old ground.
What have we found?
The same old fears.
Wish you were here."

Pink Floyd – Whish you were here.

5. Optimization of building strategy parameters

As commented previously, the approach to fuse or sinter powder using lasers is not simple as many variables are involved. This chapter presents the experimental work on fabrication of FGM using H13-Cu powders. Strategies, scan line spacing and their effect on macro and microstructure, defects and layer temperature distribution and others were presented.

Some of the results presented here have been already submitted to journals and congresses (Publication List, page 226).

5.1. Investigation of laser scan strategies and vector spacing for H13 power

The main aim of this experiment was to understand the effect of laser vector strategies on the dimensional accuracy of layers and the porosity of H13 powder. Two vector scan spacings (discussed in section 2.5.2.(c)) were also evaluated in order to understand the interaction between laser vector scanning strategies and spacing. To identify the interactions between scanning strategy and vector spacing, multi-level factorial analysis was used. Additionally, the microstructure of the obtained parts was studied.

5.1.1. Methodology

Based on the previously presented research by Su (2002), four strategies were selected to fuse the H13 powder grade of –212μm (Chapter 4, section 4.3). The first was the *filling* (or bi-directional raster) strategy based on a pattern of consecutive parallel vectors presented in Figure 5-1 (a). The second strategy was a sequence of parallel vectors as shown in Figure 5-1 (b), denominated in this work as *sequential* strategy (one-directional raster). The third strategy known as *alternated* (one-directional intercalleted raster) is a pattern of alternated spaced vectors subdivided in two scan steps (Figure 5-1 (c)). The fourth strategy, *refill* (as shown in Figure 5-1(d)) was developed by Su (2002) where a powder refill between the vectors of the first and second set of scans was introduced.

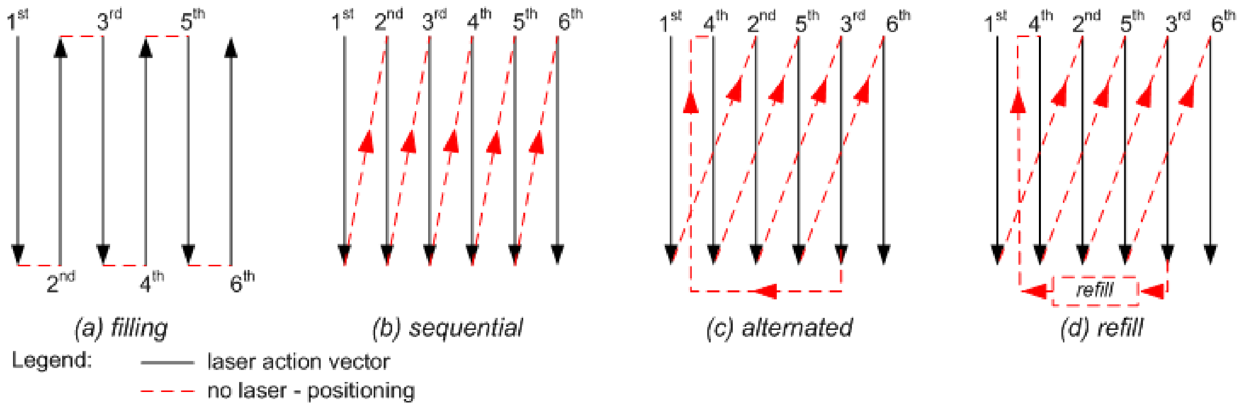

Figure 5-1. The laser scanning strategies studied.

The *filling* strategy (Figure 5-1 (a)) is the most common strategy used for laser marking and in various rapid prototyping systems. It is quick for area filling and has no dead times. It could have a high thermal stress concentration as the regions of the layer could be overheated. The *sequential* strategy was used to avoid overheating by delivering the same amount of energy for the layer regions within a longer time. The *alternated* had the same objective but reducing more the energy concentration on specific regions. Nevertheless, as evidenced in previous work by Su (2002), spatter could remove material between the vectors using this strategy, so it was developed a *refill* strategy to replace the material that was missing before applying the second set of scans raster. The refill process was an extra recoating of the layer executed between the first and second set of scans. This was performed by passing the feedhopper over the partially fused layer without moving the platform. However, it was a time consuming process. Spatter is the molten material that is ejected from the melt pool by the expansion of gases that are heated by the laser beam energy (Low *et al*, 2000). Due to this effect in laser fusion, material/powder loss occurs between the vectors of the fist scan.

As the amount of porosity could be changed by using different laser scan spacing (section 2.5.2.(c)), two spacing distances between the vectors were evaluated for each strategy. The values of the spacing were 0,5 and 0,6mm. Increasing or decreasing the space between the vectors varies the overlapping of the scan lines. Increasing the spacing can lead to porosity as powder cannot be fused so well and gaps may occur between the scan lines. Decreasing the spacing can increase the time of layer manufacturing and thermal stresses due to the greater energy input. The spacing of 0,5mm and 0,6mm causes a theoretical linear overlap of 75% and 50% for each scan spacing respectively. It means that for 0,5mm of spacing, 0,6mm of the line scan width (equivalent to the beam spot diameter, 0,8mm) were overlapped.

The specimens were built within an outer wall that was offset by 1mm. This outer wall was made using single scan lines as these are usually unaffected by spattering and layer contraction. This wall worked as a dimensional reference for the specimen contraction. Subsequent specimen layers were scanned with the vector direction rotated through 90 degrees to avoid high anisotropy in the vector scanning direction. Figure 5-2 shows a sketch of the cross hatched vectors and outer wall contour for the *sequential* strategy.

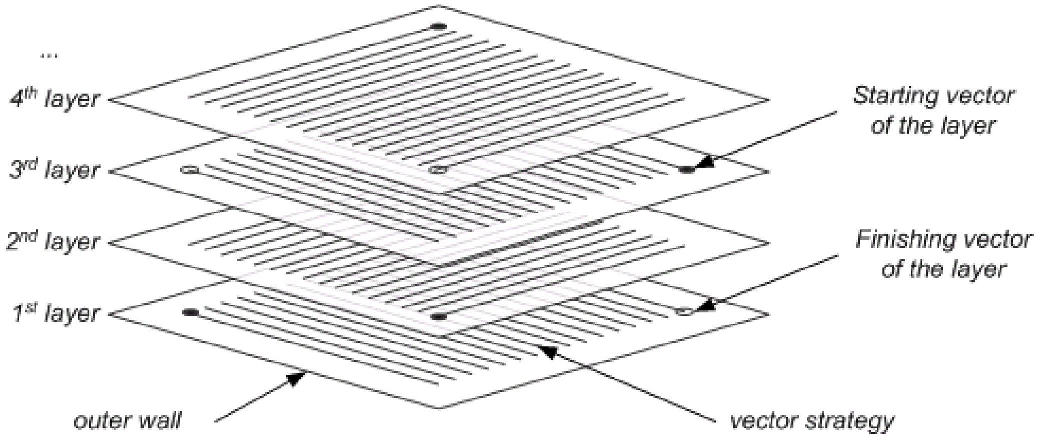

Figure 5-2. Cross hatched vectors sketch and outer wall for *sequential* strategy (only four layers shown).

Experiments were undertaken to build specimens of 9,8x9,8x3mm. They were built using fixed frames to set the layer thickness and layers were added and spread with a blade manually as described in section 4.1.1. The thickness of the spread powder was 0,5mm as the thickness of the frames used was 0.5mm. With the contraction described section 4.1.1 (Figure 4-2) and material lost by spatter, final average layer thickness was 0,38mm (specimen average height divided by the number of layers). The substrate used to attach the specimen was 2mm thick H13 tool steel sheet. The earlier described 550W pulsed Nd:YAG laser (GSI Lumonics JK701H) was used to fuse the powder. Throughout the experiments a 15l/min local flow of argon was used to reduce oxidation.

All four strategies were used under constant laser processing parameters. Based on previous work developed by Su (2002), pulse energy (E) of 10J, pulse width (w) of 5ms, pulse rate (f) of 10Hz, scan speed (v) of 3,333mm/s, average laser power (P) of 100W and energy densities (E_ρ) of 37,5J/mm^2 were used to build the specimens. No pre-heat was used in the powder bed and it was fused at room temperature (about 22^{0}C).

Preliminary test was conducted to evaluate the strategy that could reduce the porosity level. Two samples for each spacing/strategy combination were built (resulted in 8 specimens). These specimens were cross sectioned for further analysis of porosity and area. After determining what strategy was better in terms of porosity and cross section distortions, 5 samples for each of the vector line spacing (0,5 and 0,6mm) were made.

The specimens were cross sectioned, ground and polished with 1µm diamond abrasive. Macro pictures of the cross section with reference scales were taken for all specimens. The images were treated as explained in section 4.4.4 before the porosity and incomplete area were measured using Image Tool Version 3 software (UTHSCSA 2004). A scale of 1mm was used as a reference to the measurement. The reference to the height of the specimens was the outer wall contour of the specimens that was not affected by the strategies and spacings.

5.1.2. Results

The specimens built to determine the best strategy did not present a regular layer thickness. Figure 5-3 shows one of the specimens with 0,5mm spacing using the *refill* strategy. In general, the specimens obtained using *filling* and *sequential* strategies showed a depression in the middle of the specimen. In the *Alternated* strategy the scanning raster pattern was perceptible. The most uniform specimens were produced with the *refill* strategy. Figure 5-4 shows the top view from specimens obtained with 0,5mm spacing for all strategies. Spatter and balling were identified during the manufacturing of these specimens.

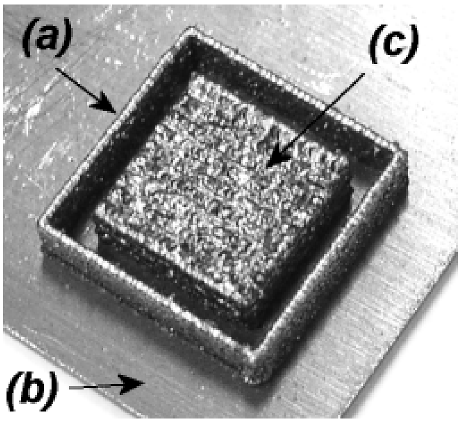

Figure 5-3. A typical result: (a) outer border, (b) substrate & (c) specimen.

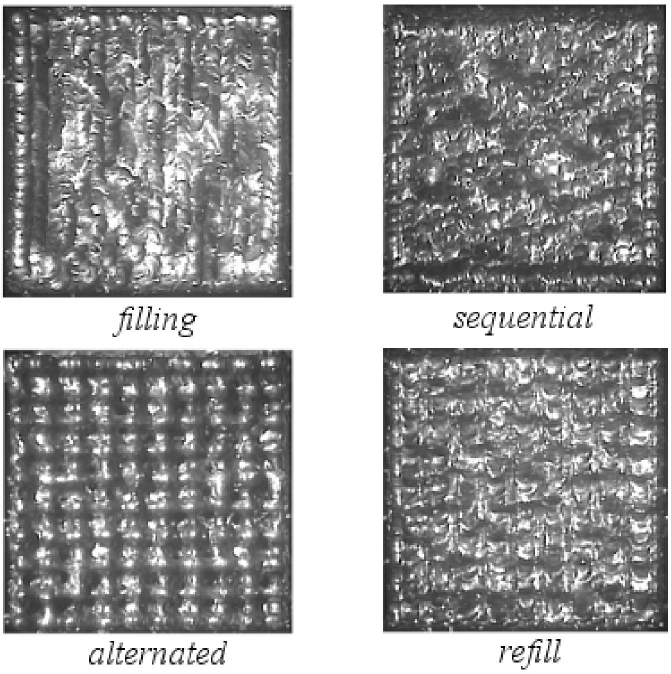

Figure 5-4. Top view of the specimens obtained using different strategies (0,5mm spacing).

The cross sections of these specimens showed that changing the spacing had a minimum influence over the porosity for all the strategies studied. *Alternated* strategy showed the highest porosity, approximately 15% of the cross section area. *Filling, sequential* and *refill* showed low porosity, 2,6%, 5% and 3% respectively, which can be considered a normal porosity range for powder metallurgy parts (German, 1994).

The porosity of the specimens was mainly formed by large pores (greater than 10µm). It was noticeable that pores appeared between the laser scans and between the layers. This pore formation was greater in the *alternated* strategy. Also, the pores found with this strategy were distributed on a hatch pattern. This phenomenon occurred because spatter and powder melting of two largely spaced vectors (without overlapping) leave the space between them without powder to fuse in the next scan between the two first vectors. This did not happen in the *refill* strategy as it replaced the material lost by spatter and melted and dragged powder by the previous vectors. For *filling* and *alternated* as the vectors were drawn side-by-side, the next vector dragged more powder from the surrounding that was not fused yet. This was one of the causes of the depression in the middle of the cross sections of the specimens produced by these strategies. The depression in the middle and not in the corner was justified by the rotation of the scanning direction for each layer build. Figure 5-5 shows cross-sections of two different specimens. The top picture is a cross section of a specimen built by the *alternated* strategy (Figure 5-5 (a)). The specimen in Figure 5-5 (b) was built with the *refill*. Both were made using 0.5mm of spacing. The images show only the contrast of the cross sections that were used to measure the pore area.

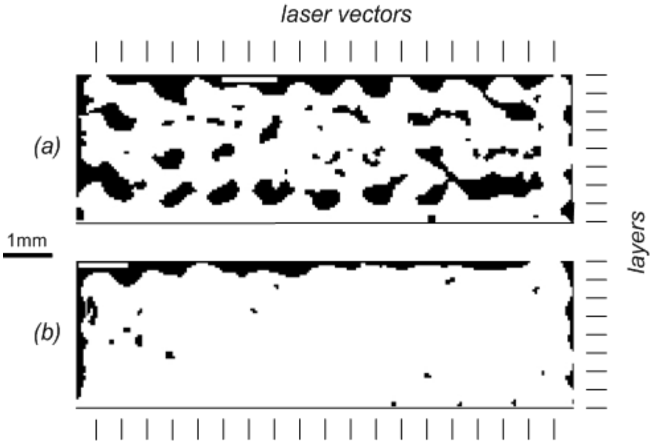

Figure 5-5. A perceptible pore pattern in the *alternated* (a) strategy in contrast with *refill* (b).

The specimens volume reduction was caused by the spatter and contraction of the melted powder which affected the shape of the specimens. This volume reduction was mainly characterized by the depression in the middle of the specimen. When the specimens were cross sectioned this volume reduction could be measured by the area missing from the cross section. The black area indicated in Figure 5-6 was the evidence of mass lost for each strategy evaluated. It was perceptible that in the *filling and sequential* strategies as shown in Figure 5-6 (both built with 0,5mm) these losses were more accentuated. The *Filling* strategy had an average area reduction of 25,1%, *sequential* 20,8% and *alternated* 10,6%. As the refill strategy had the benefit of powder refill, it had the lowest value of area reduction (5,3%).

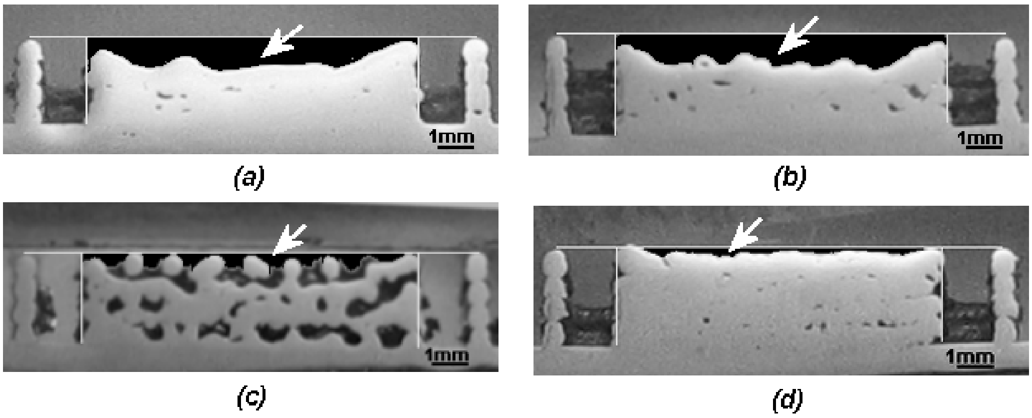

Figure 5-6. The cross section of specimens build with 0,5mm spacing (a) *filling*, (b) *sequential*, (c) *alternated* and (d) *refill* (area lost is indicated in black).

It was necessary to evaluate the overall result for each strategy. Pores and area reduction are both manufacturing defects that affect the material properties, so the summation of these described the performance of each strategy and spacing. Table 5-1 summarizes the pores and area reduction percentages for the spacing and strategies evaluated. It is noticeable that except by the *refill* strategy all others have present a high rate of cross section area losses.

Table 5-1. Porosity, area reduction and total area reduction for strategies and spacings.

	Porosity		Area reduction		Total area reduction	
	Spacing		Spacing		Spacing	
Strategy	0,5mm	0,6mm	0,5mm	0,6mm	0,5mm	0,6mm
Filling	2,3%	2,8%	26,2%	24,2%	28,5%	27,0%
Sequential	5,9%	4,2%	17,8%	23,8%	23,7%	28,0%
Alternated	14,9%	15,5%	12,8%	8,5%	27,6%	24,0%
Refill	3,6%	2,3%	4,8%	5,8%	8,4%	8,1%

Based on the fact that the *refill* strategy presented the best results and no distinction was found between the spacings used, an extra experiment with five samples of each spacing, with the *refill* strategy was made to determine the variability of these results. All samples were cross sectioned, grounded, polished and analysed as previously. The average porosity found in the specimens produced with 0.5mm of vector line spacing was 1,27% with a standard deviation of 0,95%. For 0,6mm of spacing, the average porosity was 2,1% with a standard deviation of 1,74%.

The cross section of the specimens revealed not only pores but also cracks. These cracks were mainly along the scan direction as seen in Figure 5-7 point (b). The rapid cooling from molten material to ambient temperature is possibly the main cause of the crack formations. As a large thermal gradient was present in the melt pool and the centre of the pool was the hottest and last region to solidify it cracked along the top of the bead. After polishing and etching the samples, the overlaps were also noticeable in the cross section as darker areas under the optical microscope. These areas were generated by the re-heat that occurred in the material from the previous layer (Figure 5-7(c)). Pores are also trapped in these boundaries probably due to trapped gases.

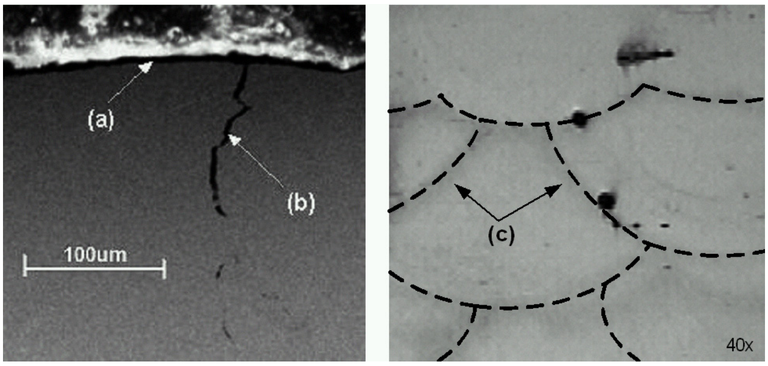

Figure 5-7. Crack across the scan direction (b), top surface of the specimen (a) and re-heat marks (c).

The microstructure of the solidified material was formed by dendrites of the H13 (Figure 5-8). These dendrites were formed by rapid cooling and were orientated towards the centre of the laser spot.

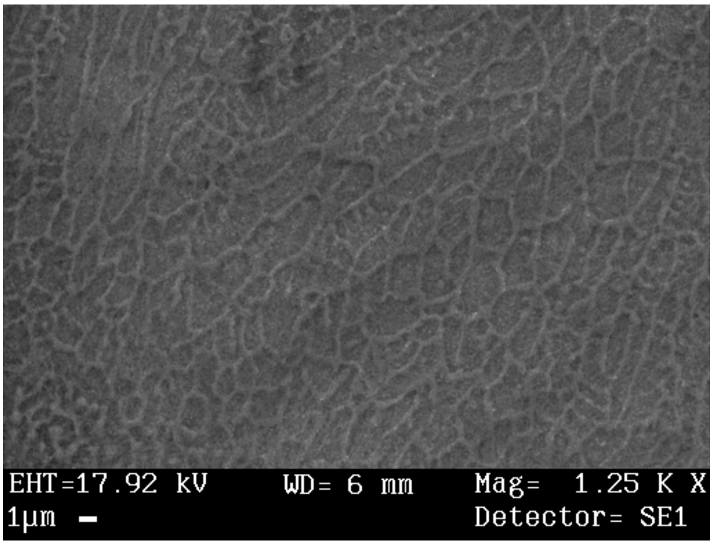

Figure 5-8. SEM micrograph of the H13 microstructure.

5.1.3. Discussion on laser strategies

The laser interaction with the powder bed was a complex phenomena evidenced by the results obtained in this experiment. The spatter was one of the major problems for the strategies evaluated. Spatter ejected material from the melt pool reducing the amount of material fused and solidified in the part. The other effect was the melting and solidification of the powder itself. Although the *filling* strategy required less time to build a layer it showed a problem with volume reduction and spatter deposited over the surface. The *sequential* strategy also had problems with the spatter but it was concentrated in a region of the layer towards the end of the process. This was not evidenced in the other strategies because of the alternated vectors that avoided spatter deposition in the layer surface.

As the *refill* strategy replaced the lost and contracted material it obviously showed the lowest porosity and volume reduction. Nevertheless it also had the longest build times due to the dead time between the vectors and the refilling. For comparison, to fuse a layer of 10x10mm using a spacing of 0,5mm with 3,333mm/s of laser scan speed and 33,333mm/s for table reposition (laser off), *filling* strategy takes about 1min, *sequential* strategy 1min10sec, *alternated* strategy 1min13sec and *refill* strategy 1min23sec. By the fact that the layer recoating and refill were executed manually by the machine operator, the recoating time on *refill* strategy was drastically affected. It is also important to point out that the laser parameters used in this experiment were not changed and different results might be obtained for other values.

The spacing change for the strategies showed little influence. Although the spacing differences evaluated was small, the 0,6mm spacing showed a large variation and 0,5mm proved to be more constant and in many results produced the lower porosity and volume reduction. The measurement of the area and pores was subjective even with attempts to keep all parameters constants. That is why the measurements were kept in percentages. The porosity found in the *refill* strategy could be considered low depending on the application of the component produced with this process.

5.2. Evaluation of the spatter lost during the laser fusion

The porosity and volume reduction were problems that could occur when fusing powder through high power pulse lasers due to incomplete melting of the powder, trapped gases and the spatter effect. The spattering of material being expelled from the beam spot zone was occasioned by the plasma. The plasma is formed by the heating of the gases and its rapid expansion. The gases molecules become so energized that they emit visible light radiation among others. Figure 5-9 shows the spattering during the laser fusion of the powder. It is possible to observe the plasma and spatter (hot melted and not melted particles) flying away from the beam spot target.

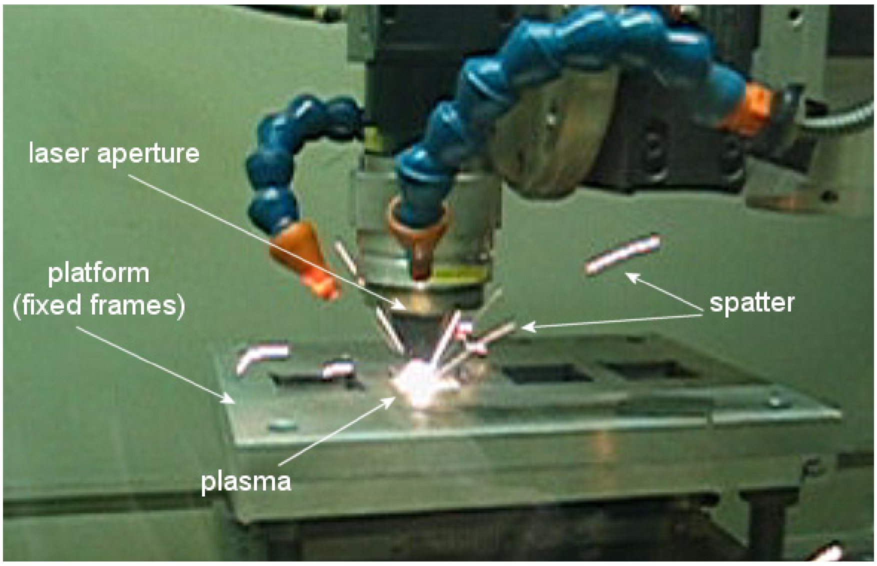

Figure 5-9. Spattering occurring during the selective laser fusion process.

As the previous results indicated that a large amount of material could be lost by the spatter, a new set of experiments was designed to estimate the amount of material lost during the process.

5.2.1. Methodology

To measure the amount of material mass loss caused by the spatter effect, a simple experiment was designed. Substrates with square grooves of 500μm depth were used to spread the powder and fuse 4 lines of powder. The lines were fused using the same parameters that were used for manufacturing the specimens (pulse energy: 10J, pulse width: 5ms, repetition rate: 10Hz, feedrate: 3,333mm/s). The mass of the substrates (M1), the mass of the substrates plus added 500μm powder layers (M2), the mass of the substrates with the powder and the fused lines (M3) and the mass of the substrates with only the fused lines (M4) were measured. Figure 5-10 shows the sequence described above for the mass measurement.

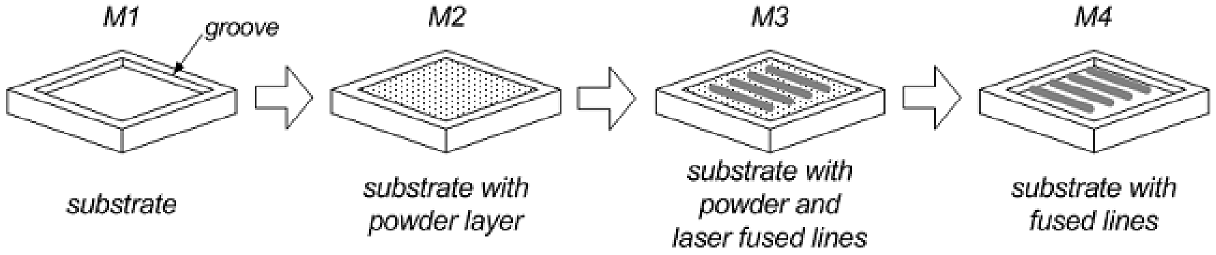
M1
groove
M2
M3
M4
substrate
substrate with powder layer
substrate with powder and laser fused lines
substrate with fused lines

Figure 5-10. Mass lost by spatter measurement sequence.

As many of the spatter particles remained in the surroundings of the substrate after the laser fusion, these were carefully brushed away prior to the weight measurement. The experiment was repeated 8 times in total to obtain the average value.

5.2.2. Results

The difference between the mass of powder and fused lines to the powder bed before the laser fusion showed great difference. The average percentage of mass lost from the difference of the powder mass after laser fusion (M3) and before laser fusion (M2) was that 18,8% of powder mass was missing for a standard deviation of 1,74%.

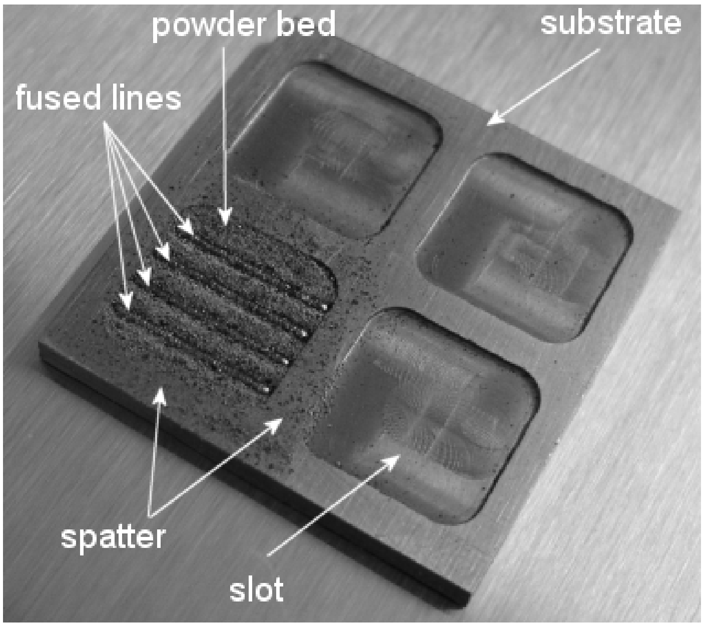
powder bed
substrate
fused lines
spatter
slot

Figure 5-11. An example of the spattering effect after the laser fusion.

5.2.3. Discussion on spattering

This mass lost from the powder bed could have two sources: vaporization of the material and mainly by the spatter. From the observations, it was reasonable to admit that low influence had the vaporisation in the results. The experiment was carried with the same laser parameters found by Su (2002) for H10 tool steel fusion. Using these pulse laser parameters, a short pulse (5ms) width with a high energy pulse of 10J, the peak power was 2kW (equation 4.04, section 4.1.3) which was considerable high. The higher the peak and or average power the higher is the probability of plasma formation and large it might be formed. So, optimization of lasers parameters needed to be studied.

5.3. Comparison of the heat distribution over the fused layer using different strategies

As described by numerical results from the literature (Matsumoto *et al*, 2002; Dai and Shaw, 2002), the laser scanning strategy affects the way heat energy is concentrated into the powder bed/layer. So a thermal camera was used to analyse comparatively the temperature distribution of the layers with the four strategies used in section 5.1.

5.3.1. Methodology

Specimens with only one layer of 30x30mm (xy building plane) and 0,50mm thick were made for each one of the four strategies (filling, sequential, alternated and refill). A substrate of mild steel 4mm thick was used in this experiment. The material used to build the layers was the -212µm grade H13 powder.

Each strategy was tested individually. Infrared images were taken after the first layer being completed. The time to take the picture was between 5-15 seconds that included time to turn off the laser, move the platform to a desirable position to take the picture, unlock the building chamber and open the chamber door and to capture the thermal image. The pictures were taken from the top of the manufactured layers using a thermal scanner model AGEMA 900.

Metallic materials reflect the infrared radiation and some adjustments must be made in the software to obtain accurate values of temperature of a body. Nevertheless, the values of the reflectivity of the powder were not available to adjust the infrared band of the camera to obtain the most accurate value.

5.3.2. Results

The thermal images captured after the completion of each layer showed varying temperature levels. It should be noted that at this point, the highest temperature obtained was from the unaffected powder around the layer. This powder temperature was raised by the energy emitted from the plasma. The powder had low thermal conductivity due to low contact area between the particles, and hence it behaved as an insulator and did not cool down as quickly as the fused material attached to the substrate. The substrate acted as a heat sink and chilled the layer built. Figure 5-12(a), 5-13(a), 5-14(a) & 15(a) show 3D temperature maps built from the thermal infrared pictures. The brighter region is the higher temperature. The dashed-line squares in these pictures show the regions of the solidified layer. The higher temperatures around the squares are within the unaffected powder commented previously.

For the *filling* strategy there were perceptible peaks of higher temperature over the layer. These peaks are probably the hotter spatter spots attached to the layer (Figure 5-12(a)). The quality of the surface matched aspects of the thermal image. In the *filling* strategy spatter is noticed and makes the surface of the layer irregular as shown in Figure 5-12(b) and surface detail in Figure 5-12(c). Figure 5-12(b) shows the first vector of the layer and the detail of surface region shown in Figure 5-12(c).

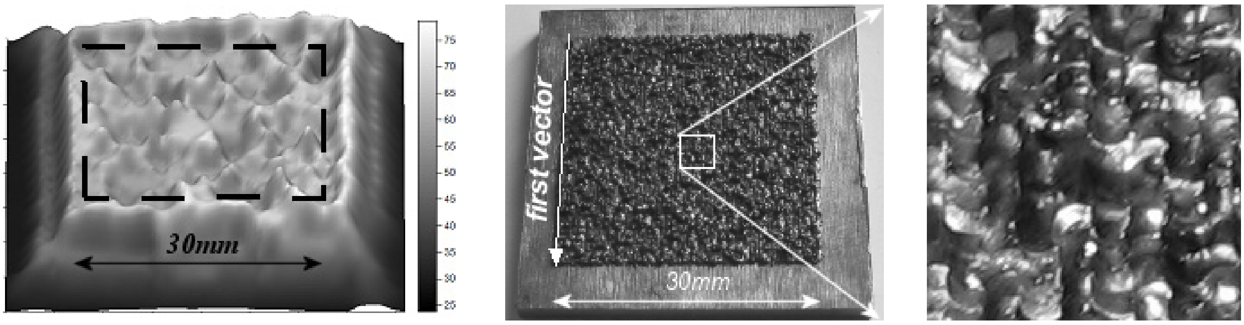

(a) (b) (c)

Figure 5-12. (a) 3D temperature map, (b) layer obtained and (c) detail of the layer surface for the *filling* strategy.

In the *sequential* strategy, spatter was also spotted but it was more concentrated in the corner where the laser scanning ended. Figure 5-13(a) shows the 3D temperature map where the end of the layer has elevated temperatures due to the concentrated spatter. Figure 5-13(b) shows the top view of the specimen where it could be seen that the end corner of the layer is irregular due to higher levels of spatter.

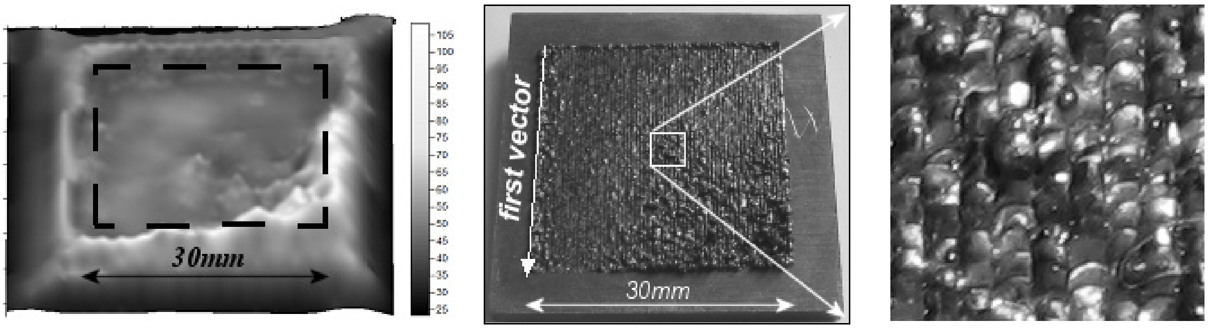

(a) (b) (c)

Figure 5-13. (a) 3D temperature map, (b) layer obtained and (c) detail of the layer surface for the *sequential* strategy.

The *alternated* strategy presented a more uniform temperature (Figure 5-14 a)). It is reflected in its more uniform surface shown in Figure 5-14(b) and Figure 5-14(c) but with valleys between the scans.

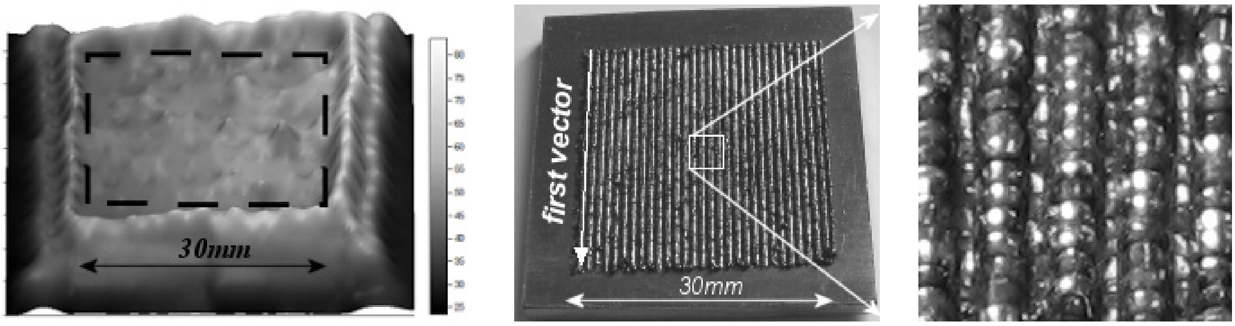

(a) (b) (c)

Figure 5-14. (a) 3D temperature map, (b) layer obtained and (c) detail of the layer surface for the alternate strategy.

The temperature over the surface of the *refill* strategy was almost uniform without spatter over the surface Figure 5-15(a). A solid and uniform pattern and a thicker layer were observed in the *refill* strategy (Figure 5-15(b) and (c)).

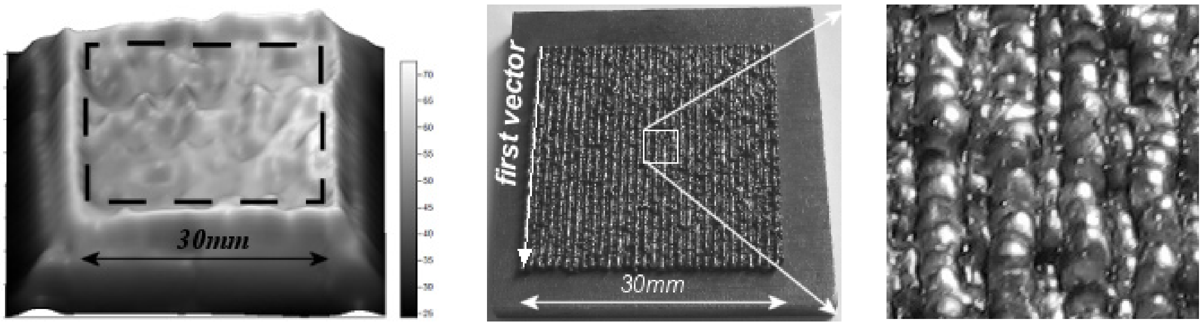

(a) (b) (c)

Figure 5-15. (a) 3D temperature map, (b) layer obtained and (c) detail of the layer surface for the *refill s*trategy.

5.3.3. Discussion on heat concentration

The temperature scales from Figure 5-12 to Figure 5-15 are not meant to represent a quantitative analysis between the strategies as the time to take the infrared pictures varied between them. Also, the use of the camera without the correct reflectivity value for the H13 powder could not provide an accurate temperature measurement. However, the results are useful as a reference for the temperature distribution over the layers. It showed that the *sequential* strategy has a problem with spatter concentration as it is "swept" by the plasma to a corner of the layer. Despite the uniform temperature of the *filling* strategy, the amount of spatter distributed over the surface was considerably higher than for *refill* and *alternated* strategies. The *refill* and *alternated* strategies distribute the temperature better over the surface as the amount energy delivered for each region was divided in two intercalated steps. Nevertheless, the *alternated* strategy has a lack of melted material in the second step as the powder between the lines of the firsts vectors had been dragged by the fused line beads or spattered by the plasma.

5.4. Investigation of the effect of strategies on the fusion of H13-Cu% mixtures

In the previous presented experiments, the strategies were investigated using only one material, the H13 powder. As the material had strong influence over the energy density coupling efficiency, results of porosity and volume reduction analysed in section 5.1 could be different when using powder mixtures of H13 and Cu. In this section, the effect of scanning strategy of three different material compositions of H13 and Cu powder are presented. The effect of the scanning strategies on porosity, cracks and area reduction (material lost in volume) were analysed.

5.4.1. Methodology

In this experiment, three powder blends of H13 and Cu powders were used in combination with the four strategies evaluated in the previous experiments (filling, sequential, alternated and refill). In order to optimise powder packing, three blends with bimodal distributions as presented in sections 4.3.2 and 4.3.3 were used: H13, H13-25%Cu and H13-50%Cu. Notice that in this case, the bimodal distribution of H13 was used in contrast with the previous experiment where the feedstock, mono modal distribution powder, was used. The average particle size of the bimodal powders was reduced compared to the feedstock powder as well.

Based on previous experiment, the four laser scan strategies (Figure 5-1) were used to identify the effect of Cu percentages on the porosity and volume reduction of the specimens produced. The specimens were built in similar way to that in section 5.1 with 9x9mm of base and 3 mm height. Again, an outer wall as a build height reference was also manufactured with each specimen (Figure 5-2 and Figure 5-3). All specimens were built by rotating the direction of the set of vectors after each layer to reduce anisotropy in the scanning raster plane. The spacing between the vectors was fixed at 0,5mm as it was proved to produce satisfactory results in the previous experiment. Argon gas assist was used at 15 l/min flow rate. The layers were manually added and spread with a blade (fixed frames method, Figure 4-1), resulting in an average thickness of 0,38mm. To avoid excessive source of variations, the laser parameters were kept constant and were the same used in the previous experiment (E:10J, w: 5ms, f: 10Hz, v:3,333mm/min). Each strategy was tested with the three different powder blends. For each one of these combinations, 5 specimens were built, cross sectioned and analysed. The cross-sectioned samples were mounted in hot pressurized resin, grounded and polished. Digital pictures were taken from each specimen using a microscope with attached digital camera. The porosity and the volume reduction were measured using ImageTool Version 3 software (UTHSCSA, 2004).

Analysis of variance (ANOVA) was used to analyse interdependence of the strategies and material factors into the results (porosity and volume/area reduction).

5.4.2. Results

The cross section analysis of the specimens showed that the porosity for all specimens (with different Cu percentages) had been changed. Figure 5-16 shows some of the cross sections of the specimens obtained. Macro porosity is perceptible along the cross section of the specimens. Also, the cross sections showed an area reduction compared to what should be the height of the specimens (as measured from the thin wall section). This area reduction is identified as white regions in the top of the cross sections in Figure 5-16.

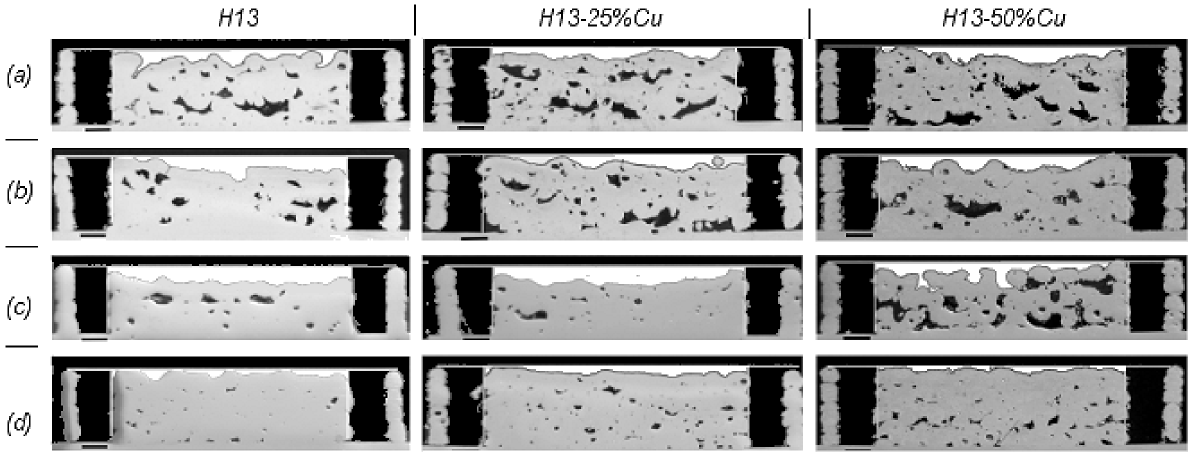

Figure 5-16. Typical cross sections[5] of specimens built with H13-Cu blends. (a) *filling*, (b) *sequential*, (c) *alternated* and (d) *refill* strategy.

The measured porosity average values in all strategies and the powder compositions are shown in Figure 5-17. The variation of the results from each combination of powder blend and strategy was great and so the arrows in Figure 5-17 indicate one standard deviation above the average value and also one standard deviation below the average value. The porosity level in the pure H13 samples was found to be lowest using the *refill* strategy. In the 25%Cu blend specimens, the porosity was found to be higher using the *filling* and *sequential* strategies. These specimens had cracks along the z-direction. These cracks were also included by the imaging software when measuring the porosity area. On the other hand, the porosity level increases for the *alternated* strategy when the Cu percentage was increased to 50%. This may be due to the fact that the surface tension was higher when the Cu percentage was increased; the material from the surrounding area was sucked into the melt pool, and caused voids in the layer. Overall, the porosity level was found to be stable and low for the *refill* strategy in all three powder compositions.

---

[5] Note: The top white region of each cross section is the area reduction in the specimen.

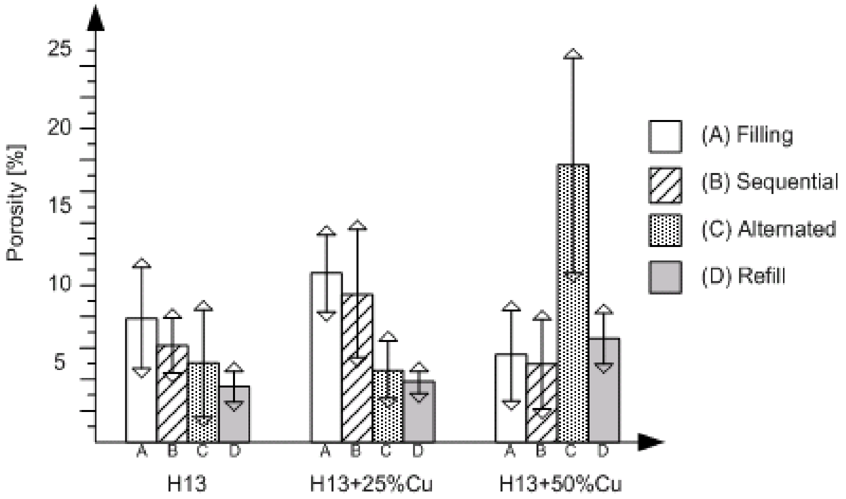

Figure 5-17. Effect of the Cu percentage and strategies over the porosity.

Statistical analysis of variance showed that the factor which affected most porosity was the Cu percentage (Table 5-2). According to the ANOVA, the strategies factor had a low P-value but not significant enough to affect the porosity. The interaction between these factors was difficult to analyse over the porosity results as the strategies was a categorical factor and not quantitative. Also, the high variability presented affected a more accurate analysis.

Table 5-2. The ANOVA table for porosity results (95% of confidence).

Source	Sum of squares	Degree of freedom	Mean Square	F-Ratio	P-Value
A: Cu%	180,00	1	180,00	7,75	0,0068
B: Strategies	76,79	1	76,79	3,31	0,0729
AA	17,94	1	17,94	0,77	0,3821
AB	63,35	1	63,35	2,73	0,1027
BB	44,30	1	44,30	1,91	0,1712
Blocks	2,36	2	1,18	0,05	0,9504
Total Error	1764,61	76	23,22		
Total corrected	2181,85	83			

The area reduction indicated in Figure 5-16 was measured for all strategies used and for each material blend (Figure 5-18). In general, the material lost for H13 and 25%Cu was higher in *filling* and *sequential* strategies. For the 50%Cu blend, the *filling, sequential* and *refill* strategies had a lower area reduction compared to all other materials, however, the area reduction was high for *alternated* strategy. The *alternated* strategy had the least variation in area reduction percentage (but higher than refill strategy) when changing from one composition to another. It could be concluded that the area reduction increased for 25%Cu and reduced when the Cu percentage increased to 50% for *filling* and *sequential* strategy. The area reduction was generally constant for the other two scanning strategies (*alternated* and *refill*).

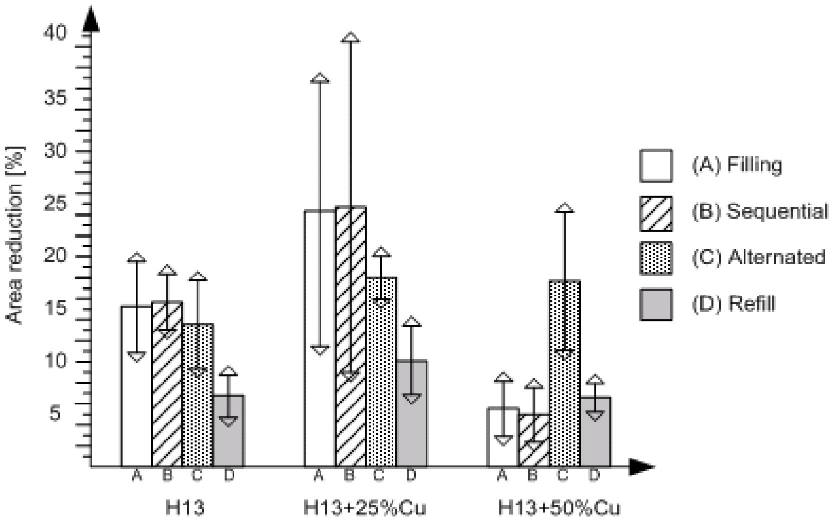

Figure 5-18. Effect of the strategies and Cu percentage over the area reduction.

The ANOVA test performed on this result, area reduction, showed that the significant factors were strategies and the quadratic effect of Cu percentage and strategies as their P-value was lower than 0,05 (Table 5-3). This indicates that those factors had major influence over the area reduction. Again, the great variability made difficult to establish correlation between strategies and Cu percentage.

Table 5-3. The ANOVA table for area reduction.

Source	Sum of squares	Degree of freedom	Mean Square	F-Ratio	P-Value
A: Cu%	12,61	1	12,6137	0,25	0,6171
B: Strategies	1422,87	1	1422,87	28,43	0,0000
AA	961,04	1	961,044	19,20	0,0000
AB	5,73	1	5,72538	0,11	0,7361
BB	307,02	1	307,023	6,13	0,0155
Blocks	17,01	2	8,5072	0,17	0,8440
Total Error	3803,76	76	50,0495		
Total corrected	6857,87	83			

5.4.3. Discussion on the Cu effect on strategies performance

In general, three strategies, *filling*, *sequential* and *alternated*, produced higher area reduction and porosity. The *refill* strategy produced around 10% in total of area and porosity loss compared to 20% and above for other strategies. This was mainly due to the densification and flow of powder into the melt pool leaving voids around the laser beads (see Figure 5-19). Also, some portion of the material was loss by the spattering effect as notice in previous experiment. The combination of these factors results in a lack of material to be fused by the subsequent scanning vector, unless this was refilled.

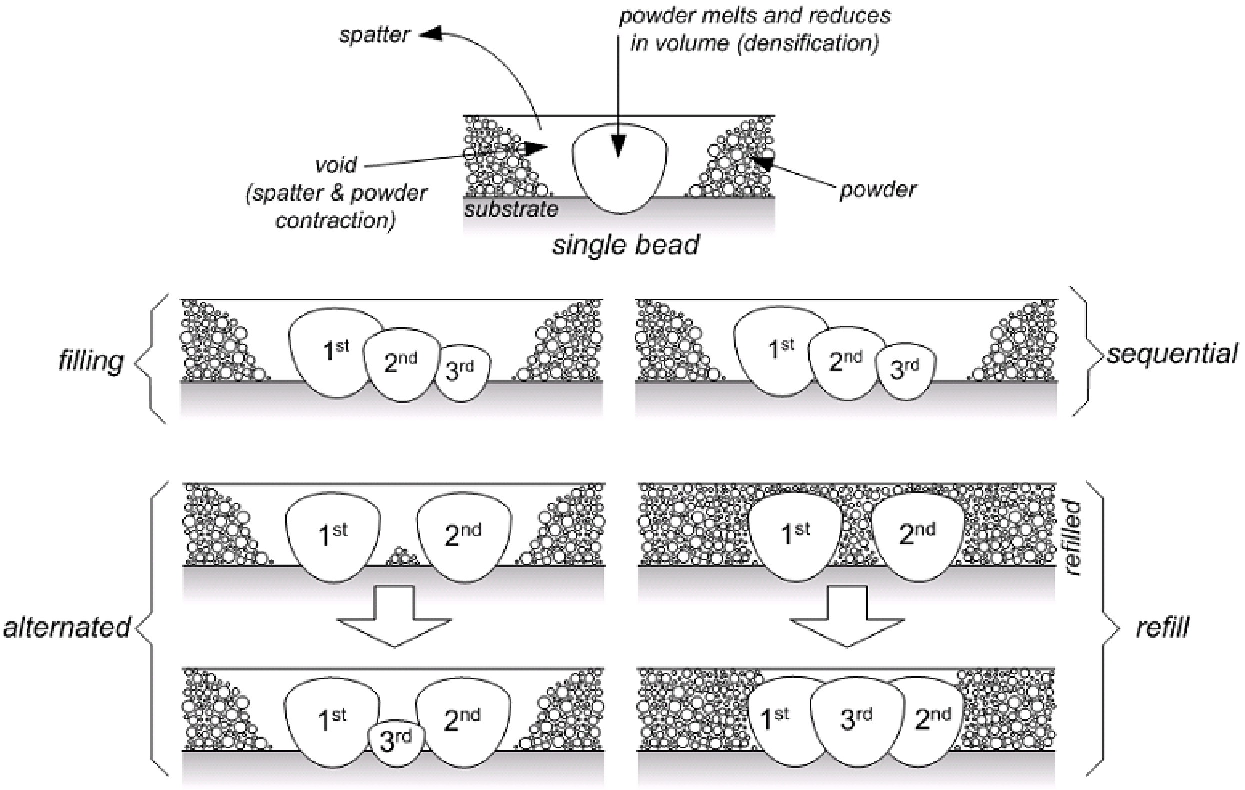
spatter
powder melts and reduces in volume (densification)
void (spatter & powder contraction)
substrate
powder
single bead
filling
sequential
1st
2nd
3rd
alternated
refill
refilled

Figure 5-19. Powder contraction and void which causes the area reduction and porosity

So, despite the ANOVA had indicated that strategies did not affect the porosity results it had to be considered that the great variability found in the experiments could be responsible for this inaccuracy. As seen in the previous experiments, the strategy had influence of the porosity results. Concerning the material composition, the ANOVA showed that it affected the porosity and the area reduction results.

The amount of Cu changed the laser coupling efficiency as Cu tends to be more reflective to the laser radiation at 1,06μm wavelength. Another factor that might have influenced the results as porosity increased with the Cu addition was the surface contact and wetability of the molten Cu.

The refill strategy was found to be the most suitable to produce denser parts with less porosity. Specimens with densities over 90% of the theoretical value were obtained. Also the area reduction was low using this strategy. This could produce solid bodies and with more repeatability.

5.5. Evaluation of the microstructure of a z-graded FGM specimen

Until the previous experiment, the materials compositions had been studied individually and only the macro defects had been analysed. There was no data about the interaction regions between the different powder compositions. This information was vital for the manufacturing of a gradient. As it is important for further work, an experiment for producing FGM specimens, graded on z direction, was made. The Z-gradient is a gradient that is based on the composition variation layer-by-layer. Most of the powder processing methods for producing

FGM are based on this approach. The difference in this experiment was that the material was fused and bonded by a laser.

5.5.1. Methodology

The powder laser fusion is a complicated phenomenon characterized by the fast localized heating, melting and solidification of the materials. In order to evaluate the microstructure of the laser fused H13 and Cu powders and how the bonding between the layers with different compositions would occur, two specimens graded in the z-direction were built. Three powders were used in this experiment: H13, H13-25%Cu and H13-50%Cu. These powders were the same specified in section 4.3, Table 4-4. The geometry of the specimens was the same presented in the previous section with a thin wallet. The first specimen was built with 4 layers of H13, 4 layers of 25%Cu and 4 layers of 50%Cu respectively. In the second specimen this order was inverted and 4 layers 50%Cu were used to start the building finishing with 4 layers of H13. This intended to identify if, due to the different order, microstructure changes could be identified along the Z build direction. As the material composition would change the cooling rate of the top layers and would provide different heat treatments to the bottom layers this change in layers order composition intended to identify if this had effect on the microstructure. A schematic drawing of the specimens can the seen in Figure 5-20.

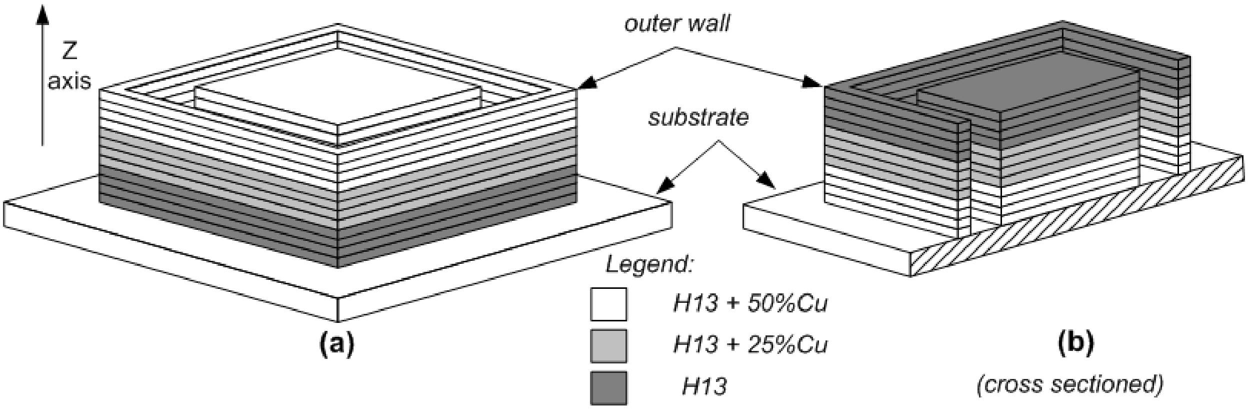

Figure 5-20. Z-graded structures built and the build orientation.

The specimens were built with the refill strategy, vector spacing of 0,5mm and manual fixed frame method from section 4.1.1. The frames were 0,5mm thick and the average layer thickness was 0,38 of the fused material. The specimens were built with the same parameters used by Su (2002) to fuse H10 powder (E:10J, w: 5ms, f: 10Hz, v:3,333mm/s). H13 substrates to attach the specimens and Ar flow to avoid excessive oxidation were used.

The samples were cross-sectioned, polished and etched for microstructure study as described in section 4.4. Optical and electronic microscopes were used to analyse the microstructure and the composition of the layers.

5.5.2. Results

The polished and etched cross sections of the graded structures produced are shown in Figure 5-21. In this figure, the fish skin effect produced by the localized fusion of the laser beads is very pronounced. It can be seen also, that the laser penetration in the first layers of the specimen (A) started with only H13, was greater than the penetration in the substrate of the second specimen started with 50%Cu powder. This was a clear indication that Cu affects the reflectivity of the powder and the laser beam could not penetrate as deep as in the pure H13 powder.

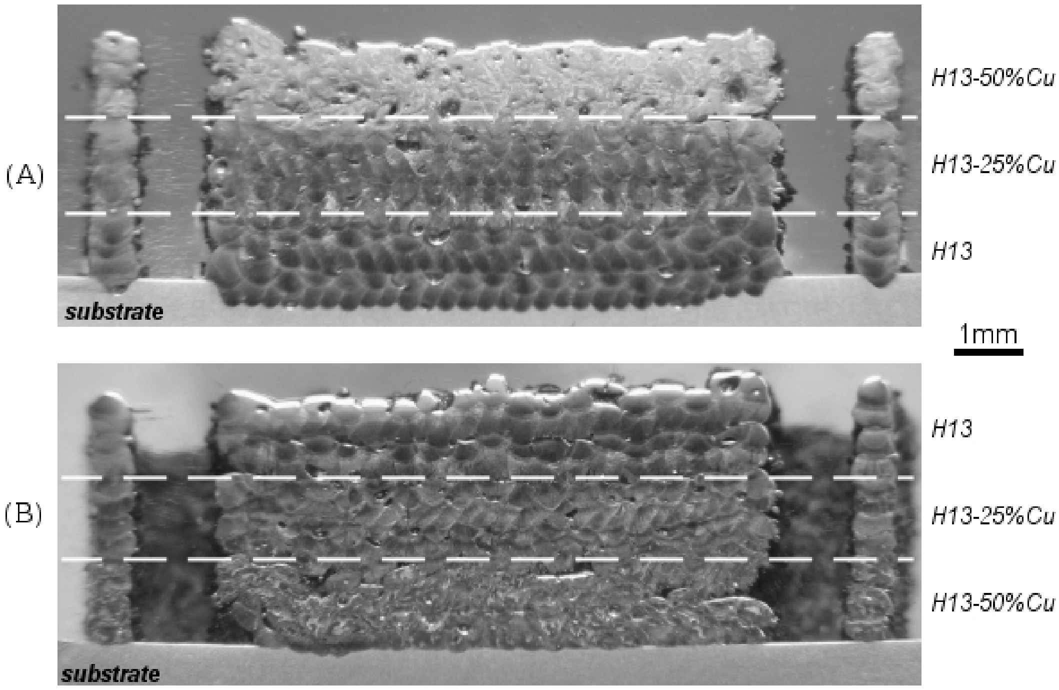

Figure 5-21. The cross section of the two graded specimens: A) starting with H13, B) starting with H13+50Cu%.

As noted in the previously presented experiment (section 5.4), specimens built with 25%Cu blend presented many cracks. These cracks were orientated along the Z building direction. Figure 5-22 shows the specimen started with H13 only polished to increase the contrast of pores and cracks (Figure 5-22-a) and etched to reveal the macrostructure of the gradient (Figure 5-22-b). The cracks formation and its orientation in the Z-axis in the middle of the cross section region (H13-25%Cu region) are noticed. The were found to be minimum in regions of H13 and H13+50%Cu. When the specimens were produced inversely (Figure 5-22-c), the cracks and the orientation were similar to the previous material composition sequence (Figure 5-22-b).

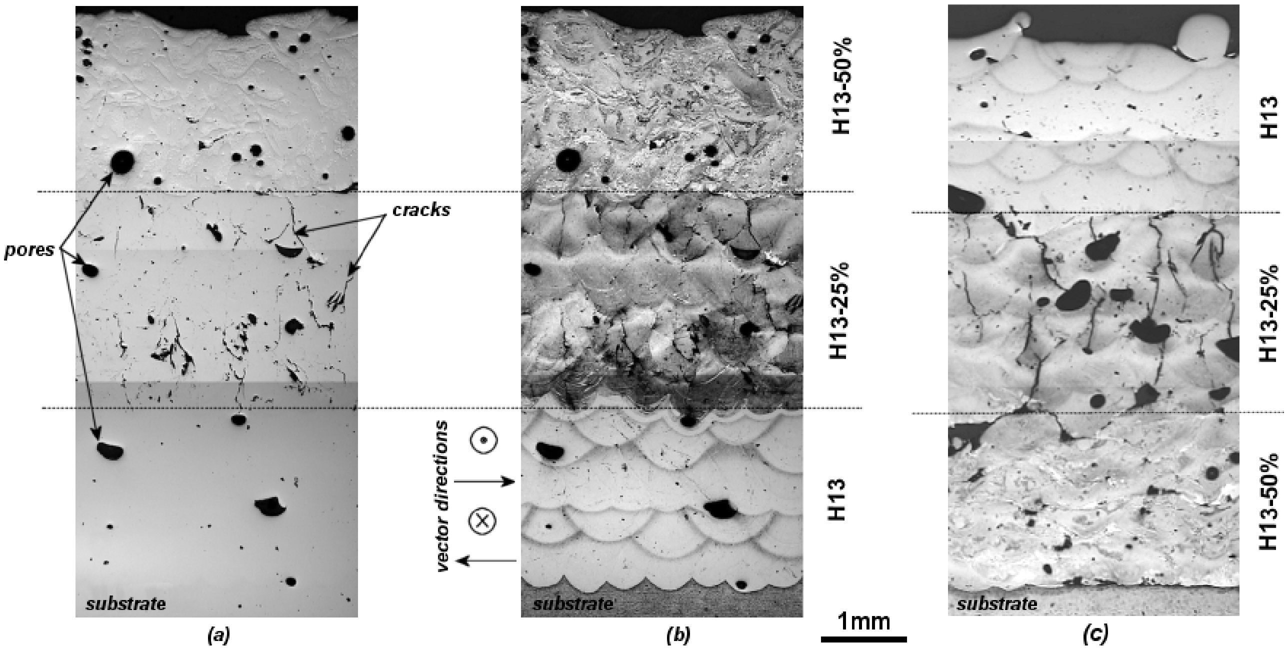
pores
cracks
substrate
(a)
H13-50%
H13-25%
H13
vector directions
substrate
(b)
1mm
H13
H13-25%
H13-50%
substrate
(c)

Figure 5-22. Polished cross section of z-graded specimens: (a) only polished, (b) and (c) etched.

The pure H13 had a microstructure of dendrites orientated to the direction of the centre of the laser spot. This was due to the high intensity from the laser and cooling effect from the base material. The dendrites were formed from the supercritical liquidus line after the laser interaction where there was then rapid cooled towards the bottom layer (Brooks *et al* 1999). An EDX analysis indicated a higher percentage of the alloying elements in the interdendritic boundaries (Figure 5-23).

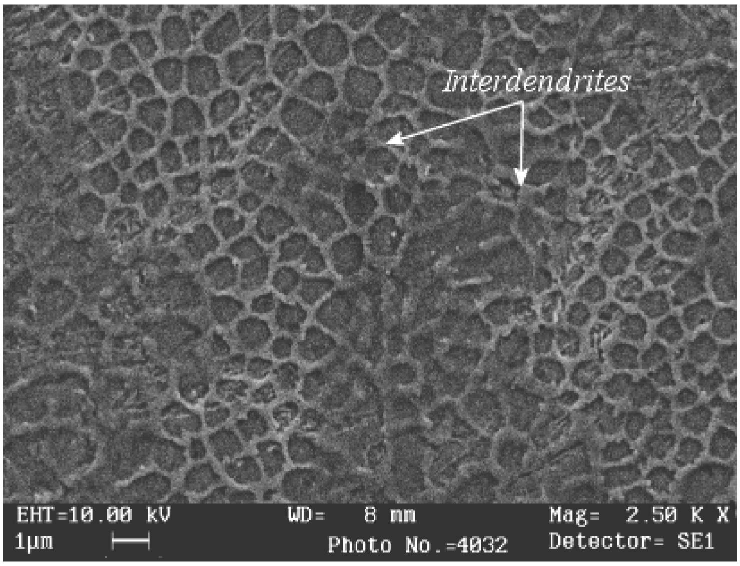
Interdendrites
EHT=10.00 kV
1μm
WD= 8 mm
Photo No.=4032
Mag= 2.50 K X
Detector= SE1

Figure 5-23. Microstructure of the pure H13.

Fine dendrites were also found in the H13-25%Cu region. The EDX analysis showed that the Cu percentage was higher in the dendrite boundaries and comprised 32% of the detectable elements in the composition. In these regions the Fe composition was found to be 61% dispersed in the interdendritic boundaries (see Figure 5-24).

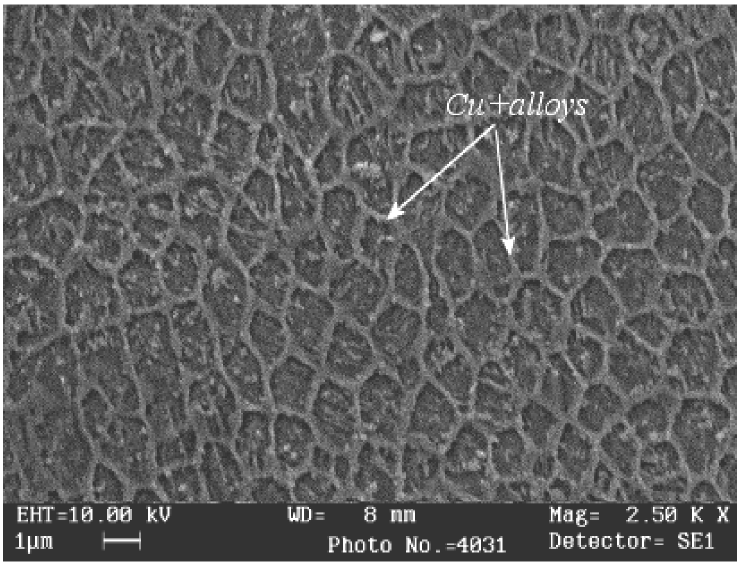
Cu+alloys
EHT=10.00 kV
WD= 8 mm
Mag= 2.50 K X
1µm
Photo No.=4031
Detector= SE1

Figure 5-24. Microstructure of the *H13+25%Cu* composition

The microstructure of H13-50%Cu presented to be a heterogeneous material. It was found very distinctive regions of isolated Cu regions of H13-Cu as found for the 25%Cu composition. In Figure 5-25, these regions are indicated. The interesting thing is the fact that spherical particles of H13-Cu were found formed in isolated Cu areas and isolated Cu regions, most of then with spherical shape, were found in the H13-Cu regions. The EDX analysis showed that spherical particles inside the Cu regions are formed by Cu and H13.

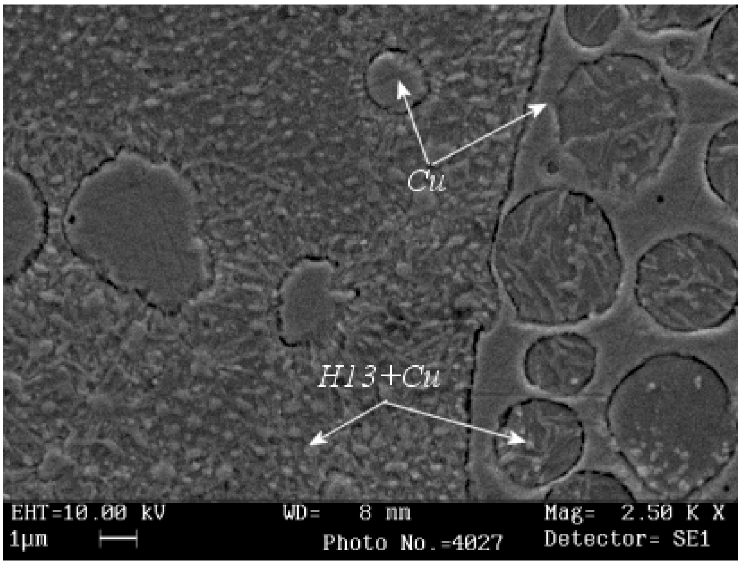
Cu
H13+Cu
EHT=10.00 kV
WD= 8 mm
Mag= 2.50 K X
1µm
Photo No.=4027
Detector= SE1

Figure 5-25. Microstructure of the H13-50%Cu composition.

Comparing both specimens built with different sequence order of compositions it was not found changes in the microstructure obtained in all tree compositions. The only difference, as commented previously was the lower laser penetration in the substrate with the H13-50%Cu powder to start to build the specimen.

5.5.3. Discussion on the z-gradient

The pure H13 powder presented a homogeneous structure but as it was solidified quickly from the supercritical temperature it was possible that internal stresses were retained in the structure. According to Dawes (1992), the defects in welds are porosity, solidification cracking, cold cracking, heat affected zone (HAZ) liquation crack and stress corrosion cracking. Porosity occurs when bubbles of gas are trapped in the bead after solidification. Solidification cracking can occur when the material has low ductility and subject to a high stress concentration. During solidification, between the solidus and liquidus lines, the alloy is incompletely solidified and is a brittle mass. The contraction of the material leads to a centralized crack in the laser bead. As H13 is a high carbon content steel, the carbon also contributed to martensite formation, which is fragile and has low ductility. Nevertheless, cracks in pure H13 were negligible and only noticeable in the last layer added, in small quantities and short in length. These cracks could be post processed by re-melting the last layer with less energy density or removing during post-processing for complete part finishing.

In the 25%Cu blend, many cracks were observed due to the thermal stress and rapid cooling during solidification. In this case, the added copper increased the thermal conductivity of the melt pool. The heat flows through the parabolic melt pool solidifies finally at the centre line of the bead. This phenomenon was noticeable as the dendrite growing directions were aligned with the heat flow. The material in the core of the melt pool solidified and the restrained contraction produced the crack from the stress generated (Figure 5-26).

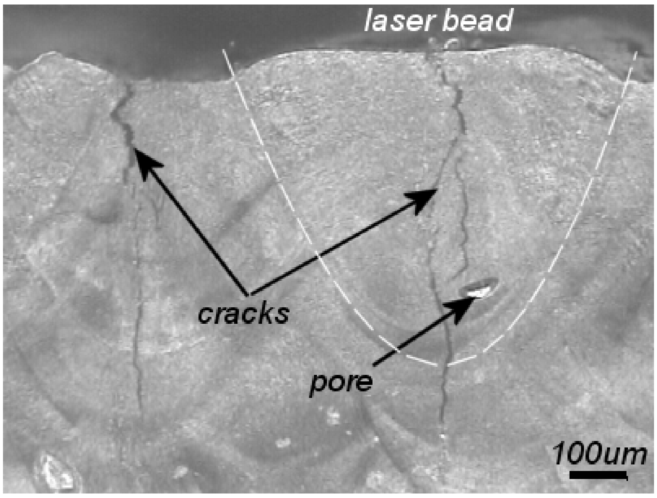

Figure 5-26. Cracks and pores formed in the cross section of a specimen made of H13+25%Cu.

With the high percentage of Cu, a heterogeneous structure was formed. There were areas that consisted mostly of a Cu matrix that had small isolated spherical areas of H13 and Cu. There were then areas that consisted mostly of a H13 and Cu matrix with small isolated spherical areas of Cu. The high percentage of Cu added might have promoted a better solidification and possibly stress relief as it has high ductility and solidifies after the H13. The inhomogeneous structure of the 50%Cu blend produced lower number of cracks but it might have caused some noticeable number of pores, higher than the other two powder compositions fused.

The cracking effect may be reduced by preheating the powder and controlled temperature building chamber. Although, Su (2002) found the laser processing parameters appropriate for the fusion of H10 power, they generated a large amount of plasma that lead to high mass losses due to the spatter effect. This occurrence of cracks and pores could be critical for the final FGM components.

5.6. Discussion on building parameters

The experiments proved that the more appropriate laser scanning strategy was the *refill* strategy. Despite the larger amount of time, it produced the more dense and with less volume missing specimens. This strategy also proved to be the one that had the more homogenous heat distributed over the layer built.

The spaces tested here for the vectors of the strategies showed that the variation observed was not high between 0,5 and 0,6mm. However, the results indicated higher densities for 0,5mm.

The fabrication of a Z gradient of Cu and H13 proved no major problem in the interfaces between the gradients steps. Nevertheless, the microstructure analysis showed that for compositions with 25%Cu cracks were present. So, the addition of copper had influence over the number of defects found in the cross sectioned specimens.

The overall conclusion was that laser processing parameters should be optimized/improved to reduce microstructure defects. Also by optimizing the laser parameters, the spattering effect that caused major lost of powder from the layers during the laser fusion process could be reduced.

Chapter 6

Selective laser fusion laser parameters experiments

"...Hoje eu desafio o mundo
sem sair da minha casa
Hoje eu sou um homem mais sincero
e mais justo comigo
Hoje eu desafio o mundo
sem sair da minha casa
Hoje eu sou um homem mais sincero e
mais justo comigo

Podem os homens vir que
nao vao me abalar
Os cães farejam o medo,
logo não vão me encontrar
Não se trata de coragem
Mas meus olhos estão distantes
Me camuflam na paisagem
Dando um tempo, tempo, tempo
pra cantar

Me deixa, que hoje eu tô de
bobeira, bobeira
Me deixa, deixa, deixa
que hoje eu to de
bobeira, bobeira..."

O Rappa – Me deixa

6. Optimization of laser process parameters

The effect of building parameters was shown in the previous chapter. The influence of strategies and vector spaces were evaluated with the objective to increase the density of the obtained specimens. With the use of the correct strategy, it was possible to reduce the amount of porosity and to correct the volume reduction caused by spattering. Nevertheless, in the experiment in Chapter 5 it was shown that cracks were present in the Cu-H13 blends. Cracks are prejudicial to the parts strength as they concentrate stress, reduce the effective cross-section area and are pre-fault for the material. As seen previously, the cracks reduction had to be studied not only by building parameters (strategies and vector spacing) but mainly by the laser processing parameters.

The laser parameters were kept constant to avoid high variation and to have better input and output from the previous experiments. In this section, laser parameters of pulse energy, pulse width, repetition rate and scan speed were evaluated for a H13-Cu powder composition. These were the laser parameters that were possible to adjust in the JK 701.

As the amount of Cu changes the properties of the powder blend, it was expected that each H13-Cu blend would need a specific set of laser parameters to reduce the defects of the specimens. So, each of the following sections explores the optimization of the laser parameters for the H13-Cu blends used in this work.

6.1. Laser processing parameters for H13-12.5%Cu composition

In this section, the powder used was the bimodal blend of H13-12,5%Cu presented in section 4.3. Based on the design of experiments, this investigation was carried in two steps. In the first approach, a preliminary experiment using Box-Behnken design was used to explore how these parameters affected the results over a determined range. Then, a second experiment using full factorial analysis was performed to optimize these parameters to the lowest values of defects, pores and cracks, in the specimens. Both statistical designs are part of the Response Surface Method (RSM) which utilizes the data collected from the experiments to plot a surface of interaction between the tested variables.

6.1.1. Manufacturing method and specimens dimensions

For both Box-Behnken and factorial analysis the way specimens were built and analysed were the same expect for the laser parameters variation. The specimen consisted on small parallelepiped with dimensions of 6x6mm square and 4mm high. The layer thickness used was 250µm. The refill scan strategy with vector spacing of 0,5mm was used in order to reduce porosity and hence increase the density as it had been proved in the previous chapter to be effective. This experiment was conducted using the pulsed high power Nd:YAG laser and argon shield gas at 15l/min was used to reduce oxidation and protect the lens and the layering method was provided by the moving platform and feedhopper described in section 4.1.2.

After the specimens being built, they were cross-sectioned in the x-y plane, mounted, ground and polished. To avoid differences in polishing, the specimens were polished on an automatic polishing machine. Images of each cross-section were taken using optical microscopes and analysed using ImageTool Version 3 software (UTHSCSA, 2004). The analysis was carried as commented in section 4.4.4. With the contrast obtained from the pictures the percentage amount of defects, cracks and pores, could be obtained for each one of the specimens.

6.1.2. Box-Behnken experiment

6.1.2.(a). Methodology

The Box-Behnken experimental design was chosen to plan the experiments as it was considered appropriate for the limited number of samples that need to be produced compared to various other design of experimental methods (Montgomery, 2001). Table 6-1 shows the experimental design summary. The lower and higher values for the experimental factors had been chosen based on previous work by Su (2002) and used in the earlier experiments. The results from the Box-Behnken design were analysed under 95% of confidence interval.

Table 6-1. Design of the Box-Behnken experiment summary.

Design Summary	
Design class	Response surface
Design type	Box-Behnken
Number of experimental factors	4
Number of responses	2
Number of runs	81
Number of degrees of freedom	58
Randomised	yes

Factors	**Lower value**	**Higher value**	**Units**
Pulse energy	5	10	J
Pulse width	4	10	ms
Repetition rate	10	20	Hz
Feedrate	2,67	5,00	mm/s

Responses	**Units**
Cracks and pores	%
Peak power	kW

The chosen response variables were the cracks and pores (cross section area defects) and the pulse peak power. As peak power is defined by direct relation between pulse energy divided by pulse width (see section 4.1.3, equation 4.04), no measurement was necessary. Instead, it served as target to reduce plasma and spatter during the laser interaction.

6.1.2.(b). Box-Behnken results and discussion

Table 6-2 presents the analysis of variance (ANOVA) with all factors and their respective values. The ANOVA of the Box-Behnken experiment shows that the significant factor that affected cracks and porosity was the pulse energy as it was the only factor with a P-value under 0,05.

Table 6-2. Analysis of variance for the cracks and pores results of Box-Behnken design.

Source	Sum of Squares	Degrees of Freedom	Mean Squares	F-ratio	P-value
A: Pulse energy	89,7048	1	89,7048	4,85	0,0309
B: Pulse Width	0,0094	1	0,0095	0,00	0,9820
C: Repetition rate	2,5719	1	2,5719	0,14	0,7103
D: Feedrate	8,9539	1	8,9539	0,48	0,4887
AA	3,6173	1	3,6173	0,20	0,6596
AB	21,023	1	21,0230	1,14	0,2899
AC	6,0031	1	6,0031	0,32	0,5706
AD	14,3787	1	14,3787	0,78	0,3808
BB	67,7555	1	67,7555	3,67	0,0597
BC	4,5686	1	4,56865	0,25	0,6206
BD	11,6787	1	11,6787	0,63	0,4294
CC	3,8205	1	3,8205	0,21	0,6508
CD	0,4986	1	0,4986	0,03	0,8700
DD	0,7932	1	0,7932	0,04	0,8365
Total error	1275,23	69	18,4816		
Total (corrected)	1518,68	83			

As some of the factors have little effect on the modal (have a high P-value), presented low effect, these less significant sources were excluded to perform the regression analysis. This was performed with respect to the hierarchy of factors. The factors that were excluded from the analysis were the quadratic factors of AA, CC and DD and the interaction factors of AC, BC and CD. Based on this analysis, the regression coefficients for the estimation of the cracks and pores were found and the equation of the fitted regression model achieved (equation 6.01).

$$\begin{aligned} Cracks\,\&Pores &= 16{,}93 + [2{,}02 * A] - [2{,}78 * B] - [0{,}06 * C] + \ldots \\ \ldots &+ [0{,}0024 * D] - [0{,}18 * A * B] - [0{,}0064 * A * D] + [0{,}20 * B^2] + [0{,}0055 * B * D] \end{aligned} \quad (\%) \text{ Eq. } 6.01$$

Using this regression model, the parameters to minimise cracks and pores were improved, pointing new values of the parameters to be evaluated. These improved parameters were: feedrate of 5mm/s, repetition rate of 20Hz, pulse width of 7,21ms and pulse energy of 10J. These parameters resulted in a reduction of cracks and pores from 15,32% to 7,19%. The defects, cracks and pores, were considerably lower for a combination of medium pulse width and high pulse energy. The combination of feedrate and repetition rate indicated that better results could be achieved at higher repetition rate and feedrate. It should be noted that the pulse overlap (section 4.1.3, equation 4.05) for the combination of 20Hz and 5mm/s increased and consequently increases the energy input. Nevertheless, these two factors had significantly less influence than the pulse energy and width. Plots of each factor and its effects on cracks and pores were presented in Figure 6-1. In order to avoid errors all the factors and interactions must be considered carefully. In each of these graphs, the factors that were not plotted were kept at their central values. The pulse width behaviour in Figure 6-1 shows that the quadratic effect is more significant than as a single factor in the ANOVA.

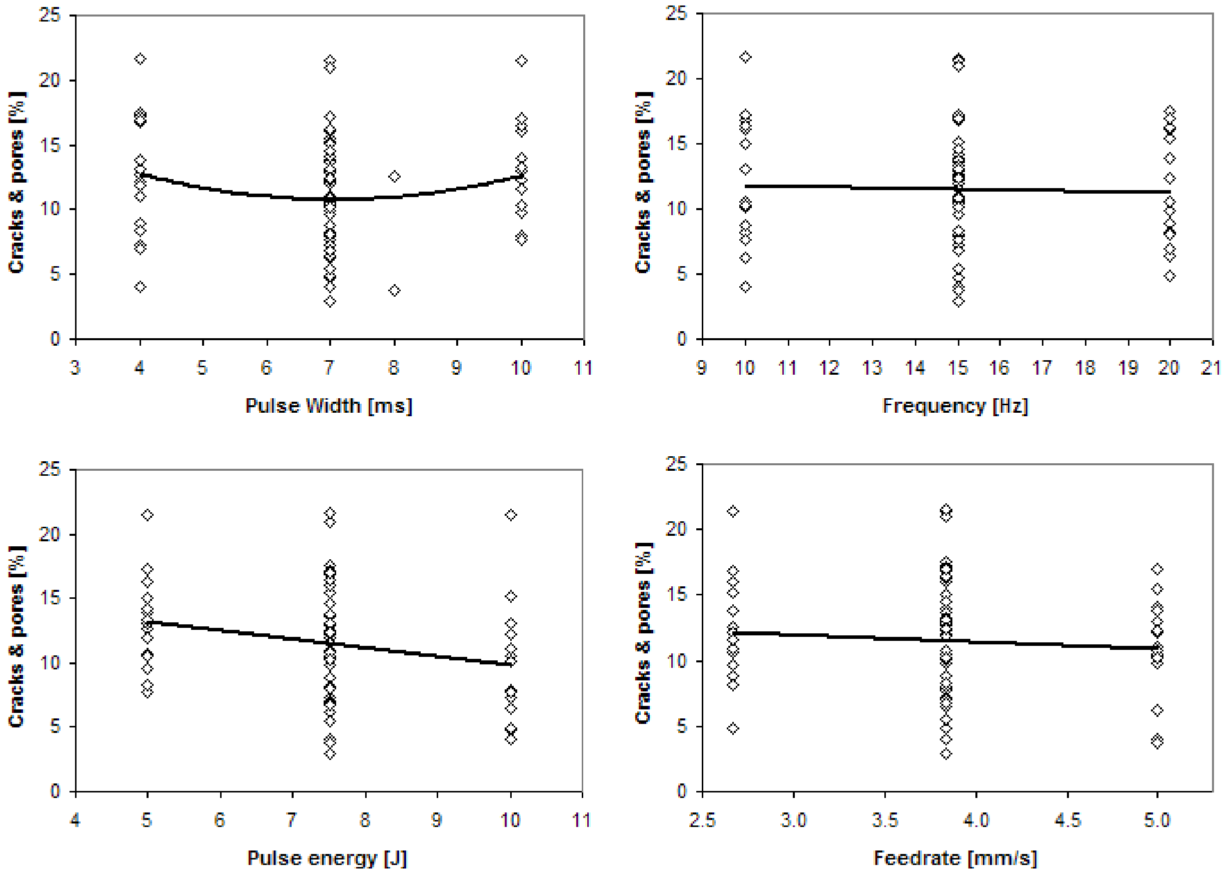

Figure 6-1. Main effect plots for cracks and porosity.

By fixing the values of the feedrate at 5mm/s and the repetition rate at 20Hz, it was possible to plot the cracks and pores response surface which is shown in Figure 6-2. The graph shows how cracks and pores were higher for lower pulse energies. The defects were high also at low pulse energies and high pulse width. Therefore, lower peak power values could increase defects. For higher peak power values, e.g. high pulse energy and lower pulse width, better results could be observed. In general, the graph in Figure 6-2, shows that it is possible to obtain fewer defects with higher pulse energies and with a wide range of pulse widths.

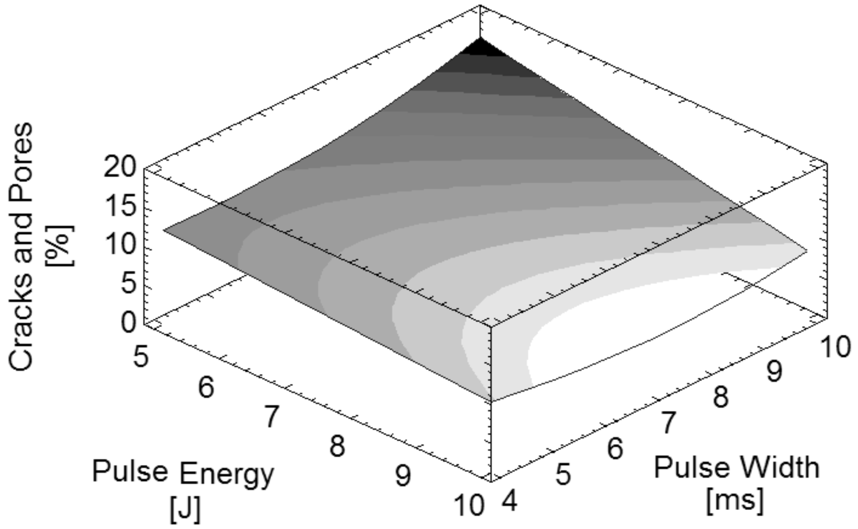

Figure 6-2. An estimated cracks and pores response against pulse energy and pulse width at fixed pulse repetition rate (5mm/s) and repetition rate (20Hz).

Figure 6-3 plots the contours of the percentage of pores and cracks over the peak power curves with constant values as a function of the pulse energy and pulse width for repetition rate of 20Hz and feedrate of 5mm/s. Due to the problem of spatter it is important to minimise peak power. Therefore, to obtain minimum defects, this graph shows that the best combinations of parameters are at the top-right corner of the graph (high pulse energy and pulse width and low peak power around this region). Figure 6-4 shows cross-sections of samples obtained with various combinations of pulse width and pulse energies. It can be seen that cracks and pores were reduced at high pulse width and high pulse energy.

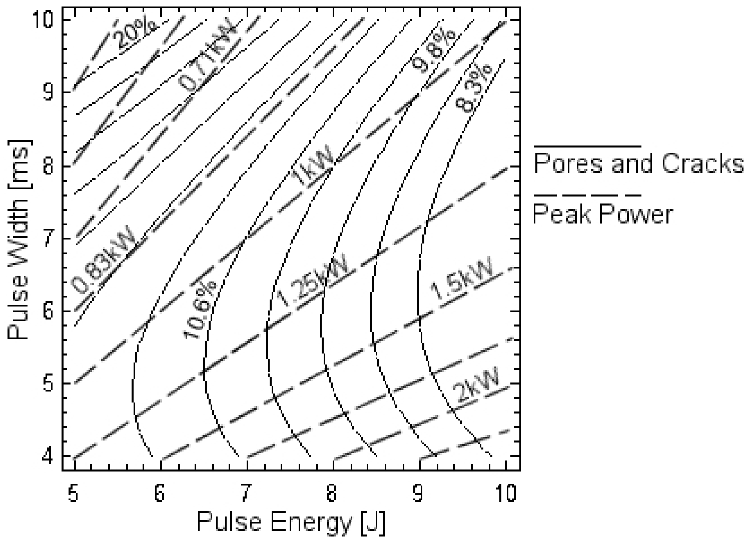

Figure 6-3. Percentages of cracks and pores contour in function of pulse energies and pulse width.

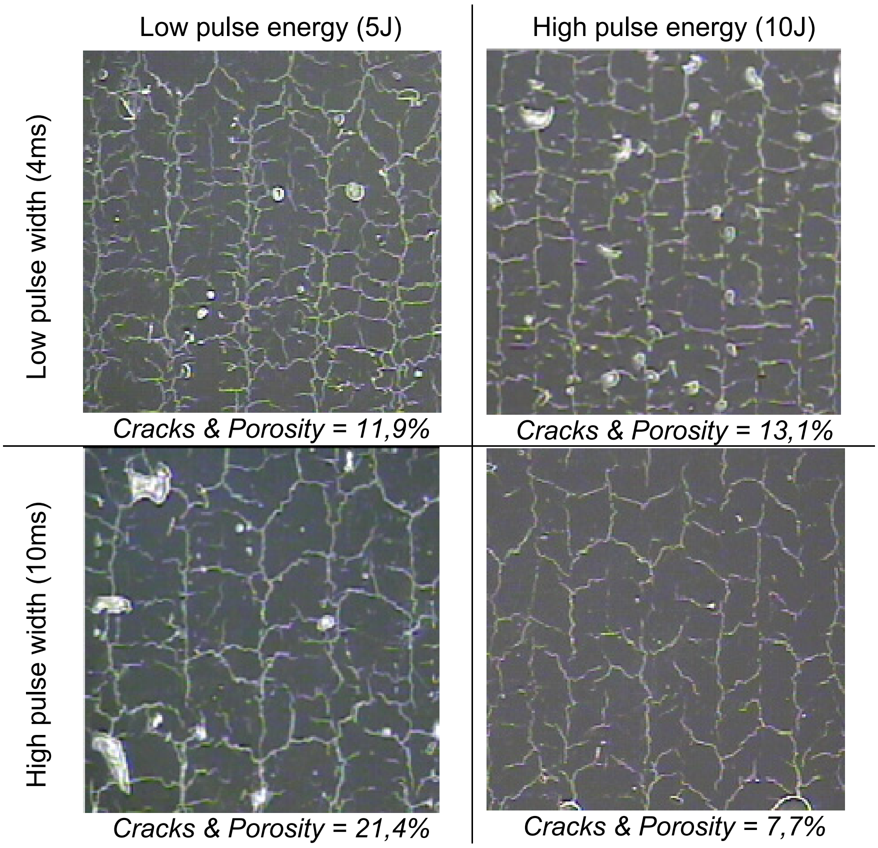

Figure 6-4. Different cross-sections obtained with combinations of pulse energy and width.

6.1.3. Factorial experiment

6.1.3.(a). Methodology

After obtaining and analysing the results of the Box-Behnken experimental design, a 3-level factorial experiment was designed for further investigation and optimisation. The Box-Behnken analysis is more suited for experiments with a larger number of variables, whereas, Factorial Analysis is simpler and easier to use. The 3-level design also improved the accuracy of the response curve as more combinations were made and repeated. So, in this design, the pulse repetition rate and feedrate were kept constant (Repetition rate: 20Hz; Feedrate: 5mm/s). Therefore, using equation 4.05 (section 4.1.3), the pulse overlap was kept fixed at 67%. The values were chosen based on the best results achieved in the Box-Behnken experiment. The best combination of pulse energy and pulse width that could reduce defects was investigated. The low and high values for pulse energy were fixed he same as in the Box-Behnken analysis and the mid level value was fixed at 7,5ms. To reduce the peak power further and hence reduce problems with spatter a larger pulse width between 11 to 20ms (20ms was the system limit) was investigated. The objective was to increase the interaction time between the laser and the melt pool. Higher pulse width at fixed pulse energy produced lower peak power and subsequently produced less plasma. All procedures to produce and analyse the samples were repeated as described before. A summary of the factorial analysis design is presented in Table 6-3.

Table 6-3. Summary of the multi-level factorial experiment.

Design Summary	
Design class	Multi-level Factorial
Design type	3 levels
Number of experimental factors	2
Number of responses	2
Number of runs	45
Number of degrees of freedom	35
Randomised	Yes

Factors (*)	**Lower level**	**Mid level**	**Higher level**	**Units**
Pulse energy	5	7,5	10	J
Pulse width	11	16	20	ms

Responses	**Units**
Cracks and pores	%
Peak power	kW

(*) all under Repetition rate: 20Hz; Feedrate: 5mm/s.

6.1.3.(b). Factorial experiment results

In this analysis, as all the factors and interactions were shown to be highly significant, none of these factors and interactions were excluded. The ANOVA pointed that the main significant factors were the pulse energy and pulse width as shown in Table 6-4. This is particularly interesting when compared to the significance obtained by the pulse width in the previous result from the Box-Behnken design. In Table 6-2, the main pulse width factor was not considered significant; however, the quadratic effect shows it is highly significant. On the other hand, Table 6-4 shows that the pulse width was the second most important factor after pulse energy. As there were only two factors to evaluate, it was possible to reduce the variation in the results.

Table 6-4. ANOVA of the multilevel factorial experiment.

Source	**Sum of Squares**	**Degrees of Freedom**	**Mean Squares**	**F-ratio**	**P-value**
A: Pulse energy	118,93	1	118,93	22,03	0,0000
B: Pulse Width	64,16	1	64,16	11,88	0,0013
AA	9,29	1	9,29	1,72	0,1967
AB	9,14	1	9,14	1,69	0,2004
BB	0,04	1	0,04	0,01	0,9319
Total error	226,74	42	5,40		
Total (corrected)	422,41	47			

Having no factor excluded, the regression analysis generated the coefficients of the equation to plot the cracks and pores response surface over the pulse energy and pulse width. Equation 6.02 presents the regression coefficients of the model from the factorial analysis.

$$Cracks\ \&Pores = 30{,}58 - [3{,}93 * A] - [0{,}65 * B] + ... \\ ..... + [0{,}15 * A^2] + [0{,}06 * A * B] - [0{,}0031 * B^2] \quad ; \quad (\%) \qquad \text{Eq.6.02}$$

The surface response obtained from this multi-level factorial experiment is plotted in Figure 6-5. The graph, plotted based on the regression analysis from the results obtained, showed that less defects were obtained with larger pulse widths and higher pulse energy. It should be noted that the estimate percentage of cracks and pores at 5J and 11ms was much lower than at 5J and 10ms in Figure 6-2. This was because Figure 6-5 represents a model with only two parameters which results in much less experimental noise and made the model more accurate.

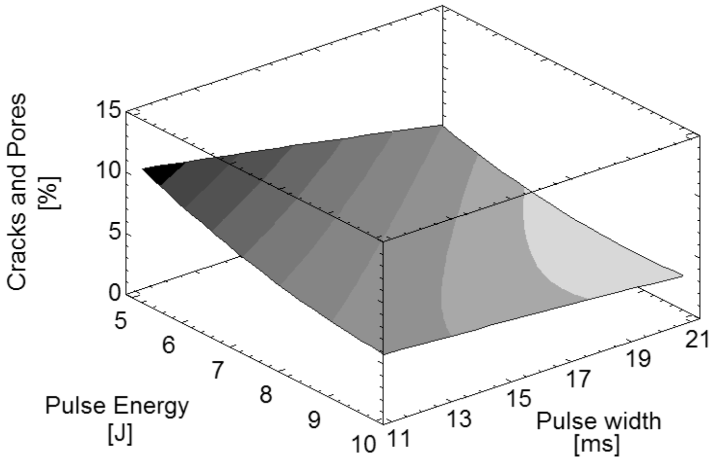

Figure 6-5. An estimated crack and pores response against pulse energy and pulse width at fixed pulse repetition rate (5mm/s) and repetition rate (20Hz).

Further analysis had to be made over the area defects found. As it was desirable to have low peak power to avoid spattering and low percentage area defects a multiple response optimization. The optimization for lower peak power and defects is plotted in greyscale regions in Figure 6-6. The lighter the area the better is the desirability achieved by low peak power and low area defects. In this case, the weights and impact of the outputs peak power and defects were kept equal. Iterative simulations changing these values showed that no significant changes occurred in the regions. Of course, the target was to maintain the expected defects area lower than 5%. So, the optimum values for pulse energy and width were 9,16J and 20ms respectively. The estimated percentage area defects for these two values was 3,58% at 0,45kW of peak power.

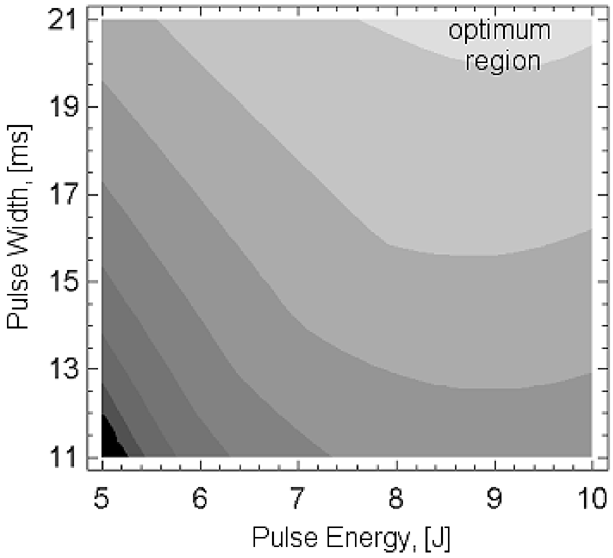

Figure 6-6. Estimated response surface contours for minimum peak power and area defects for the H13-12,5%Cu composition.

6.1.4. Overall Results and Discussion

In the Box-Behnken analysis, it indicated that larger pulse widths, even at lower peak power, reduced the amount of defects. Figure 6-2, 6-5 and 6-6 reflected the physical phenomenon that was involved during the laser fusion process of H13 and Cu powders. Lower peak power did not penetrate the new powder layer and bond it to the previously fused layer. The poor bonding between the new layer and the previous layer lead to balling. Nevertheless, in the factorial analysis, this effect was found to be smaller than in the Box-Behnken analysis. Possible cause to this was the higher variability in the Box-Behnken.

In the Box-Behnken experiment the adjusted R-squared statistics test, which performs a relation between the sum of squares obtained from the model and the sum of squares of the total corrected was 0,056. This means that the model explained only 5,6% of the variability. For the factorial design, 41,5% of the variability was explained by the model. Although the values for testing the variability were found to be low, the physical-chemical process was very complex. The results in the factorial analysis indicated the same idea from the Box-Behnken experiment: larger pulse widths reduced the amount of defects. The optimum parameters obtained from this experiment compared with the previous optimised parameters are summarized in Table 6-5.

Table 6-5. Comparison between the parameters used before and after the RSM with H13-12,5%Cu.

Parameter	Original	Box-Behnken	Factorial analysis	
Feedrate, v	3,33	5,00	5,00	mm/s
Repetition rate,f	10	20	20	Hz
Pulse energy,E	10,00	10,00	9,16	J
Pulse width,w	5,00	7,21	20,00	ms
Energy density,E_ρ	37,5	50,0	45,0	J/mm2
Average power,P	100,00	100,00	180,00	W
Peak power,P_{peak}	2,00	1,39	0,45	kW
Pulse overlap, Δp	53,7	67,1	67,1	%
Cracks and pores	15,32	7,19	3,58	%

Figure 6-7 shows the overall comparison between the default values (optimised in previous work from Su, 2002, to H10 tool steel) and the optimized parameters using RSM methodology. Transversal cracks (orthogonal to the laser scan direction) were reduced with the improved parameters. The cracks along the scan direction were found to be reduced as well. It is also perceptible that only part of the scan direction cracks was formed or present with the improved parameters. In Figure 6-7, lines and dots identify the laser scans. The lines (F) are the scan before the refill and the dots (R) are the vectors after the refill procedure. With the optimized parameters, cracks in the vectors before refilling (F vector) were not found.

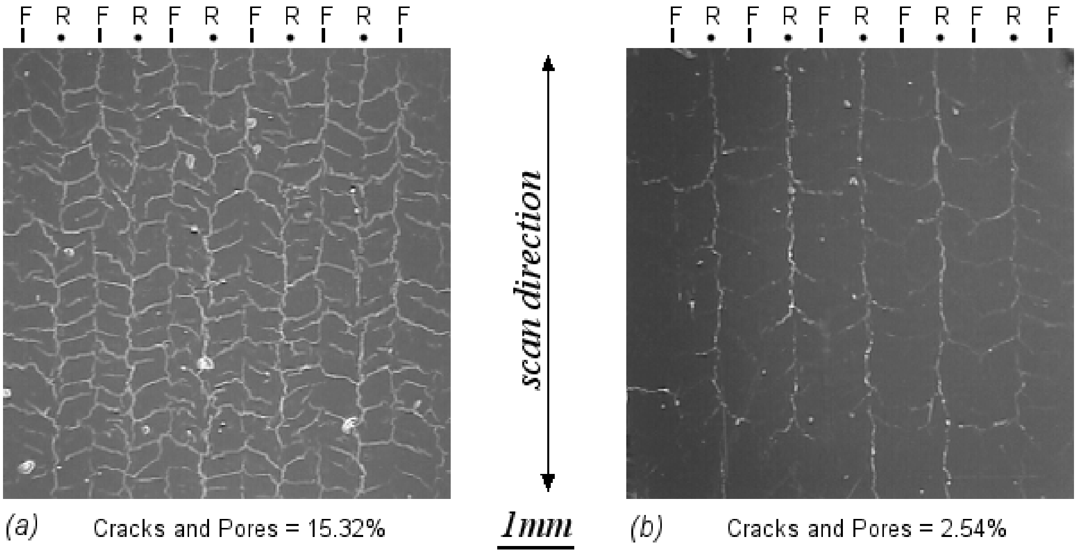

(a) Cracks and Pores = 15.32%

(b) Cracks and Pores = 2.54%

Figure 6-7. Cross sections of specimens obtained using (a) original and (b) optimized parameters (factorial analysis experiment).

6.1.5. Discussion

The response surface method proved to be useful for reducing the overall defects found in the processing of H13 and 12,5% Cu blends. Although the variability found in the first experiment was high, it was satisfactory for plotting the response surface and pointing out the new range of parameters to be tested. The second factorial experiment had less variability and the same phenomena for the reduction of defects was found.

Using larger pulse widths was more successful for producing better parts as reduction of cracks and pores was perceptible. For comparison, the original parameters (v: 3.33mm/s; f: 10Hz; E: 10J; w: 5ms, E_ρ: 37,5J/mm^2; P: 100W; P_{peak}: 2kW; Δ_p: 53,7%) showed that the defect measurements were around 15% of the cross section area of the specimens. For the final optimal results found in the factorial analysis, defects around 2-3% of the area were found (v: 5mm/s; f: 20Hz; E: 9,16J; w: 20ms; E_ρ: 45J/mm^2; P: 180W; P_{peak}: 0,45kW; Δ_p: 67,1%). The specific energy and average power had increased but the pulse peak power was reduced to less than 25% of the original value. With 20ms of pulse width, other limits of the system were used. The pulse energy for larger pulse width also can not be too high or the Nd:YAG diode overheat. The same effect happened with the repetition rate of the pulses. As more pulses were flashed with large pulses with high energy it also contributed to heat the diode. So, the exploration of higher frequencies was not possible.

As peak power had been decreased, the plasma and spatter was reduced considerably. As plasma and spatter, causes instabilities in the process that can affect the quality, the results obtained from the factorial experiment had shown that lower peak power provides a more stable process. Another source of variation during the process was the glass lens protection getting dirty by debris from the spatter. The effective energy transferred to the powder bed could be reduced with the glass being partially blocked by the debris and needed to be replaced frequently. As under the low peak power condition the spatter and plasma was low and hence the glass was not affected by debris, the energy coupling with the powder remained constant during the process. This contributed to the stability and reduced variations.

One important aspect is the use of temperature controlled environment and preheated substrates. Various references sources, pondered that tool steel should be welded with controlled temperature to avoid cracking (Uddeholm, 2004, Dawes, 1992). Other issues such as enclosed shield gas environment (to avoid oxidation), improved care with moisture and contamination could produce results. Moisture is a hydrogen promoter in the melted pool causing cracks and trapped bubbles (Dawes, 1992; Steen, 1991).

6.2. Laser processing parameters for H13-25, 37,5 and 50%Cu compositions

The previous experiment showed that it was possible to reduce cracking and pores formation for H13-12,5%Cu. Nevertheless, this research concerns building gradients that involves other H13-Cu compositions. As commented previously, the different compositions of H13-Cu had different reflection and the energy density necessary to fuse the material had to be optimized to compensate this. So, the laser parameters optimization is explored in this section for the compositions of 25, 37,5 and 50% of Cu.

6.2.1. Methodology

As in the previous experiment, the optimization of the laser parameters were near by the limits of the laser system, repetition rate and feedrate were kept constant. This was a practical assumption as for any numerically controlled system it would be difficult to fuse a gradient structure using different scan speeds and repetition rates. Also, the changing in the feedrate and repetition rate would have changed the pulse spot overlap. Thinking in the continuity of the surface roughness, the best option would be to have the same overlap to all composition of H13 and Cu. For all experiments in this section, repetition rate was set to 20Hz and feedrate to 5mm/s. Again, the combination of speed and frequency gave a pulse overlap of 67,1%.

The powders used were the bimodal powder compositions of H13 and Cu of 25, 37,5 and 50% described in section 4.3. Each powder was used to build specimens and were analysed individually. The procedures for building and analysing the specimens were all the same. Refill strategy with 0,5mm of scan vector spacing and layer thickness of 250µm was used. Specimens were 6x6x4mm and an Ar flow assisted the building at room temperature.

As only two variables were explored in this section, pulse energy and pulse width, the statistical design was the same used in the second part of the previous experiment (section 6.1.3). Again, the factorial analysis was used with three levels for each variable but a different number of runs and blocks were performed for each material composition. In Table 6-6, the design summary for each material composition is presented. The main difference between the compositions is that 25%Cu had 16 runs, 37,5%Cu had 32 runs and 50%Cu had 48 runs performed. This was made to evaluate the variability of the results for each composition and to see if the variability could be reduced by increasing the runs in the experiments. All experiment was analysed a confidence level of 95%.

Table 6-6. Factorial analysis design summary for the powder mixtures.

Design Summary			
Design class	Multi-level Factorial		
Design type	3 levels		
Number of experimental factors	2		
Number of responses	2		
Cu Percentage	**25%**	**37,5%**	**50%**
Number of blocks	4	7	8
Number of runs	16	32	48
Number of degrees of freedom	10	26	42
Randomised	Yes		

Factors (*)	**Lower level**	**Mid level**	**Higher level**	**Units**
Pulse energy	7	10	13	J
Pulse width	10	15	20	ms

Responses	**Units**
Cracks and pores	%
Peak power	kW

(*) all under Repetition rate: 20Hz; Feedrate: 5mm/s.

6.2.2. Results for H13-25%Cu

The ANOVA indicated that two factors had major influence over the results. Pulse energy and its quadratic effect due to the multi-level factorial design affected the cracks and pores into the cross-sectioned area of the specimens. The ANOVA is presented in Table 6-7. In this experiment, the variation found was lower than the 12,5%Cu design and optimization (section 6.1). The R-Squared test value was 58,7% and the adjusted for the degree of freedom was 38,1%. So the model fitted in this case was more accurate than for 12,5%Cu.

Table 6-7. ANOVA table for H13-25%Cu mixture.

Source	**Sum of Squares**	**Degrees of Freedom**	**Mean Squares**	**F-ratio**	**P-value**
A: Pulse energy	14,20	1	14,20	5,81	0,0366
B: Pulse Width	6,62	1	6,62	2,71	0,1309
AA	12,15	1	12,15	4,97	0,0498
AB	1,22	1	1,22	0,50	0,4957
BB	5,19	1	5,19	2,12	0,1757
Total error	24,43	10	2,44		
Total (corrected)	59,15	15			

The estimated surface area for the pulse energy and width is shown in Figure 6-8. The lowest values of defects were estimated to be obtained in the lighter areas of the curve. This indicated that pulse energy should be around 10 to 11J and pulse width at 10ms to obtain an estimated 2,10% of defects. Notice that considering these values the peak power is around 1kW. This results was different from those obtained for 12,5%Cu (20ms and 9,16J).

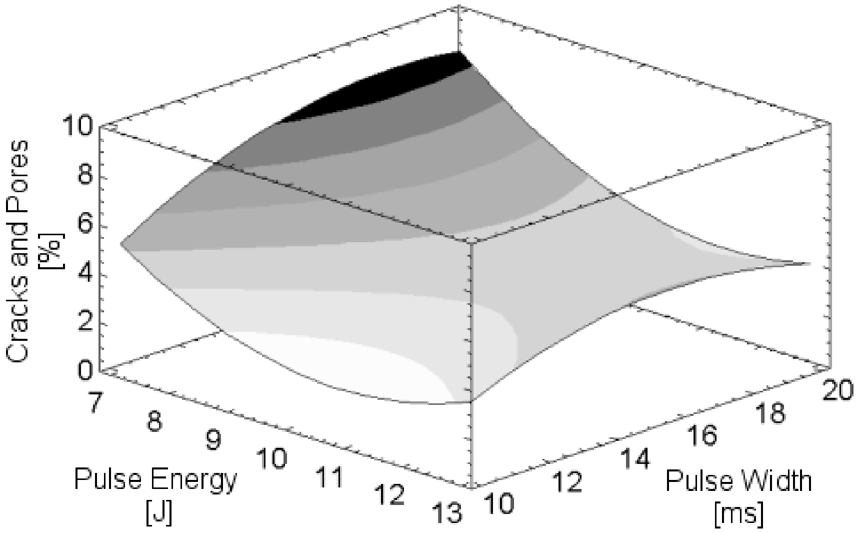

Figure 6-8. Response surface of the area defects against pulse energy and pulse width at fixed pulse repetition rate (5mm/s) and repetition rate (20Hz) for H13-25%Cu.

The multiple response analysis for the reduction of peak power and area defects is plotted in Figure 6-9. This showed that lower peak power could be obtained if larger pulse width were used. The optimum region is formed by the combination of 19-20ms of pulse width and 10-11J of pulse energy. Inside this region, the optimum pulse energy of 10,64J and pulse width of 20ms increased the estimation of the area defects to 3,96%. Nevertheless, this area defect percentage is under the 5% limit target used in the parameters optimization for 12,5%Cu. The peak power optimized was reduced to 0,53kW with these values of pulse energy and width.

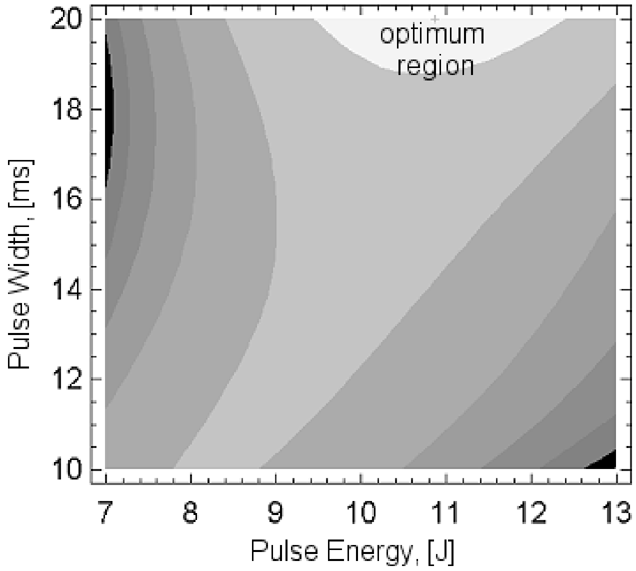

Figure 6-9. Estimated response surface contours for minimum peak power and area defects for the H13-25%Cu mixture.

6.2.3. Results for H13-37,5%Cu

As in the analysis for 25%Cu, the ANOVA table for 37,5%Cu had indicated that pulse energy and its quadratic effect were the factors that greatly influenced process. The P-values of these factors is presented in Table 6-8. Despite the larger number of samples, the variability in this experiment increased. The R-Squared and R-Square adjusted values were 50,36% and 40,82% respectively. Still, the model fitted better than the model in the analysis for 12,5%Cu.

Table 6-8. ANOVA table for H13-37,5%Cu mixture.

Source	Sum of Squares	Degrees of Freedom	Mean Squares	F-ratio	P-value
A: Pulse energy	161,75	1	161,75	14,90	0,0007
B: Pulse Width	39,91	1	39,91	3,68	0,0662
AA	61,91	1	61,91	5,70	0,0245
AB	30,28	1	30,28	2,79	0,1069
BB	2,04	1	2,04	0,19	0,6685
Total error	282,259	26	10,8561		
Total (corrected)	568,673	31			

When plotting the estimated surface curve for the cracks and pores, Figure 6-10, it was noticeable that the defects were higher compared to 25%Cu. The area defects was found to be higher in 37,5%Cu (which is 17%) compared to 10% found for 25%Cu. Yet, the surface had almost the same shape and maintained the tendency for obtaining fewer defects at 10ms of pulse width and 10,79J of pulse energy. The estimated percentage area of defects was 4,46% for these values.

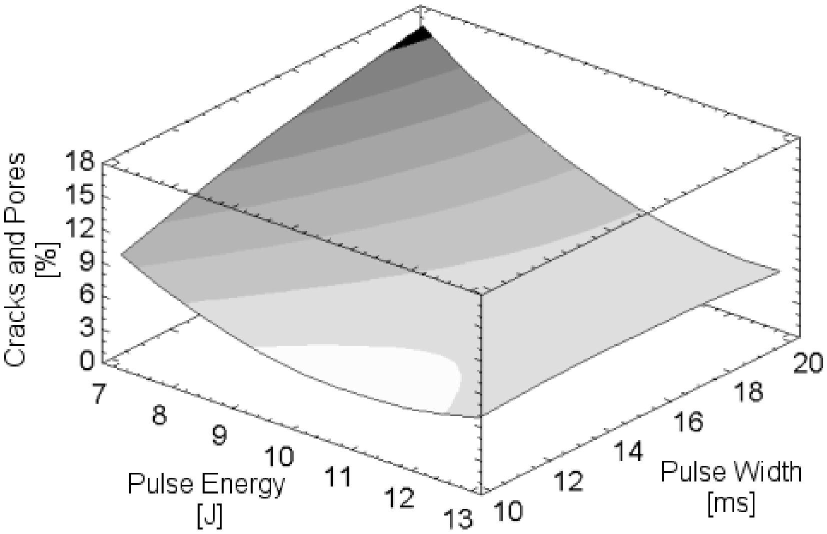

Figure 6-10. Response surface of the area defects against pulse energy and pulse width at fixed pulse repetition rate (5mm/s) and repetition rate (20Hz) for H13-37,5%Cu.

In the previous graph on Figure 6-10, the best region to achieve lower percentage of defects was around 10,23J and 10ms. The peak power in this case was considerable high (1,02kW). For 12,5 and 25%Cu mixtures the optimization of peak power and reduced defects kept the peak power around 0,5kW. As previously noticed on the experiments, the plasma generated by the laser action over the powder bed surface was directly proportional to the peak power. The reduction of the plasma leaded to process stability as the lenses are kept clean over longer periods. This low plasma, maintained the laser energy delivered to the powder constant, as lenses were kept clean and because plasmas it self absorb and diffract the laser beam. The multiple response optimization for achieving minimum defects and peak power was used. The resulted regions for each combination of pulse energy and width are plotted in Figure 6-11. Looking at the regions plotted in Figure 6-11 is possible to identify that the optimum region was larger and even good results could be obtained using larger pulse widths. Considering the variability of the model, it is possible to assume that larger pulse width would gave the same results but with lower peak power.

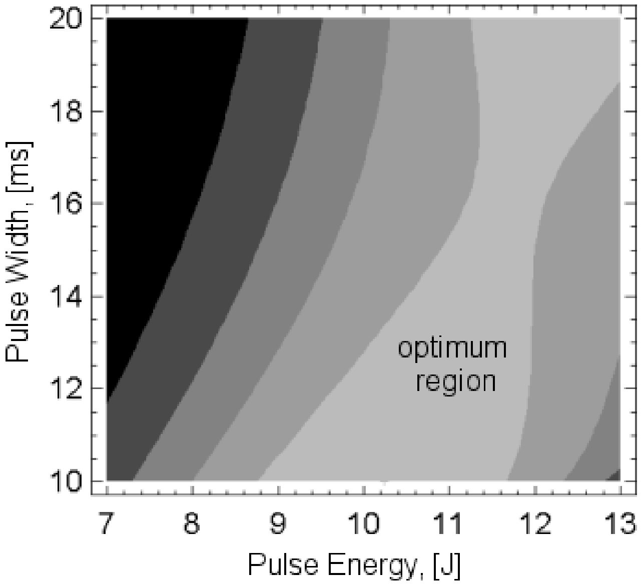

Figure 6-11. Estimated response surface contours for minimum peak power and area defects for the H13-37,5%Cu mixture.

6.2.4. Results for H13-50%Cu

The ANOVA for 50%Cu presented as the significant factors pulse width and pulse energy and its quadratic effect which was the same significant factors for 12,5%Cu. The ANOVA results obtained for 50%Cu mixture is presented in Table 6-9. The model of this mixture had better accuracy than the previous mixtures evaluated. The R-squared test showed that the model explained 57,53% of the variability in the results. The R-squared adjusted for the degree of freedom of the model changed to 52,47%.

Table 6-9. ANOVA table for H13-50%Cu mixture.

Source	Sum of Squares	Degrees of Freedom	Mean Squares	F-ratio	P-value
A: Pulse energy	217,10	1	217,10	25,58	0,0000
B: Pulse Width	197,46	1	197,46	23,27	0,0000
AA	45,77	1	45,77	5,39	0,0251
AB	4,53	1	4,53	0,53	0,4692
BB	18,12	1	18,12	2,13	0,1514
Total error	326,80	42	8,49		
Total (corrected)	839,27	47			

The estimated response surface for the area defects in function of the pulse energy and width is presented in Figure 6-12. As expected, the shape of the curve remained the almost the same showing a strong tendency. For the 50%Cu mixture the lower percentages of cracks and pores were obtained with high pulse energy and small pulse width. The values of pulse width and energy would be 10ms and 12,59J that produced 2,59% of area defects.

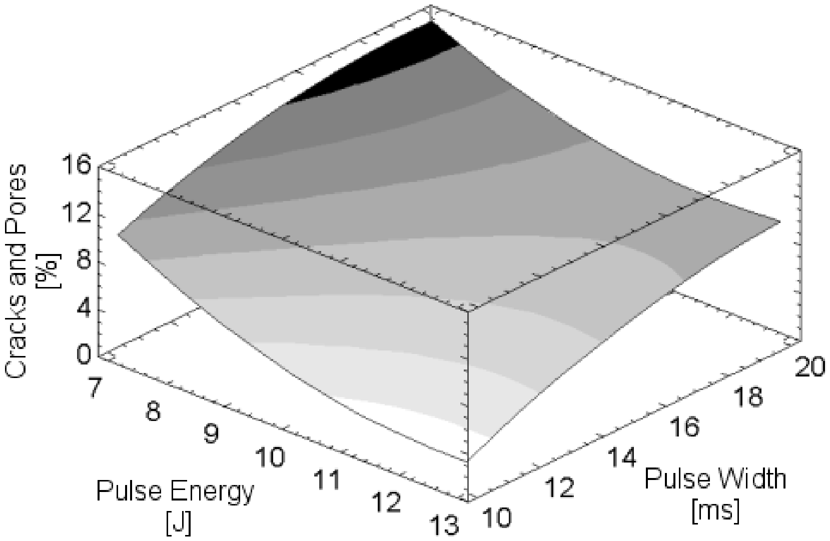

Figure 6-12. Response surface of the area defects against pulse energy and pulse width at fixed pulse repetition rate (5mm/s) and repetition rate (20Hz) for H13-50%Cu.

The calculated peak power for the previously commented pulse energy and width was 1,259kW. As the objective was to reduce both peak power and area defects a multiple response optimization was performed to the H13-50%Cu composition as well. The result of the estimated contours for the best combination of pulse width and energy can be seen in Figure 6-13. The optimum pulse width was 10ms and the pulse energy 11,23J. The minimum percentage area defects for this values was estimated to 3,04% with a peak power of 1,12kW which was high. Differently from the results obtained for 37,5%Cu where the optimum region was more flexible with small variation between small and large pulse width, for 50%Cu the optimum region was restrained to a small combination of parameters as can be seen in Figure 6-13.

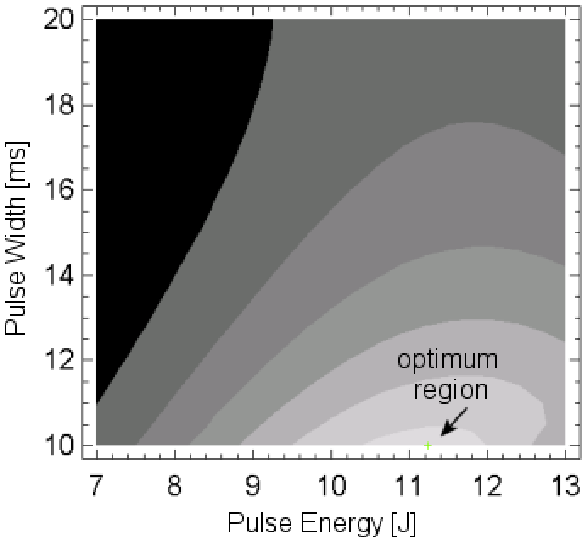

Figure 6-13. Estimated response surface contours for minimum peak power and area defects for the H13-50%Cu mixture.

6.2.5. Discussion on laser processing parameters

The experience obtained with the H13-12,5%Cu composition experiments proved to be valuable to optimize the laser parameters for 25, 37,5 and 50%Cu compositions. Using the RSM method the area defects was considerably reduced. The laser parameters resulted from the optimization are summarized in Table 6-10. The pulse energy remained almost constants. For practical use, it is necessary to comment that no such perfect values with one decimal case can be inserted in the system. In section 4.1.3, it was explained that the way pulse energy was adjusted in the laser control was by adjusting the electric pulse height electric current. So, during the process there were fluctuations of the pulse energy. These fluctuations were perceptible +/- 0,7 joules.

Table 6-10. Summary of the parameters optimization.

Parameter	Original	12,5%Cu	25%Cu	37,5%Cu	50%Cu	
Feedrate	3,33	5,00				mm/s
Repetition rate	10	20				Hz
Pulse overlap	53,70	67,10				%
Pulse energy	10,0	9,2	10,6	10,3	11,2	J
Pulse width	5	20	20	10	10	ms
Energy density	37,5	45,0	53,0	51,5	55,0	J/mm^2
Average power	100,00	180,00	212,00	206,00	220,00	W
Peak power	2,00	0,45	0,53	1,03	1,12	kW
Cracks and pores (predicted)	15,32	3,58	3,97	4,56	3,04	%

For the pulse width, the contrast was evident between the results. Larger pulses were considered better to reduce the defects for 12,5 and 25%Cu. A closer analysis shows that the peak power actually had to be doubled to reduce defects. As the energy density is not dependant of the pulse width and pulse energy remained almost constant it had a small increment. These results allow to consider that the peak power was more important than the energy density in this case of pulsed laser. The results showed a tendency that the reflectivity of Cu increased in the compositions had to be compensated by higher peak powers. The balling effect which Cu was a promoter, could be being diminished by the higher impact caused by the increased peak power. Balling was one of the sources for pores formation in the macrostructure of the specimens. The darker areas of the plots in the estimated surface curves were where more pores were counted. During the analysis of the area defects, cracks and pores were all computed together. So, when the results of higher percentages of defects were actually counting pores that have larger area than cracks.

The fact that cracks still presented in the final results lead to two ideas. The first one is that the system limits were reached and maybe a different laser system with higher frequencies or in continuous mode, with smaller spot size among other things could reduce the cracks formation. The other idea already commented previously is the need for using heated bases and controlled temperature chamber to avoid cracking. It is already common sense in the literature that tool steel welding has to be performed with the part at specific temperature range (325-375^{0}C) (Uddeholm, 2004, Dawes, 1992). A thermocouple placed below the 4mm thick mild steel substrate during the manufacturing of a large specimen showed that temperatures in that region did not went above 100^{0}C.

The feedrate and repetition rate were kept constant after the 12,5%Cu experiment. This was necessary as they were near the limits of the laser system as explained before because of the over heating of the Nd:YAG diode. Higher repetition rates could be used with higher feedrates in the case of thinner layer thickness. Thinner layers require less energy to fuse and to bond to the previous ones. Nevertheless, this requires smaller particles sizes, improved and accurate recoater system. Also, smaller powder particle sizes are more difficult to handle because they tend to agglomerate, to be difficult to spread and require even better control of moisture and contaminants. Higher scanning speeds also require some attention. The Laserdyne system used moves a CNC table for the scanning movement. The ideal system would use computer controlled scanning mirrors to improve accuracy. Therefore, Nd:YAG pulse lasers with high power output are not commonly used with these mirrors configuration.

The statistical experiments performed were useful to optimize the parameters for each one of the H13-Cu mixtures. The variability found had many sources and one of them has to be cited. The specimens grinding and polishing was executed uniformly as possible but it was difficult to have all the specimens with exactly the same surface condition. The tool steel is a hard material and Cu is soft. During the grinding and especially in the polishing care had to be taken for not occulting cracks (e.g. soft copper filling the cracks or pores).

The ideal solution would be to find a set of parameters for each composition of H13-Cu. Unfortunately, this was not practical using the JK701 Nd:YAG laser system. Programming would be of difficult implementation in this system. Also, as a minimum delay of 6 seconds to stabilise the output laser power would be necessary to change from one to other parameter. So, for fusion of small areas/short vectors it would become difficult, inaccurate and unproductive.

Finally, H13 alone had been well processed with the parameters used to fuse it with 12,5%Cu.

Chapter 7

Material characterization of H13-Cu FGM

“Todo dia essa minha labuta
Eu trabalho feito um filha da p...

Se pelo menos eu ficasse mais rico
Mas que nada, eu tô pedindo penico

Domingo eu vou pra praia
Domingo eu vou pra praia
Pode parar tudo eu vou pra praia

Porque na praia eu não tenho que trabalhar
Na praia eu não tenho que me vestir
Na praia eu só tenho que descansar
Na praia eu só tenho que me divertir”

Ultraje a Rigor – Domingo eu vou pra praia

7. Material characterization of H13-Cu

In the previous chapter, estimations of the properties of the materials were calculated based on the rules of mixtures and microstructure analysis. This chapter describes series of experiments that were performed with the intention to characterize the properties from the materials obtained in this work.

7.1. Density analysis

7.1.1. Methodology

For measuring the density of each blend, specimens were built, machined, measured and weighted. Each specimen was manufactured using the refill strategy (as explained in sections 5.1 and 5.2). Layer thickness of 250µm and laser processing parameters of: E: 9J, w: 20ms, f: 20Hz and v: 5mm/s were used. Figure 7-1 shows an example of the planed specimens with the indication of the dimensions. In total, 5 specimens were built, one for each powder mixture.

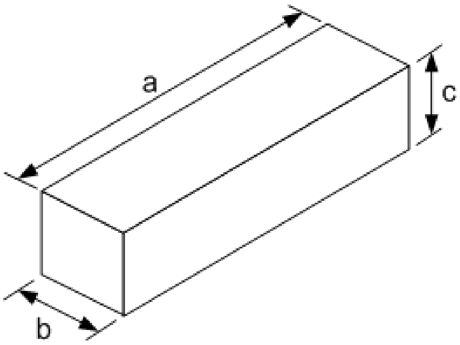

Figure 7-1. Indication of the dimensions of the specimens for density measurement.

After the building was completed, the substrates were ground off and the specimens surfaces were ground to make dense parallelepipeds. This was necessary to avoid errors in the calculation of the volume that could be affected by the roughness of the surface. As a result, the specimens did not presented equal dimensions after grinding. The a, b, c dimensions of the final grounded specimens were around 40, 6 and 9mm respectively. The dimensions of the specimens were measured using a digital calliper for calculation of the volume (V) which is obtained using equation 7.01.

$V = a.b.c$; [cm^3] Eq. 7.01

The three dimensions (a, b and c) were generated by average measuring of each side of the parallelepipeds. For measuring the mass (m), an accurate counter weight analogical balance (Stanton Unimatic, UK) was used. The density was calculated by the equation 7.02 were ρ is the density.

$\rho = m / V$; [g/cm3] Eq. 7.02

7.1.2. Density results

The specimens obtained from the selective laser fusion are shown in Figure 7-2. The substrate, as found from earlier experiments, bended in corners due to the high temperature and the contraction of the specimen during the and after the laser processing.

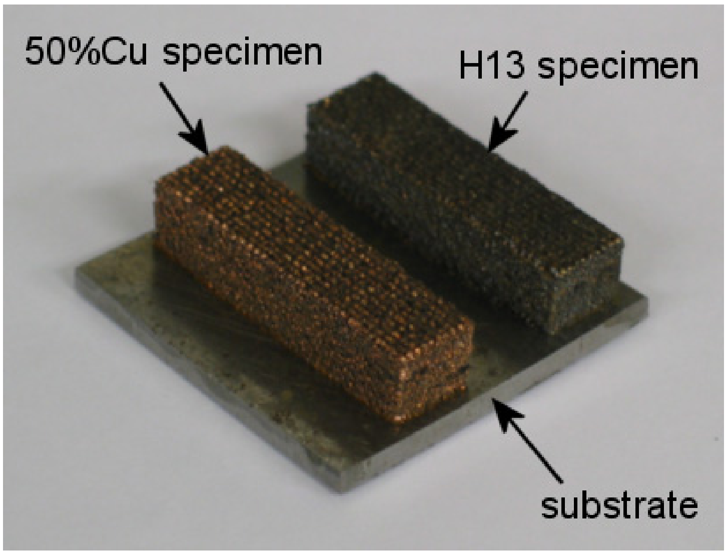

Figure 7-2. H13 and H13+50%Cu specimens after the laser fusion.

In Figure 7-3 all the specimens built for the density experiment are showed after the grinding. The specimens presented apparent full density but some corners were pitched as the material presented to be hard and fragile.

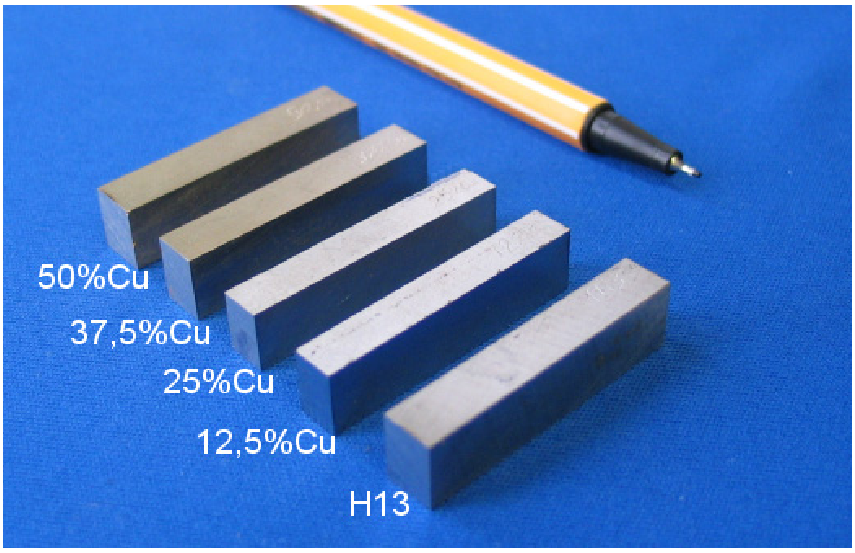

Figure 7-3. Specimens finished after grinding.

The results of the calculated volume, measured mass and calculated density are presented in Table 7-1. The density was statistically treated to calculate the upper and lower limits based on an confidence interval of 98%. The distributions for each specimen measurement appeared to be normal distribution.

Table 7-1. Volume, mass and density of the specimen of each mixture.

	Volume	Mass	Density			
	Average	Average	Average	Std. Dev.	Upper Limit	Lower Limit
	[cm^3]	[g]	[g/cm^3]	[g/cm^3]	[g/cm^3]	[g/cm^3]
H13	2,764330	21,1274	7,642864	0,0153686	7,77006	7,51573
12.5%Cu	2,328825	17,5450	7,533843	0,017337	7,67736	7,39045
25%Cu	2,149465	16,4852	7,621365	0,024455	7,82378	7,41907
37.5%Cu	2,676183	20,8680	7,797673	0,020025	7,96341	7,63201
50%Cu	3,036708	23,4318	7,716184	0,017287	7,85942	7,57333

(*) average of 6 measurements for each specimen and limits calculated for 98% of confidence for normal distributions.

Based on Table 7-1, the graph on Figure 7-4 was assembled with the average values of the density and it upper and lower limits of confidence. Strangely, despite the addition of Cu should increase the density of the material, it showed that it had decreased for H13 and 12,5% of Cu. Based on the microstructure results, it would be possible to affirm that this phenomena was because of the cracks found in this particular mixture. In the case of 50% Cu, this could be explained by the larger number of pores in specimens comparing with 37,5% of Cu mixture (5 and 6). A red dashed line shows the reference density value for H13 of 7,8g/cm^3 (Matweb, 2005-1). The density for Cu is 8,96g/cm^3 (Matweb, 2005-2).

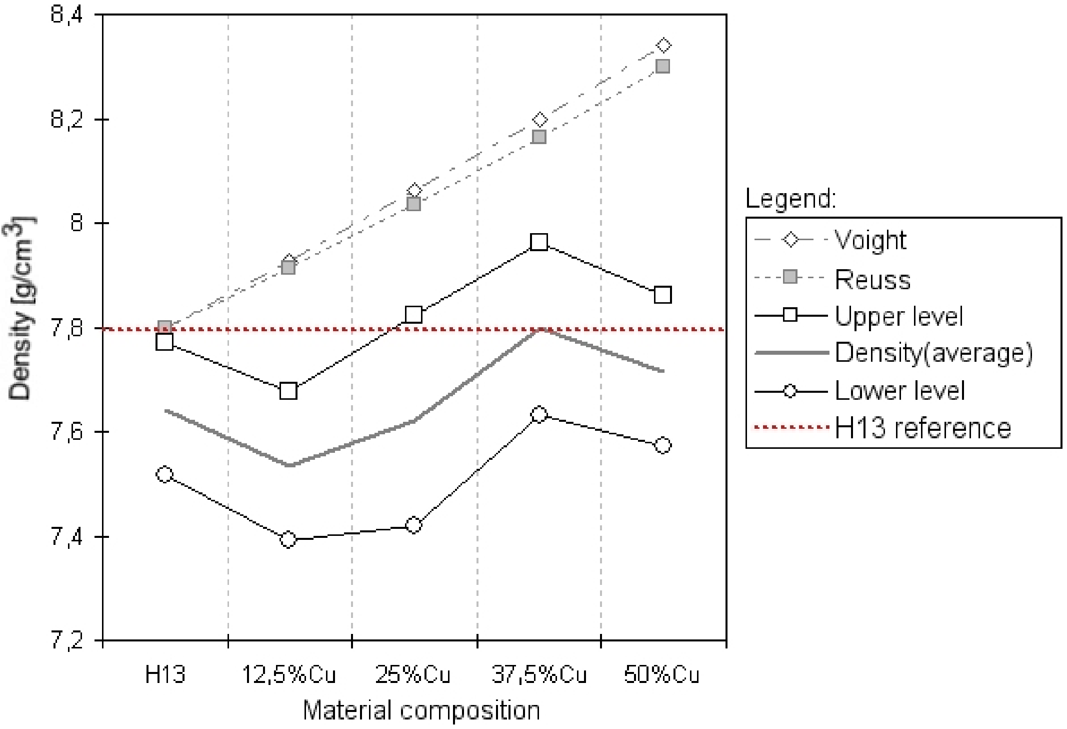

Figure 7-4. Average density against materials composition: models and laser fused parts.

The estimations of density by the rules of mixtures are also plotted in Figure 7-4. It is perceptible that the obtained density values are below from the estimations. Nevertheless, Table 7-2 shows the calculated percentage void inside each specimen when comparing the measured density and the density calculated by the rules of mixtures from Reuss and Voight

(Section 2.4.1). Although densities obtained were lower than the estimation, the voids inside each specimen were low. Parts with 90% from the theoretical values of density are considered very dense parts for most of the powder metallurgy processes, materials and applications (German, 1994; Thümmler and Oberacker, 1993).

Table 7-2. Percentage of voids (pores and cracks) for each material composition compared to the estimation by the rules of mixtures.

	Density by Voight	Density by Reuss	Average Density	Void % Voight	Void % Reuss
H13	7,800	7,800	7,64	6,82%	6,82%
12,5%Cu	7,928	7,913	7,53	6,98%	6,96%
25%Cu	8,061	8,034	7,62	7,12%	7,09%
37,5%Cu	8,198	8,163	7,78	7,25%	7,21%
50%Cu	8,340	8,300	7,72	7,41%	7,37%

(*) density values in g/cm^3.

7.2. Thermal conductivity coefficient

As commented previously, one of the most prominent applications for FGMs is thermal barrier. In the specific case of this work, the concern was not to have the thermal barrier but to improve thermal conductivity on specific regions of a tool steel based component such as an injection mould. Therefore, as the heat capacity and density, the other major property concerning the capacity of the material to transport heat energy is the thermal conductivity coefficient.

7.2.1. Methodology

The same specimens used to measure the density were used for determine the thermal conductivity coefficient of each mixture. For measuring the conductivity a Cussons Technology P5687 Thermal conductivity Apparatus (Manchester, UK) was used. A schematic drawing of this apparatus is presented in Figure 7-5. The apparatus had four thermocouples for reading the temperature in the centre section of two samples (a specimen which was being measured and an aluminium standard with the thermal conductivity coefficient already determined). A heat controlled source provided heat through the specimen, the aluminium standard and a copper base inserted into a water tank. This tank had a valve to control the water flow through the copper base and the water temperature was measured in the inlet and outlet of the tank. The water flowing out from the tank was collected into a reservoir for measuring the mass after the test. Water tank and specimens chamber were insulated to avoid heat losses and to keep the experiments in steady state conditions.

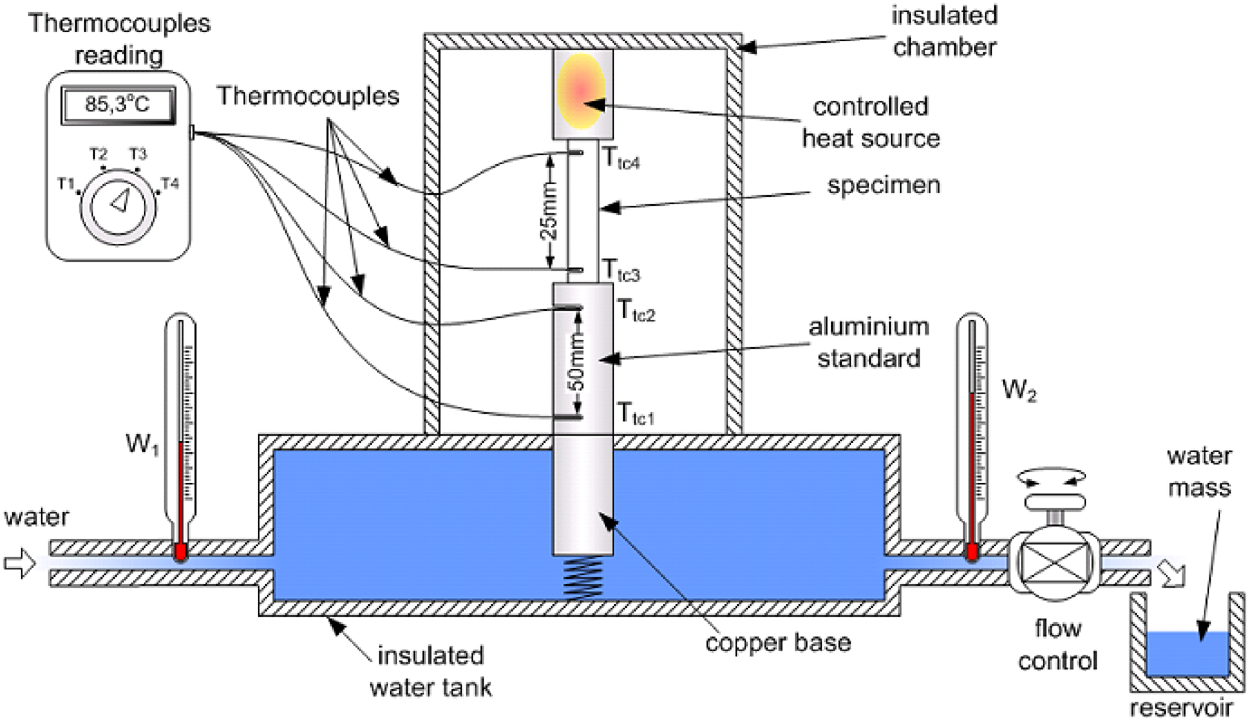
Thermocouples reading
85,3°C
T1
T2
T3
T4
Thermocouples
insulated chamber
controlled heat source
specimen
T_{tc4}
25mm
T_{tc3}
T_{tc2}
50mm
T_{tc1}
aluminium standard
W_1
W_2
water
water mass
insulated water tank
copper base
flow control
reservoir

Figure 7-5. Schematic drawing of the thermal conductivity test apparatus.

The idea of the apparatus was that measuring the energy used to heat some amount of water it would be possible to measure the thermal conductivity of a sample which was the transport medium from the heat source to the water. The rate of energy accumulated ($\dot{E}_{ac}$) by a body is defined by the variation of density (ρ), volume (V), specific heat (c) and temperature (T) over the time (t) (equation 7.03). For temperature changes in order of 10°C from the room temperature, the material properties can be considered constant. So, the energy (Q) necessary to heat the water mass from a temperature W_1 to a temperature W_2 can be calculated by equation 7.04, where M is the mass of the water.

$$\dot{E}_{ac} = \frac{d}{dt}(\rho VcT) \qquad \text{Eq. 7.03}$$

$$Q = c.\frac{M}{t}.(W_2 - W_1)\,; \quad \text{[W]} \qquad \text{Eq. 7.04}$$

For a solid body, the energy conducted by the body in the steady state condition can be calculated by equation 7.05, where k is the thermal conductivity coefficient, A is the cross section area of the body which the heat flux is perpendicular to the area, L is the distance from point 1, with temperature T_1, to point two where temperature is T_2. So, using Q from equation 7.04 calculated to heat the water, the thermal conductivity of a sample can be calculated if two points spaced by a known distance in the sample have the temperature measured during a specific time where the mass of water is collected.

$$Q = \frac{k.A.(T_2 - T_1)}{L} \Rightarrow k = \frac{Q.L}{A.(T_2 - T_1)}\,; \quad \text{[W/m.K]} \qquad \text{Eq. 7.05}$$

In order to improve the veracity of the results, the conductivity of the aluminium standard was calculated. The aluminium standard was a cylinder with a diameter of 25mm, with a length of 65mm and a distance between the two holes for the temperature measurement of 50mm. The manufacturer of the apparatus provided the standard with a thermal conductivity of 230W/mK.

Two holes were drilled in each specimen from the density experiment. The holes were spaced by 25mm and had a depth until the centre of the specimen. The contact surfaces of the specimens were polished to reduce the contact resistance between the specimens the heat source and the aluminium standard. To increase the conductivity in the contact area, a thermal paste (alumina based) was used in all contact surfaces. The specimen and standard were clamped against the heat source to improve the conductivity. Thermocouples tips also received the thermal paste before placing in the specimen/standard holes.

The experiment was conducted in steady state. The first step was to adjust the water flow with the heat source in such way to keep the difference between the temperatures W_2 and W_1 around 10^{o}C. When temperature readings achieve a steady level, the water reservoir was placed into the water outlet and measurement of the temperatures of the thermocouples and the water were measured each 120s. Reaching 600s, the mass of water in the reservoir was measured and the thermal conductivity of the specimen and the standard were calculated. For each specimen the experiment was carried twice.

7.2.2. Thermal conductivity results

The thermal conductivity coefficients calculated as a result of the measurements of the temperatures and the water mass described earlier are presented in Table 7-3. In this table, the aluminium standard thermal conductivity was also calculated. The error presented after each one of the two measurements was calculated as the 230W/mK being the reference value for the standard. For the specimens it is presented corrected value as the percentage adjustment from the error obtained from the aluminium. The average was the mean between the two corrected values from each measurement.

Table 7-3. Calculated and corrected conductivity values for the H13-Cu specimens.

	Aluminium Standard Conductivity				Specimen conductivity				
	1st	Error	2nd	Error	1st	Corrected	2nd	Corrected	Average
H13	243,09	+5,69%	200,39	-12,87%	30,31	28,58	28,58	28,87	28,73
12.5%Cu	266,09	+15,69%	244,51	+6,31%	24,24	20,43	21,76	20,38	20,58
25%Cu	254,60	+10,70%	254,95	+10,75%	27,90	24,92	27,71	24,71	24,82
37.5%Cu	207,06	-9,97%	210,85	-8,33%	36,05	39,64	37,21	40,30	39,97
50%Cu	233,44	+1,50%	230,70	+0,30%	46,19	45,50	46,71	46,57	46,04

(*) all conductivity values in W/mK.

It was noticeable that the aluminium values did not match the exact reference values. Differences from -9,97 to 15,69% were found. The same variation was perceptible in the thermal conductivity obtained for the specimens. Nevertheless, when correcting the specimens' values with the percentage error from the aluminium standard the two measurements taken for each specimen converge to the same value. The average represents well the both corrected values. So, despite the variation obtained from the experiment, it had showed coherence for the corrected thermal conductivity coefficients. The measurements, corrected values and average are plotted in Figure 7-6. The average value for H13 was calculated as 28,73W/mK. This is higher than the reference value for H13 from the literature 24,3W/mK (Matweb, 2005-1). One reason that could be considered for this higher value is because the H13 specimen used in this experiment has a dendrite microstructure which could increase the conductivity compared to the hot worked tool steel reference. The interdendrite phase that contains most of the alloy elements is interconnected differently from the worked material where this phase is broken and refined. Excluding the vanadium which is comparable low thermal conductivity all the other elements have high coefficients (chromium: 93,7W/mK; molybdenum: 138W/mK; silicium: 148W/mK).

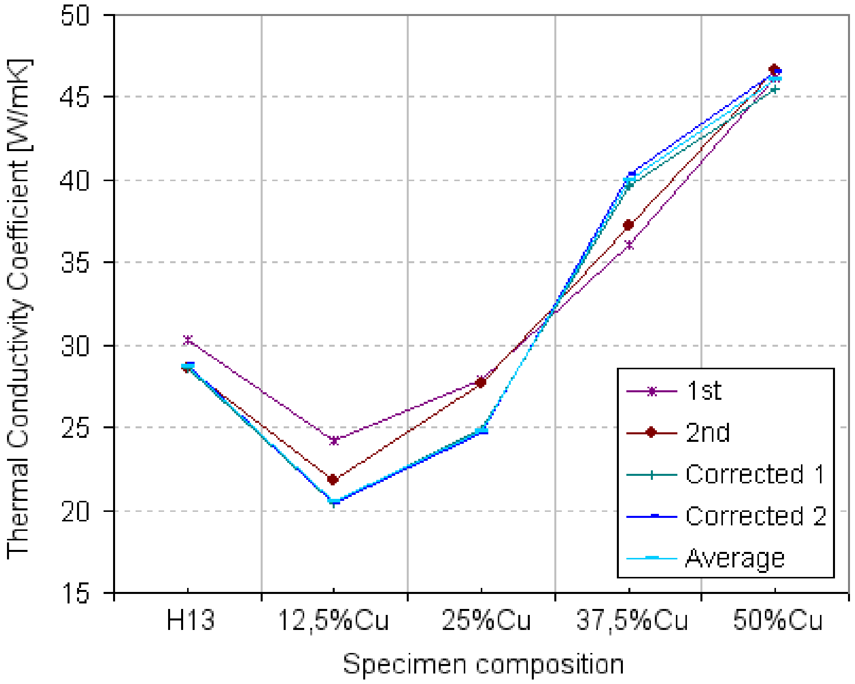

Figure 7-6. Graphical trend of the thermal conductivity measured for H13-Cu specimen.

The 12,5%Cu mixture presented a lower thermal conductivity than the H13. It probably was occasioned by the large number of cracks found in this composition. Cracks as are disruptive to the continuous flow of the energy would decrease the thermal conductivity. In the sequence, 25%Cu had higher thermal conductivity than 12,5%Cu but lower than H13. Again, this mixture presented cracks, lower than 12,5%Cu, but still present in the microstructure. A significant increase was noticed in the 37,5%Cu and 50%Cu. Nevertheless, the result shows the thermal conductivity was still low if compared to pure Cu (385W/mK).

Figure 7-7 shows a comparison of the theoretical models and the experimental for the thermal conductivity. The experimental data is represented by the average value of the correct curves obtained in the thermal conductivity experiment. It can be seen that the experimental data results were close to the thermal conductivity values obtained by the Reuss equation from ROM.

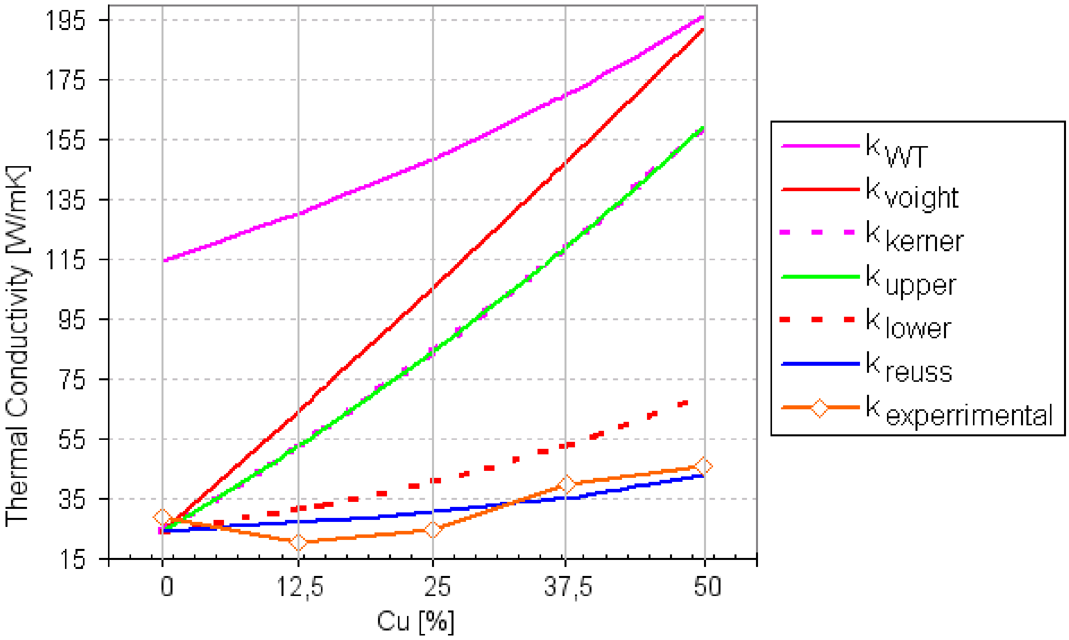

Figure 7-7. Graphical comparison between the estimated values and measured values of the thermal conductivity coefficient.

7.2.3. Conductivity comments

Although the apparatus used to measure the conductivity by an indirect method, this was successful to obtain representative values of the conductivity from the samples obtained. It had showed that despite the addition of Cu, the cracks and pores present in the microstructure of 12,5% and 25%Cu had significantly reduce the capacity of the material to conduct heat. Despite the fact that the cracks were mainly formed by the processing conditions during the laser fusion and that optimization had been previously carried to reduce the amount of defects in the microstructure still necessary to reduce even more the defects, specially, cracks. Even so the results of conductivity were low, they were well estimated by the Reuss rule of mixture. Moreover, the addition of Cu increased the conductivity of the H13 base material for the richer compositions of Cu.

7.3. Linear thermal expansion coefficient

One important property for the gradient is the linear thermal expansion coefficient. This property can determine the success or failure of a part if the gradient has too different expansion coefficients. Great divergence between the expansion coefficients of two joining materials can cause crack failure. Gradual transitions using FGM can avoid this kind of problem and is one important area of FGM (Suresh, 2001). This experiment was planned to measure the thermal expansion coefficient of the H13 and the four H13-Cu alloys built using selective laser fusion.

The coefficient is defined by the dimensional variation of the body within a temperature range. It represents the inter-atomic distance of the metallic material changing as energy is given or extracted from the body. The variation of the volume is proportional to the temperature variation. In equation 7.06, this variation is defined by the variation in the volume length (final length, L_f, minus initial length, L_0) divided by the initial length which is proportional to the temperature variation. The proportionality is defined by the linear expansion coefficient α_l.

$$\frac{L_f - L_0}{L_0} = \alpha_l.(T_f - T_0); \qquad \text{Eq. 7.06}$$

The coefficient can change with the temperature as well. So, considering the infinitesimal changes of temperature and length and isolating α_l, from previous equation, the coefficient at specific temperature can be determined by equation 7.07.

$$\alpha_l = \frac{1}{L_0}\frac{dL}{dT}; \quad [K^{-1}] \qquad \text{Eq. 7.07}$$

Copper and H13 tool steel have temperature dependent expansion coefficients. Figure 7-8 shows the variation of their coefficients with the temperature. It is noticeable the variation for Cu. As one of the characteristics of the H13, its dimensional stability, even in high temperatures is show by small changes in the coefficient.

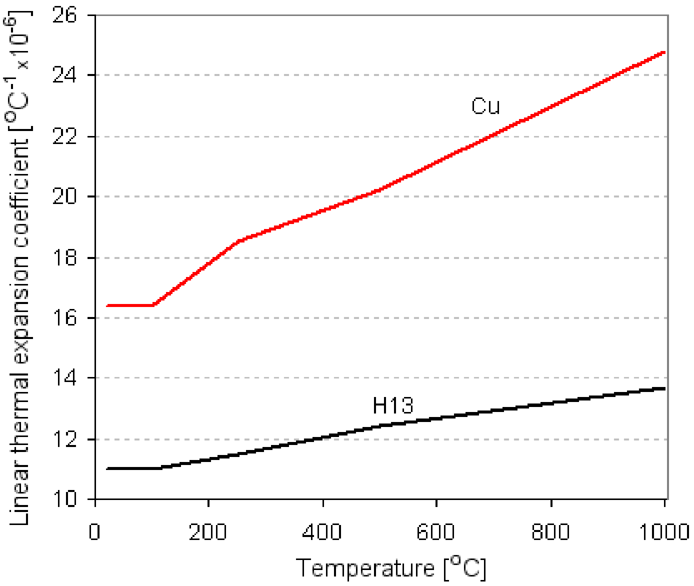

Figure 7-8. Variation of the linear expansion coefficient of the Cu and H13 (based on Matweb 2005-1 and 2005-2).

7.3.1. Methodology

Small cubic pieces of each material were taken from the specimens built for the density experiment. The dimensions and mass of each sample is presented in Table 7-4. The samples were ground with silicon carbide sand paper in its surfaces and the direction of measurement matched the x building direction in the platform.

Table 7-4. Mass and dimensions of each sample.

Composition	Mass	Height (*)	Width	Depth
	g	mm	mm	mm
H13	2,4782	9,00	5,88	6,08
H13-12,5%Cu	4,3996	12,60	7,60	6,00
H13-25%Cu	5,0023	15,58	7,00	6,00
H13-37,5%Cu	5,8947	15,70	7,10	6,98
H13-50%Cu	5,4437	15,50	7,40	6,30

(*) measurement direction.

The apparatus used to measure the expansion was a dilatomer BP Engenharia, RB 3000, located at the Laboratório de Materiais, LABMAT, at the Universidade Federal de Santa Catarina.

The samples were heated from room temperature, 25°C, until 600°C, at the rate of 10°C/min. The furnace was sealed and argon was used as protective atmosphere. The expansion of the material was recorded by the apparatus computer.

7.3.2. Linear expansion coefficient results

The variation of the length relative to the original length at room temperature of each specimen with the temperature is presented in Figure 7-9. It is noticeable that there is a slope change in the expansion curves around 125 to 175°C.

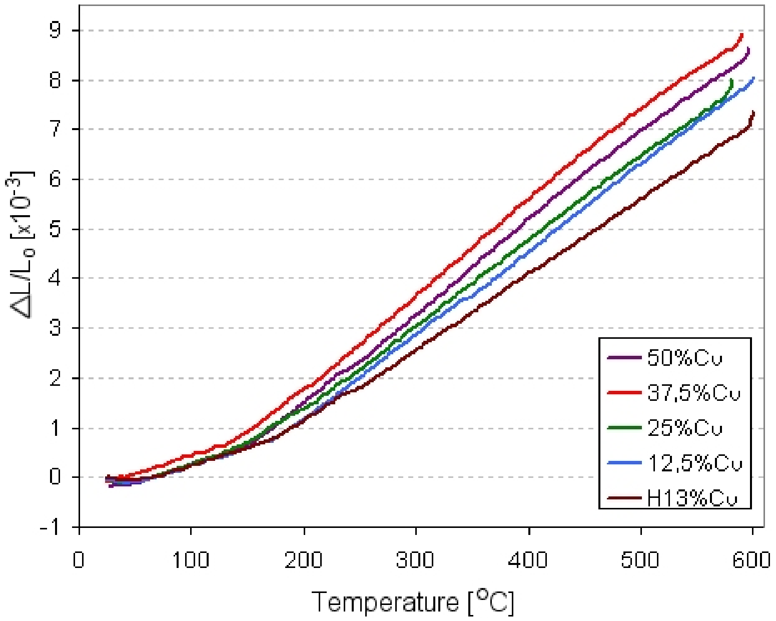

Figure 7-9. Dimensional changes of the samples with the temperature.

It is presented, in Figure 7-10, the variation of the expansion coefficient for each sample tested. The values were obtained by the equation 8.07 presented previously. Between 125 to 200°C the change in the slope of the curves in Figure 7-9 was characterized by a rapid increase in the expansion coefficients of all samples. So, between this range of temperature, this behaviour could be due to stress relieve of the samples. As they were manufactured by laser fusion of small beads, it was expected some stress restrained in the structure of the samples. So, the small values of the expansion coefficients at the beginning of the curves could be related to this stress accommodation/relief. After 225°C the curves presented an almost linear behaviour with little variation until 450°C. From this point forward, they present a small reduction in the expansion coefficient. This effect was more particularly strong in the Cu richer samples. These curves in Figure 7-10 are opposite from what would be expected normally. As Cu has higher expansion than H13, the addition of Cu should increase the expansion of the H13 material. However, this was not what had been presented. Considering the stable part of the curves between 225-450°C, the fused H13 presented the higher expansion coefficient. It was higher than the reference value of H13 from the references (Matweb, 2005-1). The reference material is already heat treated and stable when the test is performed. It was found in the results that the Cu addition did not increase the expansion coefficient of the samples. Also, it was found that H13-Cu curves were considerably lower than the results obtained for only H13.

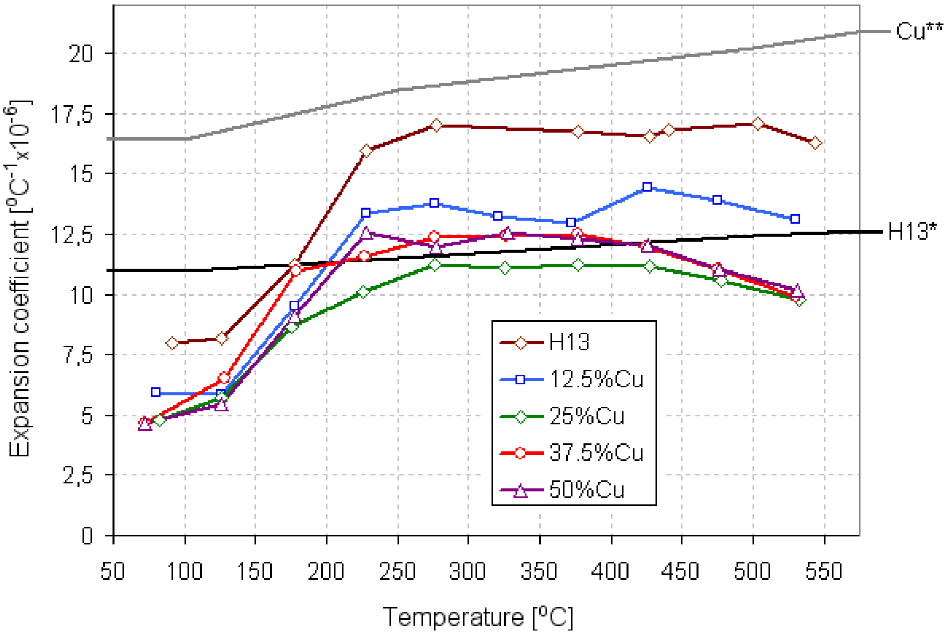

Figure 7-10. Variation of the expansion coefficients with the temperature (H13* and Cu** ref. curves).

7.3.3. Linear expansion comments

The results obtained from experimental data for the expansion coefficients could not be easily interpreted. The small expansion at the lower temperatures and the lower expansions obtained for the H13-Cu mixtures than for H13 were confusing. As commented previously, the smaller expansion coefficients at the beginning of the heating curves could be caused by the internal retained stress. This stress was so intense due to the rapid solidification and cooling (typical characteristics from laser processing) that cracks were present in the macro/microstructure as seen in previous chapters/sections. Finally, it is important to say that no further comparison was possible with the estimated values from section 2.4.4.(b), Chapter 2. Also, the state of the materials tested in this experiment was as they came out from the machine, without any heat treatment that will be required for future applications. Additionally, it is important to remember that the expansion coefficient might differ in each building direction and only one (x) direction was tested for this experiment.

7.4. Microhardness

One important property of the material is the hardness. Tool steels are know as materials for low wear due to their elevated hardness. On the other hand, Cu is well known as a soft malleable material. This section describes the microhardness testing of a graded specimen of H13-Cu.

7.4.1. Methodology

A small slab specimen was manufactured with the platform system explained in section 4.1.2 with the 45x45mm platform and multi-compartment feedhopper (second hopper design in order to produce large specimens). The 50%Cu was placed in the central compartment of hopper and sequential compositions were placed in each other compartment until the pure H13 powder. For the compositions of H13 and Cu the hopper aperture was of 3,5mm and in total the specimen was 40mm long. All the 5 bimodal powder compositions were used to build the specimens with 250μm of layer thickness over a 4mm mild steel substrate. The parameters used to build the specimens were pulse energy 10J, pulse width 20ms, feedrate 5mm/s and repetition rate 20Hz. After building the specimen, this was cut off from the platform and ground in all surfaces to get the final specimen as seen in Figure 7-11.

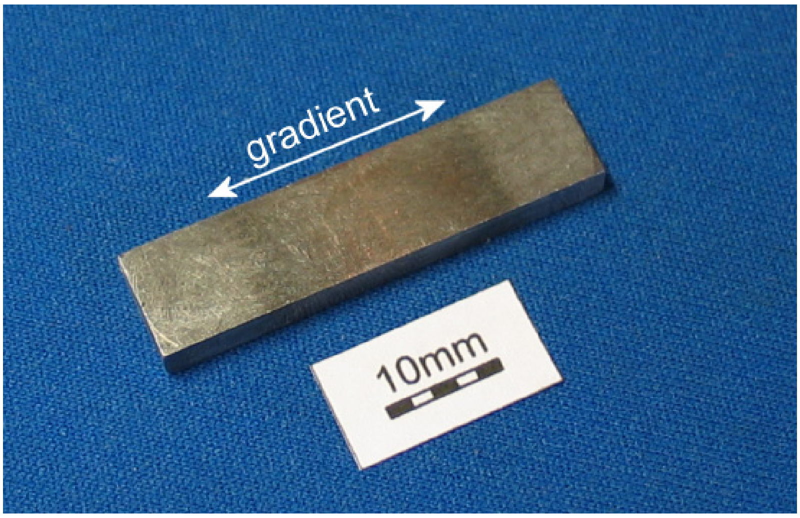

Figure 7-11. Gradient region of the specimen tested.

The microhardness was measured at different positions along the specimens with a automated apparatus using the Vickers scale (Buehler MicroMet Series 1600-3600). Each region of the specimen was measured randomly six times for the average value. Table 7-5 shows the force and duration used for the microhardness test. As the regions of H13-37,5%cu and H13-50%Cu region were softer, the force was reduced to 100gf.

Table 7-5: Microhardness test specifications.

Region/composition	Force (gf)	Duration (s)
H13	200	15
H13-12,5%Cu	200	15
H13-25%Cu	200	15
H13-37,5%Cu	100	15
H13-50%Cu	100	15

7.4.2. Results

The average values obtained with the microhardness testing are summarized with the respective standard deviations on Table 7-6. The H13 region had an average hardness of 581HV which is higher than the standard H13 (air or oil quenched) value of 549HV (Matweb, 2005-1). This was because the material did not have any thermal treatment after rapid solidification from the laser fusion. The other four with H13-Cu compositions presented a progressive decrease in their hardness. The variation for 12,5, 25, and 37,5%Cu was considered low and remained almost the same from the H13. The 50%Cu blend was difficult to measure because of the non-homogeneous structure, of the dual region formed in the structure. The force against the indentation probe had to be reduced because of the copper softness on isolated areas. As a result, measuring hardness gave great variability with a mean of 292HV. The lower value of the statistical range of the hardness for 50%Cu was 233HV. Nevertheless, there were regions were the hardness could be 110HV which was slightly higher than the Cu hardness 105HV (Matweb, 2005-2).

Table 7-6. The measured microhardness results.

Region	Vickers Hardness	Standard Deviation
H13	598,3	44,1
H13-12,5%Cu	586,1	50,2
H13-25%Cu	527,4	32,6
H13-37,5%Cu	464,3	39,8
H13-50%Cu	369,4	135,9

Figure 7-12 shows the microhardness variation results plotted with the estimations from the ROM equations. The yellow shaded region is the delimitation of the standard deviation around the average values of hardness obtained for each material composition. The estimations were low compared with the obtained results but no heat treatment was applied to the sample.

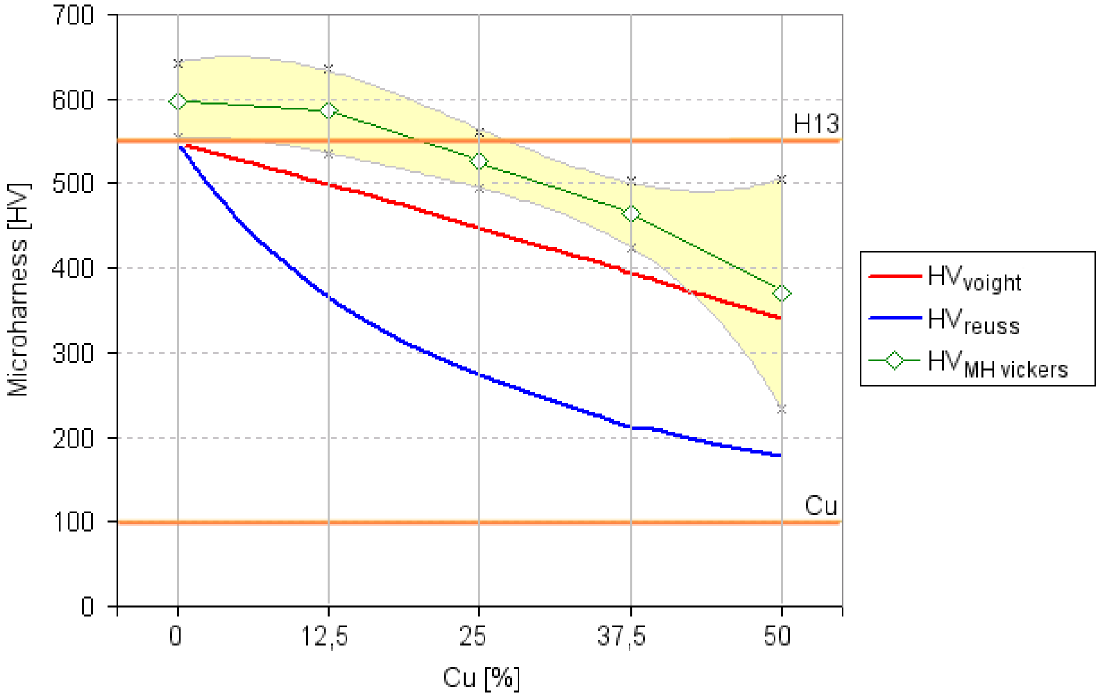

Figure 7-12. Microhardness variation along the graded specimen.

7.5. Depth and load sensing indentation

After estimating properties, it is necessary to evaluate the material properties of any FGM that could be manufacture in laboratorial scale. Nevertheless, it is not always possible to produce, for instance, a full ISO standard tensile test specimen. To have the first characteristics of the material it is very useful to evaluate the material by the hardness test. A more accurate and expansive test is the load and displacement sensing indentation (also referred as nanoindentation). The method developed by Oliver and Pharr (1992) using a Berkovich indenter (three sided pyramidal diamond indenter) can calculate the elastic modulus and the hardness of the material based on the measurements of cyclic load applied to the indenter over the material surface. It is know that the values obtained with this technique remains under 5% of error compared to standard tests (Oliver and Pharr, 1992; Fisher-Cripps; 2000).

7.5.1. DSI test methodology

A graded specimen was produced with five bimodal powder compositions presented in section 4.3. The laser parameters were set to energy pulses of 10J, pulse width of 20ms, repetition rate of 20Hz and scan speed of 5mm/s. The powder was processed at room temperature and to reduce the oxidation of the material a pure argon shield flow (15l/min) was constantly blown over the 0,8mm laser spot. To build the specimen, the refill strategy was used combined with 250µm of layer thickness and 0,5mm of vector spacing.

After obtaining the specimen, it was cross sectioned in the XZ plane (orthogonal to the XY laser scan plane and parallel to the layer addition axis, Z). The specimen was mounted in cold cast epoxy based resin, grounded until 800 mesh silicon carbide paper and then polished with cloth pads of 6µm and 1µm diamond particles dispersed in solutions. Light etching was made to identify the FGM regions with nitric acid at 2% in water during 25 seconds.

A DSI machine (Nanotest from Micromaterials, UK) was used to measure the load and displacement penetration of a diamond Berkovitch indenter over the polished surface of the specimen. The specimen mounted in the machine was submitted to 350 measurements over the surface, giving and average of 70 measurements for each grade of material between pure H13 and H13-50%Cu. The maximum applied force was 200mN and the distance between each indentation was 50µm. The indenter was kept during 30s loaded over the surface of the material for each measurement. Figure 7-13 shows a schematic view of the indentations over the specimen and the plane orientation of the polished surface.

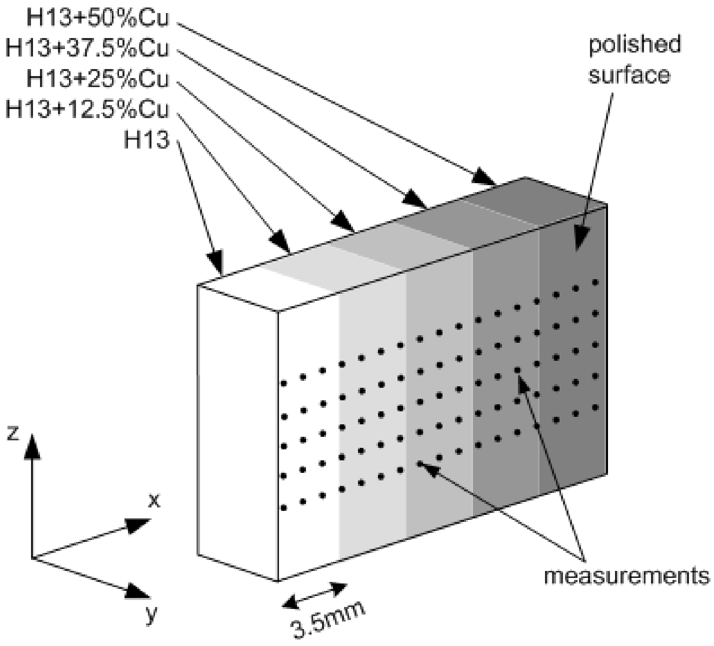

Figure 7-13. Schematic view of the DSI measurements taken in the specimen.

To increase the accuracy of the results, the test was conducted under temperature and moisture control inside the testing chamber. The elastic modulus and the hardness were automatic calculated by the DSI apparatus based on the Oliver and Pharr (1992) method. The polished surface of the specimen was analysed under optical microscope and indentations that were made over/close to pores and cracks were not counted into the results. Figure 7-14 shows the specimen mounted in the DSI machine ready for the automated measurement of the graded sample.

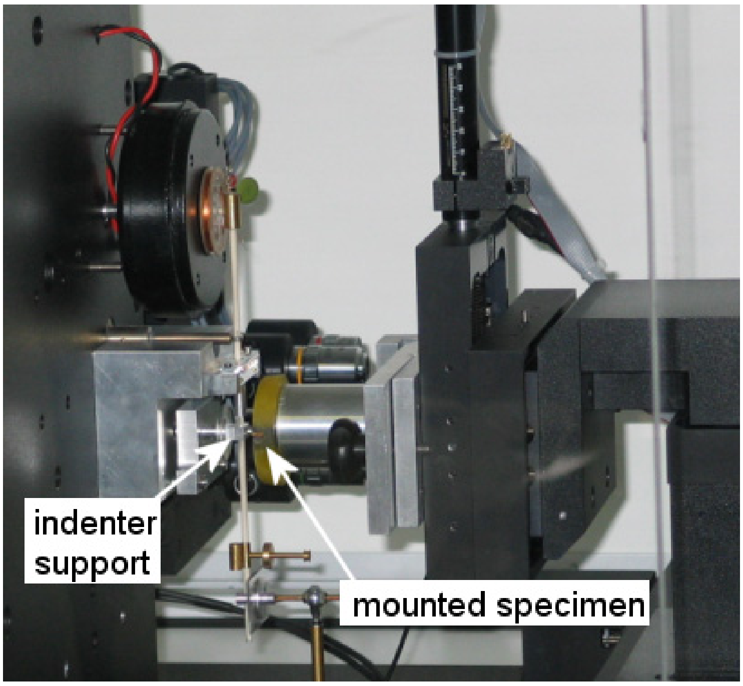

Figure 7-14. Specimen mounted in the DSI machine.

7.5.2. DSI Results

The DSI test provided and enormous amount of data for each material composition. As it could be expected, pure H13 region was the stiffest material. In Figure 7-15, representative curves of load x displacement from the DSI test are plotted. The less the indenter penetrates (displacement) into the material the harder and stiffer is the material (Oliver and Pharr, 1992). These curves in Figure 7-15 are from specific indentations realized into the material surface. For each of the 70 measurements a curve was plotted. Based on the average value of the elastic modulus of each material composition region, curves that had a value property equal or close to the average were chose to plot the graph in Figure 7-15. The compositions of H13-12,5%Cu and H13-25%Cu had presented almost the same behaviour. The 50%Cu curve shows that the material was quite soft and large amount of plastic deformation has been identified. H13+37,5%Cu showed middle term properties between the 25% and 50%Cu mixtures.

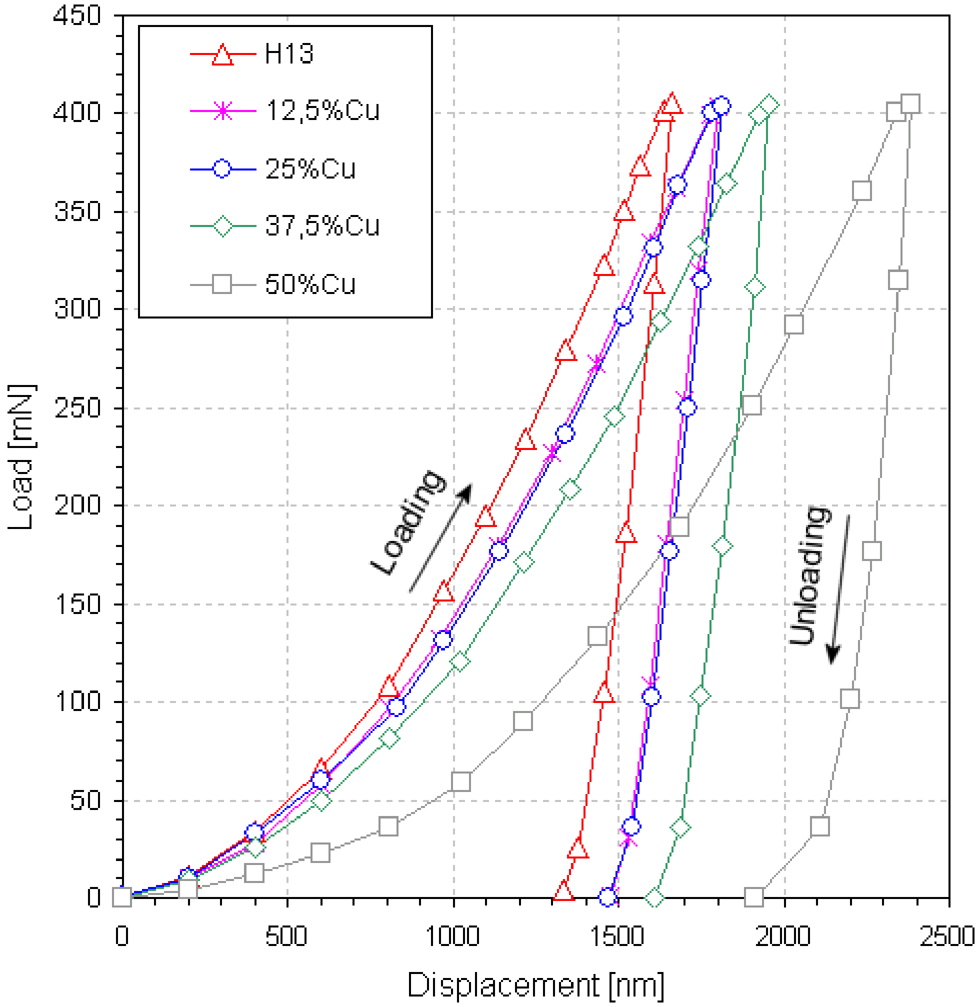

Figure 7-15. Representative average curves of Load x Displacement for each FGM region.

The average and standard deviation for the hardness obtained in the DSI are presented in Figure 7-16 in Vickers scale of hardness. Pure H13 standard deviation was quite low. Nevertheless, the hardness result was higher (7,07GPa:720,9HV) than the value found on references (5,384GPa:550HV, Matweb, 2005-1). The pink area in the graph is the standard deviation around the average (HV_{DSI}) value obtained for each composition. The Reuss (HV_{reuss}), Voight (HV_{voight}) and the results obtained from the microhardness test (section 7.4) are also plotted. It was noticeable that the results from microhardness and DSI converged with higher Cu quantities. Nevertheless, the variability from DSI test was higher than from microhardness test. This can be explained by the fact that the DSI test is more sensitive to the variations found in the microstructure as the indenter is much smaller than the indenter from microhardness test.

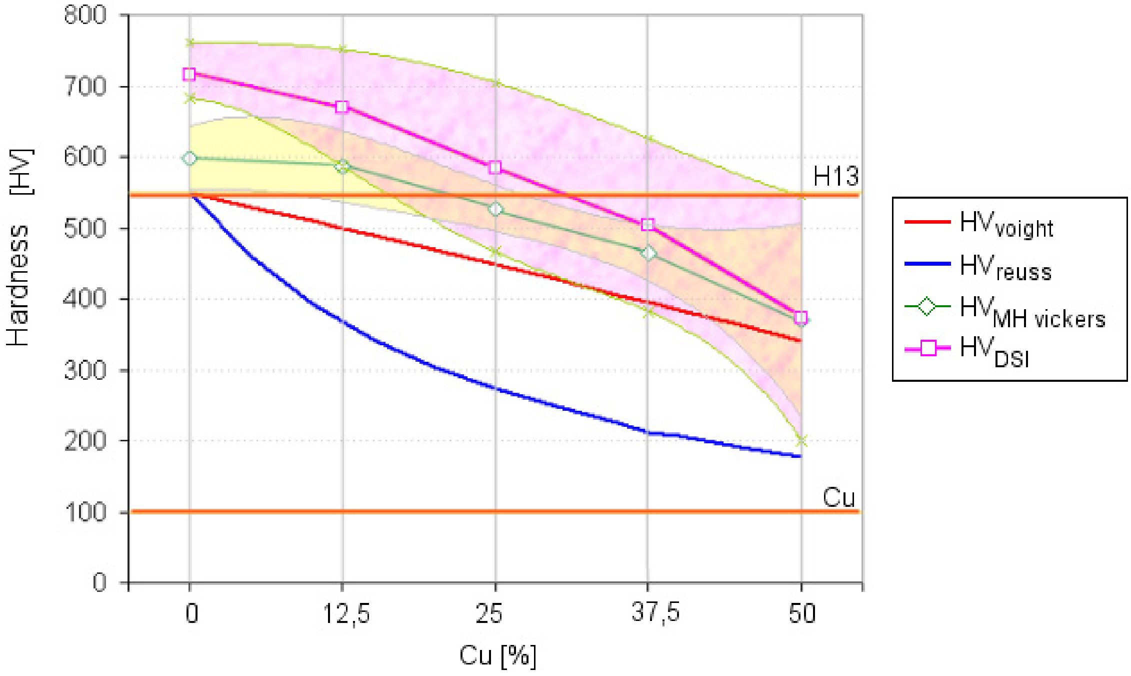

Figure 7-16. FGM hardness by microhardness and DSI measurements and ROM.

Figure 7-17(a) shows an indentation mark on the H13 area in the gradient. By the homogeneity of the microstructure the low standard deviation can be explained. It was perceptible that hardness decreased with the addition of Cu. Also the variability expressed by the standard deviation upper and lower limits, had increased with the Cu percentage. Figure 7-17(b) an indentation from the region rich in 25% of Cu is presented. The Cu which started to occupy the interdendrite space (darker regions) with the alloys of the tool steel softened the material.

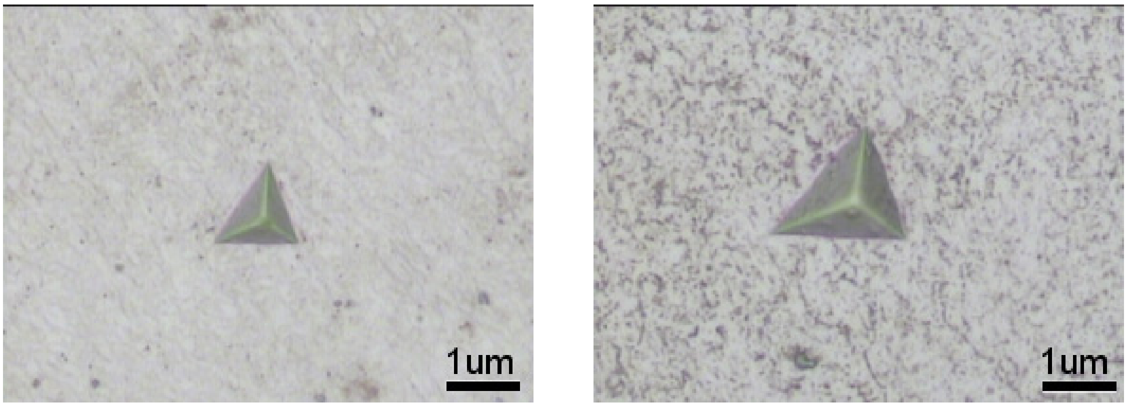

(a) (b)

Figure 7-17. Indentation marks on H13 (a) and H13+25%Cu.

In the case of 37,5%Cu and especially of 50%Cu, the Cu high content forms a heterogeneous microstructure with two phases. On Figure 7-18, two micrographs of indentations from 50%Cu region are show. It is possible to identify the phases where Cu and Cu+H13 are present. This increased the variability as the indentation could be performed on any region.

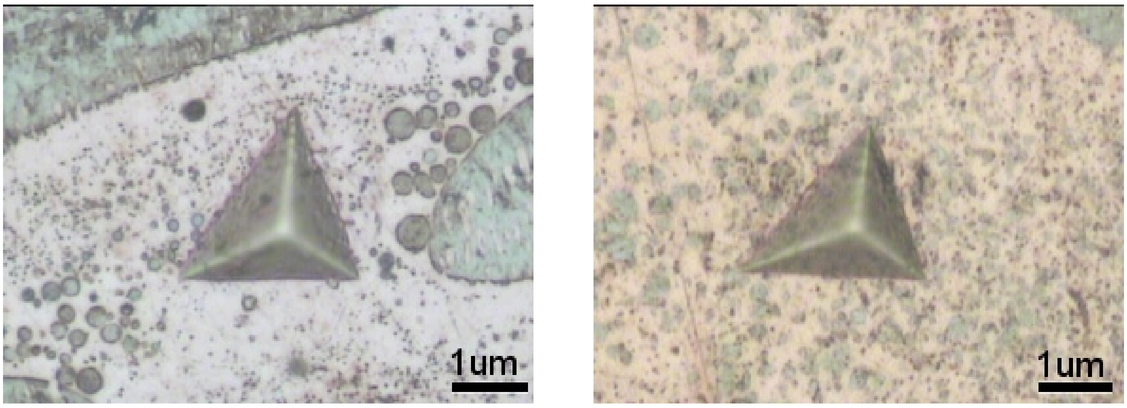

(a) (b)

Figure 7-18. Indentation marks on H13+50%Cu regions.

Figure 7-19 shows the averages and standard deviations (as a yellow region) obtained by the DSI test for each material in the gradient. The elastic modulus property decreased with the Cu addition. The fact that pure H13 had an elastic modulus too high compared to the standard it due to two facts. First, it that materials rapid solidified have refined microstructure and present elevated hardness as it is higher the amount of contours and crystalline defects. The second reason is that the surface of the sample, at this level of analysis, had suffered some degree of plastic deformation during the polishing of its surface.

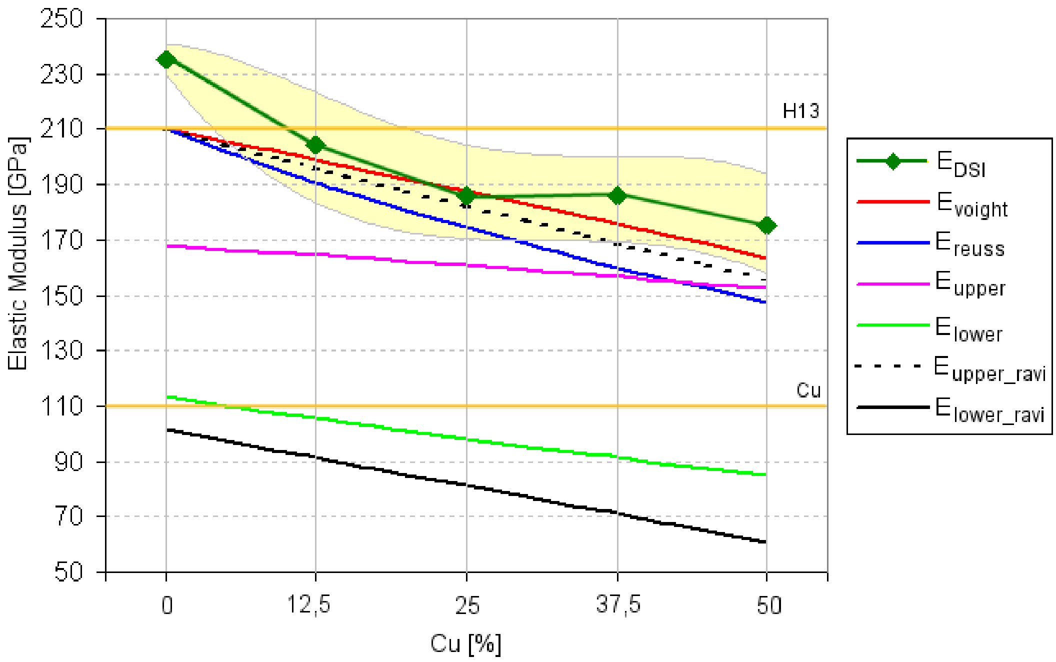

Figure 7-19. Reduced elastic modulus (average and standard deviation) and prediction models.

The modulus presented in Figure 7-19 is the corrected modulus. This correction had to be made to compensate the elasticity of the diamond indenter during the test. So, following the correction presented in Oliver and Pharr (1992) the equation 7.08 makes the relation between the reduced modulus (E_r), the corrected modulus (E_{DSI}), the indenter modulus (E_i) and the Poisson's coefficients of the material and the indenter (v and v_i, respectively). The reduced modulus was actually the calculated value by the DSI apparatus. This correction increases the elastic modulus compared from the calculated by the machine. For calculating E, the elastic modulus E_i from the indenter was considered 1141GPa and Poisson of 0,07 (Oliver and Pharr, 1992). The Poisson coefficient for each material composition was calculated using the Reuss ROM formula.

$$\frac{1}{E_r} = \frac{1-\nu^2}{E} + \frac{1-\nu_i^2}{E_i} \qquad \text{Eq. 7.08}$$

To summarize, Table 7-7 shows the results obtained by DSI and compares with reference values and estimative made with the rules of mixtures. The values of hardness and elastic modulus are higher than standard value of H13 and the estimations made with Voight and Reuss formulas.

Table 7-7. Summary of standard, estimated and measured results values.

	Hardness [GPa]				Elastic modulus [GPa]			
	Ref.(*)	voight	reuss	DSI	ref(**)	voight	reuss	DSI
H13	5,384	5,384	5,384	7,07	210	210,0	210,0	235,2
H13-12,5%Cu	-	4,897	3,597	6,55	-	198,9	190,8	204,2
H13-25%Cu	-	4,394	2,679	6,55	-	187,5	174,4	186,0
H13-37,5%Cu	-	3,873	2,119	4,93	-	175,7	160,1	185,7
H13-50%Cu	-	3,335	1,743	3,65	-	163,5	147,6	175,4
Copper	0,981	0,981	0,981	-	110	210,0	210,0	-

(*) and (**) sources: Matweb, 2005-1 for H13 and Matweb, 2005-2 for Cu.

7.5.3. DSI general comments

The microstructure obtained in the gradient of the specimen explained the great variability found in the DSI results for hardness and elastic modulus. This characteristic is expected in FGM materials and must be studied better. The distribution of phases in the microstructure can affect greatly the properties obtained (Torquato, 2001). However, the DSI results presented a good general idea for hardness and elastic modulus.

Both hardness and elastic modulus for pure H13 were higher than expected. The first reason for this is the fact that as DSI is a nano procedure it would be influenced by the grinding and polishing into the prepared surface. The surface preparation acts as a cold work hardening treatment where the material is plastic deformed. This influence is only in few microns from the surface but this is the working range from the DSI test.

Other reason for these high measured values was that the reference values are for materials that were already heat treated and hot/cold worked. No data available for the dendrite microstructure, specially when fused by laser which involves quick solidification. In Brooks *et al* (1999), the H13 fused by the LENS^{TM} process also revealed higher hardness values for the top layers built (last layers to be fused). The hardness values were also around 700HV. The internal stress retained in the martensite also might have contributed to the obtained results. Moreover, the anisotropy of the material was not considered and the Poisson's coefficient might differ in different directions of the tested sample.

As the harder, the stiffer the material is, this reflected in the elastic modulus with higher values found. The Cu had the expected effect reducing both properties analysed here. Although the results found were higher than the estimations from chapter 2.4 it is necessary to count that defects (pores and cracks) were not counted in the obtained results. This was necessary as the objective was to estimate the properties of the material that can be obtained by laser fusion technique.

7.6. Tensile test

To evaluate some of the mechanical properties of the gradient between H13 and Cu that could be manufactured by the process selective laser fusion and x-graded feed hopper, a tensile test was planned. The objective of this experiment was to obtain the elastic modulus, elongation at break and ultimate tensile strength of the gradient.

7.6.1. Design of the specimens tensile

Due to the lack of automation of the layering system and powder resources, the tensile test was planned based on the minimum size of specimens that could be made following the international standards. The specimen geometry was designed based on the BS EN 10002-1:2001 standard for proportional tests on solid bodies (not sheets, wires, tubes). Figure 7-20 shows the main dimensions of the specimen with the same nomenclature of the standard.

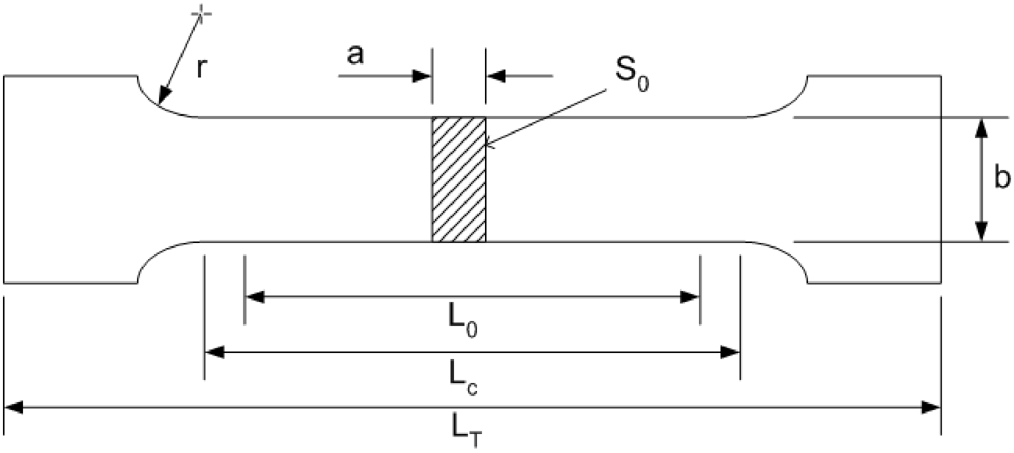

Figure 7-20. Indication of the dimensions of the specimen for tensile test.

The main restriction of the test was the insertion of the gradient inside the L_0, the original gauge length that was the length where the extensometer extremities were assembled. Each step of the gradient was planned to be 3,5mm wide. At the centre of the gradient the H13-50%Cu was be placed and the four remaining mixtures were placed symmetrically positioned at each side. In total, 9 different sectors of each material (including the H13) and H13 extensions to rest of the body formed the proof specimen. Equation 7.09 calculates the L_0 based on the these arguments.

$L_0 = 3{,}5mm * 9 = 31{,}5mm$; Eq. 7.09

This length satisfies the standard which requires the minimum of 20mm for L_0. As it was planned to be a proportional test L_0 follows the Equation 8.10 where S_o is the cross-section area of the specimen at the reduced section and k is the coefficient of proportionality (k=5,65). The section area is defined by Equation 7.11, where a is the thickness of the reduced section and b is the width of the reduced section

$L_0 = k * \sqrt{S_0}$; [mm] Eq. 7.10

$S_0 = a * b$; [mm^2] Eq. 7.11

With the minimum thickness of the S_0 section being 4mm, the width of the reduced section was calculated to 7,7708mm. The parallel length L_c, was then calculated by Equation 7.12. The minimum radius (r) used between the reduced section transition at the extremities of L_c and the ends which are gripped by the tensile test apparatus, was 12mm. With all the limitations to build the specimen, the total length was calculated to 70mm as the standard does not make any calculation for this and it depends on the grip/claws system of the tensile test machine. The dimensions designed for the specimens are listed in Table 7-8.

$L_c = L_0 + 1{,}5 * \sqrt{S_0}$; [mm] Eq. 7.12

Table 7-8. Dimensions of the tensile piece test.

Dimension	Description	Value
a	Thickness of the reduced section	4mm
b	Width of the reduced section	7,77mm
S_0	Cross-section of the reduced section	31,08mm^2
L_0	Original gauge length	31,5mm
L_c	Parallel length	39,86mm
L_T	Total length of test piece	70mm
r	Radius from the sections transitions	12mm
k	Proportionality coefficient	5.65

7.6.2. Theoretical model of a FGM tensile test specimen according to ROM

In this specimen, the test was designed to evaluate the whole gradient, not isolated portions of materials. In Figure 7-21, a schematic gradient is submitted to a traction force F. The gradient is distributed along the same direction of the traction axis. Each composition that forms the gradient is formed by a small volume unit (V_{unit}). In total, there are nine volumes that form the total volume (V_{total}) of the test length of the gradient (L).

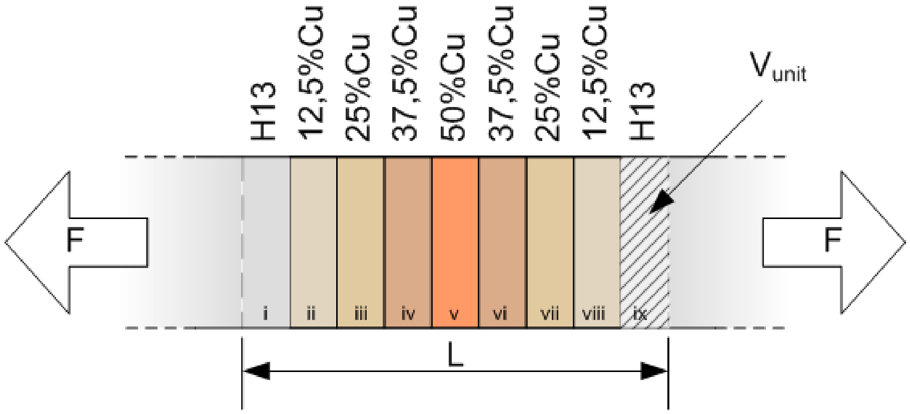

Figure 7-21. Axial gradient distribution of a specimen.

According to the Reuss rules of mixtures, this gradient can be characterized by the harmonic equation. So, in equation 7.13, the adapted model to estimate the elastic modulus (E_{FGM}) of the gradient is presented. Each portion of the gradient is represented by its volume and elastic modulus. Notice that as the gradient is symmetrical and the 50%Cu is in the middle of the gradient, it is represented only one time in contrast with the other portions that are represented twice.

$$\frac{V_{total}}{E_{FGM}} = 2.\frac{V_{uni}}{E_{H13}} + 2.\frac{V_{uni}}{E_{12,5\%Cu}} + 2.\frac{V_{uni}}{E_{25\%Cu}} + 2.\frac{V_{uni}}{E_{37,5\%Cu}} + \frac{V_{uni}}{E_{50\%Cu}}; \qquad \text{Eq. 7.13}$$

As the total volume of the gradient is equal to 9 portions of the unitary volumes of each composition (equation 7.14), equation 7.13 can be simplified to equation 7.15, which calculates the equivalent elastic modulus independent of the volume of the gradient (respecting proportions).

$$V_{total} = 9 * V_{uni}; \qquad \text{Eq. 7.14}$$

$$E_{FGM} = \left[\left(2\left(\frac{1}{E_{H13}} + \frac{1}{E_{12,5\%Cu}} + \frac{1}{E_{25\%Cu}} + \frac{1}{E_{37,5\%Cu}}\right) + \frac{1}{E_{50\%Cu}}\right)/9\right]^{-1}; \qquad \text{Eq. 7.15}$$

7.6.3. Fabrication of the specimens

As the tensile test requires proper surface finishing and dimensional control, the manufacturing of the specimens was divided in 3 steps. The first step was to obtain a pre-form from the selective laser fusion process. After, the top surface of the specimens was grounded and finally they were cut using spark wire erosion to obtain the final tensile geometry.

For the manufacturing of the specimens, the feed hopper presented in section 4.1.2 (Figure 4-7) and respective platform (45x75mm) were used. The powders used were the 5 bimodal mixtures described in section 4.3. The refill strategy used to build the specimens (sections 5.1 and 5.2). Ar shield gas (15l/min) was used to avoid oxidation and as lens protection. The specimens were divided in two sets of layer thickness: 500 and 250µm (“thick” and “thin” respectively). Each specimen was build as a simple parallelepiped of 72x12x7mm.

Differently from others experiments in this work, the layer vector orientation was not cross-hatched and all layers had the same scanning orientation along the longest dimension of the specimens. This could increase the anisotropy of the specimens but it was necessary to avoid high speed short movements by the Laserdyne motion system in the 12mm direction and to increase productivity. The reduction of vectors necessary to fill a layer leaded to reduce the amount of dead time from re-positioning the motion table. Considering that each layer recoating was manually activated and the machine could not work without assistance it was imperative to reduce the building time. In this experiment, as an attempt to avoid the substrate bending, 5mm mild steel substrates were used. The laser parameters used to build the specimens were the same optimized for the 12,5%Cu mixture (pulse energy of 10J; pulse width of 20ms; repetition rate of 20Hz and federate of 5mm/s). Two specimens were built on each run. Figure 7-22 shows a photograph taken during the laser fusion of one layer of the specimens. Examples of the parallelepipeds obtained are presented in Figure 7-23. In total, ten specimens with 250µm and four with 500µm of layer thickness were built. Despite the difference between the layer thicknesses, no visual different of defects could be seen between the two different sets.

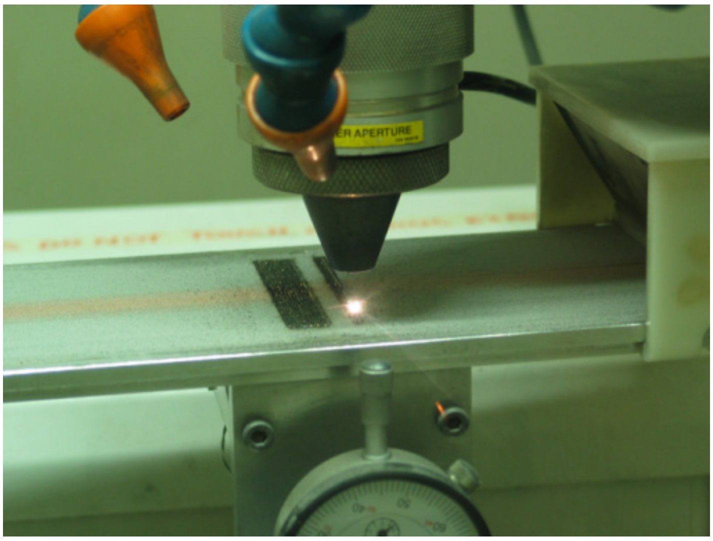

Figure 7-22. Photograph of the manufacturing of a layer for two specimens.

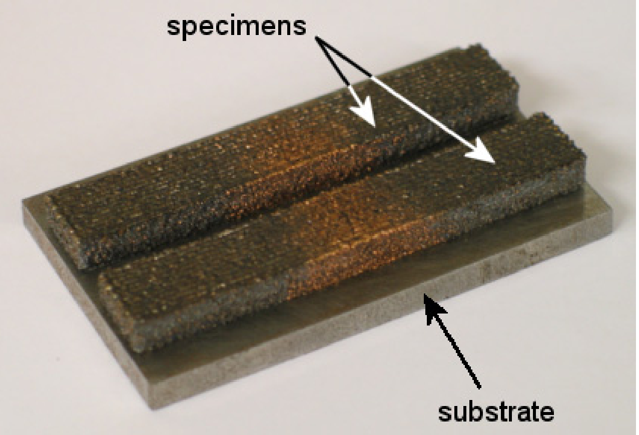

Figure 7-23. Specimens completed after the selective laser fusion.

To save time and to make easier to wire spark erosion cut the specimen, the top surface of the specimens were grounded in precision grinding machine. Afterwards, two holes were drilled in substrate in the space between the specimens to help in the preparation for the CNC wire cutting machine. The Figure 7-24 shows two specimens with their surface grounded and the holes drilled in the substrate.

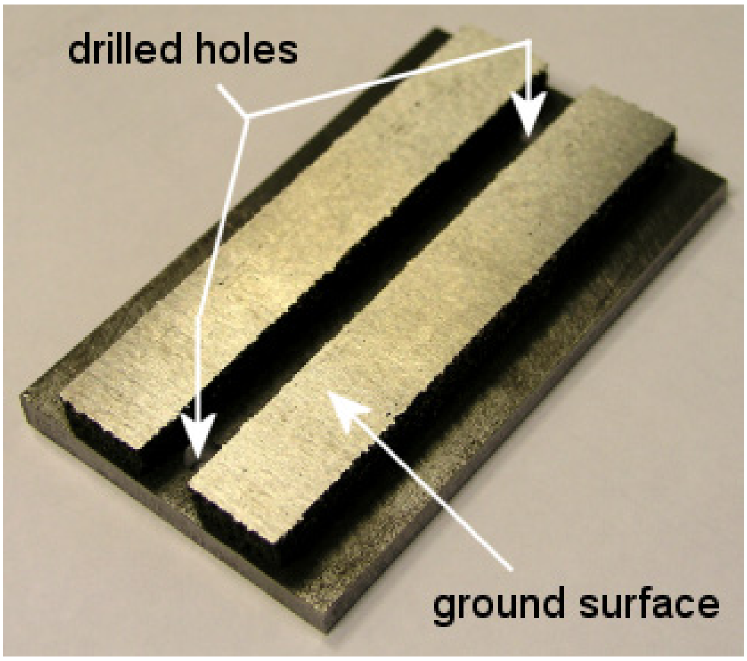

Figure 7-24. Specimens with top surface grounded and drilled holes in the substrate for the wire spark erosion process.

The spark erosion process was carried and the first step was to cut the tensile test profiles and then to cut releasing them from the substrate. The ten specimens obtained with 250µm are show in Figure 7-25.

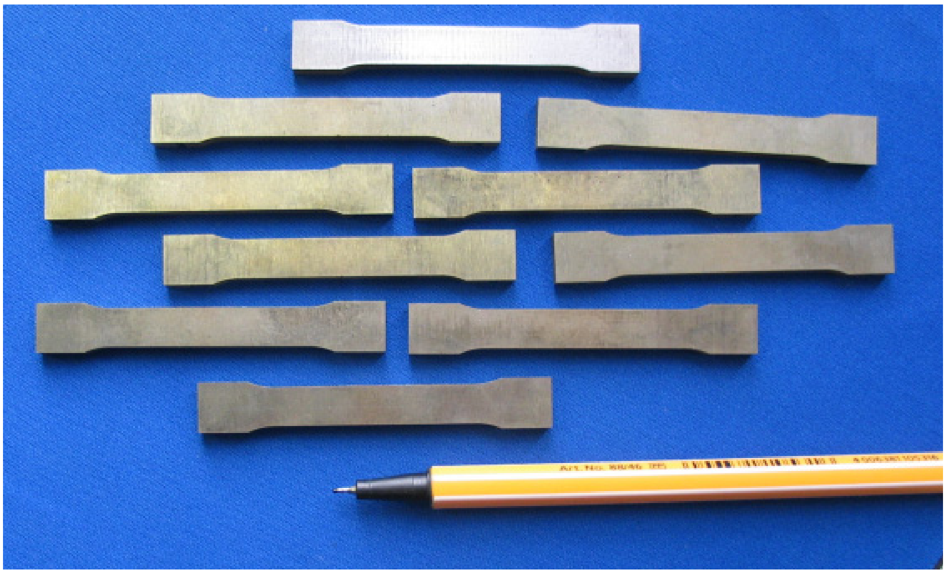

Figure 7-25. Tensile test specimens after final wire spark erosion.

After the spark erosion, great difference could be seen between the two set of specimens. The specimens manufactured with 500µm presented high porosity in contrast with the high density obtained with the specimens with 250µm. Figure 7-26 shows two specimens of each set and the position of each material composition of the gradient.

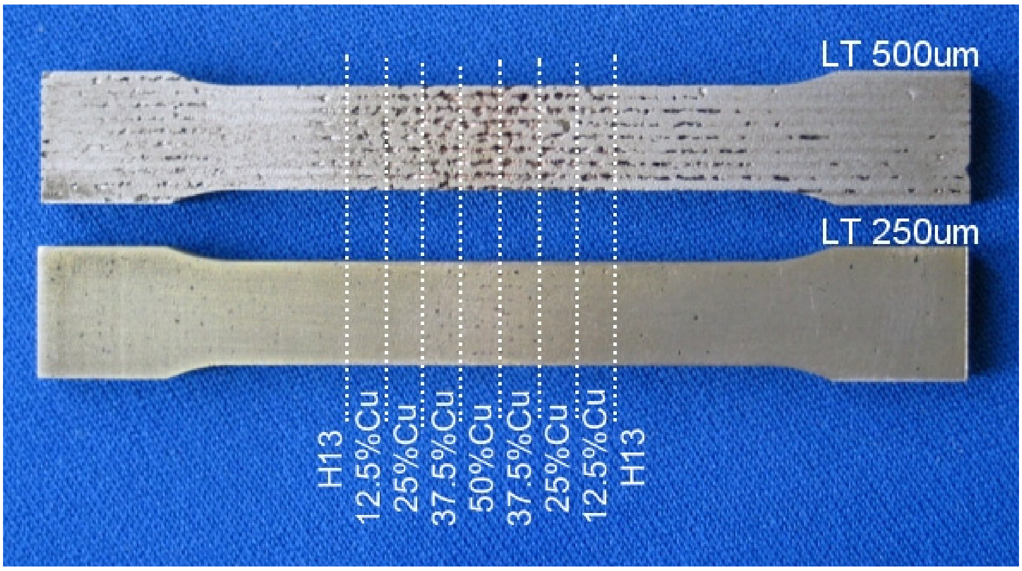

Figure 7-26. Comparison between specimens obtained with 250 and 500µm of layer thickness (LT) and the position of each material composition in the graded region.

7.6.4. Tensile test experiment preparation

The tensile specimens were tested using an Instron 1195 tensile test machine with 25mm extensometer. The test was performed at 1mm per minute rate and room temperature around 20°C. A image of the extensometer attached to the specimen mounted in the tensile machine is presented in Figure 7-27. In this figure is also possible to identify marks that were made with colour markers. These marks corresponded to the predicted powder compositions distributions from the feedhopper used to build the specimens. The extensometer was placed in such way to have all different compositions inside its range of measurement. From the fourteen FGM specimens manufactured, one was not used in the tensile tests for future demonstration purposes. So, nine specimens with 250µm and four with 500µm of layer thickness were tested.

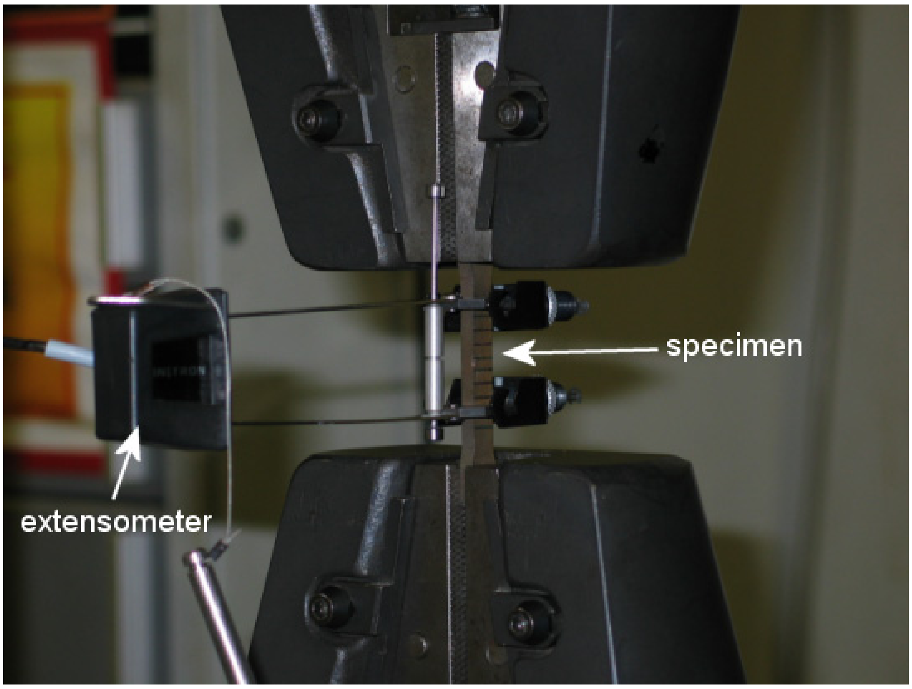

Figure 7-27. Specimen assembled in the machine claws with the extensometer attached.

7.6.5. Results of the tensile test

The data from the tensile tests was acquired and analysed using Statgraphics software for statistical analysis of the results. With all points from each stress versus strain curves, regression analyses were performed. In Figure 7-28, the individual curves for each specimen with 250μm of layer thickness are plotted. It is noticeable that there was a very dispersive behaviour of the specimens. Due to the gradient characteristics, the curves did not present a true elastic behaviour (linear). As it can be seen, the ultimate tensile strength (UTS) was lower than expected for pure annealed Cu (210MPa; Matweb, 2005-2). The average value of the UTS was 144,644±15,68MPa (interval for 95% of confidence and standard deviation of 20,4MPa). The strain at break (elongation) was 0,276±0,081% (interval for 95% of confidence and standard deviation of 0,085%). Comparing with the H13[6] (9%) and Cu[7] (14% cold draw, 60% annealed) the FGM specimen presented virtually no deformation.

---

[6] Matweb, 2005-1.

[7] Matweb, 2005-2.

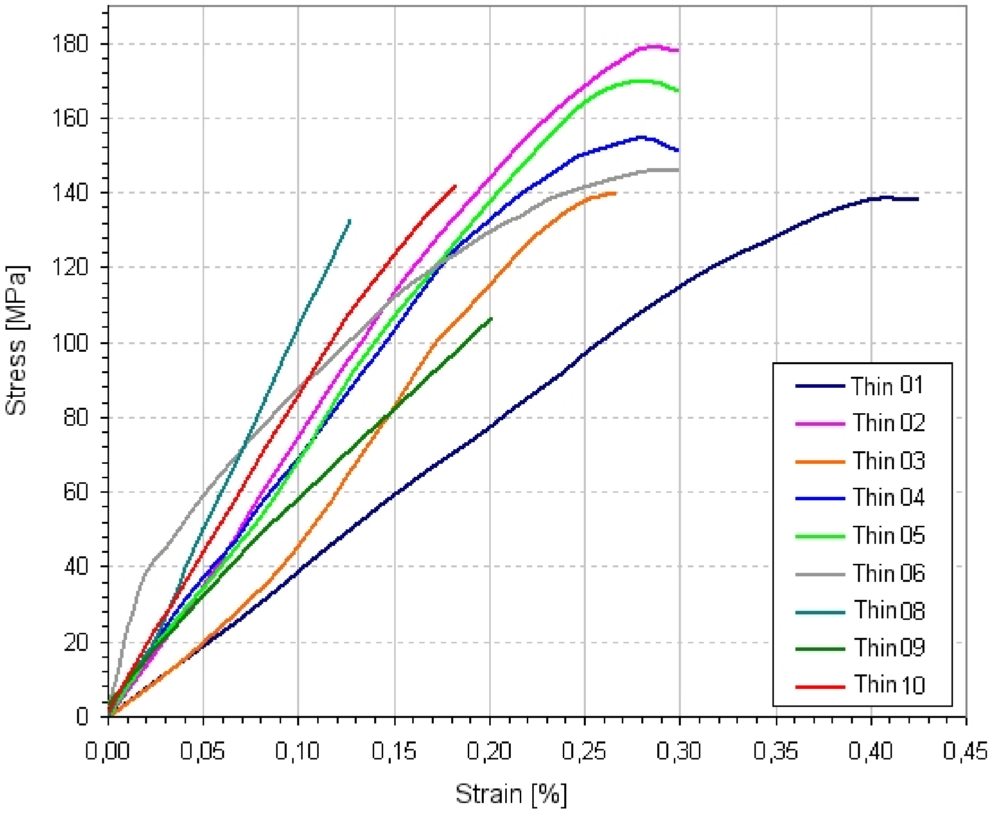

Figure 7-28. Stress x strain curves for the 250µm (thin) layer thickness specimens.

To obtain the elastic modulus, all points (stressXstrain) from the cures were plotted and a regression analysis was performed. From the diverse models applied to check the regression, a third degree polynomial equation fitted better all the range of the curves. The regression analysis is summarized in Table 7-9.

Table 7-9. Polynomial regression analysis for fine layer specimens.

Parameter	Estimate	Standard Error	T Statistic	P-Value
Constant	2,55834	4,29831	0,595197	0,5527
ε	648,652	102,201	6,34681	0,0000
ε^2	360,955	646,634	0,558206	0,5776
ε^3	-2874,83	1135,3	-2,53222	0,0124

ε: strain

Hence, the model obtained from the regression is presented by equation 7.16, where σ is the stress and ε is the strain.

$$\sigma = 2{,}55834 + 648{,}652 * \varepsilon + 360{,}955 * \varepsilon^2 - 2874{,}83 * \varepsilon^3 ; \quad \text{[MPa]} \qquad \text{Eq. 7.16}$$

In Figure 7-29, the result from the polynomial regression is presented. The blue lozenges are the experimental data. The blue solid line is the curve from equation 7.13. The red curves limits the 95% confidence interval for stress. The pink outer bounds are the limits for new observations with the same confidence interval.

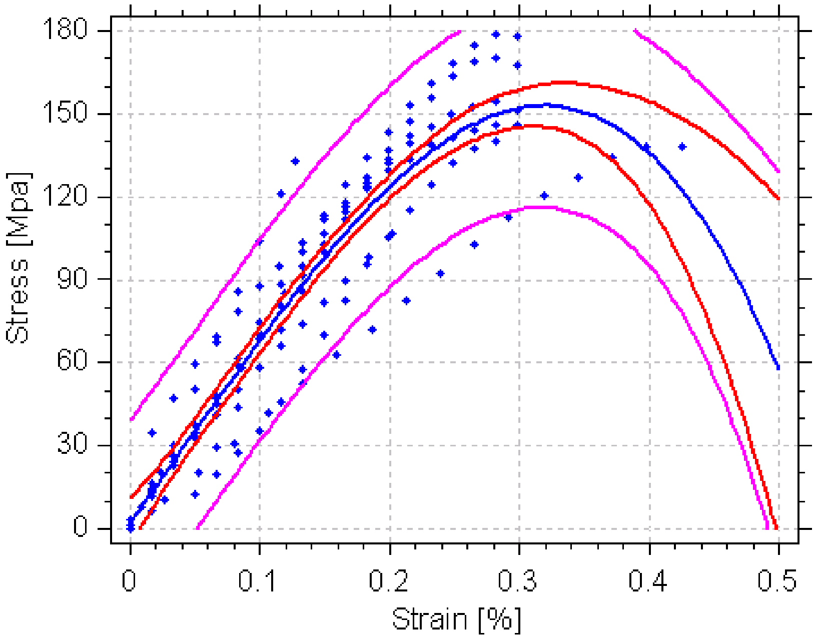

Figure 7-29. Polynomial regression applied to all points from the 250µm specimens.

The analysis of variance for the polynomial model is presented in Table 7-10. This analysis helped to determined if the model was adequate or not. The R-squared test adjusted for the degree of freedom test showed that the model explains 87,3% of the variability of the stress.

Table 7-10. Analysis of variance for fine layer specimens.

Source	Sum of Squares	Degree of freedom	Mean Square	F-ratio	P-value
Polynomial Model	332332,0	3	110777,0	333,09	0,0000
Residual	47225,3	142	332,572	-	-
Total (corrected)	379558,0	145	-	-	-

Although the third degree model represented well the curves obtained, it is preferable that a linear model to be used to calculate the elastic modulus. With the assumption that most of the stressXstrain curves in Figure 7-28 have a linear behaviour until 0,20%, a linear regression was performed within this deformation range (0-0,2%). In Table 7-11 the linear regression analysis is presented.

Table 7-11. Linear regression analysis for the fine specimens until 0,2% of deformation.

Parameter	Estimate	Standard Error	T Statistic	P-Value
Constant	5,15497	3,00347	1,71634	0,0890
ε	60669,4	2562,72	23,6738	0,0000

ε: strain

From the regression, the model fitted is represented by equation 7.17. In this equation, the coefficient of the strain represents the slope of the regression curve. This slope is the elastic modulus of the material (E=Δσ/Δε). So, for the fine layer specimens the elastic modulus calculated from the regression was 60,7GPa. This value is far below the Cu and H13 reference values (Cu[8]: 110GPa; H13[9]: 210GPa). Also, it is lower than the experimental values obtained in the DSI experiment (section 7.5).

$\sigma = 5{,}15497 + 60669{,}4 * \varepsilon$; [MPa] Eq. 7.17

The data from until 0,2% of deformation, the linear model (blue solid line), confidence interval (red lines) and the limits for new observations (pink lines) are show in Figure 7-30.

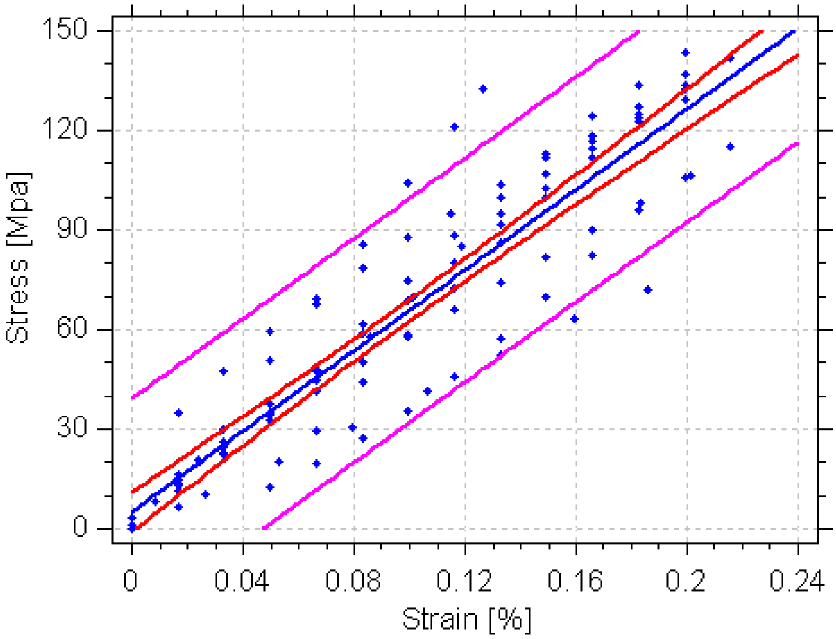

Figure 7-30. Linear regression until 0.2% of deformation for the 250µm specimens.

The analysis of variance for the models is show in Table 7-12. The R-square test adjusted for the degree of freedom pointed that the linear model explains 83,8% of the variability.

Table 7-12. Analysis of the variance of the model for fine specimens until 0,2% of deformation.

Source	Sum of Squares	Degree of freedom	Mean Square	F-ratio	P-value
Polynomial Model	160807,0	1	160807,0	560,45	0,0000
Residual	30701,1	107	286,926	-	
Total (corrected)	191508,0	108	-	-	-

---

[8] Matweb, 2005-2

[9] Matweb, 2005-1.

For the specimens built with layer thickness of 500µm the stressXstrain curves are plotted in Figure 7-31. Notice that the UTS was even lower than for 250µm specimens. The average value for the UTS was 106,40±21,12MPa (for a 95% of confidence interval and average of 13,3MPa).

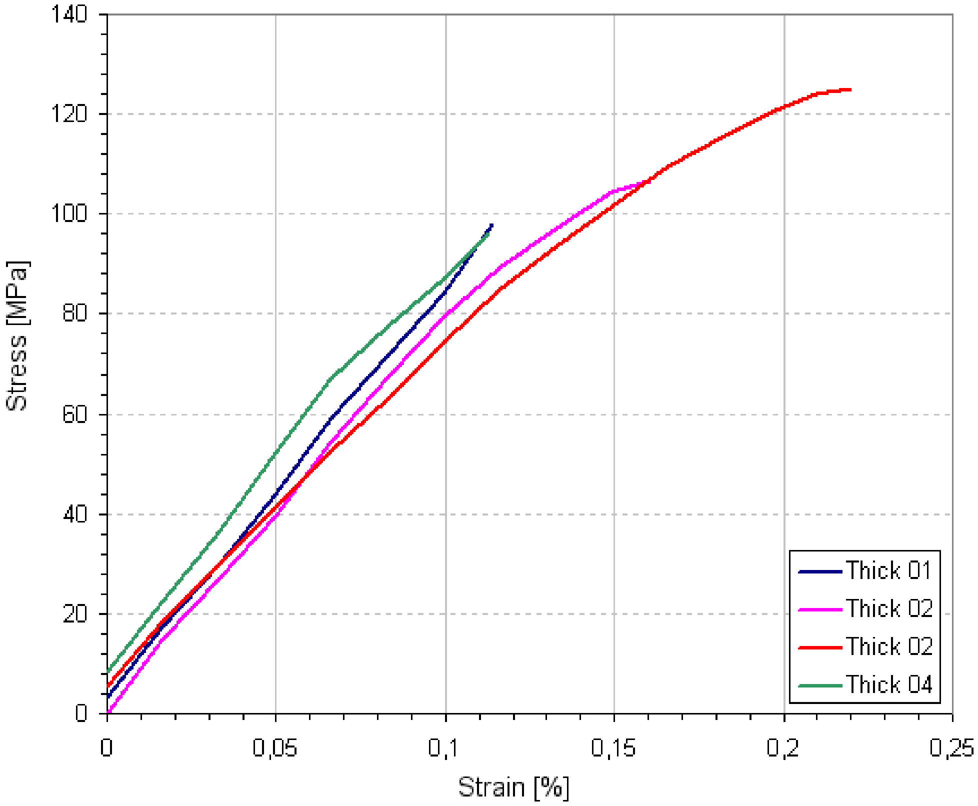

Figure 7-31. Stress x strain curves for the 500µm (thick) layer thickness specimens.

Statistical tests were performed in order to identify if the averages for the UTS and elongation at break found for 250 and 500µm were different. In both cases, it was proved with 99% of confidence that these are two different groups of specimens. So, it possible to affirm that fine layer thickness increased almost 50% the strength of the specimens.

Other test performed also calculated the elastic modulus for the thicker specimens by the same method applied and presented previously. The result for the curve slope from the linear regression showed an elastic modulus of 59,6GPa, calculated with all data (0-0,22%). The R-square test adjusted for the degree of freedom pointed that the model explained 94,7% of the variability.

Analysis of the specimens after the tensile test, it was noticed that the section broke as fragile material, presenting no area reduction. It was expected, as no deformation was perceptible in the stressXstrain curves. In addition, the colour marks along the specimens, indicating the composition region, showed that all specimens broke at the same position, in H13-25%Cu. The tested specimens, side by side, are presented in Figure 7-32.

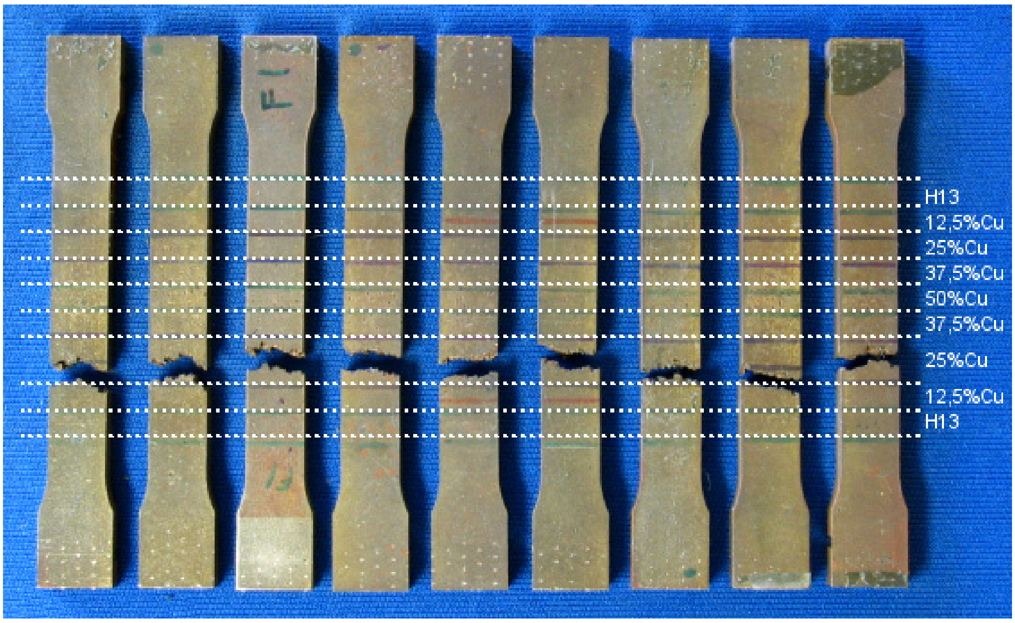

Figure 7-32. Position where the specimens broke.

Closer look at the broken section, showed that the crack followed the pattern of the laser beads, leaving a multi-planar section. In Figure 7-33, closer images of a broke section are presented. The “hand saw” effect can be observed in Figure 7-33 (a) and (c). In Figure 7-33 (b) this effect can be notice by the horizontal lines (aligned with the z building direction). A closer view is presented in Figure 7-33 (d) and cracks are identified by dashed red lines.

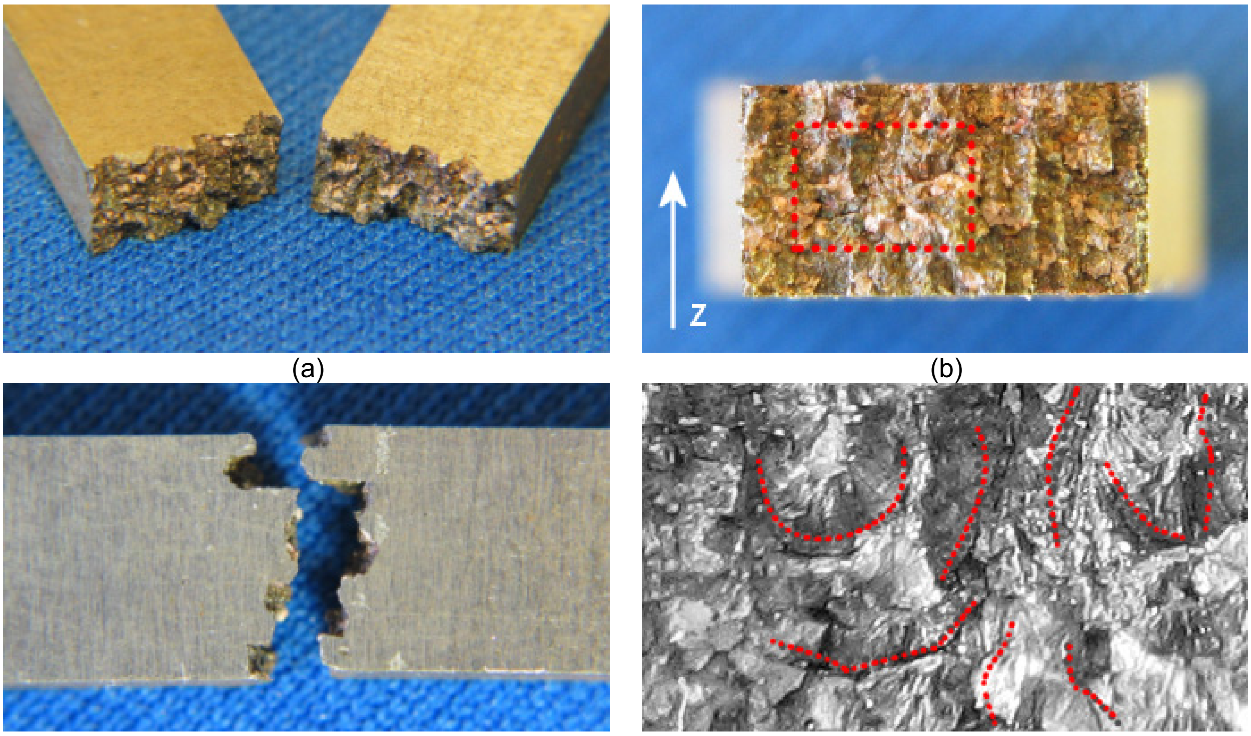

(a) (b)

(c) (d)

Figure 7-33. Closer images to a failed section of a 250µm layer thickness specimen.

An analysis using the SEM, showed that, as expected, the most probably reason for the low mechanical properties obtained came from the cracks present in the microstructure. In Figure 7-34 a SEM micrograph is presented indicating pores and cracks.

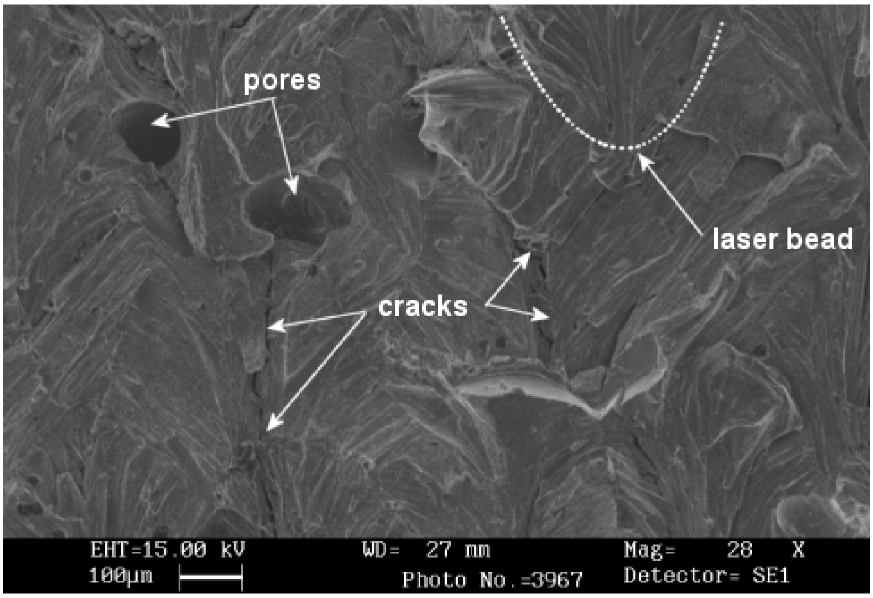

Figure 7-34. SEM micrograph from a broke section of a specimen with 250µm of layer thickness.

7.6.6. Discussion on tensile test

It is important to remember that in this experiment what was tested was the gradient of a specimen and not materials alone. In Table 7-13, it is summarized the elastic modulus, UTS and elongation at break for reference materials, DSI test, tensile test and estimated by the FGM model explained before (equation 8.15). The FGM model was calculated by three ways: using estimations by Reuss ROM, the data from the DSI lower limit (average values minus one standard deviation) and the DSI average values.

Table 7-13. Summary of the properties obtained and comparison with other results and references.

Material	Elastic modulus [GPa]	UTS [MPa]	Elongation at break
H13 (ref.)	210	1990	9%
H13 (DSI test)	235,2	-	-
12,5%Cu (DSI test)	204,2	-	-
25%Cu (DSI test)	186,0	-	-
37,5%Cu (DSI test)	185,7	-	-
50%Cu (DSI test)	175,4	-	-
Cu annealed (ref.)	110	210	60%
Cu cold draw (ref.)	110	344	14%
FGM experimental 250µm	60,6	144,6	0,276%
FGM experimental 500µm	59,6	106,4	0,152%
FGM model (Reuss)	177,4	-	-
FGM model (DSI lower)	181,3	-	-
FGM model (DSI)	197,7	-	-

The discrepant results from the elastic modulus from FGM model to the results obtained by the tensile test showed that the specimens had poor mechanical qualities. A graphical comparison between the elastic modulus is presented in Figure 7-35 The elongation at break showed that that they did not deformed. The fracture analysis also proved to show a fragile behaviour. In contrast, the elastic modulus is the elastic modulus of a ductile material. In this case, it was more ductile than pure annealed copper. These results showed that the number of defects present in the microstructure of the specimens is too high even with the laser processing optimizations. Or course, it is necessary to remember that only one laser processing parameter was used during this experiment and optimized for 12,5%Cu. As the specimens had failed in the 25% region, it might by the use of the laser parameters. Possibly, the use of specific laser parameter over each region of composition could lead to better results and random region failure. It might start to occur in the interface regions of the material compositions.

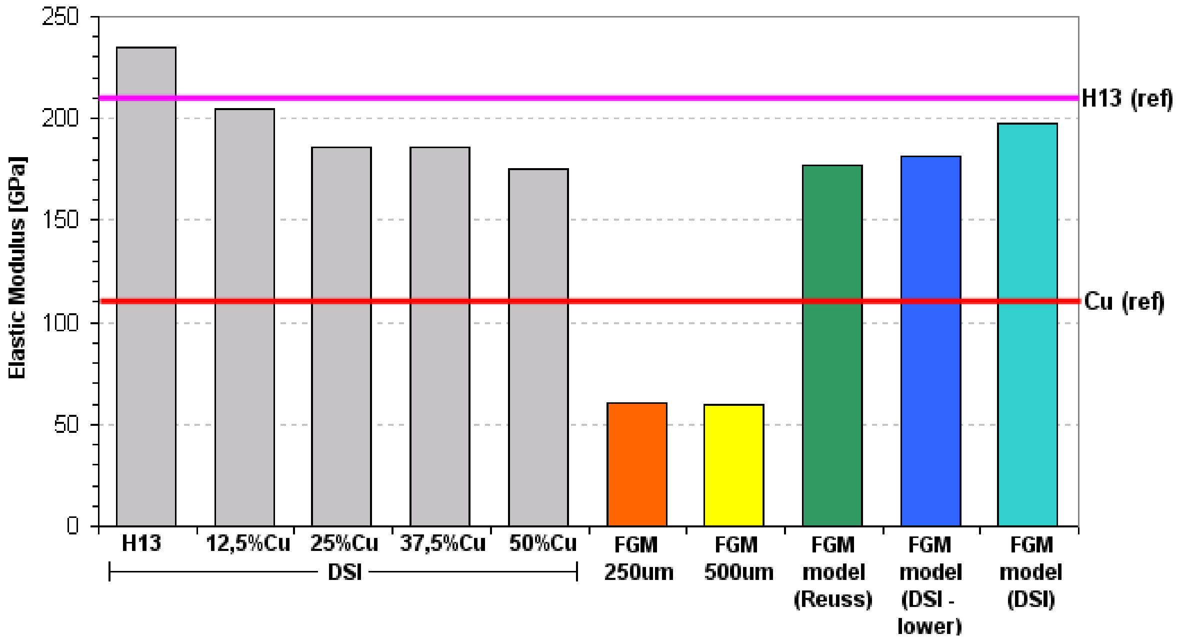

Figure 7-35. Graphical comparison between the elastic modulus of materials and FGMs.

The difference between the elastic modulus of the specimens made with 250µm and 500µm of layer thickness was small despite the fact that the thicker specimens were only four samples in total. On the other hand, the average UTS was almost 30% lower for the specimens built with 500µm. This was due to the large visible pores found in the specimen.

7.7. General comments on the obtained properties

In this chapter, the compositions and the gradient were evaluated in different forms. Despite the limitation, the process revealed a successful to obtain dense parts. Although, parts/specimens were dense, the presence of defects in the microstructure contributed to poor results in some tests such as the tensile test experiment. Possibly, the major defect that affected the results was the cracks. Despite the effort to reduce them in chapter 6, they still present in the microstructure. They acted as stress concentration points, area reduction and internals barriers. Nevertheless, the cracks presence has an origin that relates not only to the laser processing but also to the environment condition (non-heated chamber) and no post-processing after building with heat treatment. Regardless the attempt to avoid moisture with the use of silica bags to store to powder, it might be also one of the contributors to cracking pores.

Chapter 8

Applications of FGM H13-Cu parts

"…
Sabes tudo o que acontece ao redor do meu mundo
Espero que a memória não me falhe mais
Você chegou me fez pensar e acreditar que vida é boa
...
Deixa que eu vou
Vou na marola vou na fé
Vou nessa porque o tempo já me avisou..."

Dazaranha – Deixa

8. Applications of FGM H13-Cu parts

The purpose of developing new FGM combinations like the tool steel and copper performed in this work was to investigate the applicability on technical/commercial products. One section of this chapter describes the investigations of H13-Cu parts produced for injection moulded inserts. The performance of the insert and the effect on the injection moulded part are discussed. The other section shows that more complex shapes are possible to obtain using this process in the adapted machine.

8.1. Evaluation of potential use of FGM H13-Cu mould for injection moulding

The use of FGM to obtain performance injection moulds was one of the stimuli for this research. Despite the limitations of the laser system used in this work, this experiment was planned to evaluate the influence of the Cu addition to the H13 matrix. The effect of the addition of Cu in the mould temperature and in the injected polymer part crystallinity degree comparing to the H13 base material was analysed. In theory, the addition of Cu would increase the thermal conductivity of the mould. So, the work was divided in two parts, numerical modelling of the heat transfer and experimental injection moulding.

The first part presents the numerical model of the heat transfer from the injected part to the mould and the metallic inserts. The difference of the temperature along the time between the model for the thermal material properties of pure H13, Cu and an approximation for H13+50%Cu were analysed.

In the injection moulding experiment, FGM bars (mould inserts) were manufactured by laser fusion and placed in a stereolithography mould. Polypropylene (PP) parts were produced injecting the polymer over these metallic inserts. Two outputs were analysed from this experiment: temperature of the mould surface and crystallinity degree of the PP parts. The temperature of the mould was measured by thermocouples in the exact same position taken in the numerical model. The degree of crystallinity of the parts, moulded with different inserts, was analysed by differential scanning calorimetry (DSC).

The idea behind the DSC test was that due to different cooling rates, the degree of crystallinity can change. The lower the cooling rate the greater is the number of crystals in the polypropylene. The slow cooling allow the polymer chains to organize them selves, forming crystalline structures. A rapid cooling rate helps the polymer to holds an amorphous structure. When heating a plastic, more heat will be necessary to dissolve the crystals (more stable and lower energy state) until melt the plastic completely. This phenomenon can be seen in the DSC curves measuring the energy absorbed by the sample before melting (Harris *et al*, 2004).

8.1.1. Methodology

8.1.1.(a). Numerical model methodology

The injection moulding cycle is transient and thermal conductivity is not the only material property that counts when analysing the heat transfer. Density and specific heat capacity also rules the capability of the material for storing or transporting heat energy (Incropera and DeWitt, 1990). In the volume control presented in Figure 8-1, the variation of the energy accumulated by the mass inside the volume can be modelled by equation 8.01.

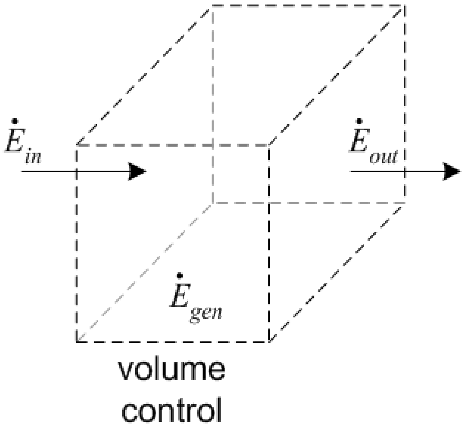

Figure 8-1. Volume control for the heat.

$$\dot{E}_{in} - \dot{E}_{out} + \dot{E}_{gen} = \left.\frac{dE}{dt}\right|_{vc} \qquad \text{Eq. 8.01}$$

The energy that enters ($\dot{E}_{in}$) plus the energy generated ($\dot{E}_{gen}$) inside the volume minus the energy lost ($\dot{E}_{out}$) to the surroundings is equal to the variation of energy (*E*) of the mass inside the volume along the time (*t*). In the case of a mould, in the moments after the melted material fills the mould impression, there is no heat generated in defined volume control. Considering the heat transfer in unidirectional, the equation 8.01 becomes more simplified for the heat flux through an area *A,* generating equation 8.02. Simplifying the area, equation 8.03 is obtained. In these equations, *q"* represents the heat fluxes, *ρ* is the material density, c_p symbolizes the specific heat, *T* is the temperature and *x* is the axis of the direction of the heat flux.

$$q_{in}''.A - q_{out}''.A + 0 = \int_x \rho.c_p.\frac{\partial T}{\partial t} A dx \qquad \text{Eq. 8.02}$$

$$q_{in}'' - q_{out}'' = \int_x \rho.c_p.\frac{\partial T}{\partial t} dx \qquad \text{Eq. 8.03}$$

The temperature in the mould, away from the impression, could be considered constant. Taking this consideration, the heat fluxes, in a very short period can be considered constant and it could be described as in equation 8.04, where *k* is the heat conduction coefficient.

$$q'' = k\left.\frac{\partial T}{\partial x}\right|_x \qquad \text{Eq. 8.04}$$

There is no easy solution for solving equation 8.04 and a numerical model is usually necessary to solve it. A two-dimension model of an injection moulded part inside a stereolithography (SL) mould in contact with a metallic insert is show in Figure 8-2. This model considered no contact resistance between the parts, moulds and insert surfaces. The initial conditions were that the temperature in the nodes inside the area that represents the hot polypropylene injected part was 195^{0}C and the temperature for all other nodes, including the connected nodes of the part with other areas was 20^{0}C. Temperature was calculated by employing a quadrangular mesh formed by planar 4 nodes elements. The nodes chosen to be analysed are indicated in Figure 8-2. Thermocouple temperature, T_{tc}, matched the same position in the experimental work and insert surface temperature, T_{is}, matched the region from where DSC samples were taken in the PP part. The model and analysis were performed using Ansys software.

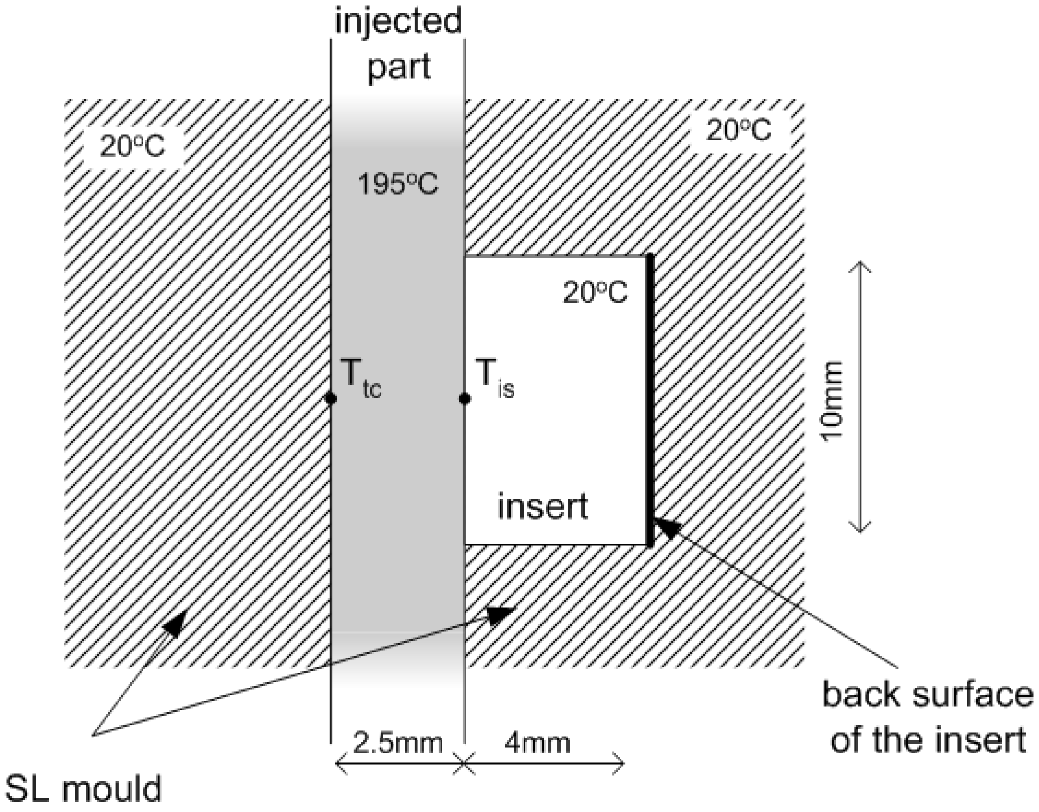

Figure 8-2. 2D model for the heat transfer of an injected part in contact with a metallic insert in a SL mould (initial temperature indicated for each area of the model).

For inputting the material properties (density, specific heat and thermal conductivity) in the numerical model, tabled values were used. However, the H13+50% material properties values were estimated based on the rules of mixtures well covered previously in section 2.4.1. The materials properties used in the model are presented in Table 8-1.

Table 8-1. Material properties used in the numerical model.

Model area	Material	Density	Heat capacity	Heat conduction
		(g/cm^3)	(J/g.^{o}C)	(W/m.K)
SL mould	RenShape 7580 resin [1]	1,22	2,00 (*)	0,2 (*)
Part	Polypropylene [2]	1,00 (**)	2,00	0,13
Insert	H13 [3]	7,80	0,460	24,3
	Cu [4]	8,96	0,385	385,0
	H13+50%Cu – Voight	8,34	0,425	192,2
	H13+50%Cu – Reuss	8,3	0,422	43,1

(*) estimative
(**) average

[1] – Huntsman (2005)
[2] – Matweb (2005-4)
[3] – Matweb (2005-1)
[4] – Matweb (2005-2)

8.1.1.(b). Injection moulding experiment methodology

To investigate the effect that FGM have on injection moulded parts, graded inserts of H13 and Cu were manufactured using selective laser fusion and the multi compartment hopper from section 4.1.2, Figure 4-6. The laser processing parameters were energy pulse: 10J, pulse width 20ms, repetition rate 20Hz and scan speed 5mm/s. The layer thickness used was 250μm with the refill strategy and Ar to reduce oxidation. Five powders compositions were used in the feedhopper to produce a symmetrical gradient with 50%Cu in the middle. The powders used were the same described in section 4.3. After building the specimens, they were post processed by cutting off the substrate and grinding its surfaces. The final dimensions of the grade insert and the especial distribution of the gradient on it are presented in Figure 8-3. Each different blend was fused on 3.5mm wide as it was spaced in the feed hopper. A pure H13 was made from stock annealed H13 by cutting and grinding and had the same dimensions than the FGM specimen.

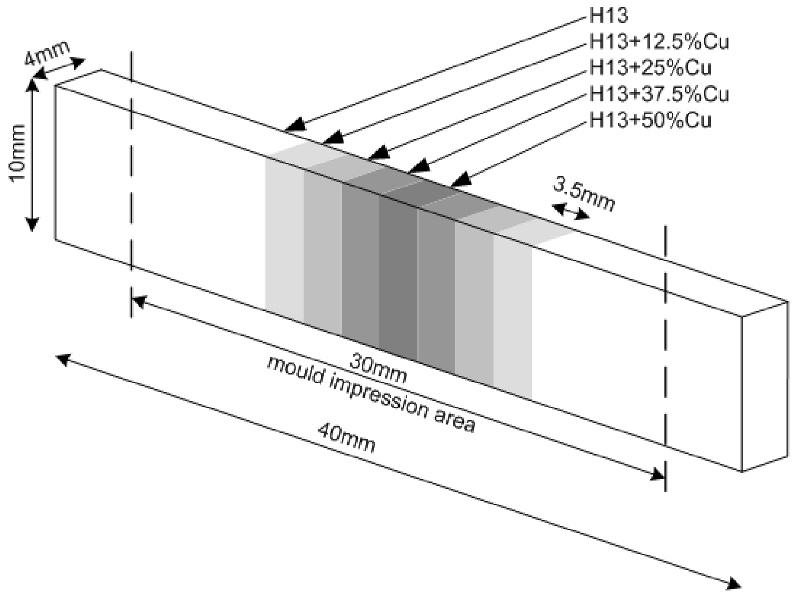

Figure 8-3. FGM insert and the disposition of the gradients.

An injection mould was designed specifically for holding and changing the inserts. The design of the impression consisted on a simple slab 30x60x2,5mm. The process used to build the mould was the stereolithography. This choice was taken because stereolithography resins have low thermal conductivity and can work as an insulator. Therefore, the influence of the metallic inserts would be more distinctive. The mould design considered also the position to insert two thermocouples to read the mould temperature during the injection cycles. The position of the thermocouples is show in Figure 8-4.

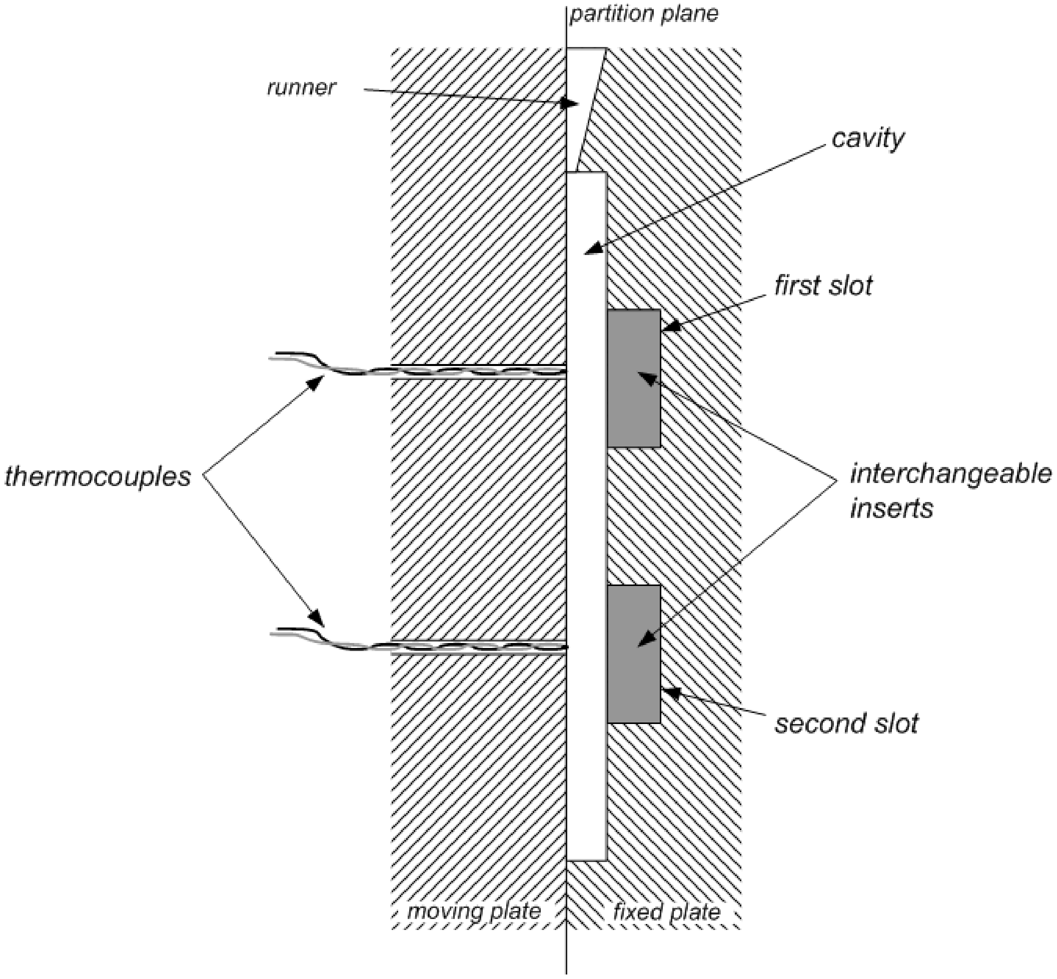

Figure 8-4. Position of the thermocouples in the cavity.

The mould was build using a 3D Systems SLA7000 stereolithography machine in Huntsman RenShape 7580 resin. The K type thermocouples were positioned and glued to the moulds surface using a commercial epoxy bi-compound resin (Araldite). After the epoxy glue got hard, it was sanded until exposure of the thermocouple tips. Figure 8-5 shows in detail the mould finished and assembled in the bolsters ready to be mounted in the injection moulding machine. The injection moulding machine used was a Battenfeld TM750/210 and thermocouples were connected to a CR10X datalogger from Campbell Scientific. Data was collected each 5 seconds and the room temperature was 20°C. The injection moulding material was the Solvay Eltex-P HY202 polypropylene (PP).

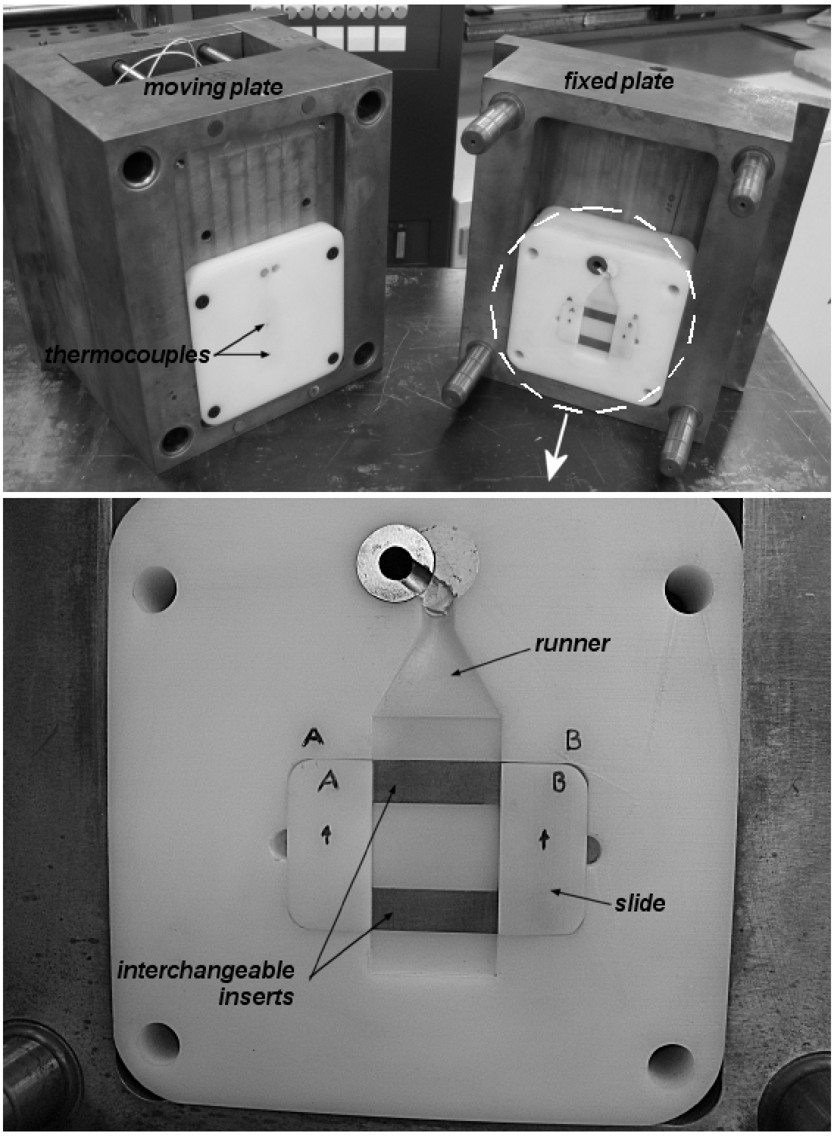
moving plate
fixed plate
thermocouples
runner
A
B
A
B
slide
interchangeable inserts

Figure 8-5. Injection mould (above) and in detail the interchangeable inserts (below).

The injection moulding procedure started placing the FGM insert in the first slot and the H13 in the second slot. After 20 injection cycles, the inserts were swapped and the FGM insert was placed in the second slot and the H13 to the first slot and more 20 cycles were performed. Table 8-2 shows the injection moulding cycle and the inserts position on each slot corresponding to Figure 8-4.

Table 8-2. Injection moulding order and position of the inserts.

	First slot	Second slot
Injection moulding A series (IMA)	FGM insert	H13 insert
Injection moulding B series (IMB)	H13 insert	FGM insert

Between each mould opening a delay of 120s was taken to allow the inserts to cool down. Release agent was not necessary as the geometry was geometrically simple and an ejection draft angle was used in the mould impression surfaces to make part ejection easier (1,5^{o}). The injection moulding parameters were kept constant and they are presented in Table 8-3. The low injection and holding pressures are typical for stereolithography moulds. Most of the SL resins get soft above 80^{o}C and high pressures and temperatures must be avoided in order to increase moulds life.

Table 8-3. Injection moulding parameters.

Parameter	*Setting*
Clamping Force	64kN
Injection Pressure	160bar
Injection Speed	10ccm/s
Injection Temperature	195^{o}C (nozzle)
Holding Pressure	60bar (during 1s)
Cooling time	30s
Time before next injection (open mould)	120s

Differential Scanning Calorimetry (DSC) of polypropylene parts obtained in the second and sixteenth cycles of the A and B injection moulding series were taken. The apparatus used for these tests was a Shimadzu DSC-60. The samples were taken from the polypropylene parts, on the exact same position for all parts. The positions were the face in contact with the inserts (FGM and H13) on the same spot where the thermocouple was placed. Figure 8-6 shows these regions in more detail. The PP samples having masses between 5 to 7mg were inserted on aluminium pans for DSC, covered and placed in the apparatus. The tests were performed from the room temperature (19-21^{o}C) until 300^{o}C with a heating rate of 10^{o}C/min. The results were analysed using the Shimadzu ta60 version 1.51 analysis software. The main objective of the DSC tests was to compare the degree of crystallinity of part obtained using different inserts in the injection moulding impression. The percentage of crystallinity can be calculated by equation 8.05. ΔH is the heat of fusion for the polymer tested and the $\Delta H_{100\%}$ is the heat of fusion for the same polymer in 100% crystallinity (Potsh and Michaeli, 1995).

$$\chi\% = \frac{\Delta H}{\Delta H_{100\%}} \qquad \text{Eq. 8.05}$$

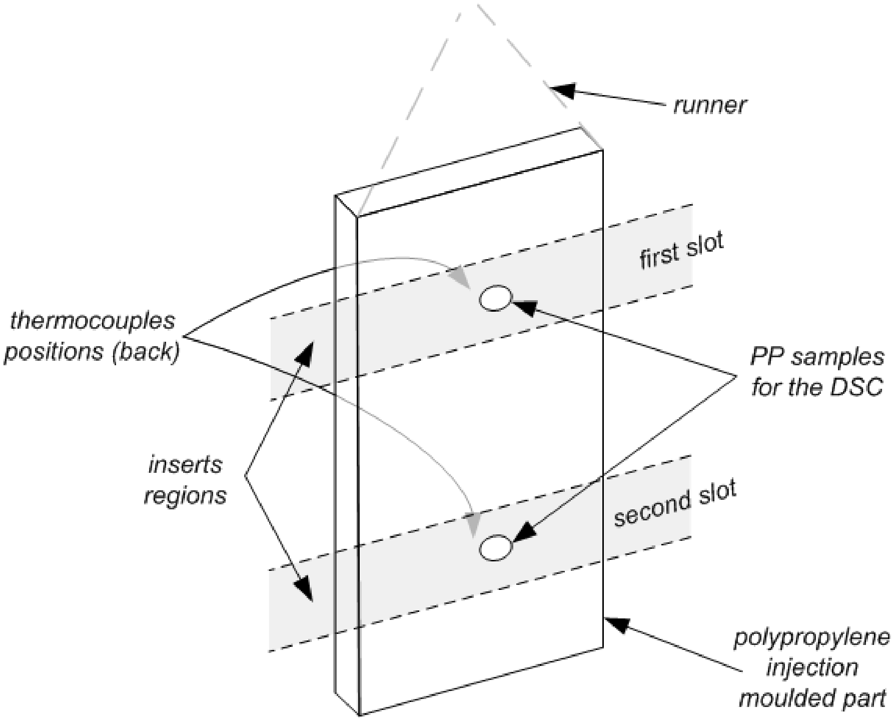
runner
first slot
thermocouples positions (back)
PP samples for the DSC
inserts regions
second slot
polypropylene injection moulded part

Figure 8-6. Regions from where the PP samples were taken from the specimens.

8.1.2. Results

8.1.2.(a). Numerical Analysis Results

In total, six analyses of the time versus temperature in T_{tc} and T_{is} (refer to Figure 8-2) were made. In these analyses, all nodes except for the nodes inside the volume that represents the injected part were at initial temperature of 20°C and they could change the temperature with time. The nodes inside the area that represented the PP part were at initial temperature of 195°C. The first four analyses were performed as described before were in each analysis the insert material property was change (H13, H13-50%Cu-voight, H13-50%Cu-reuss and Cu). Another two analyses were performed considering that the nodes in the back surface of the insert were kept at constant temperature of 20°C, not changing along the time. This was made to simulate in the case of using a cooling channel in the back of the insert. On these analyses, the H13 and H13+50%Cu by the rule of mixtures from Reuss equation properties were used for the inserts. The analysis and its legends in parenthesis are listed below.

1. Insert with thermal properties equal to H13 (H13);
2. Insert with thermal properties equal to Cu (Cu);
3. Insert with thermal properties calculated by Reuss equation (Reuss);
4. Insert with thermal properties calculated by Reuss equation (Voight);
5. Insert with thermal properties equal to H13 and back surface cooled at 20°C (H13 - Cooled);
6. Insert with thermal properties calculated by Reuss equation and and back surface cooled at 20°C (Reuss - Cooled);

The measured temperature in the node which represents a thermocouple (T_{tc}) had show that no significant improvement would be achieved by changing the material of the insert. Figure 8-7 shows the temperature T_{tc} versus the time. The difference between the temperature curves is so small that it is difficult to identify the curves in the graph. The difference in temperatures is only perceptible between the curves from the cooled to the not cooled inserts.

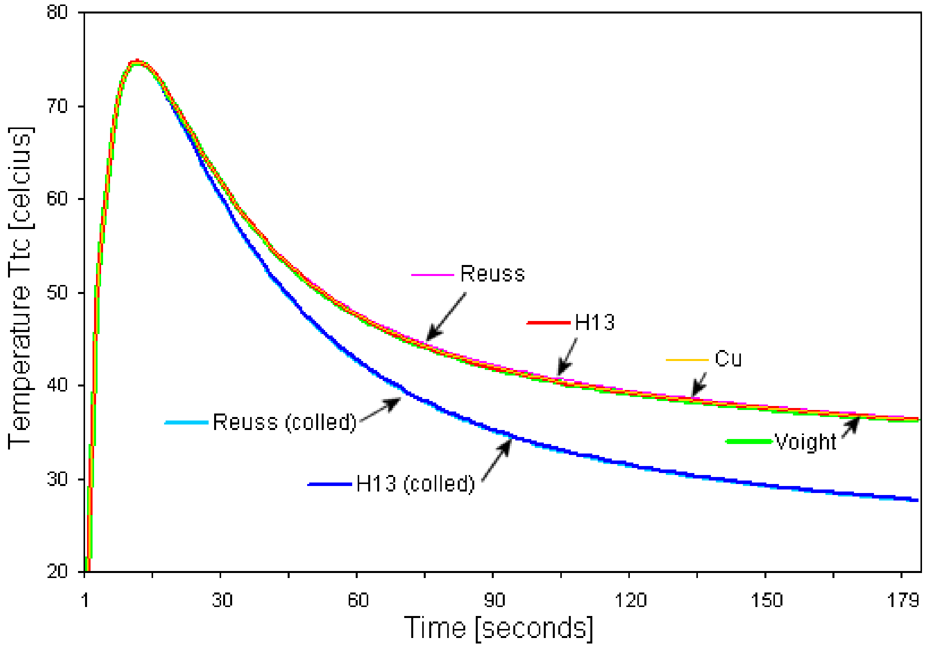

Figure 8-7. Estimated temperature of the thermocouple (T_{tc}, mould surface) along the time simulating different material properties for the insert.

In the node of the surface of the insert (T_{is}) the difference was more perceptible. Figure 8-8 shows the temperature along the time for T_{is}. In the back cooled analyses it was perceptible that the insert with intermediary properties between Cu and H13, according to the Reuss formula for the mixture, transport the energy more quickly than the pure H13. For the analyses without cooling, the only curve that showed dissimilarity from the others was again the curve from the inserts assigned with the properties calculated by the Reuss formula.

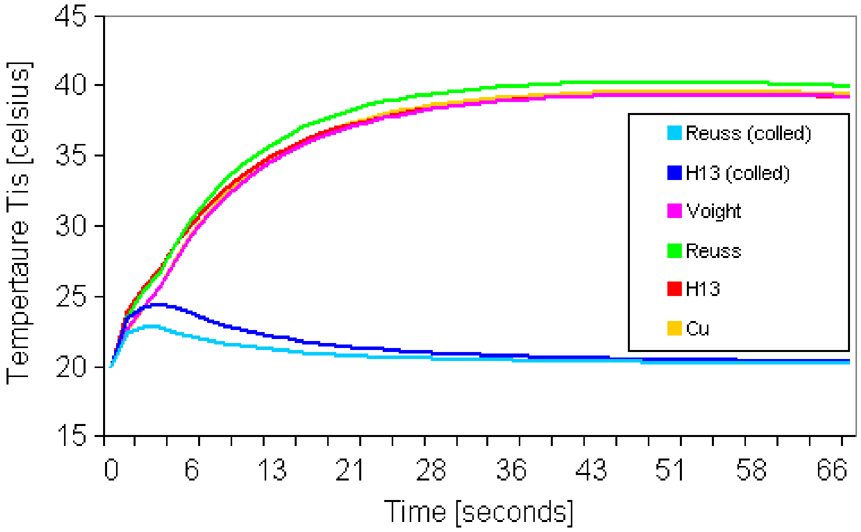

Figure 8-8. Temperature of the insert surface (T_{is}) along the time simulating different material properties for the insert.

8.1.2.(b). Injection Moulding Experiment Results

The temperature of the mould showed different results from those obtained from the numerical experiments. The temperature of the thermocouples plotted along the time in Figure 8-9 and Figure 8-10, was higher than the temperature in the results from the numerical analyses (Figure 8-7). It also presented large difference between temperatures using the two different inserts. The temperature with the FGM insert was considerably higher in both positions (1st and 2nd slots).

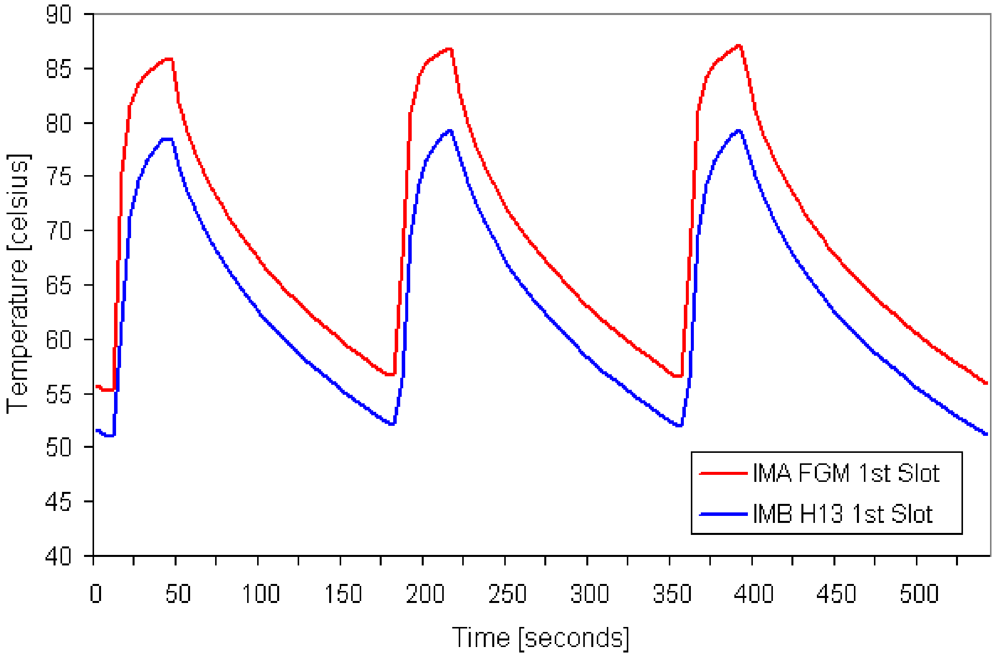

Figure 8-9. Temperature of the mould during the injection moulding series at the first slot with different inserts.

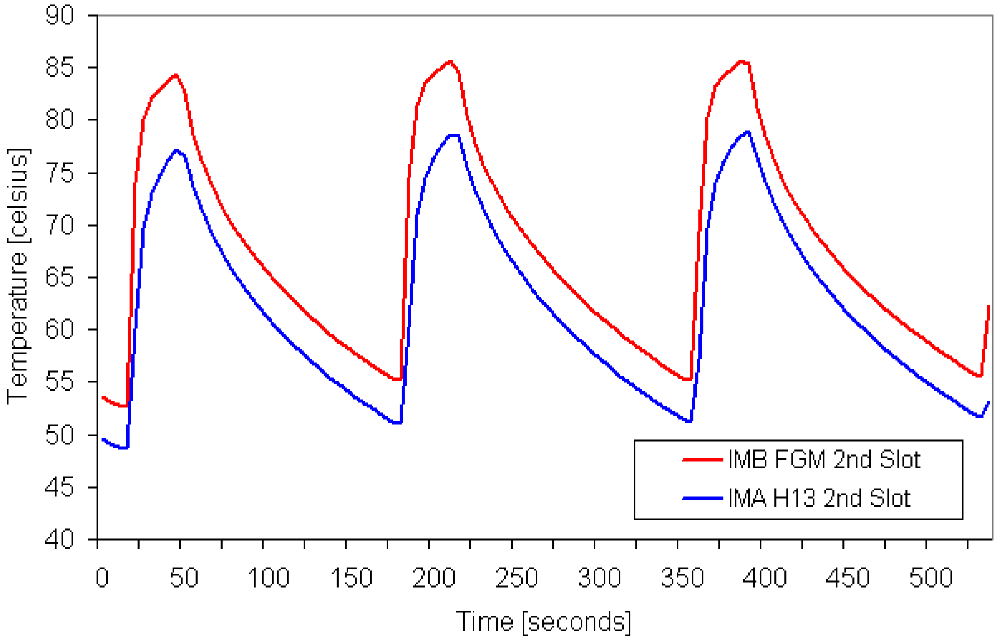

Figure 8-10. Temperature of the mould during the injection moulding series at the second slot with different inserts.

The DSC results reflected the results obtained with the thermocouples. The FGM insert presented higher temperature and lower capacity to absorb the heat from the part. This was identifiable by the higher energy necessary to dissolve the more crystalline samples moulded over the FGM insert. The curves of the DSC shown in Figure 8-11 and Figure 8-12 also present that the hotter the mould higher crystallinity was observed in the samples. Table 8-4 resumes the curves in values point the difference between the energy per gram that was necessary to melt the samples. Also, the percentage crystallinity is calculated based on equation 7. The reference 100% crystalline polypropylene value used was 209J/g (Marineli and Bretäs, 2003).

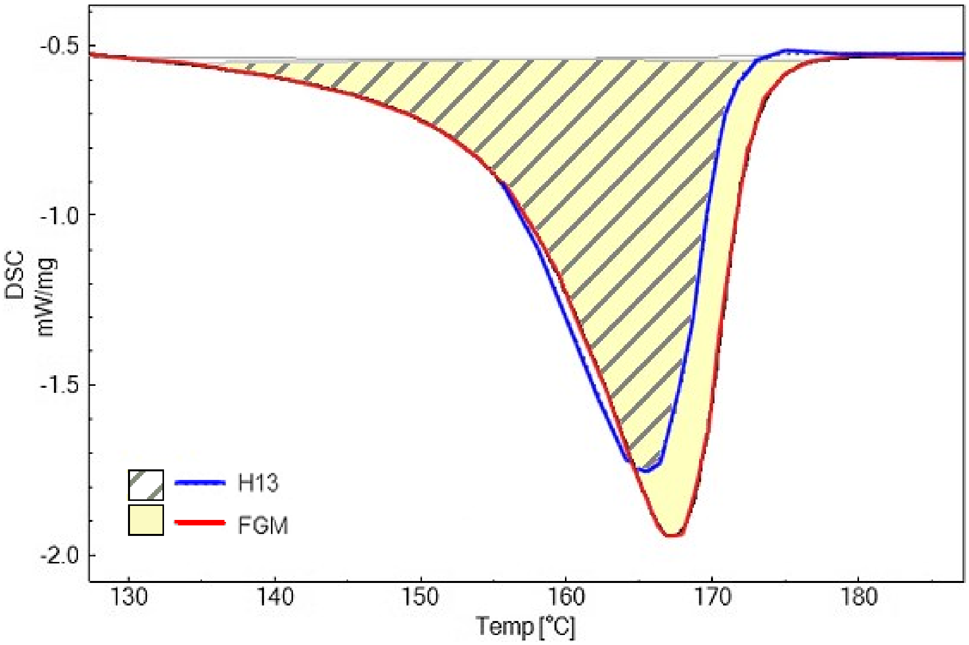

Figure 8-11. Calorimetric plot of the samples taken from parts of the 2nd cycles at the same position (1st slot).

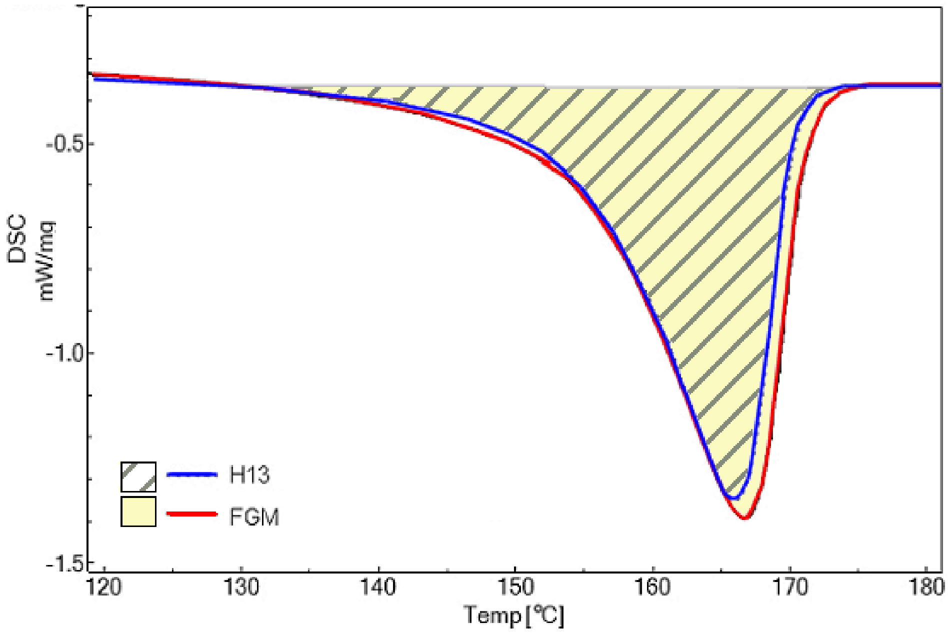

Figure 8-12. Calorimetric plot of the samples taken from parts of the 16th cycles at the same position (2nd slot).

Table 8-4. DSC summary of the PP samples analysed.

Slot	Injection Moulding Series	Insert	Peak Temperature	Heat	Heat/mass	Crystallinity Degree
			^{o}C	mJ	J/g	%
1st	IMA	FGM	167,22	635,10	109,50	52,4
	IMB	H13	165,28	548,09	94,50	45,2
2nd	IMB	FGM	166,69	464,57	76,16	36,4
	IMA	H13	165,99	382,.85	63,81	30,5

8.1.3. Discussion

The numerical results were necessary to show how, in this case, were the materials of the inserts have small difference between the heat capacity and are insulated by a SL case. There was no great difference was perceptible in the cooling performance of the insert. When simulating a cooling channel, the 50%Cu-H13 insert showed better performance even with its properties calculated by a conservative equation (Reuss) which was found to be close to the real properties obtained from earlier experiments (Chapter 7, section 7.2). Consequently, it can be assumed that the numerical analysis was based on similar results from experimental data. It also showed that, the heat capacity was an important factor according to the application. The heat capacity had more influence over the temperature and DSC results for the insert without the cooling channel. It was predicted by the theory and by the numerical model as copper has can transport energy at higher rates but stores poorer than the lower conductivity material H13. This was perceptible in Figure 8-8 where the combination of lower heat capacity and conductivity of the Reuss assigned properties increased the temperature of the insert surface comparing to the other materials properties. The practical experimental results had differences comparing to the numerical results. Nevertheless, they show the same idea that the FGM insert had lower capacity to store heat energy than the pure H13. A cooling channel localized in the back of the insert might had provided the support knowing that it would have transported the heat better than without cooling channels. Unfortunately it was not possible to implement because of the stereolitography mould limitations. Also, the difference between the temperature values in the numerical and practical results occurred because the initial conditions of the numerical analysis were of a room temperature mould. The temperature presented in the practical results was the temperature after at least 10 initial cycles of the machine when the process reached stability and the mould was hotter.

The DSC results showed no surprise as the temperature studies in the numerical and practical experiments had show that the FGM mould was absorbing the heat slower than the pure H13 insert. Although the properties of the 50%Cu-H13 mixture were unknown, it is reasonable to say that these properties are lower than the expectation comparing the thermal performance of pure Cu. Factors that might be affecting the results were already identified in previous work (Beal *et al*, 2004). Porosity and cracks in the microstructure of the different proportions of Cu and H13 affect the thermal properties. Additionally, the 3D effect of the heat transfer through the central 50%Cu-H13 and the side-by-side mixtures as show in Figure 8-3 had some influence in the results as well.

Although the indication that the conductivity of the Cu-H13 mixtures was lower than expected, it showed that it could be used for achieving different cooling rates in the mould. Higher proportions of Cu might increase the thermal heat transfer capabilities of these regions. Even so, care must be taken as the mechanical properties are not characterized and it would be expected that the material being more soft and less tough.

8.2. Obtaining complex geometries

Most of the specimens presented in this work were basic parallelepipeds. Despite the limitations in the system used in this work, limited complex shapes could be obtained. This section presents that a complex shape can be produced and hence shows the potential of the process if the system can be integrated with more sophisticated LCC and CAD/CAM software.

8.2.1. Geometry design and manufacturing

Using the manufacturing technique and the platform and hopper previously seen (section 4.1.2) a complex geometry was programmed using the G-code accepted by the Laserdyne. Figure 8-13 shows the CAD model of the geometry intended to be built in this experiment. It was inspired on a differential heat sink pipe which could have differential conductive fins. In Beal *et al* (2004), it had been shown that specimens obtained by selective laser fusion had an confidence interval from 0,27 to 1,75% of dimensional variability in the X and Y axis and from -13,58 to 0,25% in the Z axis. It was indicated that dimensional control could be improved but no dimensional concern such as focus diameter correction was taken in this experiment. The G-code program was laboriously written by the user and layers were cross-hatched to increase isotropy. The geometry program was based on two single layers repeated as many time the user wanted. The height of the specimen was determined by the interruption of the user and layers were 0,25mm thick. The laser scan strategy used was the refill as described in Sections 5.1 and 5.2.

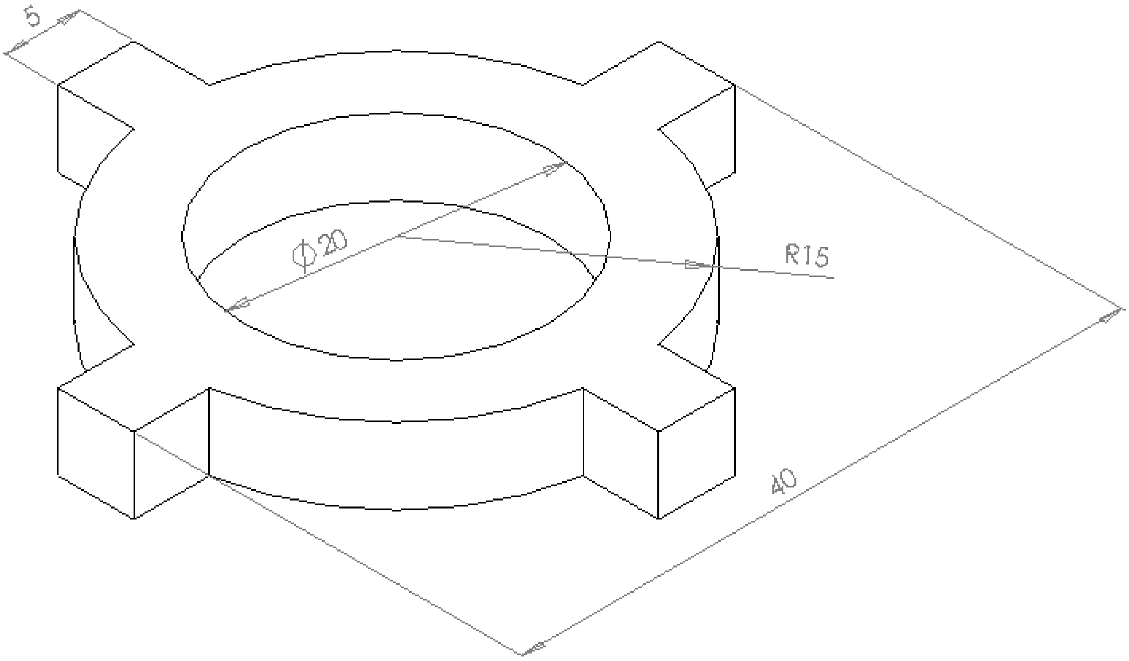

Figure 8-13. CAD model of the designed complex geometry.

The powders used in this experiment were the same presented in Table 4-4 (section 4.3) with five mixtures from pure H13 to 50%Cu in bimodal distributions. The laser processing parameters used were energy pulse of 10J, pulse width of 20ms, repetition rate of 20Hz and scan speed of 5mm/s.

8.2.2. Results and comments about the complex shape

The complex shape geometry was obtained without any difficulties. The surface of the part was rough as expected as show in Figure 8-14. The gradient is noticeable as the richer regions of copper have it's own characteristic colour. The major advance of using powder fusion is that over hang features can be obtained by the same techniques employed on LENS^{TM} and DMLS processes. To build such features in metals, these processes employ the use of supports attached to the substrate. Some features, depending on shape and complexity might be built without supports at all. However, possible distortions caused by stresses from the thermal restrained contractions and expansions during the manufacturing process might require better control of the process and post processing techniques. One possible way for avoiding or reducing this phenomenon is by using controlled temperature chamber, pre-heated powders and environment shield gas to avoid oxidation. Other additional technique for reducing distortion and cracks is applying stress relive heat treatments before removing parts from the supports and substrates. It is important to remember that H13 tool steel is a material that requires different heat treatments to achieve its condition of dimensional stability.

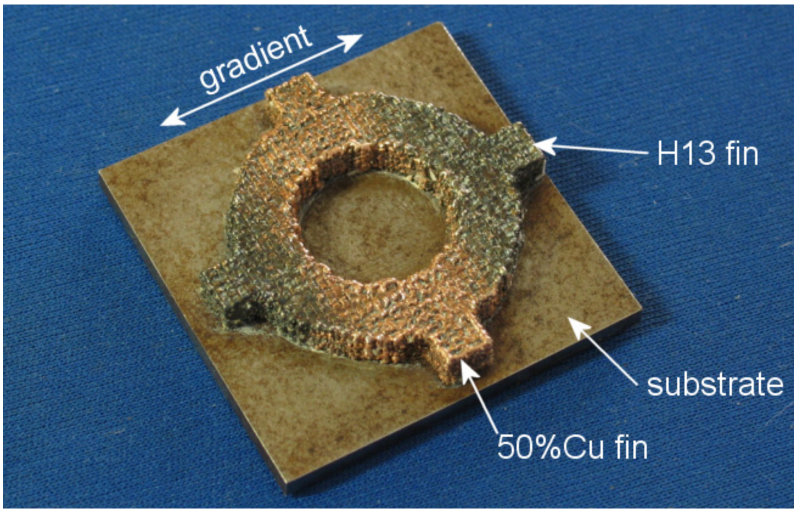

Figure 8-14. Graded complex geometry obtained.

The roughness of the surface also could be considerably smaller in the H13 and H13+12,5%Cu regions. This is because the laser parameters used to build the part were optimized to this mixture of H13 and Cu. Small laser spot, smaller particle sizes, heated and shielded chamber and optimum laser parameters applied to each region of the gradient could considerable reduce roughness and increase parts accuracy. Also, there is the possibility of remelting the top surfaces of the part to obtain better surface finish.

8.3. Summary about applications and complex shapes

The general idea of this chapter was to present practical usage of H13 and Cu graded structures build by selective laser fusing. In the injection moulding experiment, the results pointed that the richer Cu regions have more ability to transfer heat energy than to store it. The heat transfer capabilities of the material could not be explored in the injection moulding due to technical limitations to build cooling channels at that moment.

The complex geometry built expanded the possibilities of building parts with the laser welding system used in this work. Nevertheless, for future developments, it would not be possible to continue with G-Code programming. Automated G-code generation can be applied to the system from bitmaps obtained from the TNO Innerspace software. This BMP files are representations from slices of a voxel space where STL geometries can be inserted and gradients with some level of complexity can be designed. Unfortunately, this could not be completely implemented in this work and no results could be presented here. Furthermore, a proper system design for the development of the manufacturing technique would require vector programming to optimize the process to obtain complex parts.

Chapter 9

Conclusions

"The heart is a bloom, shoots up through the stony ground
But there's no room, no space to rent in this town
You're out of luck and the reason that you had to care
The traffic is stuck and you're not moving anywhere
You thought you'd found a friend to take you out of this place
Always
Someone you could lend a hand in return for grace
Always

It's a beautiful day
The sky falls and you feel like
It's a beautiful day
Don't let it get away…."

U2 – Beautiful Day

9. Conclusions

The objective of this work was to investigate the fabrication of functionally graded parts of H13 and Cu for injection moulding application. Theoretical models were used to estimate the properties from mixtures of H13 and Cu. Based on the selective laser fusion technique, a Nd:YAG laser was used to fuse mixtures of H13 and Cu powders tailored in specific sizes and proportions. Building strategies and laser processing parameters were optimized to achieve specimens with high density. The new materials compositions obtained were characterized by various techniques to measure required mechanical and thermal properties. Based on the objectives and scope presented in chapter 3, the following conclusions could be made:

Optimization of building strategy parameters:

- Dense parts of H13 and H13-Cu were obtained by the selective laser fusion process using a high power pulsed Nd:YAG laser. From the evaluated alternatives, the best laser scan strategy was the *refill* strategy with a vector spacing of 0,5mm and layer thickness of 250µm to obtain dense parts of H13;
- The other tested strategies (*filling, sequential* and *alternated*) had produced high porosity and distorted shape of the samples (area reduction);

Optimization of laser processing parameters:

- The response surface method proved to be very useful to optimize the laser parameters to obtain dense specimens from the powders and their mixtures. Using this statistical tool, the optimised laser parameters were identified in order to reduce porosity and cracks;
- These identified optimum parameters for each of the powder mixtures used in this work are listed in Table 9-1. These parameters assure densities over 90% from the theoretical densities values;

Table 9-1. Summary of the optimized laser processing parameters.

Parameter	H13	12,5%Cu	25%Cu	37,5%Cu	50%Cu	
Feedrate	5,00					mm/s
Repetition rate	20					Hz
Pulse overlap	67,10					%
Pulse energy	9,2		10,6	10,3	11,2	J
Pulse width	20		20	10	10	ms
Energy density	45,0		53,0	51,5	55,0	J/mm^2
Average power	180,00		212,00	206,00	220,00	W
Peak power	0,45		0,53	1,03	1,12	kW

(*) all Cu % in weight.

- These parameters also reduced the plasma and spattering effect for each H13-Cu composition evaluated. As a consequence, the volume distortion (reduction) of the samples also was reduced. In addition, the cracks and porosity were minimized. It was evidenced that the higher the Cu percentage the higher the laser energy required to fuse the material properly. However, high laser energy could lead to plasma and spattering;

Characterization of the H13-Cu gradient:

- The analysis of the specimens showed homogeneous microstructures with addition of Cu between 12,5 and 25% (weight) to the H13 powder. The Cu was present with the alloying elements of the H13 inserted between the dendrites of martensite. At 37% of Cu mixed with H13, heterogeneous microstructures were formed. Cu isolated areas were found;
- Cracks and pores were present in the samples. Pores formation could be associated with laser scanning strategy, vector spacing, Cu percentage and trapped gas. Nevertheless, the use of *refill* laser strategy with layers 250µm thick had reduced drastically the presence of pores to all H13-Cu compositions.
- The optimization of the laser processing parameters showed that cracks were drastically reduced but not eliminated. Cracks were formed in the centre of the laser beads as a result of the final solidification and contraction of the brittle martensite of the H13. The Cu addition aggravated the cracking phenomenon, specially for 12,5 and 25%Cu. For higher Cu percentages the isolated Cu regions might worked as stress relieve agent.
- The obtained samples from the powder mixtures had been characterized and their measured properties were compared to the prediction models presented in the literature review (2.4, pp. 29). The properties measured for each composition are presented in Table 9-2;

Table 9-2. Summary of the measured properties for each mixture.

Mixture Property	**H13**	**12,5%Cu**	**25%Cu**	**37,5%Cu**	**50%Cu**	
Density	7,64	7,53	7,62	7,78	7,72	g/cm^3
Thermal Conductivity	28,73	20,58	24,82	39,97	46,04	W/mK
Expansion Coefficient	11,22	9,49	8,64	10,97	9,08	$^{o}C^{-1}.10^{-6}$
Microhardness	598,3	586,1	527,4	464,3	369,4	HV
Hardness DSI	7,07	6,55	6,55	4,93	3,65	GPa
Elastic Modulus DSI	235,2	204,2	186,0	185,7	175,4	GPa

- Graded tensile test specimens formed by five different materials, from H13 to H13-50%Cu were fabricated and tested. It was shown that the mechanically weakest composition was H13-25%Cu. The cracks phenomenon was identified as the key factor that affected the specimens' elongation, elastic modulus and ultimate tensile strength;

Evaluation of a graded mould:

- The work also proved that graded tools of H13 and Cu could be used for injection moulding. However, it was found that the graded mould should be used when heat transport is possible from one hot region to a cold region. The results showed that the part crystallinity can be affected by the Cu presence into the H13. As a consequence, the properties of the injected material could be affected by shorter cooling cycles. Therefore, parts can be ejected more rapidly from the mould increasing the productivity.
- Complex shapes can be obtained by this process with automation of the recoater system and CAM software improvements. To obtain complex graded distributions of material compositions it requires the development of a full Local Composition Control system.

9.1. Contributions to the research world

The methodology used in this work was valuable to explore the fabrication of functionally graded materials by selective laser fusion. The approach to settle first the building parameters followed by the laser processing optimization had been successful. The materials properties characterization was necessary to know the potential of the process. As a consequence, this work had contributed to the scientific community as innovative in the following aspects:

- Contributed operating process parameters using a high power pulsed Nd:YAG laser to process pre-placed powders beds of H13 and H13-Cu mixtures;
- The application of Response Surface Methodology and the summary of the optimized laser processing parameters to achieve high density parts and identified the most important parameters for the pulsed Nd:YAG laser for the selective laser fusion process;
- Multi-compartments hoppers were successfully used to build functionally graded parts by material composition variation;
- The knowledge of producing x-graded inserts by selective laser fusion process for injection moulding of plastic parts. The work to a significant level has proven that the FGM mould can be fabricated and applied in the actual moulding work;
- The material properties of H13-Cu samples obtained compared with theoretical prediction models;

9.2. Recommendations for future work

Due to the available resources, there were various other issues which were not incorporated in this work. Some of these recommendations were realized and noted by the author from the investigations conducted. This section briefly summarises the issues arises in the author's discussion and thoughts. For future research work, some important recommendations could be done concerning three main aspects: processing H13 and Cu, improvements of the selective laser fusion system and injection moulds further evaluation.

9.2.1. Processing H13 and Cu gradient

From the Chapters 5 and 6, the conclusion remaining from the results obtained is that still is necessary to perform experiments to produce gradient specimens without defects such as cracks. Some are cited below.

- Different power level: the particle size of the power has great influence over the kinetics of the fusion process. Smaller particle size of power has the advantage to produce thinner layers and to have high surface energy. Consequently, lower energy densities and peak powers are necessary to fuse the powder. Moreover, with reduced particles it is possible to obtain better dimensional control. Other advantage could be the use of smaller spot diameter but it means that energy density could increase. New investigations on the laser parameters optimization could be required. Nevertheless, small particles are more difficult to handle as they have tendency to agglomerate and to oxidize comparing with larger particles. Another disadvantage is that even for bimodal distributions of powder, smaller sizes also present lower apparent density. This means that the fused material will have higher rates of contraction comparing to the pre-placed spread powder. All this indicates that a compromising solution must be studied.
- Higher Cu percentage: the highest percentage of Cu investigated in this work was 50%. It will be beneficial to study even higher concentrations of Cu and to measure the mechanical and thermal properties obtained. Higher percentages might be more interesting for injection moulds with differential heat control. Gradients from 0 to 100% copper could be also interesting for applications on electrical machinery/apparatuses for high power lines.
- Reduction of the step of the gradient: due to the limitations of the platform and particle sizes for this work, the step of gradient was increased from 12,5% of Cu in each composition. Producing discrete gradients with smaller steps might increase the quality of the gradient producing better parts with more continuous transitions from each phase.
- Post processing (heat treatments): any tool steel is very sensitive to heat treatment. In the case of selective laser fusion, the heat treatment could have to start in the machine with the already commented control of a heated chamber. After the building, it is also necessary to study the effect of lowering the temperature of the part and post processing with heat treatments to achieve the required mechanical properties. For instance, if the application of

the part requires high accuracy a milling operation is necessary but the material cannot be in its harder state to go through such operation. Heat treatment as annealing must be performed before milling operations. To achieve the desired mechanical properties, tempering, quenching and stress relieve must be performed in sequence. The Cu regions will have different behaviours than only H13. So, further research on these subjects could be required.

- Different lasers: all results obtained in this work could be different if using other lasers. The results presented in Chapter 6, pointed that larger pulse widths are necessary to reduce defects. In practical point of view, this leads to continuous lasers to be more appropriate to fuse the powder. Most lasers used in rapid prototyping machines are continuous or they emulated in high frequencies continuous like mode. However, continuous wave lasers have lower average power and it could require further optimization. The type of laser will affect the results too as the absorption of the laser energy depends on the wavelength of the laser.
- *In loco* processing: there are other alternatives to process the material during the parts fabrication. One is the use of different pulse shapes with pre-pulses and pos-pulses to achieve better penetration or post process the material. Using bifocal lenses to heat the material prior the laser pulse is another alternative. In addition, as described in Abe *et al* (2001), two lasers could be used to increase the quality of the fused bead. One Nd:YAG could be used to fuse the material and a CO_2 could be used to pre-heat the powder or to post-heat the solidified bead. This study could be very important to avoid post-processing in ovens. However, it will increase cost with machinery, programming and building time.
- Further material characterization: as it could be seen in results shown in Chapter 8, the tensile test experiment tested the whole gradient but not the individually each one of the material compositions. A complementary experiment could be to build tensile specimens made with each one of the compositions and to test them individually.

Most of the subjects of research above exposed will require to investigate again the laser processing and building parameters.

9.2.2. Selective laser fusion system improvements

9.2.2.(a). Hardware

The selective laser fusion process has many things to be implemented and adjusted in order to produce full dense quality parts. In this work, a welding Nd:YAG system was adapted to be used as melting powder system. Some of the necessary developments are listed below.

- Temperature controlled chamber: the major problem occurred into the specimens obtained in this work was the cracks. This could avoid the martensite formation during the cooling period of the fused material. After the fusion, slow decreasing of part temperature to the ambient temperature might avoid the brittle and crack susceptible martensite formation. The use of proper heating elements with dynamic control to keep the substrate, part and power in the correct temperature for proper processing could reduce the cracks and increase the mechanical properties of the parts produced by this technology.

- Shielded chamber: the laser sintering and cladding systems available nowadays can use proper atmospheres of nitrogen to avoid oxidation. This is very important on many aspects. The first one to avoid the oxidation is the oxygen presence, especially with the use of controlled high temperature. The second objective is that by the necessary vacuum to make the proper shielding with nitrogen, moisture is reduced from the chamber and powder. This contributes to reduce hydrogen presence in the welding that is responsible for plasma, pores and cold cracking. The development of a full shielded chamber could reduce the amount of laser energy to fuse the material as well. This means that the peak power and energy density laser processing parameters could be reduced. Consequently, plasma and spattering could be decreased as well.
- Local composition control: functionally graded materials remain dependent of the manufacturing process. In this work, an x-graded system was used to manufacture graded specimens. Despite that there are advantages discussed earlier about using the x-graded system, it does not satisfy the free-form required by FGM components. The alternatives are as presented by Kumar *et al* (2004) and Yang *et al* (2004) for obtaining graded layers of powders. This could be the most significant improvement to fabricate FGM parts successfully by layered-additive manufacturing methods.
- Laser scanning system: the system in this work had an XY table that made the scan movement as the laser fired over the powder. This had an advantage that the spot distance of the laser from the material remains constant independently of the size of the part being fabricated. Nevertheless, XY tables moving has problems with inertia, especially in high speeds and short vector lengths, and consequently, poor dimensional control. This could add a better control of the process having a moving optics head or scanning mirrors.
- Fully automated machine: during this work, all the recoating procedure was executed manually. This fact probably is one of the strongest sources of variation in the results presented in chapters 5 and 6, which affected the material properties in chapter 7. The control of the layer thickness and the powders compositions deposited cannot be constant as it should be by a proper automated system. The production of parts, at any scale, for any kind of material, graded or not, will be dependent on a fully automated machine. Consequently, it is necessary the development of proper system that can control laser, platform and recoater.

9.2.2.(b). Software

Additive layer manufacturing technologies are characterized by being fully automated. The degree of automation depends greatly on the development of proper software. The work developed in this research was all based on manual programming in G-code for CNC machines. This took considerable time and did not allow to build complex shapes. Three main issues related to software development are suggested here:

- Translation from FGM data: as exposed on Chapter 2, section 2.3.1, there are researches on describing FGM in CAD data. Bridge software, like TNO Innerspace can manipulate STL files from CAD data and apply gradients to transform in voxel data. With this voxel file, it is possible to program layers to G-code that can be produced by a CNC system like the Laserdyne. During this work, a test program with this finality was built but it was not completely adjusted for entering the result program in the Laserdyne control. Proper control of parameters and optimization to increase accuracy could be a research subject together with the development of the full-automated recoater and layering systems.
- Programming FGM layers: if data can be obtained from software like the TNO Innerspace, this must be properly handled to execute the correct programming parameters according to the materials being processed. In Chapter 6, different laser processing parameters were optimized for each material composition. If gradient information comes into the voxel file, the CAM software for programming the layers should be able to apply the correct laser and building parameters for each graded region. Implementation of such capabilities require proper database with what parameters should be used for each material available.
- Supports planning and generation: a major concern on additive layer manufacturing is to keep the free-form ability of built parts. In this research, specimens started attached to substrates. All technologies that fully melt the metallic powder use substrates to hold the part in position and to build up stable layers. To produce over hand features, it is necessary to develop supports as the one used on the stereolithography process. Recently, EOS (DMLS process) and Optomec (LENS^{TM} process) had developed supports for metallic parts built by their processes. These supports consist on a structure made with the metallic powder connecting the part to the substrate. In post processing steps after the part being complete, they can be easily sawed off. Such development could be essential to obtain complex shapes by selective laser fusion.

9.2.3. Developments for injection moulds

For the injection moulds, many research subjects might be explored. Some are cited below:

- Complex geometry improvements: a study developed with the software commented earlier to improve the manufacturing of overhanging surfaces and to increase the precision of the process could be useful to achieve moulds with higher degree of complexity including conformal cooling channels.
- FGM design methodology for moulds: to obtain the desired performance on a FGM mould it could be necessary to develop proper design methodologies. This study might

include how to use the data from an injection moulding filling simulation software to base the decisions for the gradients geometry and gradient material.

- Adding extra functionally: FGM is not restricted to heat transport for injection moulds but it could be used to increase surface wear resistance and smart sensor such as embed pressure and temperature sensors.

10. References

#

3D SYSTEMS. *NASA send Duraform part into space.* 2002-1. PDF File. Accessed on: <http://www.3dsystems.com/appsolutions/casestudies/pdf/CS_NASA.pdf>. Last access: Jan 2005.

3D SYSTEMS. *Boing sees growing value & versatility in SLS system and Duraform material*. 2002-2. PDF File. Accessed on: <http://www.3dsystems.com/appsolutions/casestudies/pdf/CS_Boeing.pdf>. Last access: Jan 2005.

A

ABE, F.; OSAKADA, K.; SHIOMI, M.; UEMATSU, K.; MATSUMOTO, M. *The manufacturing of hard tools from metallic powders by selective laser melting.* Journal of Materials Processing Technology 111, pp 210-213. ISSN: 0924-0136. 2001.

ABOUDI, J., PINDERA, M.J., ARNOLD, S. M. *Higher-Order Theory for Functionally Graded Materials*. Research and Technology 2000 – Glenn Research Center al Lewis Field. Cleveland. Ohio, USA. pp. 105-106. 2000.

AGARWALA, Mukesh; BOURELL, David; BEAMEN, Joseph; MARCUS, Harris; BARLOW, Joe. *Direct selective laser sintering of metals*. Rapid Prototyping Journal. Volume 1. Number 1. pp. 173-179. MCB University Press. ISSN 1355-2546. 1995.

AHRENS, Carlos H.; RIBEIRO, Armando de Sá.; BEAL, Valter E. *An Alternative Cooling Technique for Stereolithography Moulds*. Proceedings of Time-Compression Technologies 2001 Conference. Manchester, United Kingdom; September 26th &27th, 2001.

ARNOLD, S. M. *Higher-Order Theory—Structural/MicroAnalysis Code (HOT–SMAC) Developed*. Research and Technology 2001 – Glenn Research Center al Lewis Field. Cleveland. Ohio, USA. pp. 128-129. 2001.

ASHBY, Michael. *Material Selection in Mechanical Design*. Butterworth-Heinemann. 2 edition. ISBN 0750643579. 1999.

B

BEAL, V. E.; ERASENTHIRAN, P.; HOPKINSON, N.; AHRENS, C.H.; DICKENS, P. *Fabrication of x-graded H13 and Cu powder mix using high power pulsed Nd:YAG laser.* Proceedings of Solid Freeform Fabrication Symposium, pp 187-197, Austin, USA. 2004.

BHASHYAM, S., SHIN, K.H., DUTTA, D. *An integrated CAD system for design of heterogeneous objects*. Rapid Prototyping Journal Volume 6. Number 2. pp. 119–135. Emerald Group Publishing Limited · ISSN 1355-2546. 2000.

BHATT, R. T. *Feasibility of Actively Cooled Silicon Nitride Airfoil for Turbine Applications Demonstrated.* Research and Technology 2000 – Glenn Research Center al Lewis Field. Cleveland. Ohio, USA. pp. 34. 2000

BOURELL, David L.; MARCUS, Harris L.; BARLOW, Joel W.; BEAMAN, Joseph J. *Selective laser sintering of metals and ceramics*. The International Journal of Powder Metallurgy. Volume 28, No 4, pp 369-381. 1992.

BROOKS, J., ROBINO, C., HEADLEY, S., GRIFFITH, M. *Microstructure and property optimization of LENS™ deposited H13 tool steel*. Solid freeform fabrication symposium, Austin, Texas, USA. 1999.

C

CALDER, Neil. *Rapid Manufacturing of Functional Materials*. Proceedings of Time-Compression Technologies 2001 Conference. Manchester, United Kingdom; September 26th & 27th, 2001.

CALLISTER, W. D., Jr. *Fundamentals of Material Science and Engineering – An interactive e-text*. 5th Edition. John Wiley & Sons Inc. ISBN 0-471-39551-X. USA. 2001.

CASTILLO, M., MOORE, J.J., SCHOWENGERDT, F.D., AYERS, R.A., ZHANG, X., UMAKOSHI, M., YI, H.C., GUIGNE, J.y., *Effects of gravity on combustion synthesis of functionally graded biomaterials*. Advances in Space Research 32. pp. 265-270.2003. Elsevier Science Limited. ISSN: 0273-1177. 2003.

CENTER FOR EPIDEMIOLOGIC RESEARCH. *Former Beryllium Workers Medical Surveillance Program*. Oak Ridge Institute for Science and Education, Oak Ridge, Tennesse, USA. Accessed on: <http://www.orau.gov/cer/BMSP_pro/be-home.htm>. Last acces: Dec. 2005.

CHAVEZ, P. The Laser Engineered Net Shaping (LENS™) Process is Fueling a Paradigm Shift in Modern Manufacturing Applications. From the Inside Out. OPTOMEC. 2000.

CHU, C., ZHU, J., YIN, Z., WANG, S. *Hydroxyapatite–Ti functionally graded biomaterial fabricated by powder metallurg*y. Materials Science and Engineering A217. pp. 95–100. Elsevier Science Limited. ISSN: 0921-5093. 1999.

COMIER, Denis; HARRYSSON, Ola; WEST, Harvey; *Characterization of H13 steel produced via electron beam melting.* Rapid Prototyping Journal Volume 10. Number 1. pp. 35–41. Emerald Group Publishing Limited · ISSN 1355-2546. 2004.

D

DAI, K.; SHAW, L. *Distortion minimization of laser-processed components thought control of laser scanning patterns*. Rapid Prototyping Journal. Volume 8 – Number 5. pp. 270-276. MCB University Press. ISSN 1355-2546. 2002.

DALGARNO, K., STEWART, T., *Production tooling for polymer moulding using the RapidSteel process*. Rapid Prototyping Journal, 7(3), 173-179. MCB University Press. ISSN 1355-2546. 2001.

DAWES, C. *Laser welding – a practical guide*. Abington Publishing. England. ISBN 1-85573-034-0. 1992.

DOMACK, M. S.; BAUGHMAN, F. M. *Development of nickel-titanium graded composition components: case study.* Rapid Prototyping Journal. Volume 11 – Number 1. pp. 41-45. MCB University Press. ISSN 1355-2546. 2005.

E

EMERENKO, V.N.; NAIDICH, Yu.V.; LAVRINENKO, I.A. *Liquid-Phase Sintering*. Consultants Bureau, 1970.

ENSZ, M. T., GRIFFITH, M. L., RECKAWAY, D. E. *Critical issues for functionally graded material deposition by Laser Engineered Net Shaping (LENS™)*. Proceedings of the 2002

International Conference on Metal Powder Deposition for Rapid Manufacturing, San Antonio, TX, USA, pp.195-202. 2002.

EOS GmbH _ Electro Optical Systems. *Working Principle of Laser-Sintering*. Web page at:<http://www.eos-gmbh.de>. Last access: November 2003.

F

FESSLER, J., NICKEL, A., LINK, G., PRINZ, F. FUSSEL, P. *Functional Gradient Metallic Prototypes through Shape Deposition Manufacturing*. Proceedings of the Solid Freeform Fabrication Symposium, University of Texas at Austin, Austin, Texas, August 1997.

FISHER-CRIPPS, A. C. *A review of analysis methods for sub-micron indentation testing*. Surface Engineering, Surface Instrumentation & Vacuum Technology – Vaccum 58, 569-585. Pergamon/Elsevier. ISSN 0042-207X. 2000.

G

GERMAN, Randall M. *Liquid Phase Sintering*. Plenum Press, New York, USA. ISBN 0-306-42215-8. 1985.

GERMAN, R. M. *Power Metallurgy Science.* 2nd Edition. New Jersey, USA. MPIF: 1994. 472p. ISBN 1-878954-42-3. 1994.

GOPAKUMAR, S. *RP in medicine: a case study in cranial reconstructive surgery*. Rapid Prototyping Journal Volume 10. Number 3. pp. 207–211. Emerald Group Publishing Limited · ISSN 1355-2546. 2004.

GRIFFITH, M. L.; ENSZ, M. T.; PUSKAR, J. D.; ROBINO, C. V.; BROOKS, J. A.; PHILLIBER, J. A.; SMUGERESKY, E.; HOFMEISTER, W. H. *Understanding the microstructure and properties of components fabricated by Laser Engineered Net Shaping (LENS*^{TM}*)*. Materials Research Society. Symposium Proceedings on Solid Freeform and Additive Manufacturing, Volume 625, pp 9-20, San Francisco, CA, USA, 2000.

GSI LUMONICS. *Operation & Maintenance Manual for JK701 & JK702 Nd:YAG lasers*. GSI Lumonics. Rugbi, England. 2000.

GSI LUMONICS, *Multiflex optical-fibre beam-delivery system (single fibre) – Instruction Manual: Operation, maintenance and service*. GSI Lumonics. Rugbi, England. 1987.

H

HARRIS, R. A.; FOUCHAL, F.; HAGUE, R. J. M.; DICKENS, P. M. *Quantifying part irregularities and subsequent morphology manipulation in stereolithography plastic injection moulding.* Plastics Rubbers and Composites. Vol 33. no 2/3. pp 92-98. ISSN: 0959-8111 print. 2004

HATANAKA, M., CUTKOSKY, M., *Process planning for embedding flexible materials in multi-materials prototypes*. Proceedings of DETC'03: 2003 ASME Design Engineering Technical Conferences and Computers and Information in Engineering Conference Chicago, Illinois USA, September 2-6, 2003.

HOPKINSON, N.; HAGUE, R. J. M.; DICKENS, P. M. *Rapid Manufacturing - An Industrial Revolution for the Digital Age*. Wiley. ISBN 0470016132. November 2005.

HOPSON, G. D., PAULSEN, J. S. *Columbia STS-107: SSME Flight Readiness Review*. Space Shuttle Program. January 2003. Program 107 Report. NASA. Pdf document in < https://tdksc.ksc.nasa.gov/servlet/dm.web.Fetch/10_ssme.pdf?gid=23662>. Last access; Feb. 2005.

I

INCROPERA, Frank P., de WITT, David P. *Fundamentos de Transferência de Calor e de Massa*. Terceira Edição. Livros Técnicos e Científicos Editora S.A. ISBN 85-216-1051-3. 1992.

J

JACKSON, T. R. *Analysis of functionally graded material object representation methods*. Submitted thesis to the Department of Ocean Engineering, MIT – Massachusetts Institute of Technology. June 2000.

JACOBS, Paul F. *Rapid Prototyping & Manufacturing – Fundamentals of Stereolithography*. New York, NY, USA. RPA/ASME Press, ISBN 0-87263-425-6. 1992.

JACOBS, Paul F. Stereolithography and other RP&M Technologies. New York, NY, USA. RPA/ASME Pres, ISBN: 0872634671. 1996.

JAMIESON, R., HOLMER, B., ASHBY, A. *How rapid prototyping can assist in the development of new orthopaedic products – a case study*. Rapid Prototyping Journal. Volume 1, Number 4, pp. 38–41. MCB University Press ISSN 1355-2546. 1995.

JAXA; JST. *FGMs Database. 2002*. Web page < http://fgmdb.nal.go.jp/e_index.html>. Last access March, 2005.

JEPSON, L., BEAMAN, J., BOURELL, D., JACKSON, B., Mc ADANs, D., PEREZ, J., WOOD, K., 2003, *Multi-material selective laser sintering: empirical studies and hardware development,* White Paper, Laboratory for Freeform Fabrication, The University of Texas, Austin, USA.

JIANG, W.; MOLIAN, P.; *Laser based flexible fabrication of functionally graded mould inserts.* International Journal of Advanced Manufacturing Technology, 19, pp 646-654. Springer-Verlag London, Ltd. ISSN: 0268-3768 print. 2002.

JIANG, Wenping; NAIR, Rajeev; MOLIAN, Pal. Functionally graded mold inserts by laser-based flexible fabrication: processing modeling, structural analysis, and performance evaluation. Journal of Materials Processing Technology, Elsevier. In press paper. ISSN: 0924-0136. 2005.

K

KHOR, K.A., GU, Y.W., QUEK, C.H., CHEANG, P. *Plasma spraying of functionally graded hydroxyapatitey Ti–6Al–4V coatings.* Surface and Coatings Technology 168. pp. 195–201. Elsevier Science Limited. ISSN: 0257-8972. 2003.

KIEBACK, B.; NEUBRAND, A.; RIEDEL, H. *Processing techniques for functionally graded materials*. Materials science and Engineering A362. pp. 81-105. Elsevier. ISSN 0921-5093. 2003.

KLOCKE, F.; CELIKER, T.; SONG, A-.T.; *Rapid metal tooling*. Rapid Prototyping Journal. Volume 1. Number 3. pp. 32-42. MCB University Press. ISSN 1355-2546. 1995.

KNOPPERS, G.E.; GUNNINK, J.W.; van den HOUT; J.; van VLIET, W.P. *The reality of functionally graded materials products.* Proceedings of Solid Freeform Fabrication Symposium, pp 38-43, Austin, USA. 2004.

KRUTH, F-P.; MERCELIS, P.; VAN VAERENBERGH, F.; FROYEN, L. ROMBOUTS, L. *Binding mechanism in selective laser sintering and selective laser melting.* Rapid Prototyping Journal. Volume 11, Number 1, pp. 26–36. MCB University Press ISSN 1355-2546. 2005.

KOUKKA, Henri. *The Whole RP Family Tree.* Last update June 2001. Web page <http://ltk.hut.fi/~koukka/RP/rptree.html>. Last access Feb, 2005.

KUMAR, A., WOOD, A. (1999), *Representation and design of heterogeneous components*. Proceedings of the 1999 Solid Freeform Fabrication. Symposium, Austin, TX, USA. pp. 179-86.

KUMAR, P., SANTOSA, J. K., BECK, E., DAS, S *Direct-write deposition of fine powders through miniature hopper-nozzles for multi-material solid freeform fabrication*. Rapid Prototyping Journal, 10(1), 14-23. MCB University Press. ISSN 1355-2546. 2004.

L

LAUX, T., KILLINGER, A., AUWERTER-KURTZ, M., GADOW, R. WILHELMI, H. Functionally graded ceramic materials for high temperature applications for space planes. Proceedings of 5th International Symposium on Functionally Graded Materials. Dresden, Germany. October 1998.

LI, Y.; GARGIULO, E. P.; KEEFE, M. *Studies in Direct Tooling Using Stereolithography*. Transactions of ASME, Vol. 122, pg. 135, May 2000.

LIU, H.; MAEKAWA, T., PATRIKALAKIS, N.M., SACHS, E.M., CHO, W. *Methods for feature-based design of heterogeneous solids*. *Computer-Aided Design* 36. pp. 1141-1159. Elsevier Ltda. 2003.

LOW, D. K. Y., LI, L., BYRD, P.J. *The effect of process parameters on spatter deposition in laser percussion drilling*. Optics & Laser Technology, 32, 347-354. ISSN: 0030-3992. 2000.

LÜ, L., FUH, J., WONG, Y.-S.; *Laser-induced materials and processes for rapid prototyping.* Kluwer Academic Publisher. Norwell, USA. ISBN 0792374002. 2001.

M

MARINELLI, A. L.; BRETÃS, R. E. S. *Blends of polypropylene resins with a liquid crystalline polymer: I- Isothermal crystallization*. Journal of Applied Polymer Science. Volume 87, Issue 6. Pages: 916-930**.** ISSN 1097-4628*.* 2003.

MATSUMOTO, M., SHIOMI, M., OSAKADA, K., ABE, F. *Finite element analysis of single layer forming on metallic powder bed in rapid prototyping by selective laser processing*. International Journal of Machine Tools & Manufacture, 42, 61-67. ISSN 0890-6955. 2002.

MATWEB. *Search: AISI Type H13 Hot Work Tool Steel, air or oil quenched from 995-1025°C*. Access on <http://www.matweb.com>. Last access: Feb. 2005-1.

MATWEB. *Search: Copper, Cu; Annealed, Cold Drawn & Cold-Worked*. Access on <http://www.matweb.com>. Last access: Feb. 2005-2.

MATWEB. *Search: Beryllium Copper*. Access on <http://www.matweb.com>. Last access: Feb. 2005-3.

MATWEB. *Search: Polypropylene, Molded.*. Access on <http://www.matweb.com>. Last access: Feb. 2005-4.

MENGES, George; MOHREN, Paul. *How to Make Injection Molds*. 2nd Edition Munich, Germany: Hanser, 504p. ISBN: 1-56990-0620. 1993.

MONTGOMERY, D. C. *Design and analysis of experiments*. 5th edition. J. Wiley & Sons. USA. ISBN 0-471-31649-0. 2001.

MIRONOV, V., BOLAND, T., TRUSK, T., FORGACS, G., MARKWALD, R.R. *Organ printing: computer-aided jet-based 3D tissue engineering.* Trends in biotechnology. Vol. 21 No 4. pp. 157-161 Elsevier. April 2003.

MIYAMOTO, Y.; KAYSSER, W. A.; RABIN, B. H.; KAWASAKI, A.; FORD, R. G. *Functionally Graded Materials: Design Processing and Applications*. Kluwer Academic Publishers. Dordrecht, NL. ISBN 0-412-60760-3. 1999.

N

NORTON, R. L. *Machine Design: An Integrated Approach*. New Jersey, USA: Prentice-Hall Inc, New Jersey. ISBN 0-13-555475-6. 1996.

O

OLIVER, W. C.; PHARR, G. M. *An improved technique for determining hardness and elastic modulus using load and displacement sensing indentation experiments*. Journal of Materials Research, Published by the Materials Research Society. Volume 7, Number 6, pp. 1564-1583. ISSN: 0884-2914. June 1992.

OSPREY METAL POWDERS. *Microfine Powder – H13 Datasheets*. Web Site <http://www.ospreymetals.co.uk>. Accessed on November 2003.

P

PATIL, Lalit; DUTTA, Debasish; BHATT, A.D.; JURRENS, K.; LYONS, K.; PRATT, M.J.; SRIRAM, R.D. *A proposed standards-based approach for representing heterogeneous objects for layered manufacturing*. Rapid Prototyping Journal. Volume 8 – Number 3. pp. 134-146. MCB University Press. ISSN 1355-2546. 2002

PINILLA, J. M. PRINZ, F. B. *Lead-time reduction through flexible routing: application to Shape Deposition Manufacturing*. International Journal of Production Research. Taylor & Francis. Volume 41, Number 13, 2957 – 2973. ISSN Print 0020-7543 ISSN Online 1366-588X. September 2003.

POGSON, S. R.; FOX, P. SUTCLIFFE, C. F.; O'NEILL, W. *The production od copper parts using DMLR*. Rapid Prototyping Journal. Volume 9 – Number 5. pp. 334-343. MCB University Press. ISSN 1355-2546. 2005.

POMPEA, W., WORCH, H., EPPLE, M., FRIESS, W., GELINSKY, M., GREIL, P., HEMPELE, U., SCHARNWEBER, D., SCHULTE, K. *Functionally graded materials for biomedical applications*. Materials Science and Engineering A362. pp. 40–60. Elsevier Science Limited. ISSN: 0921-5093. 2003.

PÖTSCH, Gerd; MICHAELI, Walter. *Injection molding: an introduction.* Hanser/Gradner Publications. ISBN 3-446-17196-7. 1995.

R

ROOP KUMAR, R., MARUNO, S. *Functionally graded coatings of HA–G–Ti composites and their in vivo studies*. Materials Science and Engineering A334. pp. 156–162. Elsevier Science Limited. ISSN: 0921-5093. 2002.

RVACHEV, V., SHEIKO, T., SHAPIRO, V. and TSUKANOV, I. *Transfinite Interpolation over Implicitly Defined Sets*. Technical Report SAL 2000 – 1, Spatial Automation Laboratory, University of Wisconsin, Madison, USA. 2000.

RUSS, John C. DEHOFF, ROBERT, T. *Practical Stereology*. 2nd Edition. Kluwer Academic/Plenum Publishers, NY, USA. ISBN 0-306-46476-4. 2000.

S

SANGHERA, B., NAIQUE, S., PAPAHARILAOU, Y., AMIS, A. *Preliminary study of rapid prototype medical models.* Rapid Prototyping Journal. Volume 7. Number 5. pp. 275-284. MCB University Press . ISSN 1355-2546. 2001.

SHISHKOVSKY, Igor. *Synthesis of functionally gradient via RP methods*. Rapid Prototyping Journal. Volume 7, Number 4, pp. 207-211, MCB University Press. ISSN 1355-2546. 2001.

SIU, Y.K., TAN, S.T. *Representing CAD modelling of heterogeneous objects*. Rapid Prototyping Journal. Volume 8. Number 2. pp. 173-179. MCB University Press. ISSN 1355-2546. 2002.

SMITH, W. F. *Structure and properties of engineering alloys*. Second Edition. McGraw-Hill, Inc. ISBN 007591725. 1993.

STEEN, W. M. *Laser Material Processing*. Springer-Verlag. ISBN 3-540-19670-6. 1991.

STORCH, S., NELESSEN, D., SHAEFER, G., REITER, R., *Selective laser sintering: qualifying analysis of metal based powder systems for automotive applications*. Rapid Prototyping Journal., Volume 9. Number 4. pp. 240-251. MCB University Press · ISSN 1355-2546. 2003.

SU, W. *Layered Fabrication of Tool Steel and Functionally Graded Materials with a Nd:YAG Pulsed Laser.* PhD Thesis. Loughborough University. Loughborough, United Kingdom. 2002.

SUN, Wei; JIANG, Tao; LIN, Feng. *A processing algorithm for freeform fabrication of heterogeneous structures*. Rapid Prototyping Journal. Volume 10. Number 5. pp. 316–326. MCB University Press. ISSN 1355-2546. 2004.

SURESH, S.; MORTENSEN, A. *Fundamentals of functionally graded materials*. Institute of Materials, London. ISBN 1-86125-063-0. 1998.

SURESH, S. *Graded materials for resistance to contact deformation and damage*. Science Magazine, Science's Compass Review. Vol 292. ISSN 1095-9203. 29 Jun 2001.

SUSTARSIC, B., DOLINSEK, S., KOSEC, L., SKRABA, P., MEDVED, J. *Morphological and microstructural characteristics of metal powders for DMLS*. Proceedings of the World PM2004 Conference held in Vienna, October 17-21 2004.

SWANN, S. *Integration of MRI and stereolithography to build medical models: a case study*. Rapid Prototyping Journal. Volume 2. Number 4. pp. 41–46. MCB University Press. ISSN 1355-2546. 1996.

T

TAMINGER, Karen M. B., HAFLEY, Robert A., DICUS, Dennis L. *Solid Freeform Fabrication: An Enabling Technology for Future Space Missions*. Proceedings of 2002 International Conference on Metal Powder Deposition for Rapid Manufacturing.. San Antonio, TX, USA. April 8-1-, 2002.

TARRANT, Mary Katherine. *Lasers in Chemistry: Nd:YAG.* Web page. Accessed on <http://www.lasalle.edu/academ/chem/laser_web/ndyag_laser.html> 2002. Last access Feb. 2005.

THÜMMLER, F.; OBERACKER, R. *An introduction to powder metallurgy*. The Institute of Materials. The University Press, Cambridge, UK. ISBN 0-901716-26-X. 1993.

TOP GRADE MOLDS, *Complete Injection Mold Design and Manufacturing Services*. Folder. Top Grade Molds Ltd. Ontario, Canada, 2003.

TORQUATO, Salvatore. *Random Heterogeneous Materials: microstructure and macroscopic properties*. Springer. ISBN 0-387-95167-9. 2001.

U

U. S. DEPARTMENT OF ENERGY. *Development of functionally graded materials for manufacturing tools and dies and industrial processing equipment.* Energy Efficiency and Renewable Energy. Industrial technologies program. Industrial materials for the future. Web page: <www.eere.energy.gov>. June 2004.

U. S. DEPARTMENT OF ENERGY. *Development of functionally graded materials for manufacturing tools and dies and industrial processing equipment.* Energy Efficiency and Renewable Energy. Industrial technologies program. Industrial materials for the future program review. PDF presentation file: < http://www.eere.energy.gov/industry/imf/pdfs/project_presentations/14_functionallygradedpresentation.pdf>. June 2005.

UDDEHOLM. *Treatment of tool steel: Welding of tool steel.* Uddeholm, download, steel treatment. <http://utab.uddeholm.com/> pp1-15 Last access Sept. 2004.

UTHSCSA Website. *ImageTool Version 3.0.* The University of Texas Health Science Center at San Antonio. Web page at: <http://ddsdx.uthscsa.edu/dig/itdesc.html>. Accessed on January 2004.

V

VITALE BROVARONE, C.; VERNÉ, E.; KRAJEWSKI, A.; RAVAGLIOLI, *A. Graded coatings on ceramic substrates for biomedical application*s. Journal of the European Ceramic Society 21. pp. 2855–2862. Elsevier Science Limited. ISSN: 0955-2219. 2001.

VLOC. *YAG Yttrium Aluminium Garnett Laser Materials*. Pdf Brochure accessible in <http://www.vloc.com/PDFs/YAGBrochure.pdf>. Last access, February 2005.

Y

YAN, Y., WU, R., ZHANG, R., XIONG, Z., LIN, F. *Biomaterial forming research using RP technology.* Rapid Prototyping Journal Volume 9. Number 3, pp. 142–149. Emerald Group Publishing Limited · ISSN 1355-2546. 2003.

YANG, S., EVANS, J. R.G. Acoustic control of powder dispensing in open tubes. Powder Technology, 139, 55-60. ISSN: 0032-5910. 2004.

W

WANG, F., SHOR, L., DARLING, A., KHALIL, S., SUN, W., GUÇERI, S., LAU, A. Precision extruding deposition and characterization of cellular poly-e -caprolactone tissue scaffolds. Rapid Prototyping Journal Volume 10, Number 1, pp. 42–49. Emerald Group Publishing Limited · ISSN 1355-2546. 2004-1.

WANG, N.; MOKADEM, S.; RAPPAZ, M.; KURZ, W.; Solidification cracking of superalloy single- and bi-crystals. Acta Materialia, 52 pp 3173-3182. Elsevier Ltda. ISSN 1359-6454. 2004.

WATARI, F., YOKOYAMA, A., SASO, F., UO, M., KAWASAKI, T. *Fabrication and properties of functionally graded dental implant.* Composites Part B. pp 5-11. Elsevier Science Limited. ISSN: 1359-8368. 1997.

WOHLERS, Terry. *Wohlers Report 2004*. Wohlers Associates, Inc. ISBN 0975442902. USA, 2004.

WU, Benjamin M.; BORLAND, Scott W.; GIORDANO, Russell A.; CIMA, Linda G.; SACHS, Emanuel M.; CIMA, Michael J. *Solid free-form fabrication of drug delivery devices*. Journal of controlled release. 40, pp 77-87. Elsevier. 1996.

11. Resumo Estendido[10]

FABRICAÇÃO DE GRADIENTES FUNCIONAIS ENTRE AÇO FERRAMENTA E COBRE POR FUSÃO SELETIVA A LASER USANDO UM FEIXE DE LASER PULSADO Nd:YAG DE ALTA POTÊNCIA PARA APLICAÇÕES EM MOLDES DE INJEÇÃO

VALTER ESTEVÃO BEAL

11.1. Introdução (Capítulo 1)

O desenvolvimento de novos produtos requer que novos materiais, novas tecnologias de fabricação e metodologias de projeto sejam utilizadas. Esta tríade projeto, materiais e fabricação são interdependentes. Como exemplo, um projetista que deseja aumentar a performance de um produto pode requerer novos materiais que possam dar maior leveza e rigidez a determinado componente. No entanto, para dar forma a este componente utilizando novos materiais é necessário que existam tecnologias de fabricação que sejam eficazes em produzir com os custos estabelecidos e nas especificações do projeto.

Neste contexto, a disponibilidade de novos materiais e processos é essencial para que novos produtos sejam desenvolvidos. Um foco de desenvolvimento nos últimos 25 anos é a área de *functionally graded materials* (FGM), ou materiais com gradientes funcionais. No conceito básico, FGM são materiais, ou ingredientes, que são interligados por um gradiente, ou seja, uma variação das proporções entre um ingrediente e outro. Essa ligação tem como objetivo aumentar a performance de um componente através da otimização de forma e função. Citando um exemplo da natureza, um osso de um mamífero possui maior densidade e poros muito pequenos na região periférica. Já no seu interior, a densidade é baixa e formada por grandes poros. A alta densidade da parte externa do osso permite que este seja rígido e a porosidade interna lhe dá leveza. Neste caso o ingrediente que forma a transição gradual entre cada “tipo” de osso é a porosidade. Engrenagens de aço também podem possuir características de FGMs. A superfície da engrenagem deve ser resistente à abrasão e por isso deve ter elevada dureza. No entanto, o resto da engrenagem deve suportar impactos e o número de ciclos de vida estimados no projeto. Para aumentar a dureza da engrenagem somente em sua superfície, pode-se recorrer a cimentação que é o enriquecimento de carbono na superfície da engrenagem. O ingrediente no caso é o teor de carbono que gradualmente varia da superfície para a parte interna da engrenagem.

O conceito dos FGMs é muito parecido com o dos materiais compósitos que é o de unir materiais que quando combinados, exibirão propriedades conjuntas, aproveitando o melhor de cada um. No entanto há uma diferença básica, compósitos exibem uma nítida distinção entre as fases que o compõem enquanto que nos FGMs esta região não é tão distinta.

---

[10] Referências citadas neste texto estão no capítulo anterior (a partir da página 199).

Obviamente, isso é uma comparação geral e normalmente depende da escala em que se está analisando.

Apesar da idéia de cópia da natureza ser bastante simples, a maioria das aplicações potenciais de FGMs ainda mantém-se restrita a nichos de elevado custo e a produção em escala laboratorial. As causas para este desenvolvimento relativamente moroso são as dificuldades em controlar a composição do gradiente e de produzir peças com forma e gradientes complexos.

No final dos anos 80, novas tecnologias de fabricação surgiram. A principal diferença destas tecnologias em relação as tecnologias tradicionais era que estas eram baseadas no princípio de adição de camadas. Usualmente chamadas de prototipagem rápida (RP, *Rapid Prototyping*), estas tecnologias podem produzir peças em baixo volume de produção, virtualmente em qualquer forma e material. A variedade de materiais é limitada, no entanto, processos RP podem construir peças em metais, cerâmicas e polímeros (Jacobs, 1992).

Tecnologias RP possuem elevado grau de automatização e também são conhecidas por impressoras tridimensionais porque elas “imprimem” peças sólidas a partir de dados gerados em computador. Desenhistas industriais e engenheiros podem construir e verificar peças projetadas diretamente no computador sem erros de interpretação, falta de precisão ou demora. O princípio básico das tecnologias RP é construir, camada por camada, o material correspondente aos dados do computador da peça projetada. Os materiais utilizados na construção podem ser resinas liquidas, fios pastas, lâminas e pós. São diversas as maneiras com as quais é dada forma a estes materiais e as camadas são unidas. Para citar algumas formas: lasers e lâmpadas ultravioletas, lasers de potência, spray de aglutinante, extrusão de material fundido entre outras.

Estas tecnologias de fabricação por adição de camadas (LMT, *Layered Manufactuting Technology*) têm sido usadas para construir ferramentas para moldagem por injeção. Dependendo da tecnologia e do material utilizados para construir o molde, complexidade da cavidade do molde (ou, peça a ser injetada) e do material a ser injetado estes moldes podem ser competitivos aos moldes tradicionais (fundidos/usinados). É possível construir moldes que podem durar de dezenas até dez mil ciclos de moldagem dependendo da tecnologia, material e aplicação. Uma das vantagens é obter um molde de geometria complexa em um curto período de tempo. A outra vantagem é a possibilidade de incluir canais de forma livre (*conformal cooling*) para controle da extração de calor da cavidade. Estes canais podem ser projetados e construídos incorporados ao molde pelas máquinas RP. Um bom projeto pode extrair calor mais efetivamente que canais fabricados tradicionalmente por usinagem (Ahrens *et al*, 2001; Dalgarno and Stewart, 2001).

Apesar de moldes RP com canais de forma livre poderem ser utilizados para a fabricação de peças injetadas, é necessário otimizar melhor a extração de calor da cavidade do molde. Como exemplo, detalhes pequenos, finos e longos podem não ser beneficiados de uma extração eficiente de calor. Isto pode ocasionar ciclos de injeção prolongados para permitir que todas as regiões da peça injetada possam atingir um estado sólido para poder ejetar a peça do molde. Adicionalmente, a solidificação diferencial do material da peça pode causar diversos efeitos colaterais. Não é rara a inserção de modificações no projeto da peça para corrigir ou evitar defeitos causados por isso. Alguns destes defeitos são, rechupes, linhas de solda e empenamento (Menges and Mohren, 1993; Pötsch and Michaeli, 1995). A limitação para o uso destes canais incorporados de forma livre não está limitada somente a geometria da cavidade do molde. O projeto do sistema de extração (gavetas e pinos extratores), canais de injeção, ponto de injeção, planos de partição e a tecnologia de fabricação para obter estes detalhes aumentam as dificuldades para extrair calor da cavidade.

O uso de tecnologias de prototipagem rápida para produzir componentes FGM tem sido investigado por muitos pesquisadores (Shishkovsky, 2001). Como tecnologias RP podem produzir peças de forma livre em diferentes materiais, é possível usá-las para produzir componentes FGM. A maioria das pesquisas que investigam a fabricação de FGM por prototipagem rápida processa os materiais utilizando um raio laser como fonte de calor. Como lasers podem ser facilmente automatizados e podem fornecer elevadas densidades de energia com precisão e velocidade, eles podem processar virtualmente qualquer material (Steen, 1991). Outro aspecto de FGM e RP é o uso de materiais na forma de pós elementares para fusão ou pré-sinterização por laser.

Combinadas as tecnologias de FGM e RP poderiam aumentar a performance de moldes de injeção em muitos aspectos. Regiões específicas na superfície do molde poderiam ser endurecidas para a redução de desgaste. Regiões ou detalhes na cavidade do molde poderiam ser enriquecidas com materiais de maior condutividade térmica que o material base, como por exemplo, o cobre. Assim, seria possível extrair calor com maior eficiência para reduzir defeitos das peças obtidas e também para aumentar a produtividade do molde.

Um material comumente utilizado para a construção de moldes é o aço ferramenta AISI H13. Este material suporta aplicações em temperaturas elevadas com pouco desgaste e com boa tenacidade (Smith, 1993; Norton, 1996). No entanto, a condutividade térmica do H13 é baixa (24W/mK, Matweb, 2005-1). Baseado nesta desvantagem, para aumentar a extração de calor da cavidade, canais com um fluido com temperatura controlada (exemplo, água com aditivos) são utilizados. O fluido requer um *chiller* para manter a temperatura baixa e constante (no caso de refrigeração) e extrair controladamente o calor da peça injetada. Usualmente, a extração de calor não é um problema para geometrias simples, mas no caso de peças mais complexas, ou aplicações que requeiram maior precisão, a extração inapropriada de calor pode causar defeitos nas peças produzidas como discutido anteriormente. Nestes casos, especialmente quando canais de forma livre não podem ser utilizados no molde em regiões específicas, cobre poderia ser adicionado ao molde durante a sua construção. No entanto, é necessário desenvolver um processo que possa construir estes tipos de gradientes entre o H13 e o cobre.

11.2. Definição do problema (Capítulo 3)

Como foi exposto anteriormente, FGMs são limitados nos materiais disponíveis em tecnologias de fabricação que permitam a obtenção de formas e gradientes complexos. No entanto, FGM tem grande potencial para melhorar a performance de muitos componentes, desde a indústria médica até a aeroespacial. Apesar de várias combinações de materiais e processos terem sido desenvolvidos, estes só atendem em sua grande maioria a escala laboratorial e alguns poucos casos industriais de larga escala.

Algumas pesquisas têm apresentado amostras de FGM produzidas por tecnologias de fabricação por adição de camadas. Os três principais focos de desenvolvimento de FGM por estas tecnologias são: controle de composição localizada, software e processamento de material.

As tecnologias que são capazes trabalhar com diferentes tipos de materiais, usualmente utilizando lasers como fonte de calor localizada, têm sido exploradas mais intensivamente. Pesquisas com adição volumétrica por laser (ex. LENS) mostraram que é possível produzir FGM a partir de metais. A composição dos materiais pode ser controlada pelo ajuste da composição do fluxo de pós soprados em direção ao ponto focal do laser sobre o material processado. Até o momento, esta é a tecnologia que apresenta o melhor sistema de controle de composição localizada. No entanto, esta tecnologia possui algumas desvantagens, como baixa precisão e complexidade geométrica limitada, quando comparada a outras tecnologias de fabricação por adição de camadas.

Porém, tecnologias com pós pré espalhados em camadas como fusão e sinterização seletivas por laser possuem maior precisão e capacidade de produzir peças complexas em um único material. Algumas pesquisas têm investigado a deposição automatizada de diferentes pós em camadas, mas estão em estágios iniciais de desenvolvimento. Até o momento, nenhum sistema completamente efetivo foi criado e testado. Os materiais com gradientes funcionais fabricados por estes processos, fusão ou sinterização seletiva, são limitados e possuem gradientes apenas na direção do eixo x de adição de camadas. Somente o gradiente entre camadas com diferentes composições tem sido investigado. Adicionalmente, a maioria dos estudos envolveu gradientes entre ligas metálicas e materiais para resistência ao desgaste ou barreira térmica. Nenhuma pesquisa investigou a fabricação de gradientes para produzir regiões com maior condutividade térmica em cavidades de moldes para injeção. Ainda, os estudos não têm explorado as propriedades dos materiais obtidos. A maioria é restrita ao estudo da dureza e microestrutura obtida nos gradientes.

11.2.1. Hipóteses

Moldes e ferramentas usualmente são os itens de maior custo inicial de um processo de manufatura contínua se não forem o maior custo do projeto inteiro. A performance destas ferramentas depende de muitos fatores baseados nos materiais, projeto e fabricação da peça a ser processada por esta ferramenta e a própria ferramenta. Como resultado, em muitos casos, é imperativo que estas ferramentas atinjam o máximo de performance. Esta performance pode ser medida pelo grau de complexidade da cavidade de injeção, a taxa de produção e a expectativa de vida do molde.

O aço ferramenta H13 é considerado um aço resistente a altas temperaturas com estabilidade dimensional, baixo desgaste e alta tenacidade. Suas propriedades mecânicas o tornam ideal para a fabricação de moldes e ferramentas (Norton, 1996, Smith 1993). No entanto, a performance térmica do H13 pode ser considerada pequena por ter baixa capacidade para conduzir energia térmica. O coeficiente de condutividade térmica do H13 é 24.3W/mK (MatWeb, 2005-1). Alternativas para melhorar a condutividade de um molde para injeção são o uso de canais de refrigeração/aquecimento e insertos de uma liga de cobre-berílio (Cu-Be). Canais de refrigeração/aquecimento dependem da geometria do molde, são restritos pelo processo de fabricação e possuem efeito limitado em detalhes finos, pequenos ou complexos. Insertos de cobre-berílio são caros, não ecológicos e apresentam na superfície do molde uma mudança abrupta de propriedades entre o inserto e o material base. Porém, estes apresentam um coeficiente de condutividade térmica elevada (100-130W/mK; Matweb, 2005-3). O objetivo desta pesquisa foi investigar a fabricação de materiais com gradientes funcionais para serem usados na fabricação de moldes de injeção de alta performance térmica com baixo impacto ecológico, complexidade geométrica e projeto térmico preciso. Esta pesquisa focou o desenvolvimento de componentes com gradientes funcionais entre aço ferramenta (AISI H13 ou BS EN ISO 4957:2000 XV40CrMoV5-1) e cobre. O uso do cobre adicionado ao H13 poderia aumentar a condutividade térmica da nova liga formada. Uma distribuição controlada no material de base H13 poderia otimizar a extração de calor de peças plásticas durante o resfriamento do ciclo de moldagem por injeção. Este tipo de otimização poderia reduzir a contração diferencial e defeitos como empenamento, linhas de solda e rechupes.

Para construir geometrias de forma livre considerando o controle de composição local do cobre adicionado ao H13, o processo de fusão seletiva por laser foi escolhido para ser usado na fabricação de peças com gradientes funcionais. Como visto na introdução apresentada anteriormente, o processo de fusão seletiva por laser, baseado na tecnologia de fabricação por adição de camadas, oferece a possibilidade de fabricar peças com máxima densidade. Este processo pode ser utilizado para atingir as especificações para a produção de novos materiais formados pela mistura de cobre e aço ferramenta. Neste processo, o uso de um laser pulsado Nd:YAG de alta potência pode ser preferível por ser recomendado para o processamento de metais em decorrência do seu comprimento de onda quando comparado ao laser de CO_2 (Steen, 1991).

11.2.2. Objetivos

Como já mencionado anteriormente, o objetivo desta pesquisa foi produzir materiais com gradientes funcionais a partir de pós elementares de H13 e cobre, utilizando um laser Nd:YAG pulsado de alta potência focando a aplicação em moldes para injeção.

Os alvos da pesquisa para atingir o objetivo principal foram:

- Investigar o processo de fusão por laser dos pós de H13 e misturas de pós de H13 e cobre;
- Otimizar os parâmetros de processamento do laser para obter elevadas densidades nas peças fabricadas.
- Caracterizar os novos materiais formados e estruturas FGM;
- Avaliar a performance de um molde com gradiente funcional produzido por este processo.

11.3. Materiais e métodos (Capítulo 4)

Neste estudo, foi utilizado um laser pulsado de Nd:YAG, modelo GSI Lumonics JK701H. A energia do laser era conduzida por um cabo de fibra ótica até o eixo de uma máquina de controle numérico. A máquina, Laserdyne 350, era uma unidade de controle numérico com 3 eixos de movimentação, sendo composta de uma mesa x-y e um eixo z no qual o cabeçote de abertura do feixe do laser era montado. Esta máquina com controle numérico integrado, possibilitava através da programação em código G, a movimentação dos eixos em sincronia com o funcionamento do laser. Esta máquina como um todo (laser e controle numérico) era um equipamento específico para a soldagem e furação por laser. Detalhes do sistema da máquina podem ser vistos na Figure 4-10[11] (pág. 70).

Na mesa x-y da máquina sistemas de adição de camadas foram adaptados a fim de se implementar a fabricação por adição de camadas. Dois sistemas de fabricação foram utilizados: sistema de adição por lâminas fixas e sistema de adição por plataforma e funil. O sistema de lâminas fixas funciona com lâminas pré-cortadas. Sobre um substrato colocado na base de um suporte, uma lâmina de 0,5mm de espessura era colocada. O pó era espalhado manualmente sobre o corte interno da lâmina com a ajuda de uma espátula. O laser em sincronia com os movimentos da mesa era acionado e fundia o material da camada de pó solidificando junto ao substrato até formar uma camada conforme a programação inserida pelo usuário. Para adicionar uma nova camada, mais uma lâmina era posta sobre a anterior, uma nova camada de pó era espalhada dentro do recorte da lâmina e novamente o laser fundia mais uma camada anexando a nova camada sobre a anterior. O processo era repetido até alcançar a altura desejada. Detalhes deste processo podem ser vistos na Figure 4-1 (pág. 63). Este método foi utilizado para os estudos preliminares.

---

[11] Devido a limitações da indexação de objetos do software de editoração utilizado neste trabalho, entendam-se os termos em inglês Figure por Figura e Table por Tabela neste resumo.

Para aumentar a precisão na espessura das camadas e possibilitar a deposição de gradientes sobre uma mesma camada, foi desenvolvido um outro método, também manual, de deposição de camadas. Com o uso de uma mesa niveladora e um relógio comparador, um substrato era colocado sobre a plataforma da mesa niveladora que podia ser ajustada conforme o acompanhamento do relógio comparador. Baixando a plataforma em 0,25mm, uma camada de pó de mesma espessura era espalhada sobre o substrato com a ajuda de um funil de vários compartimentos individuais. O laser fundia uma camada de pó sobre o substrato, a plataforma era baixada novamente em 0,25mm e o funil espalhava nova camada sobre a anteriormente feita. Assim o processo seguia continuamente até completar a fabricação das amostras. Detalhes sobre este sistema de deposição de camadas podem ser vistos nas Figure 4-3 (pág. 65) e Figure 4-4 (pág. 65). As plataformas e suportes foram feitos em alumínio e os funis foram fabricados por estereolitografia.

Para a deposição do pó pelo sistema de plataforma móvel, três funis com vários compartimentos individuais foram desenvolvidos. Os funis tinham como função espalhar camadas com gradientes de pós, por isso, foram desenvolvidos para que cada compartimento individual dos funis trabalhasse isoladamente com uma mistura de pó de H13 e cobre. Dois funis foram utilizados para plataformas de tamanho máximo, x-y, de 45x45mm e um funil, para a fabricação de corpos de prova para ensaio de tração, para plataforma de 45x75mm. Imagens CAD representativas dos funis podem ser vistas em Figure 4-5 (pág. 67), Figure 4-6 (pág. 67) e Figure 4-7 (pág. 68). As principais dimensões dos funis são apresentadas na Table 4-1 (pág. 68) que faz referência a figura esquemática Figure 4-8 (pág. 68). Um exemplo de camada de pó em gradiente espalhada pelo funil da Figure 4-5 (pág. 67) é apresentado na Figure 4-9 (pág. 69).

Como material a ser processado, foram utilizadas três fontes de pós metálicos: pó de H13 de formato esférico com granulometria menor que 212µm, pó de cobre com formato esferóide irregular, também com granulometria menor que 212µm e pó esférico de cobre com 80% da granulometria inferior a 22µm. Todos os pós foram fornecidos pela Osprey Powder e foram fabricados por atomização por gás. As características destes pós podem ser verificadas na Table 4-3 (pág. 77) e micrografias são apresentadas nas Figure 4-16, Figure 4-17 e Figure 4-18 (pág. 77 e 78). Para melhorar a densidade aparente das camadas de pó depositadas, na maior parte dos experimentos, foram utilizadas misturas de pós com distribuição bimodal de tamanhos de partículas. Para tanto, os pós com granulometrias de até 212µm foram peneirados e separados em duas distribuições conforme mostra a Table 4-4 (pág. 79). Cada mistura possui duas distribuições principais dos tamanhos de partículas divididas entre o Cu e o H13. Para verificação da distribuição bimodal, na Table 4-5 (pág. 81) são apresentados os percentuais de cada tamanho de partículas analisadas em um analisador por difração laser. Nas Figure 4-19 e Figure 4-20 (pág. 80) são apresentadas as respectivas curvas das distribuições para cada uma das misturas. A fração entre as partículas pequenas e as grandes ficou aproximadamente 1:7 o que seria o ideal, matematicamente, para aumentar a densidade aparente do pó para partículas com formato esférico.

11.4. Otimização dos parâmetros das estratégias de construção (Capítulo 5)

Neste capítulo foram estudadas estratégias para a construção de peças a partir do processo de fusão seletiva por laser. No total, cinco experimentos foram realizados sendo os objetivos e resultados alcançados brevemente descritos nos próximos tópicos. Em todos os experimentos relativamente a este tópico, foi utilizado o método de construção por lâminas fixas com espessuras de camadas de pó depositado de 0,5mm resultando em camadas solidificadas com valor médio de 0,38mm.

11.4.1. Investigação sobre estratégias de deslocamento vetorial do laser e espaçamento dos vetores na fusão de pó de H13

Objetivo: Avaliar estratégias de deslocamento vetorial do foco do laser sobre a superfície da camada de pós e o espaçamento entre os vetores das estratégias com relação a geometria e defeitos encontrados nas amostras. Somente o pó de H13 foi testado neste experimento.

Método: Com base da literatura quatro estratégias (*filling*, *sequential*, *sequential alternated* e *refill* (Figure 5-1, página 87) e dois espaçamentos (0,5 e 0,6mm) foram testadas na construção de amostras. As amostras foram seccionadas transversalmente e fotografias de suas seções foram analisadas digitalmente quanto ao formato da seção e ao número de poros. Os parâmetros do ajuste do laser utilizados foram baseados no trabalho de Su (2002) (Energia do pulso (E) 10J, largura do pulso (w) 5ms, velocidade vetorial (v) 3,333mm/s, freqüência do pulso (f) 10Hz, potência média (P) 100W, pico de energia do pulso (P_{peak}) 2kW e densidade de energia (E_p) 37,5J/mm^2).

Resultado: Com estratégias *filling* e *sequential* fabricou-se amostras com poucos poros no entanto o formato das seções das amostras apresentou distorção excessiva. Em contraste, as amostras fabricadas pela estratégia *sequential alternated,* apresentaram boa forma da seção mas um elevado grau de porosidade. A estratégia que apresentou o melhor resultado, tanto quanto ao quesito formato da seção e baixa porosidade foi a estratégia *refill*. Uma figura bastante representativa entre as diferenças dos resultados obtidos é apresentada na Figure 5-6 (pág. 91). Os espaçamentos testados apresentaram pouca diferença nos resultados, no entanto, o espaçamento de 0,5mm apresentou melhores resultados (menor porosidade nas amostras).

11.4.2. Avaliação da perda de material fundido por detritos expelidos durante a fusão a laser

Objetivo: Mensurar a perda de massa por detritos expelidos durante o processo de fusão pela ação do laser. Na Figure 5-9 (pág. 94) é possível visualizar os detritos sendo expelidos durante o processo de fusão por laser.

Método: Substratos especiais para a fabricação de camadas únicas foram utilizados. A massa do substrato com o pó espalhado, antes da fusão e após a fusão, era mensurada (ver Figure 5-10, página 95, para elucidação). Os parâmetros do laser foram E: 10J, w: 5ms, v: 3,333mm/s, f: 10Hz, P: 100W, P_{peak}: 2kW e E_{ρ}: 37,5J/mm^2 (Su, 2002).

Resultado: A redução de massa por detritos apresentou ser elevada (18,8%) devido à elevada potência de pico utilizada nos parâmetros do laser. A rápida expansão e contração do plasma formado pelo aquecimento dos gases na região do foco do laser foi responsável pelo expelimento dos detritos.

11.4.3. Comparação da distribuição do calor sobre camadas fundidas utilizando diferentes estratégias

Objetivo: Comparar a distribuição de temperatura sobre a superfície de camadas fabricadas com diferentes estratégias de deslocamento vetorial do laser.

Método: Camadas individuais para cada uma das quatro estratégias (*filling*, *sequential*, *sequential alternated* e *refill*) foram fabricadas com o pó de H13 (parâmetros do laser: E: 10J, w: 5ms, v: 3,333mm/s, f: 10Hz, P: 100W, P_{peak}: 2kW e E_{ρ}: 37,5J/mm^2). Após a fabricação de cada camada, uma câmera de infravermelhos capturava imagens das camadas indicando a temperatura na superfície das amostras.

Resultado: A distribuição da temperatura sobre a superfície das camadas foi afetada pelas diferentes estratégias utilizadas. As estratégias *filling* e *sequential* demonstraram ser as camadas com maior concentração de calor. A *sequential* ainda apresentou uma segunda desvantagem que foi o acúmulo de detritos no último canto da camada a ser fundido. As camadas *sequential alternated* e *refill* apresentaram uma distribuição mais homogênea de temperatura. Nas Figure 5-12 (pág. 97), Figure 5-13 (pág. 97), Figure 5-14 (pág. 98) e Figure 5-15 (pág. 98) apresentam mapas 3D da distribuição de calor sobre cada uma das estratégias vetoriais testadas.

11.4.4. Investigação do efeito das estratégias na fusão de misturas de cobre e H13

Objetivo: investigar a influencia das estratégias e da adição de cobre (25 e 50%) sobre a geometria e defeitos nas amostras.

Método: Três composições bimodais de pós foram utilizadas: uma de H13 e outras duas com 25 e 50% de cobre. Novamente, as quatro estratégias foram utilizadas para fabricar corpos de prova. Fotografias da seção dos corpos de prova foram analisadas digitalmente quanto ao percentual de defeitos e geometria das amostras. Análise de variância foi utilizada para interpretar os resultados. Os parâmetros do laser utilizados foram os mesmos dos experimentos anteriores (E: 10J, w: 5ms, v: 3,333mm/s, f: 10Hz, P: 100W, P_{peak}: 2kW e E_{ρ}: 37,5J/mm^2).

Resultado: Na Figure 5-16 (pág. 100) é apresentado um quadro com seções de amostras representativas para cada combinação de mistura e estratégia. A estratégia que apresentou melhor desempenho (geometria e defeitos) foi a estratégia *refill*. A adição de cobre afetou os resultados, aumentado o número de defeitos (principalmente poros) nas amostras.

11.4.5. Avaliação da microestrutura de uma amostra com gradiente FGM na direção Z

Objetivo: Fabricar gradientes de H13 e Cu na direção de adição de camadas e avaliar a microestrutura dos materiais.

Método: Três composições bimodais de pós de H13, H13-25%Cu e H13-50%Cu foram utilizadas para fabricar duas amostras. A primeira mostra foi construída com quatro camadas de H13, quatro camadas de H13-25%Cu e quatro camadas de H13-50%Cu. A segunda amostra foi construída na ordem inversa iniciando pelo H13-50%Cu. Figure 5-20 (pág. 104) apresenta um esquema das amostras fabricadas. As amostras foram fabricadas com os mesmos parâmetros do laser utilizados nos experimentos anteriores. Após obtenção das amostras, estas foram seccionadas, embutidas, lixadas e polidas para análise em microscópios óticos e eletrônicos de varredura.

Resultado: Porosidade foi encontrada distribuída em todos os materiais. No entanto, a mistura de H13-25%Cu aparentou ter maior porosidade e apresentou fissuras ao longo da direção Z nas duas amostras fabricadas. Na Figure 5-22 (pág. 106) são apresentadas micrografias das amostras evidenciando poros, fissuras, aspecto “pele de peixe” pelo processamento do laser e homo e heterogeneidade dos materiais. O material com 25% de cobre apresentou uma estrutura homogênea com o cobre distribuído entre o espaço interdendrítico, misturado junto aos elementos de liga do H13. Na mistura com 50% de cobre, o material formou uma estrutura heterogênea com regiões isoladas de cobre e regiões formadas por cobre e H13 como na configuração do material com 25% de cobre. Micrografias de cada material podem ser observadas nas Figure 5-23 (pág. 106), Figure 5-24 (pág. 107) e Figure 5-25 (pág. 107).

11.5. Experimentos sobre parâmetros do laser (Capítulo 6)

Os parâmetros de ajuste do laser para processar as misturas de pós de H13 e Cu foram investigados. No primeiro experimento foram estudados os parâmetros para a mistura de H13-12,5%Cu. Em outro experimento, com base na metodologia empregada para a primeira mistura, foram otimizados os parâmetros para a fusão de H13 com 25, 37,5 e 50% de cobre. Como os experimentos anteriores apontaram, a estratégia mais apropriada foi a *refill* com 0,5mm de espaçamento entre os vetores. Portanto ela foi utilizada nos experimentos realizados posteriormente. Outra distinção destes experimentos é o uso do método de fabricação com plataforma e funil. Com isso, a espessura de camada de pó depositada passou a ser de 0,25mm, metade da utilizada nos experimentos anteriores.

11.5.1. Parâmetros do laser para o processamento de mistura de H13-12,5%Cu

Objetivo: Otimizar os parâmetros do laser (energia e largura do pulso, freqüência e velocidade vetorial) a fim de reduzir o número de defeitos na mistura H13-12,5%Cu.

Método: Através das metodologias de projeto de experimentos, amostras com diversas combinações dos quatro parâmetros citados foram fabricadas. Inicialmente foi utilizado o método Box-Behnken para estabelecer a janela de parâmetros mais apropriada. Em um segundo passo, uma análise fatorial completa, somente para os parâmetros energia e largura do pulso foi realizada. As amostras eram fabricadas, seccionadas, polidas e analisadas digitalmente.

Resultado: a largura e a energia do pulso do laser apresentaram-se como parâmetros de maior importância no controle de defeitos nas amostras. Porém as combinações com a velocidade vetorial e freqüência tiveram grande influência também. Com a ampla gama de combinações do experimento Box-Behnken foi possível determinar velocidade vetorial e freqüência de pulsos mais adequadas. A fixação destes parâmetros aumentou a confiabilidade do modelo estatístico apesar de que, devido aos fenômenos envolvidos no processo, esta ficou relativamente baixa. Com o experimento fatorial a confiabilidade aumentou um pouco. Os parâmetros iniciais utilizados por Su (2002) (E: 10J, w: 5ms, v: 3,333mm/s, f: 10Hz) geravam em torno de 15% de defeitos na seção das amostras. Com a otimização final através do experimento fatorial (E: 9,16J, w: 20ms, v: 5mm/s, f: 20Hz) foi possível obter uma média entre 2-3% de defeitos das seções das amostras com 12,5%Cu. A principal diferença entre os parâmetros é o aumento da largura do pulso do laser. Com isso, a energia de pico foi reduzida de 2kW para 0,45kW.

11.5.2. Parâmetros do laser para o processamento de mistura de H13-25, 37,5 e 50%Cu

Objetivo: Otimizar os parâmetros de processamento do laser para as misturas de H13 com 25, 37,5 e 50% de cobre.

Método: O mesmo método de experimento fatorial descrito no tópico anterior e utilizado com velocidade vetorial e freqüência fixas em 5mm/s e 20Hz, respectivamente.

Resultado: Assim como no experimento anterior, novos parâmetros de processamento do laser foram encontrados para cada uma das misturas utilizadas. A Table 6-10 (pág. 130) apresenta todos os parâmetros considerados ótimos para cada uma das misturas. Foi verificado que com o aumento da proporção do cobre fez-se necessário aumentar a energia do pulso, aumentando a potência de pico. A razão mais direta para este fato é que, para fundir o material, a maior refletividade do cobre à luz do laser precisou ser compensada por um aumento na potência (ou densidade de energia).

11.6. Caracterização experimental de propriedades de FGM de H13-Cu (Capítulo 7)

Este capítulo descreve a obtenção das propriedades das misturas de H13-Cu. Assim, o desempenho do método de fabricação, dos materiais formados pe;as composições de H13 e Cu, assim como o desempenho do gradiente foram avaliados.

11.6.1. Análise da densidade

Objetivo: Mensurar a densidade de cada uma dos cinco materiais obtidos (H13, H13-12,5%Cu, H13-25%Cu, H13-37,5%Cu e H13-50%Cu);

Método: Paralelepípedos individuais de cada mistura foram construídos com os parâmetros do laser ajustados em E: 10J, w: 20ms, v: 5mm/s, f: 20Hz. Após a fusão estes foram retificados. Suas massas e dimensões foram obtidas e a densidade calculada.

Resultado: As amostras finalizadas após a retífica podem ser visualizadas na Figure 7-3 (pág. 136). Na Table 7-1 (pág. 137) são apresentados as densidades obtidas com respectivos intervalos de confiança. Na Figure 7-4 (pág. 137) é apresentada a tendência da densidade obtidas das amostras. Foi possível identificar que a densidade da mistura com 12,5%Cu é menor que puro H13. Isso se deve ao fato do maior número de defeitos internos presentes nesta mistura. Com o aumento de cobre na mistura com 25%Cu a densidade alcança a densidade inicial do H13 fundido por laser. A mistura com maior densidade obtida foi com 37,5% de Cu. Teoricamente, a mistura de 50%Cu deveria ter maior densidade, no entanto, a provável maior quantidade de defeitos na forma de poros fez com que mesma tivesse densidade levemente superior a do H13 fundido. Apesar de que, na média, as misturas apresentaram valores de densidade baixos quando comparados com estimativas feitas através das regras das misturas, estas podem ser consideradas elevadas ou normais para processamento de pós.

11.6.2. Coeficiente de condutividade térmica

Objetivo: Mensurar o coeficiente de condutividade térmica para cada um dos materiais obtidos pelo processo de fusão seletiva a laser.

Método: Um equipamento para medir condutividade térmica analiticamente foi utilizado (Figure 7-5, página 139). Cada um dos paralelepípedos fabricados para o experimento de densidade foi utilizado neste experimento e seus coeficientes de condutividade térmica foram obtidos.

Resultado: Na Table 7-3 (pág. 140) são apresentados os valores lidos e corrigidos com base em uma amostra de alumínio aferida como referência durante os experimentos. Na média, os valores da condutividade térmica para 12,5%Cu e 25%Cu ficaram abaixo do valor de condutividade obtido para o H13. Na Figure 7-6 (pág. 141) estes valores são colocados junto com suas variações. Quando estes valores são desenhados juntos com as estimativas pelas regras das misturas (Figure 7-7, página 142, entre outros modelos), foi possível perceber que os valores se aproximam das estimativas pela fórmula de Voigh (2.4, do texto em inglês). Os possíveis valores inferiores obtidos para 12,5% e 25%Cu provavelmente corresponderam à um número maior de defeitos internos assim como na densidade mensurada.

11.6.3. Coeficiente de expansão linear

Objetivo: Obter o coeficiente de dilatação linear dos materiais.

Método: Amostras retificadas de cada material foram inseridas individualmente em um equipamento para medir a variação linear das amostras com o aumento da temperatura.

Resultado: A dilatação das amostras mostrou que, pelo material não ter passado por tratamento térmico, ocorreram variações instantâneas dos coeficientes de dilatação. Nas temperaturas inicias (<150^{o}C) os materiais possuíam coeficiente de dilatação menor do que acima de 200^{o}C. Entre 200 e 600^{o}C o coeficiente foi mais estável. O maior coeficiente de dilatação encontrado foi o do H13 seguido pela amostra com 12,5% de Cu. A microestrutura mais homogênea destas amostras deve ter favorecido a expansão do material.

11.6.4. Microdureza

Objetivo: Obter a microdureza em escala vickers dos materiais.

Método: Amostras com gradientes entre H13 e H13-50%Cu com incrementos de 12,5% de cobre foram testadas em equipamento apropriado.

Resultado: A dureza medida em cada região das amostras mostrou que o material é menos duro à medida que aumenta o percentual de cobre. No entanto, quanto maior o percentual de cobre maior a variação nos resultados obtidos devido a heterogeneidade da microestrutura para altos percentuais de Cu. A Table 7-6 (pág. 147) apresenta os valores de dureza obtidos na escala vickers. A dureza do H13 ficou acima da referência bibliográfica. Isso porque o material solidificado rapidamente possui uma microestrutura refinada (dendrítica).

11.6.5. Nanodureza

Objetivo: Mensurar, pelo método de nanodureza, o módulo de elasticidade e a dureza do gradiente.

Método: Através do método desenvolvido por Oliver e Pharr (1992), uma amostra com gradiente entre H13 e H13-50%Cu foi submetida a diversos ciclos[12] de medição da nanodureza em diferentes pontos ao longo do gradiente das amostras (Figure 7-13, pág. 149).

---

[12] Total de 305 ciclos, cerca de 70 ciclos por composição.

Na Figure 7-14 (pág. 150) pode ser visualizada a amostra montada na máquina de nanodureza.

Resultado: Assim como os resultados do teste de microdureza, os resultados do experimento de nanodureza mostraram que a dureza e o módulo de elasticidade decaem com o aumento do percentual de cobre e a variabilidade nos resultados aumenta. Na Figure 7-15 (pág. 151) curvas de carga e penetração representativas para cada região do gradiente são apresentadas. Os resultados de dureza foram um pouco mais elevados que os resultados obtidos pelo ensaio de microdureza. No entanto, a variabilidade ficou maior devido ao tamanho do indentador que passa a ser mais sensível a variações na microestrutura. O módulo de elasticidade ficou um pouco acima do calculado pelas regras das misturas. A Table 7-7 (pág. 154) sumariza os resultados obtidos nos experimentos e compara com os valores de referência e valores estimados.

11.6.6. Ensaio de tração

Objetivo: Realizar o ensaio de tração em corpos de prova com gradientes entre H13 e H13-50%Cu.

Método: Um corpo de prova foi projetado conforme normas (ISO e EU). Nas extremidades o corpo de prova foi fabricado com H13 e no meio H13-50%Cu. O gradiente entre estes materiais ficou contido dentro da região de colocação do extensômetro no corpo de prova. Foram fabricados corpos com camadas de 0,25 e 0,50mm de espessura utilizando os parâmetros do laser otimizados para 12,5% de Cu.

Resultado: Todos corpos de prova quebraram na região dos corpos formada por H13-25%Cu. A Figure 7-32 (pág. 166) mostra os corpos de prova fabricados com espessura de camada de 0,25mm. Na Figure 7-33 (pág. 166) são apresentadas imagens de seções dos corpos de prova ensaiados. Fissuras são perceptíveis na Figure 7-33 (d). Nestas fissuras, visualizadas com um microscópio eletrônico de varredura (Figure 7-34; pág. 167), é possível identificar a orientação vertical na direção de construção z (eixo de adição de camadas). A Table 7-13 (pág. 167) apresenta os resultados do módulo de elasticidade, elongação e resistência a tração obtidos com o ensaio. Os resultados obtidos mostraram que a deformação plástica dos corpos de prova foi quase nula. A resistência mecânica ficou abaixo da resistência mecânica do cobre utilizado como referência. A presença das fissuras resultantes do processamento do material foi apontada como maior causa da redução das propriedades mecânicas. Na Figure 7-35 (pág. 168) uma comparação visual entre o módulo de elasticidade é apresentada entre os resultados, padrões e estimativas.

11.7. Aplicações de componentes feitos de H13-Cu FGM (Capítulo 8)

11.7.1. Avaliação do uso potencial para moldagem por injeção

Objetivo: Avaliar se moldes poderiam ser beneficiados com a diferenciação das propriedades térmicas pelo uso de FDMs entre H13 e Cu.

Método: Um experimento numérico foi utilizado para avaliar o desempenho de insertos de H13 e Cu, com e sem refrigeração, em um molde isolante. Posteriormente, o inserto foi construído e a temperatura do molde foi aferida. Também se mediu o grau de cristalização do material onde os insertos teriam maior influência sobre a extração de calor.

Resultado: Tanto os resultados numéricos quanto os resultados reais apresentaram a mesma tendência. Devido ao Cu ter menor capacidade de armazenar energia do que o H13 mas possuir elevada capacidade de transporte de energia, os resultados apresentaram que a região da peça moldada sobre o inserto com gradiente ficou mais cristalina do que a moldada sobre o H13. Isso indicou, como nos resultados numéricos, que a peça naquela região (H13-50%Cu) resfriou mais lentamente do que na região do H13. No entanto, os resultados numéricos apontaram que, no caso de construção de um molde com canais de refrigeração que o inserto possa transferir o calor da cavidade para uma região mais fria, a região composta por H13-50%Cu teria vantagem sobre o resfriamento do material.

11.7.2. Obtenção de geometrias complexas

Objetivo: Demonstrar a possibilidade de obter geometrias mais complexas, mesmo no sistema atual de fabricação.

Método: A fabricação de uma geometria mais complexa foi programada e executada.

Resultado: Foi possível obter a geometria como o esperado. A geometria projetada poderia ser utilizada para extração diferencial de calor em tubulações industriais específicas.

11.8. Conclusões (Capítulo 9)

O objetivo desta pesquisa foi investigar a fabricação de componentes feitos com materiais com gradientes funcionais entre H13 e Cu para a aplicação em moldagem por injeção. Modelos teóricos foram usados para estimar as propriedades de misturas de H13 e Cu. Baseado na técnica de fusão seletiva a laser, um laser de Nd:YAG foi utilizado para fundir misturas de pós de H13 e Cu ajustados em tamanhos e proporções específicas. Estratégias de construção e parâmetros de processamento foram otimizados para produzir amostras com alta densidade. As novas composições de materiais obtidos foram caracterizadas por diferentes técnicas para medir propriedades mecânicas e térmicas. Baseado nos objetivos e delineamento apresentados na seção 11.2, as seguintes conclusões puderam ser feitas:

Otimização das estratégias de construção:

- Componentes densos de H13 e H13-Cu foram obtidos pelo processo de fusão seletiva a laser utilizando um laser Nd:YAG pulsado de alta potência. Das alternativas estudadas, a melhor estratégia de deslocamento vetorial do laser foi a estratégia *refill* com um espaçamento entre vetores de 0,5mm e espessura de camada de 250µm para obter componentes densos de H13;
- As outras alternativas testadas (*filling, sequential* e *alternated*) produziram elevada porosidade e formas distorcidas nas amostras;

Otimização dos parâmetros de processamento do laser:

- Para produzir amostras densas a partir dos pós e misturas, o método de superfícies de resposta provou ter sido muito útil para a otimização dos parâmetros do laser. Através da utilização desta ferramenta estatística, os parâmetros otimizados do laser foram identificados para que os defeitos poros e fissuras fossem reduzidos;
- Estes parâmetros ótimos identificados para cada mistura de pós utilizada neste trabalho são listadas na Table 9-1 (pág. 191). Estes parâmetros asseguram densidades acima de 90% dos valores teóricos;
- Estes parâmetros também reduziram a formação de plasma e expelimento de detritos para cada composição estudada de H13-Cu. Como conseqüência, a distorção (redução) de volume das amostras também foi reduzida. Adicionalmente, fissuras e porosidades foram diminuídas. Foi evidenciado que quanto maior o percentual de cobre maior a energia do laser requerida para fundir o material. No entanto, elevada energia do laser favorece a formação de plasma e expelimento de detritos;

Caracterização do gradiente H13-Cu:

- A análise das amostras mostrou a formação de microestruturas homogêneas com a adição de Cu entre 12,5 e 25% (em massa) ao pó de H13. O Cu estava presente com os elementos de liga do H13, inseridos entre as dendritas de martensita. A partir de 37% de Cu misturado ao H13, microestruturas heterogêneas foram formadas. Áreas isoladas de Cu foram identificadas;
- Fissuras e poros estiveram presentes nas amostras. A formação de poros pode ser associada a utilização da estratégia vetorial do laser, espaçamento dos vetores, percentual de Cu e gás aprisionado. No entanto, o uso da estratégia *refill* com camadas de 250µm de espessura, reduziram drasticamente a presença de poros para todas as composições de H13-Cu;

- A otimização dos parâmetros do laser mostrou que fissuras foram drasticamente reduzidas, mas não eliminadas. As fissuras formaram-se no centro do cordão de material fundido pelo laser, como resultado da solidificação e contração final da frágil martensita do H13. A adição de Cu agravou o fenômeno das fissuras, especialmente para 12,5 e 25%Cu. Para percentuais mais elevados de Cu, as regiões de Cu isolado podem ter servido como agentes de alívio de tensões;
- As amostras obtidas das misturas de pó foram caracterizadas e suas propriedades medidas foram comparadas com modelos de estimativa apresentados na revisão bibliográfica (2.4, pág. 29). As propriedades mensuradas para cada composição são apresentadas na Table 9-2 (pág. 192);
- Corpos de prova para tração com gradiente formado por cinco diferentes materiais, de H13 a H13-50%Cu foram fabricados e testados. Foi demonstrado que a composição de H13-25%Cu tinha a menor resistência mecânica. O fenômeno de fissuras foi identificado como o fator chave que afetou o alongamento, módulo de elasticidade e tensão de ruptura das amostras;

Avaliação de um molde com gradiente:

- O trabalho também provou que ferramentas com gradientes de H13 e Cu podem ser utilizadas para moldagem por injeção. No entanto, foi detectado que o molde com gradiente deve ser utilizado quando o transporte de calor é possível de uma região quente para uma região fria. Os resultados mostraram que o grau de cristalinidade das peças pode ser afetado pela presença do Cu no H13. Como conseqüência, as propriedades do material injetado podem ser afetadas por menores ciclos de resfriamento. Assim sendo, peças podem ser ejetadas mais rapidamente do molde, aumentando a produtividade;
- Peças complexas podem ser obtidas por este processo com a automação do sistema de reposição de camadas e melhorias no software CAM. Para obter gradientes com distribuição complexa de composição de materiais é requerido o desenvolvimento completo de um sistema de Controle de Deposição Localizada.

11.8.1. Contribuições para o mundo científico

A metodologia utilizada neste trabalho foi de grande valia para explorar a fabricação de materiais com gradientes funcionais pelo processo de fusão seletiva por laser. O procedimento para determinar primeiramente os parâmetros de construção, seguido pelos parâmetros de processamento do laser foi bem sucedido. A caracterização das propriedades dos materiais foi necessária para conhecer as potencialidades do processo. Como conseqüência, este trabalho contribuiu para a comunidade científica como inovador nos seguintes aspectos:

- Contribuiu operando parâmetros de processamento utilizando um laser Nd:YAG pulsado de alta potência para processar camadas pré-depositadas de pó de H13 e misturas de H13-Cu;
- A aplicação da metodologia de superfícies de resposta e o sumário dos parâmetros do laser otimizados para obter peças de elevada densidade e a identificação dos parâmetros mais importantes para o laser pulsado de Nd:YAG para o processo de fusão seletiva a laser;
- Funis multi-compartimentais foram utilizados com sucesso para construir componentes com gradientes funcionais por variação da composição do material;
- O conhecimento para a produção de insertos com gradientes na direção X pelo processo de fusão seletiva a laser para a moldagem por injeção de peças plásticas. O trabalho provou de maneira significativa que o molde FGM pode ser fabricado e aplicado na moldagem por injeção;
- As propriedades das amostras de material H13-Cu obtidas comparadas com modelos teóricos de predição;

12. Publications List

Title:	Fabrication of x-graded H13 and Cu powder mix using high power pulsed Nd:YAG laser
Authors:	V. E. Beal P. Erasenthiran N. Hopkinson P. Dickens C. H. Ahrens
Type:	Technical congress paper
Name:	Proceedings of Solid Freeform Fabrication Symposium, pp 187-197, Austin, USA
Date:	September 2004
Abstract:	The manufacturing of Functionally Graded Material (FGM) parts using Solid Free Form manufacturing technologies has been carried out since early 1980. At present, most of the powder manufacturing techniques are being focused on layering powder with different powder blend compositions with Z gradients (graded in direction of layer build). Although, there are a few researchers working on multi powder feeder and deposition system, the study of laser fusion of the deposited powder (by a powder deposition system) is minimum or not known to date. Consequently, the manufacturing of functionally graded structures is still geometry limited. This work was focused on the manufacturing of X-graded (graded along the powder bed plane) specimens with H13 tool steel and Cu mix. Five bimodal powder blends were used with a multi-container feed hopper to spread powder layers for the selective laser fusion of the powder. The powder was fused using a high power Nd:YAG pulsed laser using a specific scanning strategy to reduce porosity. Specimens were produced with graded Cu within the H13 matrix. The specimens were analysed for dimensional accuracy, microstructure, porosity, cracks and micro hardness of the FGM.
Keywords:	functionally graded materials, laser fusion

Title: Scanning strategies and spacing effect on laser fusion of H13 tool steel powder using high power Nd:YAG pulsed laser

Authors: V. E. Beal
P. Erasenthiran
P. Dickens
C. H. Ahrens
N. Hopkinson

Type: Technical journal

Name: International Journal of Production Research (Taylor & Francis)

ISSN: 0020-7543 (printed version)

ISSN: 1366-588X (online version)

Date: Submitted in 2004, accepted April 2005, proofed, waiting for publication.

Abstract: Layered manufacturing technologies have been used to produce complex parts of diversified materials through different physical/chemical manufacturing principles. Nevertheless a few materials are commercially available to build parts suitable for engineering applications. In this paper, the powder fusion of H13 tool steel is investigated. A high power Nd:YAG pulsed laser source on a CNC machine was used to fuse the powder, layer by layer, building solid cubes for further analysis. Four different laser vector scanning strategies were evaluated by comparing the results of porosity and layer distortion. The complexity of the laser/powder interaction shows that a complex strategy must be used to avoid porosity and distortion.

Keywords: laser fusion, rapid manufacturing, tool steel

Title: The Effect of Scanning Strategy on Laser Fusion of H13 and Cu Mix Powders Using High Power Pulsed Nd:YAG Laser

Authors: V. E. Beal
P. Erasenthiran
N. Hopkinson
P. Dickens
C. H. Ahrens

Type: Technical journal

Name: International Journal of Advanced Manufacturing Technology (Springer)

ISSN: 0268-3768 (printed version)

ISSN: 1433-3015 (electronic version)

Date: Submitted in 2004, accepted April 2005, proofed, waiting for publication.

Abstract: In recent years, research has been undertaken on manufacturing of Functionally Graded Materials (FGM) using Layered Manufacturing Technologies (LMT), also commonly known as Rapid Prototyping (RP), Solid Freeform Fabrication (SFF) etc. The use of LMT to build complex FGM parts could meet optimum engineering design for various applications such as high performance die-casting tools. In this context, H13 tool steel is considered a suitable material because of the high resistance to thermal fatigue and dimensional stability. Nevertheless, H13 with a low heat conduction coefficient is not thermally efficient for certain part geometries. With this in mind, the use of functionally graded techniques to disperse copper to specific regions/volumes of a H13 mould could lead to higher performance of the tool. The laser fusion of different proportions of Cu (0, 25 and 50% by weight) powder dispersed in H13 were analysed in this work. Additionally, different laser strategies were used to statistically analyse effects with respect to the composition of Cu. It was found that the refill strategy produces better results compared to all other scanning methods. The H13 with 25%Cu mix produced a homogeneous structure but cracks were observed along the cross section of the 25%Cu specimens. The pure H13 had a lower porosity with fine dendrite structures. The H13 with 50%Cu produced a non homogeneous structure. This paper also discusses the microhardness tests results with respect to Cu composition and scanning strategy. Also, in order to identify the effect of powder composition layer on the subsequent layers and the cooling rate effect, samples were produced and analysed. One started with 100% H13 and ended with H13+50%Cu while other started with H13+50%Cu and ended with 100% H13.

Keywords: layered manufacturing, rapid manufacturing, functionally graded materials, selective laser fusion

---

Title: Optimisation of processing parameters in laser fused H13/Cu materials using the response surface method (RSM)

Authors: V. E. Beal
P. Erasenthiran
N. Hopkinson
P. Dickens
C. H. Ahrens

Type: Technical journal

Name: Journal of Materials Processing Technology (Elsevier)

ISSN: 0924-0136 (printed version)

ISSN: --- (electronic version)

Date: Submitted in 2004, accepted May 2005, waiting for final proof.

Abstract: The goal for functionally graded materials is to obtain a solid structure with more than one material in different regions according the functionality and tailored by graded transitions. This increases the capabilities of the structure as each graded region exhibits different functions in the designed application. As an example, tool steel (H13) could be graded with copper (Cu). H13 is a hard material with dimensional stability, low distortion and wear resistance which is suitable for making mould and dies. On the other hand, Cu extracts heat efficiently and could be more suitable in regions where cooling/heating channels are not effective in mould and dies. This paper presents the investigation of laser fusion of a mixture of H13 and Cu powders. In previous work, cracks and porosity formed in the H13/Cu regions when the Cu content was between 12.5 and 37.5%. In order to eliminate or reduce cracks and porosity, Response Surface Methodology (RSM) was used to understand the relationship between laser processing parameters and the defects (cracks and porosity). This study was carried out using Box-Behnken methods. Thereafter, factorial analysis was performed using the most significant factors, obtained from Box-Behnken analysis. The analyses showed that cracks and porosity were reduced successfully. Regression analyses were performed on both methods in order to predict the defects model. The optimised process parameters reduces the cracks and porosity from 15.32 to 2.54%. Microhardness tests on both specimens produced using original and the optimised parameters shows no difference.

Keywords: laser fusion, functionally graded materials, layer manufacturing, response surface methodology

Title: Evaluating the use of FGM inserts on the injection moulding of plastics parts

Authors: V. E. Beal
P. Erasenthiran
N. Hopkinson
P. Dickens
C. H. Ahrens

Type: Technical journal

Name: Imech (UK)

Date: Submitted in 2005

Abstract: The need for increasing productivity and shape complexity on moulding industry push the research in the tool optimization. A field of research is the development of functionally graded materials for injection moulds. The use of distinctive regions of higher heat conduction or wear resistance can be useful for producing better and cheaper injection moulded parts. For higher conductivity, this can be achieved locally adding, for example, copper to a mould base material such as tool steel. In this work, the use of Cu-tool steel functionally graded materials insert is evaluated. A stereolithography injection mould was built and polypropylene parts were injected. The degree of crystallinity of the moulded parts was evaluated by DSC test. The temperature of the injection moulding was also evaluated.

Keywords: functionally graded material, injection moulding, rapid manufacturing, crystallinity

Title: Fabrication of H13/Cu Graded Materials Using High Power Pulsed Nd:YAG Laser

Authors: P. Erasenthiran
V. E. Beal
N. Hopkinson
P. Dickens
C. H. Ahrens

Type: Congress / Conference paper

Name: Proceedings of PM2TECH2005 – International Conference on Powder Metallurgy & Particulate Materials, Montreal, Canada

Date: June 2005

Abstract: This paper presents a detail investigation of laser fused tool steel (H13) and Cu powder blends in order to optimise heat control on injection mould tools. Various percentages of Cu in H13 powder were pre-mixed before laser fusion. An optical fibre delivered high power pulsed Nd:YAG laser (550W) was used in this investigation. Parts were built layer by layer. Parts produced were above 90 percent dense. The optimised parameters were used to fabricate the Cu-H13 graded parts. These parts produced different results from homogeneous to heterogeneous microstructure. High content of Cu in the powder formed isolated region of Cu matrix structure from H13-Cu region. The hardness and elastic modulus was measured by load and displacement sensing indentation. Both measured properties on the fused materials were higher than reference materials and variability had increased with the Cu percentage.

Keywords: Laser material processing, functionally graded materials, selective laser fusion

---

Title: Fabrication of Functionally Graded Materials using High Power Nd: YAG Laser

Authors: P. Erasenthiran
V. E. Beal
N. Hopkinson
P. Dickens
C. H. Ahrens

Type: Congress / Conference paper

Name: Proceedings of Sintering 05 – 4th International Congress on Science, Technology and Applications of Sintering, Grenoble, France

Date: August 2005

Abstract: A functionally graded material (FGM) specimen was manufactured by laser fusion technology from H13 and Cu powder. This graded specimen was built with the intention to test the capabilities to increase the thermal conductivity of the base material (H13) by adding different weight proportions of Cu. This material could be used in the manufacturing of optimized heat transfer injection moulding tools. A high power pulsed Nd: YAG laser (550W) was used to fuse the powders layer-by-layer. The specimen, after post processing, was submitted to microhardness test to study the effect on hardness along the graded region of H13-Cu. Also, the specimen was placed over a hot plate and infrared images were taken using thermal imaging camera. The analysis of the images proved that there was a tendency of the heat to flow at the richer Cu regions.

Keywords: Laser material processing, functionally graded materials, selective laser fusion